ABSTRACT

Title of dissertation: BROADBAND IN-PLANE RELATIVE PERMITTIVITY CHARACTERIZATION OF RUDDLESDEN-POPPER $Sr_{(n+1)}Ti_{(n)}O_{(3n+1)}$ THIN FILMS

Nathan D. Orloff, Doctor of Philosophy, 2010

Dissertation directed by: Professor Ichiro Takeuchi, and Dr. James C. Booth

Department of Physics

We present a broadband on-wafer measurement technique for the characterization of the in-plane complex relative permittivity of a thin-film test wafer and a companion substrate test wafer from 100 Hz to 40 GHz, and potentially to 110 GHz. From 100 Hz to 300 MHz, the approach uses an ensemble of interdigitated capacitors with different interdigitated active lengths ℓ = (0.100 mm, 0.325 mm, 0.875 mm, 1.835 mm, 2.9 mm) fabricated on both test wafers. Within this regime, from 100 Hz to 1 MHz, the measurements were performed with an inductance-capacitance-resistance meter. From 1 MHz to 300 MHz, the scattering parameters of the set of interdigitated capacitors were measured with a radio frequency vector network analyzer. In the high frequency regime, 300 MHz to 40 GHz, we measure scattering parameters of a set of coplanar waveguides of active lengths ℓ = (0.420 mm, 1.270 mm, 2.155 mm, 3.22 mm, 3.993 mm, 5.933 mm) fabricated on the test wafers. We extracted the capacitance

and conductance of the interdigitated capacitors and coplanar waveguides on the test wafers for the appropriate frequency regimes. We then obtained a mapping function from 2D finite element simulations that relates the change in capacitance of the thin-film test wafer relative to the companion substrate test wafer to the real part of the in-plane relative permittivity. The imaginary part of the in-plane relative permittivity was obtained from the real part of the in-plane relative permittivity and the in-plane loss tangent.

We applied this broadband dielectric spectroscopy technique to explore the frequency-dependent relative permittivity of unstrained Ruddlesden-Popper series $Sr_{n+1}Ti_nO_{3n+1}$(n = 1, 2, 3) thin films as a function of temperature and dc electric field. At room temperature, the in-plane relative permittivities (ϵ_{11}) obtained for $Sr_{n+1}Ti_nO_{3n+1}$(n = 1, 2, 3) were 42$\pm$3, 54$\pm$3, and 77$\pm$2, respectively, and were independent of frequency. At low temperatures, ϵ_{11} increased with a behavior consistent with an incipient ferroelectric, and paraelectric behavior developed in $Sr_4Ti_3O_{10}$.

In 2004, J. H. Haeni, *et al.* showed that $SrTiO_3$($n = \infty$) on $DyScO_3$(110) undergoes a ferroelectric to paraelectric phase transition around room temperature [1]. As a means to understand the origins of the loss and tunability in strained $SrTiO_3$($n = \infty$), we performed our broadband dielectric spectroscopy technique on epitaxial thin-films of Ruddlesden-Popper series $Sr_{n+1}Ti_nO_{3n+1}$(n = 2, 3, 4, 5, 6) on the rare-earth scandate substrates, $DyScO_3$(110) and $GdScO_3$(110). For these thin films, $DyScO_3$(110) and $GdScO_3$(110) corresponded to biaxial tensile strain of approximately 1% and 1.7%, respectively. The thin films were 50 nm thick on $DyScO_3$(110) and 25 nm thick on $GdScO_3$(110), which ensured uniform strain throughout the film. We report the dependence of the critical temperature, tunability, and loss tangent on series number and strain at 1 MHz. We also examined the broadband frequency dependent dielectric properties of these thin films as a function of temperature, electric field, series number and strain.

BROADBAND IN-PLANE RELATIVE PERMITTIVITY CHARACTERIZATION OF RUDDLESDEN-POPPER $Sr_{(n+1)}Ti_{(n)}O_{(3n+1)}$ THIN FILMS

by

Nathan D. Orloff

Dissertation submitted to the Faculty of the Graduate School of the
University of Maryland, College Park in partial fulfillment
of the requirements for the degree of
Doctor of Philosophy
2010

Advisory Committee:
Professor Ichiro Takeuchi, Chair/Advisor
Dr. James C. Booth, Co-Advisor
Professor Steven M. Anlage
Professor J. Robert Anderson
Associate Professor Ian Appelbaum
Professor Robert M. Briber

DEDICATION

This is for Jaclyn, and my Mom, and Dad.

As it neared the top of the grade, which had so discouraged the larger engines, it went more slowly. However, it still kept saying, "I–think–I–can, I–think–I–can." It reached the top by drawing on bravery and then went on down the grade, congratulating itself by saying, "I thought I could, I thought I could."-Mary C. Jacobs

ACKNOWLEDGMENTS

The first and most important lesson I learned while in pursuit of this degree was that it is impossible to solve life's hardest problems working alone. The work I have done is largely a result of advice and help of my mentors, peers, friends and family. If I properly thanked all the people who have helped me along this path I am sure this section would be longer than my thesis. You deserve more thanks than just your name in a list, and there are some of you I am sure I have missed. So, if you are reading this, then please accept my apology and remember I could not have done this without *you*.

Prof. D. I. & S. N. Orloff, L. Kaiser, J. Kaiser, Dr. M. & R. Wilson, J. & B. Kaiser, S. & R. London, R. & B. Hoffman, Drs. J. & D. Doran, M. & L. Schriber, M. & M. Orloff, M. & D. Lizmi, E. & S. Dennis, M. Dennis, J. Dennis, F. Orloff, C. J. & J. Long, Dr. E. Engelson, Dr. J. K. Hall, B. Smith, W. Young, A. Gretes, M. Hanlon, J. Mays, J. Kanner, L. Kirn, Dr. J. Miller, Mr. C. & A. McCann, Dr. M. R. Clary, B. Christy, Dr. C. Stark, Dr. K. Gustofson, Dr. R. Artuso, Dr. P. Redl, Prof. B. R. Conrad, Prof. J. Mateu, Dr. S. K. Dutta, Prof. J. R. Simpson, Dr. S. Hemmady, Dr. D. Mercia, Prof. S. C. Lee, Prof. A. Lewandowski, Prof. J. R. Dorfmann, Prof. C. Collado, Mr. E. Rocas, X. Li, Y. Wang, A. Haddock, Dr. S. R. Lee, Dr. S. L. Clement, Dr. D. Gu, Dr. G. C. Hilton, J. A. Beall, Dr. F. Altomare, Dr. P. Dresselhaus, Dr. Y. Xu, Dr. T. M. Wallis, Dr. P. Kabos, L. Vale, Dr. J. Higgins, Dr. M. Janezic, Dr. D. F. Williams, D. Walker, R. Ginley, Dr. M. Kelley, S. Rivera, T. Gleason, L. O'Hara, B. Kozlowski, J. Hessing, R. Monkfort, L. DeSalvo, N. K. Morris, Prof. T. Cohen, Prof. S. Wallace, Prof. N. Chant, Prof. H. D. Drew, Prof. J. Goodman, Prof. S. Kamba, Prof. S. Stemmer, Prof. C. J. Fennie, T. Birol, C. H. Lee, Prof. I. Appelbaum, Prof. R. M. Briber, Prof. J. R. Anderson, Prof. S. M. Anlage, Prof. D. G. Schlom, Prof. I. Takeuchi, and Dr. J. C. Booth. I profoundly thank J. P. King for his support during the course of this work and Prof. D. I. Orloff for his critical review of this dissertation.

Finally, I thank my soon to be wife, J. R. Dennis. My love for you always grows.

Contents

List of Tables

List of Figures

Nomenclature

β Cole-Cole function, exponent related to the distribution of relaxation times

ℓ active length ..... [mm]

ϵ_{11} real part of the relative in-plane permittivity .....

ϵ_∞ Cole-Cole function, high frequency limit of the real part of the relative permittivity .....

ϵ_s Cole-Cole function, low frequency limit of the real part of the relative permittivity .....

γ propagation constant .....[1/m]

ω angular frequency ..... [rad·Hz]

σ conductivity ..... $[\frac{1}{\Omega \cdot \mathrm{m}}]$

$\tan(\delta_{film})$ the loss tangent of the film .....

$\tan(\delta_{LCR})$ the loss tangent of the device measured by the LCR meter .....

$\tan\delta_{11}$ in-plane loss tangent .....

τ Cole-Cole function, relaxation time .....[s]

C capacitance per unit length .....[F/m]

C_{film} the contribution of the film to the capacitance per unit length ..... [F/m]

C_{LCR} capacitance measured by the LCR meter .....[F/m]

C_{sub} capacitance per unit length of the device on the substrate .....[F/m]

C_{tot} total capacitance per unit length of the device on the thin film .....[F/m]

G conductance per unit length .....[1/(Ω·m)]

G_{film} the contribution of the film to conductance per unit length ..... 1/(Ω·m)

G_{sub} conductance per unit length of the device on the substrate ..... [1/(Ω·m)]

G_{tot} total conductance per unit length of the device on the thin film ... [1/(Ω·m)]

K_{11} real part of the in-plane relative permittivity .....

K_{film} mapping function, real part of the in-plane relative permittivity .....

K_{sub} mapping function, real part of the in-plane relative permittivity .....

L inductance per unit length .....[H/m]

R resistance per unit length .....[1/(Ω·m)]

T_1 Port 1 error box in T-parameter formalism .....

T_2 Port 2 error box in T-parameter formalism .....

Y_g shunt admittance .....[1/Ω]

Y_s series admittance .....[1/Ω]

Z characteristic impedance .....[Ω]

Z_r reference impedance, ...[50Ω]

c center conductor or center conductor width .....

CPW coplanar waveguide .....

Cs series capacitor .....

DUT device-under-test .....

g gap or gap width .....

g-s-g ground-signal-ground .....

g.p. ground plane .....

HF high frequency .....

IDC interdigitated capacitor .....

LCR meter Inductance-Capacitance-Resistance meter .....

LF low frequency .....

OS series open .....

RF radio frequency .....

Rs series resistor .....

S1 symmetric offset short circuit reflect .....

$Sr_{n+1}Ti_nO_{3n+1}(n = 1, 2, 3)$ Ruddlesden-Popper series for $SrTiO_3$ .....

RP Ruddlesden-Popper .....

Chapter 1

Introduction

1.1 Motivation

For hundreds of years, dielectric characterization has been the focus of a significant amount of theoretical and experimental research. A simple query on 'dielectric spectroscopy' on most literature search databases will produce tens of thousands of results. Why are dielectrics so interesting? This is actually not so easy to answer. One could rattle off dozens of examples of dielectrics that are in everyday use, from the piezoelectric disk in the pickup on an electric guitar to the transistors that are in computer processors. There are important applications for electric field tunable (*i.e.* voltage controlled) dielectrics throughout the frequency spectrum from dc to hundreds of gigahertz and beyond (See Fig. 1.1). It is certainly true that the search for new dielectric materials provides an opportunity to solve problems that have the potential to have an immediate impact on everyday life, and for many that is excitement enough to dedicate years of research to the study of dielectrics. But physicists, material scientists, and electrical engineers care about dielectrics for more than just their practical applications. Understanding the underlying physics behind why a material exhibits a specific response under a given set of conditions is to many as important, if not more, than just observing the response. In order to to understand the underlying physics of a material system, scientists perform experiments as function of a variety of independent variables, such as temperature, electric and magnetic field, composition, compressive stress, and tensile strain.

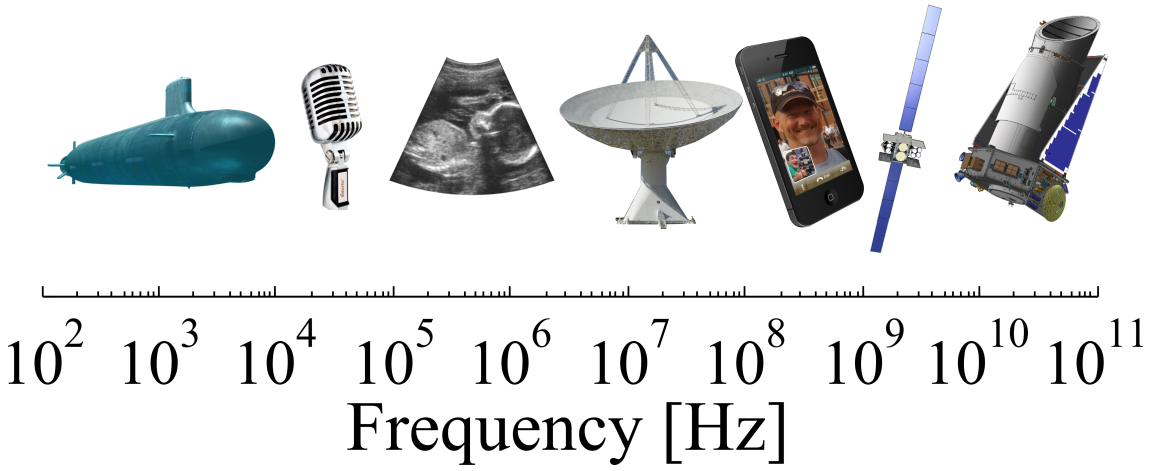

Figure 1.1: Applications of Dielectrics as a Function of Frequency

A representation of some of the practical applications of dielectrics as a function of frequency. Several frequency bands below 10^4 Hz are used almost exclusively for military communications. For example, submarines use very low frequency radio waves to receive information while submerged. The low frequencies around 10^5 Hz are commonly used for AM broadcasting. In the MHz (10^6 Hz) regime, there are a variety of medical application that use piezoelectrics to convert mechanical vibrations into electrical signals. The range near 10^7 Hz is important for radio telescopes. Cellular communication devices transmit and receive information in the range around 10^8 Hz. These terrestrial networks communicate with base stations that transmit the signal to satellites around the frequency range of 10^9 Hz. Above 10^{10} Hz, new technologies are being developed. For example, the Kepler Space Telescope uses frequencies around 10^{10} Hz for down-linking data at fast bit rates.

Frequency dependence of the permittivity function from Maxwell's equations ($\epsilon = D \cdot E^{-1}$) is one of the several ways we can understand the fundamental electrodynamics of an electrically polarizable material. Even in a simple polar solution, like salt water, the frequency dependence of the complex permittivity reveals a substantial amount of information about the dynamics of the system. Let's consider this example problem. When a small amount of NaCl is dissolved into a large volume of water a sequence of events unfolds. The polar water molecules break the ionic bonds between the sodium and chlorine atoms to form positively (Na+) and negatively (Cl-) charged ions. This

causes some of the water molecules, which are joined together by hydrogen bonds, to split apart and surround the sodium and chloride ions. If an electromagnetic wave with an angular frequency ω propagates into our salt water solution, we can use Maxwell's equations to understand how the propagation of that wave is dependent on the frequency.

In our simple salt water solution, we actually have two contributions to the complex permittivity of the solution for frequencies below 100 GHz. The first is simply due to the dc conductivity of the salt water, which arises from the translation of the sodium and chloride ions. From Maxwell's equations, we know that we can absorb the total current density (J) into the electric flux density (D) by modifying the complex relative permittivity by $\frac{\sigma}{\omega}$, where σ is the dc conductivity. Right away, we know that as frequency increases this term vanishes, but at higher frequencies another phenomenon comes into play. Water molecules can be thought of as finite-sized dipoles. At low frequencies, the water molecules freely rotate to anti-align with the applied electric field minimizing the electric field in the salt water. As frequency increases, the dipoles can no longer track the electric field, which results in a phase difference between the electric field of the wave and the electric field in the material. This phase difference corresponds to absorption. If we continue to increase ω (to a certain point), the water molecules cease rotating all together and the imaginary part of the relative permittivity (red line Fig. 1.2) goes to zero and the real part of the relative permittivity (blue line Fig. 1.2) goes to a constant that is determined by an additional relaxation mechanism at higher frequencies.

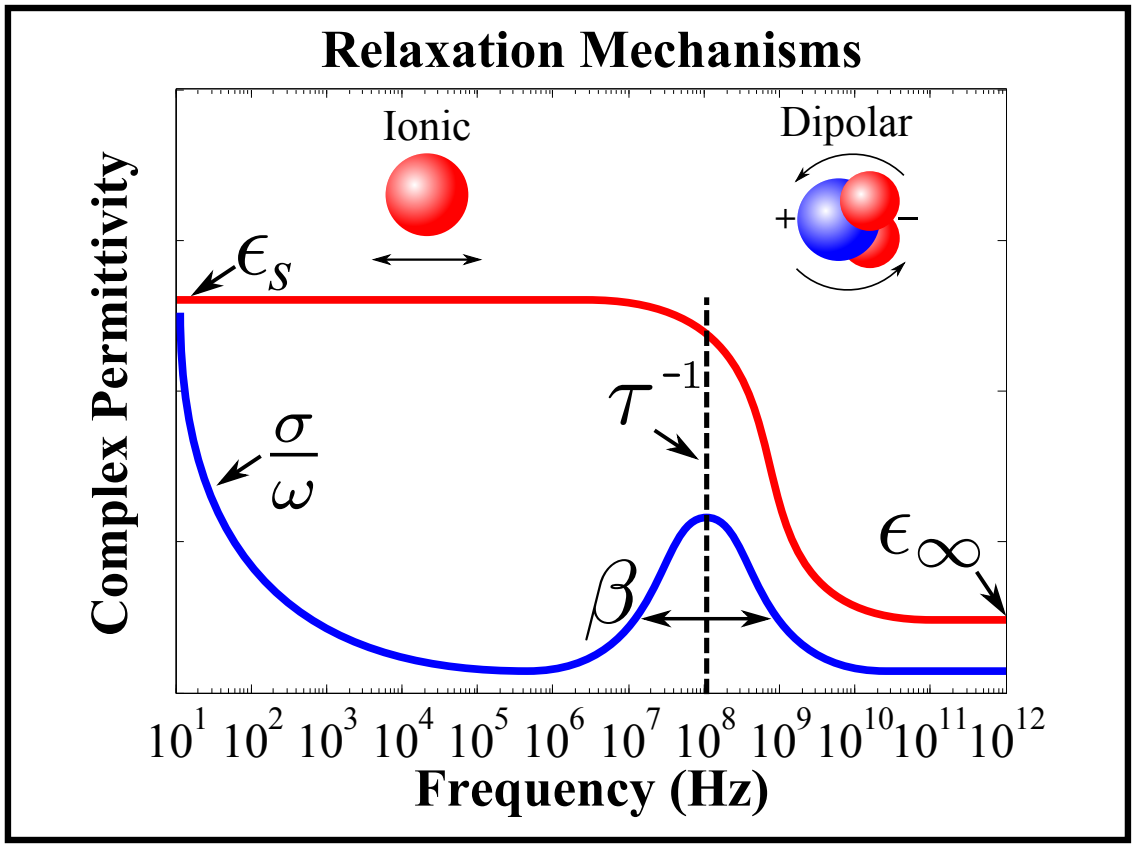

Figure 1.2: Examples of Relaxations Mechanisms

A schematic of the dielectric relaxation as a function of frequency for a polar molecule described by the Cole-Cole function. The imaginary part of the permittivity function is shown as the blue curve, and the corresponding real part is shown as the red curve. Within the frequency range of 10^1 Hz to 10^{12} Hz, two common sources of frequency dependence are dipole relaxation, and ionic conductivity. The Cole-Cole function for a simple polar molecule can be described by the low frequency limit of the permittivity (ϵ_s), the high frequency limit of the permittivity (ϵ_∞), an ionic conductivity term (σ), a relaxation time (τ), and a parameter (β) that characterizes a distribution of relaxation times around τ.

We show an illustration of the complex permittivity of a conducting polar liquid, like the example problem, in Fig. 1.2 where the y-axis is arbitrary. We also show the Cole-Cole fit parameters and the corresponding frequency domains of the complex permittivity function where they are important[3]. The Cole-Cole equation is given by,

$$\tilde{\epsilon} = \epsilon_\infty + \frac{(\epsilon_s - \epsilon_\infty)}{1 - (i\omega\tau)^\beta} - i\frac{\sigma}{\omega}, \tag{1.1}$$

where the static permittivity is ϵ_s, the upper frequency permittivity limit is ϵ_∞, and the relaxation time is τ. Also in Eq. 1.1, we include the parameter β that describes a distribution of relaxation times. The remaining parameters (σ and ω) were defined in the example problem. In the context of the example problem, the relaxation time τ is the characteristic time it takes the dipoles to rotate to anti-align with the electric field. The upper frequency permittivity limit (ϵ_∞) in the example problem was determined by an additional relaxation process that occurs at a higher frequency.

This simple example problem illustrates that the frequency dependence of the complex permittivity reveals a lot about the underlying electrodynamics of a system. In fact, even in the simple system, τ and σ are fundamentally dependent on temperature. In crystal substrates and thin films, the behavior of the complex permittivity as a function of frequency can often be related to and understood in the same basic concepts as the example problem. Historically, measuring frequency dependence over the frequency range shown in Fig. 1.2 has been particularly challenging, especially for solid state systems like thin films. It is the goal of this research to understand the intrinsic electrodynamics of a given material system that gives rise to this frequency dependence. In order to accomplish this goal, we have developed a characterization technique for performing quantitative broadband dielectric spectroscopy of the thin-film systems. We then apply this technique to a series of materials to explore the dependence of the complex permittivity on frequency, temperature, electric field, and material composition all in an effort to understand the fundamental electrodynamics of the materials discussed in the coming chapters.

1.2 Outline of this Dissertation

Chapter 1 introduces the motivation behind this research and explains how frequency dependence can be related to fundamental dynamics in a material system by considering a simple example problem. We then frame the example problem in the context of this work.

Chapter 2 discusses the broadband measurement system and cryogenic on-wafer probe station. We discuss the planar devices (interdigitated capacitors and coplanar waveguides) used in the broadband dielectric spectroscopy approach. We examine the on-wafer calibration techniques used to correct the broadband measurement system. After we establish the correction techniques, we give an overview of the on-wafer metrology approach used to obtain the distributed capacitance and conductance of the planar devices. We then describe the 2D finite element simulations used to obtain mapping functions that relate the distributed capacitance to the real part of the in-plane relative permittivity from 100 Hz to 40 GHz. We also perform error propagation and estimate the uncertainty in the technique. We conclude by demonstrating the approach on a thin-film test wafer and a companion substrate test wafer.

Chapter 3 discusses the characterization of the real part of the in-plane relative permittivity of the first three members ($n = 1$, 2, and 3) of $Sr_{n+1}Ti_nO_{3n+1}$ Ruddlesden-Popper (RP) series single-phase epitaxial thin films grown by molecular beam epitaxy. We show that the measured in-plane relative permittivity for each series number at low temperatures is consistent with the value obtained from density functional theory. By combining measurements results from interdigitated capacitors and coplanar waveguides, we are able to measure the in-plane relative permittivity from 500 Hz

to 40 GHz. We then systematically explore the dependence of the in-plane relative permittivity on series number, temperature, and dc electric field.

Chapter 4 applies the broadband dielectric spectroscopy technique to strained $Sr_{n+1}Ti_nO_{3n+1}$ RP series on $DyScO_3(110)$ (1% tensile strain) and $GdScO_3(110)$ (1.7% tensile strain). We show that the critical temperature of the strained $Sr_{n+1}Ti_nO_{3n+1}$ RP series members systematically increased with increasing series number. The same series numbers grown on $GdScO_3(110)$ have transition temperatures approximately 60 K higher than those on $DyScO_3(110)$. In comparison to fully relaxed thin films [4], we find that the samples that are under tensile strain of 1% and 1.7% show an increase of nearly an order of magnitude at the transition temperature in the the real part of the in-plane relative permittivity for most of the films. The strained $Sr_{n+1}Ti_nO_{3n+1}$ RP series thin films that we measure in these experiments show significantly greater electric field tunability when compared to their unstrained counterparts in Ref. [4]. Despite the presence of a high permittivity, high electric field tunability, and transition temperatures that in some cases is close to room temperature, the materials exhibit little to no dispersion above the transition temperature. Below the transition temperatures, the materials show power-law-like dispersion, which has been seen in several relaxor ferroelectrics [5]. These materials share many characteristics with relaxor ferroelectrics [6], yet their losses remain near the threshold of the measurement well into the gigahertz regime. This is in direct contrast with strained $SrTiO_3/DyScO_3(110)$, which has significant losses even well above the transition temperature at 300 K [1]. We find that several of these materials have figures of merit from 6 GHz to 7 GHz that are remarkably high, in many cases greater than FOM > 50. For the 50 nm thick $Sr_7Ti_6O_{19}/DyScO_3(110)$ ($n = 6$), the loss tangent is $\tan(\delta_{11}) = 0.003 \pm 0.003$ in the range from 6 GHz to 7 GHz. Within this frequency range, this sample has a figure of merit of FOM ≈ 140 with an absolute lower bound of FOM $= 60$, which

is among the highest figures of merit ever reported. Moreover, the real part of the in-plane relative permittivity for $Sr_7Ti_6O_{19}/DyScO_3(110)$ ($n = 6$) does show evidence of dispersion below 40 GHz, which suggests that the loss tangent may remain very low even to 40 GHz.

In Appendix A, we included a variety of details that may be helpful to the reader: Instrument Settings, Definition of S-parameters, Error Propagation for Coplanar Waveguides, Illustration of the Lithography Process, Derivation of Characteristic Impedance from an Error Box, Uncertainty in Permittivity, and X-ray Diffraction Results for the materials studied in Chapter 3.

Chapter 2

Broadband In-Plane Relative Permittivity Measurements

2.1 Abstract

We present a broadband on-wafer measurement technique for the characterization of the in-plane complex relative permittivity of a thin-film test wafer and a companion substrate test wafer from 100 Hz to 40 GHz, and potentially to 110 GHz. From 100 Hz to 300 MHz, the approach uses an ensemble of interdigitated capacitors with different interdigitated active lengths, ℓ = (0.100 mm, 0.325 mm, 0.875 mm, 1.835 mm, 2.9 mm), fabricated on both test wafers. Within this frequency regime, from 100 Hz to 1 MHz, the measurements were performed with an inductance-capacitance-resistance meter. From 1 MHz to 300 MHz, the scattering parameters of the same set of interdigitated capacitors on the test wafers were measured with a radio frequency vector network analyzer. In the high frequency regime, 300 MHz to 40 GHz, we measured scattering parameters of a set of coplanar waveguides with different active lengths, ℓ = (0.420 mm, 1.270 mm, 2.155 mm, 3.22 mm, 3.993 mm, 5.933 mm), fabricated on both of the test wafers. We extracted the capacitance and conductance per unit length of the interdigitated capacitors and coplanar waveguides on the test wafers for the appropriate frequency regimes. We then obtained a mapping function by means of 2D finite element simulations that relates the change in capacitance per unit length of the thin-film test wafer (relative to the companion substrate test wafer) to the real part of the relative in-plane permittivity. The imaginary part of the in-plane relative permittivity was obtained from the real part of the in-plane relative permittivity and the in-plane loss tangent.

2.2 Introduction

Quantitative measurements of the complex relative permittivity as a function of frequency can yield important information about the frequency-dependent relaxation mechanisms in a given material system. Moreover, quantitative measurements can provide an important benchmark for comparisons among different characterization techniques [7]. With the direct measurement of complex relative permittivity, a fundamental material property, we can eliminate the need for a reference material as required for relative techniques. Aside from elucidating the fundamental electrodynamics of a material system, dielectric characterization of ferroelectrics, as well as other dielectrics, is important for a wide variety of practical applications: low frequency communication systems for military applications [8, 9], radio frequency identification [10], piezoelectric converters for biomedical applications [11], and various microwave components for the communications industry [12, 13]. In part due to the practical significance, the design, synthesis, and characterization of materials with low loss and high electric field tunability over a broad frequency range has been the focus of a variety of research. In many cases, these efforts have often require expertise across different disciplines.

The growth of epitaxial thin films is particularly important, because it provides a means to develop new material systems. There are numerous different growth techniques: including pulsed-laser deposition [14], molecular beam epitaxy [15], and sputtering [16]. These growth techniques each provide its own unique way to grow designer materials that in many cases cannot be found in nature. Epitaxial thin films also allow for the study of effects like strain [1], which are difficult to achieve with a bulk material. Given importance of thin-film material systems, experimentalists have developed a wide array of dielectric spectroscopy techniques. In the far-infrared and terahertz regimes, among the various techniques perhaps the most common is terahertz transmission spectroscopy [17]. At fixed frequencies in the millimeter and cen-

timeter wavelengths, open-cavity resonant techniques like the Fabry-Perot resonator [18] and split cylinder resonator [19] can be used to characterize thin film, but these techniques are limited by the filling factor of the film and can only be used to measure a few frequencies. Whispering gallery resonators provide yet another accurate dielectric characterization technique, however, much like the open-cavity resonators, this approach can only be used over a very narrow-band [20]. Aside from these measurement approaches, lumped-element capacitors have been widely used to characterize thin films over a very broad spectrum for frequencies in most cases less than a few gigahertz. At high frequencies, lumped-element capacitors show distributed effects as the guided wavelength approaches the length of the lumped-element devices, which renders the circuit model used to extract the capacitance inaccurate [4]. Several transmission line type approaches exist for characterizing the complex relative permittivity of thin films [2, 21, 22]. One of the more recently developed approaches used planar transmission lines to extract the complex relative permittivity of thin films [2, 4, 23–25]. Unlike lumped-element capacitors, planar transmission lines are described by a distributed circuit model, and ,therefore, the description of these devices is only limited by the the integrity of the mode that propagates down the transmission line.

The focus of this research is on the development of an accurate dielectric characterization technique that will enable us to explore the frequency dependent nature of thin-film materials from 100 Hz to 40 GHz. In the following sections, we describe in detail our thin film dielectric characterization approach. We show the set of instruments used to perform the measurements in the low frequency, radio frequency, and high frequency regimes. We introduce the planar lumped element and distributed devices used in the measurement procedure. We detail the devices used to perform on-wafer calibrations and the frequency regimes where those calibrations are applied. We describe how these correction techniques are applied to a thin-film test wafer and a companion substrate test wafer. Once we have described the on-wafer correction

procedure, we describe how to extract the complex in-plane relative permittivity of the thin-film test wafer. Finally, we demonstrate this technique with a $LaAlO_3$ calibration wafer, a $Sr_7Ti_6O_{19}/DyScO_3(110)$ thin-film test wafer, and a $DyScO_3(110)$ companion substrate test wafer.

2.3 Measurement System

In order to measure the frequency dependence from 100 Hz to 40 GHz of the complex relative in-plane permittivity, we use three instruments: a low frequency (LF) inductance-capacitance-resistance (LCR) meter (100 Hz - 1 MHz), a radio frequency (RF) vector network analyzer (1 MHz - 300 MHz), and a high frequency (HF) vector network analyzer (300 MHz - 40 GHz) (See Fig. 2.1(b)). The LF LCR meter measures a complex voltage and current to extract a complex admittance. Both the RF and HF vector network analyzers measure complex scattering parameters (S-parameters). The measurement instruments were connected through a series of switches and semi-rigid coaxial cables to test port inputs at the front of the HF vector network analyzer. This allows us to use the pair of flexible phase-maintaining test port cables labeled 'Port 1' and 'Port 2' in Fig. 2.1(a) to perform measurements with each measurement instrument without the need to disconnect cables. The instrument settings can be found in App. A.1.

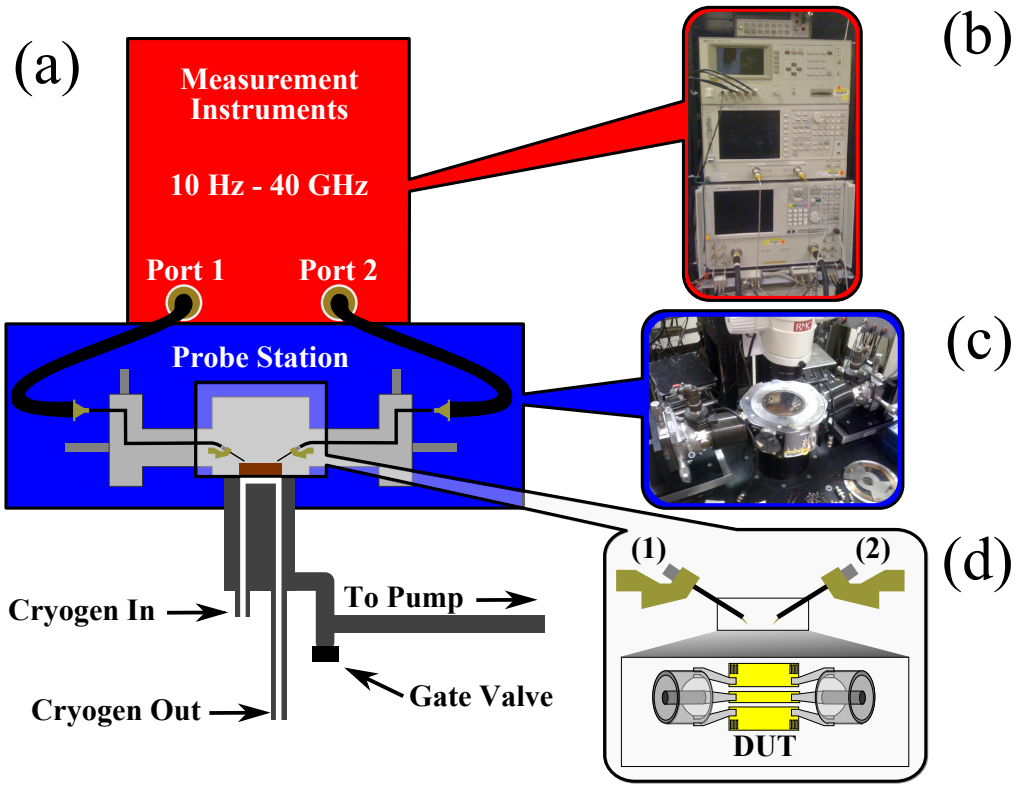

Figure 2.1: Broadband Measurement System

(a) A schematic of the broadband measurement system with continuous frequency coverage from 100 Hz to 40 GHz. (b) The red block shows the measurement equipment, which includes a multimeter, an inductance-capacitance-resistance (LCR) meter (100 Hz - 1 MHz), a radio frequency vector network analyzer (30 kHz to 6 GHz), and a high frequency vector network analyzer (10 MHz to 40 GHz). Each measurement instrument was routed through a series of switches to phase-maintaining flexible coaxial cables at the front of the high frequency vector network analyzer. The cables, labeled 'Port 1' (1) and 'Port 2' (2) in (a), were connected to a cryogenic measurement system shown in blue (c). (d) Stainless steel semi-rigid coaxial cables connect the room temperature measurement system to ground-signal-ground probes, which allow us to measure planar device-under-test (DUT) in a vacuum. The DUT is thermally grounded to a copper chuck that is temperature controlled by a cold finger, which is cooled by an open-flow of cryogens (liquid helium or liquid nitrogen).

In Fig. 2.1, we show the measurement system (Fig. 2.1(b)) with the cryogenic probe station (Fig. 2.1(c)). The flexible phase-maintaining coaxial cables were connected to a pair of rigid coaxial cables that were routed through compression seals to

the inside of the cryogenic probe station (Fig. 2.1(d)), which was maintained under vacuum at a specific temperature. The temperature was controlled with an open-flow of liquid helium and a pair of heaters that were embedded in a removable copper chuck. The rigid coaxial cables were connected to a pair of ground-signal-ground (g-s-g) air-coplanar wafer probes (Fig. 2.1(d)). The g-s-g probes allow us to perform measurements of a device-under-test (DUT) of our choosing at a given temperature, electric field, and frequency.

Before we perform any on-wafer measurements, the RF and HF vector network analyzers were calibrated with coaxial calibration standards. The 2.4 mm female and male 1-port coaxial calibration standards included a symmetric offset short circuit reflect, a shunt offset open, a shunt offset low-band load, and a shunt seven-position offset sliding load. Because the end of the phase-maintaining flexible coaxial cable at 'Port 1' was female and 'Port 2' was male, a thru was created by directly connecting 'Port 1' to 'Port 2'. For the HF vector network analyzer, we used all of the coaxial calibration standards. The RF vector network analyzer was corrected to the end of 'Port 1' and 'Port 2 with the same calibration standards, except for these frequencies we omitted the shunt seven-position sliding loads for both ports. Although the coaxial calibration step could, in principle, be eliminated for the HF vector network analyzer (because we can directly measure the internal switch terms with an additional sampler [26]), we have found experimentally that it improved the phase noise at low frequency for the on-wafer measurements made by this instrument. For the RF vector network analyzer, the coaxial calibration was unavoidable, because we were unable to measure the internal switch. Both the coaxial calibration for the RF and HF vector network analyzers were verified with a 2.4 mm symmetric coaxial short circuit reflect with no delay length, commonly called a flush or flat short. We repeat the coaxial calibration steps until the error in the verification standard was less that ± 0.1 % at 40 GHz, which typically corresponds to significantly less error at lower frequencies. The calibration

for the LF LCR meter was performed on-wafer, and will be described in a following section.

2.4 Planar Devices

Once the RF and HF measurement systems were calibrated, and ,therefore, corrected to the end of the flexible phase-maintaining coaxial cables at 'Port 1' and 'Port 2', we proceeded to measure the on-wafer planar devices. For these experiments, we measured two types of planar devices: the interdigitated capacitor (IDC) and the coplanar waveguide (CPW). The IDC is a planar lumped-element capacitor often modeled by a lumped element π-network with an admittance matrix. IDCs were used under the assumption that the electric field was position independent along the length of the interdigitated fingers. For an IDC with only three fingers, this requirement was equivalent to the statement that the guided wavelength was much longer than the active length of the IDC. A CPW is a planar transmission line that is modeled by a distributed circuit model.

2.4.1 Interdigitated Capacitors

In Fig. 2.2, we show a schematic of the IDCs used in these experiments. In Fig. 2.2(a), there are two sets of three 10 μm wide fiducial marks spaced 10 μm apart on both sides of the IDC, which were fabricated as voids in the ground planes (g.p.). The g-s-g probes were positioned via x-y-z micrometers beside the middle of the three fiducial marks on either side of the device, lowered slowly into contact, and lowered further to achieve 20 μm of over-travel (or skate) to the end of the third fiducial mark. This ensured precise and repeatable measurements of each device.

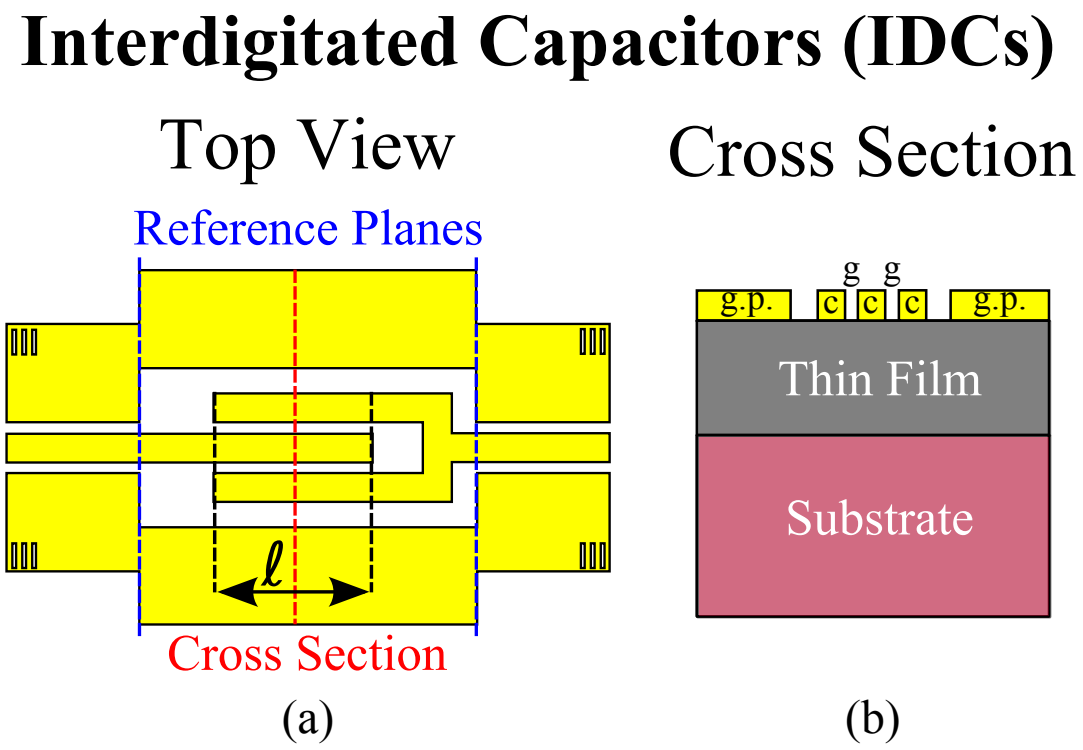

Figure 2.2: Interdigitated Capacitors

(a) We show an interdigitated capacitor (IDC) with an active length (ℓ). The blue dashed lines indicate the reference planes of the on-wafer calibrations. The red dashed line is the cross section shown in (b). In (b), we show the cross section of an interdigitated capacitor. The electrodes (yellow) were deposited on a thin film (grey), which is grown on a substrate (light red). The interdigitated finger widths (c) were spaced by the gaps (g). The remaining dimensions, including the distance between the interdigitated fingers and ground plane (g.p.) are not critical, because they were many times the gap (g).

The on-wafer calibrations define the reference planes, shown as the blue dashed lines in Fig. 2.2(a). The area in between the reference planes is the active area of the IDC, and it is modeled as a series admittance, Y_s, with Y-parameters (See App. A.2). The active length (ℓ) is the length that the interdigitated fingers overlap. The red dashed line in Fig. 2.2(a) indicates the line over which the cross section, shown in Fig. 2.2(b), is taken. Figure 2.2(b) shows the cross section of the IDC. The IDC has three

interdigitated fingers of width, c, spaced by the gaps, g. The remaining dimensions were designed to be many multiples of the gap width and were not critical for these experiments. For these experiments, the IDC finger width was c = 60.0 μm $\pm$ 0.5 μm, the gap was g = 20.0 μm $\pm$ 0.5 μm, and the conductor thickness was 760 nm $\pm$10 nm. The active lengths of the IDCs were ℓ = (0.100 mm, 0.325 mm, 0.875 mm, 1.835 mm, 2.9 mm) with an uncertainty comparable to uncertainty in the cross-sectional dimensions.

We measured both the LF and RF response of each IDC in a single contact, and repeated the process sequentially for all of the IDC devices. In the LF regime, the LCR meter directly converts the impedance into an admittance, which was recorded as a capacitance and loss tangent as a function of frequency. The LF measurements could be converted into Y_s as

$$Y_s = \tan(\delta_{LCR}) \cdot \omega C_{LCR} + i\omega C_{LCR}, \tag{2.1}$$

where the capacitance measured by the LCR meter is C_{LCR}, the loss tangent of the device measured by the LCR meter is $\tan(\delta_{LCR})$, and ω is the angular frequency. In the RF regime, we measured the complex S-parameters as a function of frequency. The corrected S-parameters of each device were converted into admittance parameters (Y-parameters). The Y-matrix of an IDC can be written as

$$Y_{IDC} = \begin{pmatrix} Y_g + Y_s & -Y_s \\ -Y_s & Y_g + Y_s \end{pmatrix}. \tag{2.2}$$

Practically, we took the average of the off-diagonal elements of Eq. 2.2 as, $Y_s = (Y_{21} + Y_{12})/2$, to extract the series admittance. The representative lumped element equivalent circuit model for an IDC is shown in Fig. 2.3, where Y_g is the shunt admittance and Y_s is the series admittance.

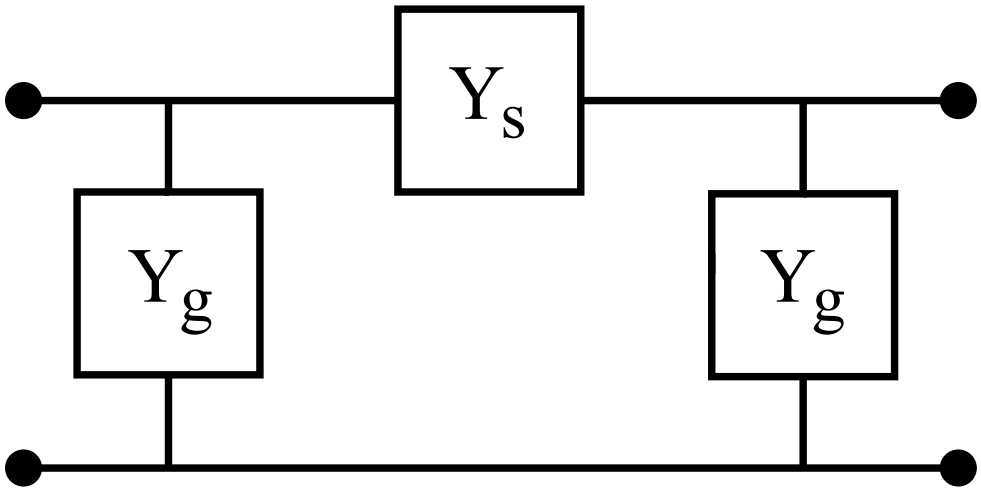

Figure 2.3: Interdigitated Capacitor Equivalent Circuit Model

The equivalent circuit model of an interdigitated capacitor, commonly called a π-network. The shunt admittance is labeled Y_g and the series admittance is labeled Y_s.

Once we have obtained Y_s for all the IDCs of varying active length $\ell =$ (0.100 mm, 0.325 mm, 0.875 mm, 1.835 mm, 2.9 mm) as a function of frequency, we extracted the distributed capacitance and conductance per unit length of the device. This was achieved by performing a linear fit as a function of ℓ at each measurement frequency for $\Re(Y_s)$ and $\Im(Y_s)/\omega$. We can rewrite the series admittance as

$$Y_s = Y_o + \ell \cdot (G + i\omega C), \tag{2.3}$$

where C and G are the capacitance and conductance per unit length of the IDC and Y_o is a parasitic admittance that was irrelevant for our measurements. In this step,

we also obtained the uncertainty in the slopes, ΔC and ΔG, which was later used to estimate the uncertainty in the measurement. We then applied this approach to extract the capacitance and conductance per unit length of the IDCs on the thin-film test wafer ($C_{tot} \pm \Delta C_{tot}$ and $G_{tot} \pm \Delta G_{tot}$) and companion substrate test wafer ($C_{sub} \pm \Delta C_{sub}$ and $G_{sub} \pm \Delta G_{sub}$). Finally, we took the difference to arrive at the contribution of the film,

$$\begin{aligned} C_{film} &= C_{tot} - C_{sub} && (2.4) \\ G_{film} &= G_{tot} - G_{sub} && (2.5) \\ \tan(\delta_{film}) &= \frac{G_{film}}{\omega C_{film}}, && (2.6) \end{aligned}$$

where C_{film} is the contribution of the film to the capacitance per unit length, G_{film} is the contribution of the film to conductance per unit length, and $\tan(\delta_{film})$ is the loss tangent of the film. The uncertainty in the capacitance and conductance per unit length of the film is given by,

$$\begin{aligned} \Delta C_{film} &= \sqrt{(\Delta C_{tot})^2 + (\Delta C_{sub})^2} \\ \Delta G_{film} &= \sqrt{(\Delta G_{tot})^2 + (\Delta G_{sub})^2}, && (2.7) \end{aligned}$$

and the uncertainty in the film loss tangent is,

$$\Delta \tan(\delta_{film}) = \sqrt{\frac{1}{(\omega C_{film})^2} \cdot (\Delta G_{film})^2 + \left(\frac{G_{film}}{(\omega C_{film}^2}\right)^2 \cdot (\Delta C_{film})^2}. \quad (2.8)$$

Eqs. 2.7, 2.8 are fully general for any frequency regime once we have obtained $C_{tot} \pm \Delta C_{tot}$, $G_{tot} \pm \Delta G_{tot}$, $C_{sub} \pm \Delta C_{sub}$, and $G_{sub} \pm \Delta G_{sub}$.

2.4.2 Coplanar Waveguides

In Fig. 2.4, we show a CPW [27]. Figure 2.4(a) shows a top view of a CPW. The CPWs used in these experiments have active lengths ℓ = (0.420 mm, 1.270 mm, 2.155 mm, 3.22 mm, 3.993 mm, 5.933 mm). The CPW consists of a center conductor of width, c, spaced equidistantly about a pair of ground planes (g.p.) by a gap, g (See Fig. 2.4(a)). On either side of the CPW, there were two sets of three fiducial marks. The measurements were taken by g-s-g probes that were positioned beside the middle of the three fiducial marks, lowered into contact, and then the probes were lowered further such that the over-travel was 20 μm, or to the end of the third fiducial mark. This set the reference planes of the measurements, which are indicated by the blue dashed lines in Fig. 2.4(a). The red dashed line in Fig. 2.4(a) indicates the line along which the cross section is taken, which is shown in Fig. 2.4(b). In Fig. 2.4(b), we illustrate the cross-sectional geometry of a CPW on a thin-film test wafer.

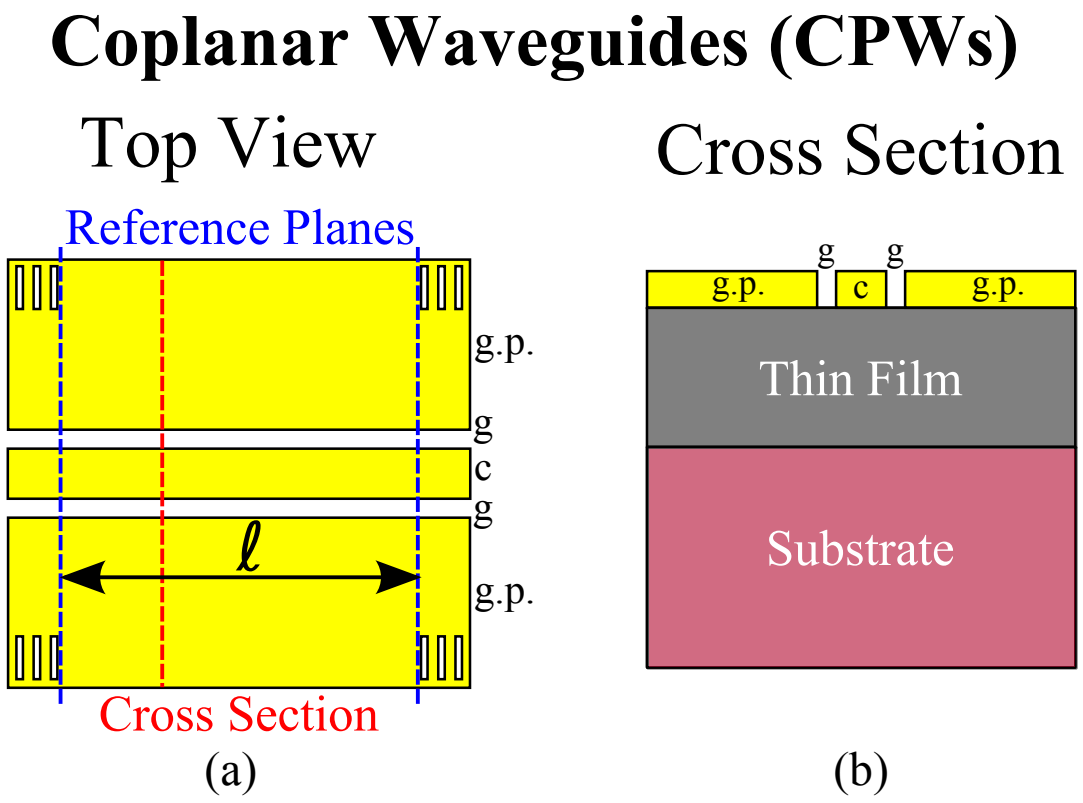

Figure 2.4: Coplanar Waveguides

(a) Shows a coplanar waveguide (CPW) with an active length (ℓ). The blue dashed lines indicate the reference planes of the on-wafer calibrations. The red dashed line is the cross section shown in (b). In (b), we show the cross section of a coplanar waveguide. The electrodes (yellow) were deposited on a thin film (grey), which was grown on a substrate (light red). The center conductor (c) is centered about the ground planes (g.p.) by a gap (g).

At fixed position in time and space, the electric field lines along the CPW structure, like that shown in Fig. 2.4(b), were configured such that the electric field lines extended from the outer conductor to the center conductor (See Fig. 2.5). If the film has a larger real part of the in-plane relative permittivity than the substrate (as in Fig. 2.5), then the electric field lines will be more dense in the thin film than in the substrate. This has the effect of increasing the distributed capacitance of the CPW.

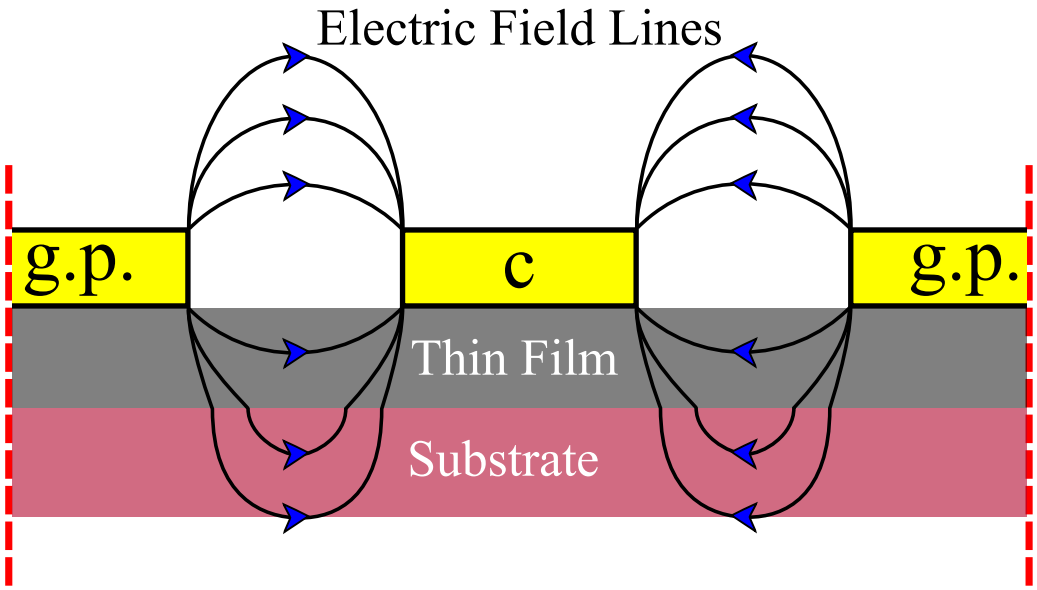

Figure 2.5: Electric Field Lines for a Coplanar Waveguide on a Thin Film

A schematic of the electric field lines in a coplanar waveguide at a fixed position in space and time. The center conductor is labeled "c" and the ground planes are labeled "g.p.". The red dashed lines indicate that the ground planes, thin film, and substrate continue outside the field of view.

As stated previously, a CPW is described by a distributed equivalent circuit model. This is because a CPW is symmetric along the device length, which is not the case for an IDC. The equivalent distributed circuit for a CPW is shown in Fig. 2.6. The circuit consists of a distributed resistance (R), inductance (L), capacitance (C), and conductance (G) per unit length. Intuitively, the C is due to stored charge between the center conductor (c) and ground planes (g.p.). Likewise, the leakage, or the ability to move charge from the center conductor to the outer conductor, is simply described as a G in parallel with the C. L can be understood from the magnetic field lines that loop around the center conductor and R is due to the resistive losses

in the CPW conductors as the wave propagates down the transmission line. Both R and L are frequency dependent, because as frequency increases the skin depth of the metal decreases. The decrease in skin depth means the R is increasing with increasing frequency. Also, as the skin depth decreases, the magnetic field lines penetrate the conductors to a lesser extent, and L tends to a constant at sufficiently high frequency that is purely due to the geometry of the conductors [28].

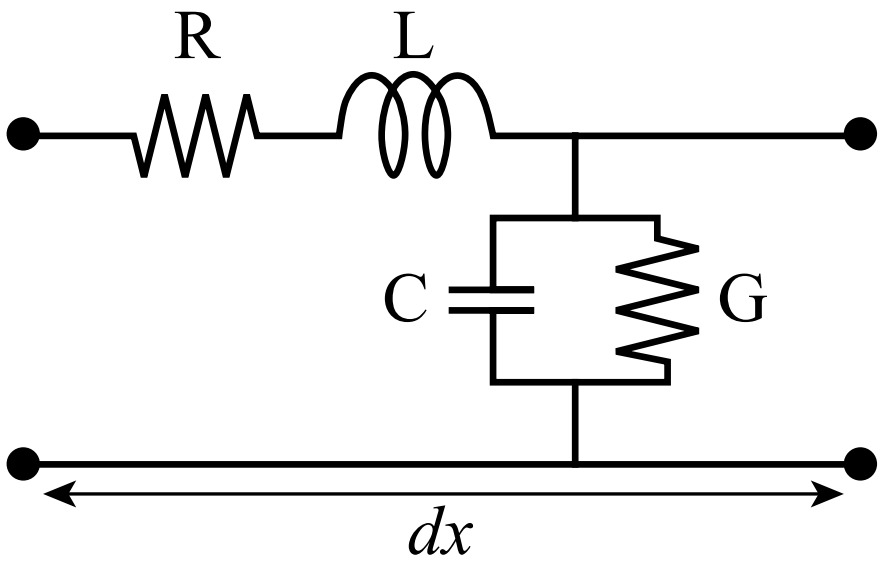

Figure 2.6: Equivalent Distributed Circuit Model for a Coplanar Waveguide

The equivalent distributed circuit model for a coplanar waveguide, which includes a distributed resistance (R), inductance (L), capacitance (C), and conductance (G).

A time varying voltage and current (an electromagnetic wave) will propagate down a CPW with a propagation constant (γ) given as

$$\gamma = \sqrt{(R + i\omega L)}\sqrt{(G + i\omega C)} \tag{2.9}$$

The characteristic impedance (Z) of the CPW is given by

$$Z = \frac{\sqrt{(R + i\omega L)}}{\sqrt{(G + i\omega C)}}. \tag{2.10}$$

Eqs. 2.9 and 2.10 can be derived directly from Maxwell's equations [29] or more easily from the differential form of Kirchhoff's laws, commonly called the Telegrapher's Equations. There are many approaches to writing down an expression that describes how an electromagnetic wave propagates down a CPW; perhaps the most simple to understand is the T-parameter formalism. The T-matrix (T) for a transmission line relative to the characteristic impedance Z is

$$T_\ell = \begin{pmatrix} e^{-\gamma \cdot \ell} & 0 \\ 0 & e^{\gamma \cdot \ell} \end{pmatrix}. \tag{2.11}$$

Eq. 2.11 is modified on the left and the right hand sides by impedance transformers when a measurement is corrected relative to some reference impedance [29].

Much like the IDC case, for dielectric thin-film test wafers (or materials where the relative permeability (μ) is 1) the distributed parameters of interest are the C and G. If one could measure both γ and Z with infinite accuracy, then the C and G could be solved directly $\gamma \cdot Z = G + i\omega C$. Although in practice we can measure γ with high accuracy and precision with the multiline thru-reflect-line characterization technique [30, 31], obtaining an accurate measurement Z is very challenging. The calibration comparison approach [32] is an example of a technique that can be used to approximate Z. This is discussed in Sec. 2.5.

In the technique employed here, we extracted C and G directly from from measurements of γ with two very similar approaches. In the first approach, and the one we consider the more accurate, we empirically measured the dc resistance of the conductors along with the S-parameters for the CPWs of different lengths. We then extracted the dc conductivity of the transmissions lines with a linear fit as a

function of length, and with the known cross-sectional geometry of the CPW. We then constructed a model of the CPW with the same cross-sectional dimensions of the conductors and dielectric materials. We defined the conductor properties using the dc measurements of the conductivity. We then ran a series of 2D finite element simulations, sweeping the frequency while holding the geometry fixed. From these 2D finite element simulations, we directly obtained R_{sim} and L_{sim} of the CPW, which for a dielectric thin film in the quasi-static limit should be entirely due to the properties and dimensions of the conductors. This enabled us to extract the C and G directly from γ as

$$G + i\omega C = \frac{\gamma^2}{(R_{sim} + i\omega L_{sim})}. \tag{2.12}$$

The second approach simply fits R and L with a shape-preserving interpolant, where R and L were obtained from Z as derived in [32]. This technique was considerably faster, but was less accurate, because the R and L can have unphysical frequency dependence. In many instances, however, the deviation from the fit and simulation was small enough that the difference between the two approaches was negligible. This will be discussed in greater detail in Sec. 2.4.3. In the latter case, we obtained R_{fit} and L_{fit} and modified Eq. 2.12, accordingly.

2.4.3 Propagation of Error for Coplanar Waveguides

There are only two sources of error in a measurement the S-parameters of a CPW: the uncertainty in the complex S-parameters and uncertainty in the length of the transmission line. In practice, it is challenging if not impossible to directly relate the uncertainties in the S-parameters and line lengths analytically to the uncertainty in the C and G. Fortunately StatistiCAL, software developed at the National Institute of Standards and Technology to perform the multiline TRL algorithm, calculates a 95%

confidence interval in the effective permittivity calculated from a covariance matrix with the CPW S-parameter measurements [31]. Admittedly, this error was at best an over-estimate of the actual uncertainty in the effective permittivity. Nonetheless, it was useful to use in an effort to approximate the uncertainty in γ. We calculated the uncertainty γ from the uncertainty in the effective permittivity obtained from StatistiCAL as,

$$\Delta\gamma = \left(\frac{\omega}{2c\sqrt{\Re(\epsilon)}}\right)\Re(\Delta\epsilon) + i\left(\frac{\omega}{2c\sqrt{\Im(\epsilon)}}\right)\Im(\Delta\epsilon). \tag{2.13}$$

Making a series of approximations and calculating the orders of magnitude (See App. A.3), we obtained an approximate expression for the uncertainty in the C and G from Eq. 2.13,

$$\Delta G + i\omega\Delta C \approx \left(2\cdot\left|\Re\left(\frac{\gamma}{R+i\omega L}\right)\right|\cdot|\Delta\gamma_r|\right) + i\omega\left(2\cdot\left|\Im\left(\frac{\gamma}{R+i\omega L}\right)\right|\cdot|\Delta\gamma_i|\right), \tag{2.14}$$

where the symbol $\Re$ denotes the real part and $\Im$ denotes the corresponding imaginary part of a complex number.

2.5 On-wafer Metrology

The foundation of the entirety of this work was built on the premise that we were able to perform accurate and precise on-wafer measurements of the planar devices. In Sec. 2.3, we discussed the measurement system and the corresponding coaxial calibrations, but in order to make accurate measurements of planar devices it was essential to perform on-wafer calibrations.

We accomplished accurate on-wafer calibrations by use of a 'calibration wafer'. In Fig. 2.7, we show a photograph of a calibration wafer. We fabricated the calibration

devices on a substrate that has a permittivity that was close to the permittivity of the test wafer. When we study a thin film, we intentionally choose a substrate that has a permittivity that is similar to the companion substrate test wafer, because most thin films simply perturb the effective permittivity of the CPW. For the materials discussed in Sec. 2.6 and Ch. 4, we chose to use $LaAlO_3$ because the real part of the in-plane relative permittivity was approximately $K_{11} \approx 24$ with a loss tangent less than $\tan(\delta_{11}) < 0.001$ [33] over the parameter space of the measurement. The devices on the calibration wafer were patterned on a 2 inch wafer with a two layer lithography process called lift-off-resist, which is illustrated in Fig. A.2. The 2 inch wafer was diced into $12\,\text{mm} \times 12\,\text{mm}$ wafers. The conductors on the calibration wafer consisted of a 10 nm Ti adhesion layer with a 750 nm thick Au electrode layer for a total thickness of 760 nm. The cross-sectional geometry of the CPWs on the calibration wafer were c = 60 μm $\pm$ 0.5 μm, g = 20 μm $\pm$ 0.5 μm, and g.p. = 200 μm $\pm$ 0.5 μm. The active lengths of the CPWs were ℓ = (0.420 mm, 1.270 mm, 2.155 mm, 3.22 mm, 3.993 mm, 5.933 mm), and were nominally identical to the CPWs on the test wafers. The active lengths of the CPWs were carefully chosen to minimize the error in the multiline thru-reflect-line calibration technique [30].

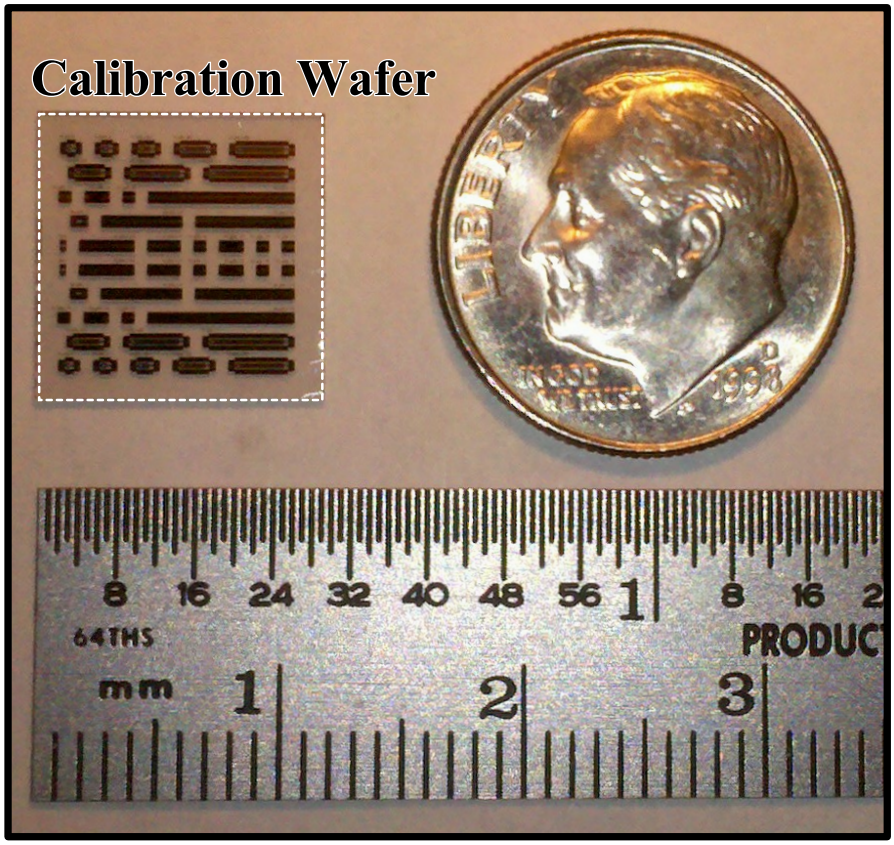

Figure 2.7: A Photograph of a Calibration Wafer

A photograph of a calibration wafer with devices fabricated on $LaAlO_3$. The conductors were 750 nm of Au deposited on a 10 nm Ti adhesion layer. Each calibration wafer includes a set of duplicate calibration standards in case a standard was destroyed in the measurement process or were worn down due to repeated measurement.

One of the cornerstones of this project was the extraction, modeling, and removal of the effects of the section semi-rigid coaxial cables and the g-s-g probes that lead up to the device-under-test (See Fig. 2.1(d)). A formal discussion of the calibration approach specifically developed during the course of this project can be found in Ref. [34]. In lieu of a detailed description, we present a cursory discussion presenting some of the crucial concepts in Ref. [34]. We start by considering the uncorrected S-parameter measurement of an arbitrary planar device: If we convert the S-parameters of our device into the T-parameter formalism (See App. A.2), then we can interpret the measurements of the arbitrary devices as

$$M_{measured} = T_1 \cdot (M_{corrected}) \cdot T_2. \tag{2.15}$$

In Eq. 2.15, the effects of the cables inside the probe station and the g-s-g probes can be thought of as separate matrices: T_1 for Port 1 and T_2 for Port 2. The goal of our on-wafer calibration was to extract T_1 and T_2, and thereby obtain the corrected measurement of our arbitrary device,

$$M_{corrected} = (T_1)^{-1} \cdot (M_{measured}) \cdot (T_2)^{-1}, \tag{2.16}$$

The matrices T_1 and T_2 are commonly termed 'error boxes' and can be obtained by performing a series of measurements of well-understood devices on the calibration wafer. If we could obtain T_1 and T_2 exactly, then the matrix $M_{corrected}$ would be unaffected by the error boxes and hence the actual T-matrix of the device, M_{actual}.

The measurement procedure for the calibration wafer is shown in Fig. 2.8. The devices on the calibration wafer included six CPWs (L1 = 0.420 mm, L2 = 1.270 mm, L3 = 2.155 mm, L4 = 3.22 mm, L5 = 3.993 mm, L6 = 5.933 mm), a symmetric 0.210 mm offset short circuit reflect (S1), a 0.210 mm offset series resistor (Rs), a 0.210 mm offset series capacitor (Cs), and a 0.210 mm offset series open (OS). The LCR meter measurements of the LF regime were corrected with the OS and L1 standards (light grey shaded region in Fig. 2.8). In this measurement configuration, the OS and L1 devices corresponded to a series open and a series short, because the LCR meter measured the time dependent voltage between the center conductors of Port 1 and Port 2. The vector-network analyzer measurements of the RF regime were corrected with S-parameter measurements of Rs, L1, L6, and S1 (light red shaded region in Fig. 2.8). The lumped element circuit parameters of the Rs calibration standard were completely characterized following the procedure outlined in Refs. [34, 35]. We measured L6 in the RF regime to directly extract the γ and Z from the S-parameter

measurements, as described in Ref. [36], which allowed us to translate the reference planes of the measurement (set at the center of L1 by the calibration) to the end of the probe tips. The vector-network analyzer measurements of the HF regime were corrected with Rs, Cs, S1, L1, L2, L3, L4, L5, and L6 (light blue shaded region in Fig. 2.8). We used the multiline thru-reflect-line calibration technique [30, 32] in combination with the series resistor calibration technique. Following the approach discussed in Ref. [29], we transformed the obtained error boxes to 50 Ω with the reference planes set at the end of the probe tips for the RF and HF regimes. The CPW line lengths were designed to minimize the normalized standard deviation error function as discussed in Ref. [30]. We minimized the error function in a custom algorithm where we input the following information: the minimum CPW length (ostensibly limited by cross-talk between the g-s-g probes), the maximum CPW length (limited by the size of the wafer), and the number of desired lines. We also input an approximate propagation constant, where R, L, and C were obtained from 2D finite element simulations and G was assumed to be zero. For this set of CPWs, L3 and L4 were also constrained to be consistent with the measurements in Ref. [4, 23–25, 34].

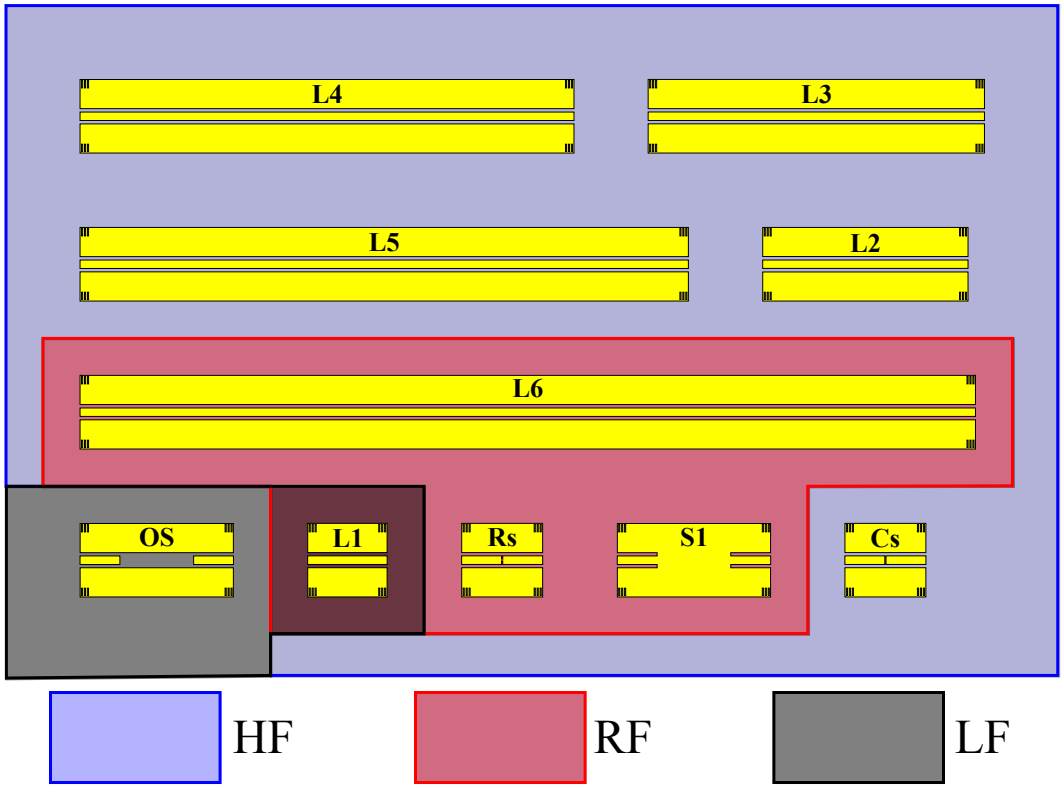

Figure 2.8: Broadband Calibration Procedure

A schematic of the on-wafer calibration procedure for the low frequency (LF) (grey), radio frequency (RF) (light red), and high frequency (HF) (light blue) regimes. The LF (grey) regime was corrected on-wafer with a series open (OS) and a series short (L1), which was also the thru for the RF and HF calibrations. The RF (light red) regime was corrected on-wafer with the longest coplanar waveguide (L6), a series-resistor (Rs), a symmetric short circuit reflect (S1), and a thru (L1). The HF regime was corrected on-wafer with a set of coplanar waveguides (L2, L3, L4, L5, L6), a thru (L1), a symmetric short circuit reflect (S1), a series capacitor (Cs), and a series resistor (Rs).

After we performed the necessary measurements on the calibration wafer Fig. 2.9(a), the measurement reference impedance was set to 50 Ω by the method described in Ref. [34] and the reference planes were at the end of the probe tips as shown in Fig. 2.9(b). We subsequently measured the companion substrate test wafer Fig. 2.9(c) and the thin-film test wafer Fig. 2.9(d). The devices fabricated on the companion substrate test wafer and thin-film test wafer were also patterned with the

lift-off-resist approach (See Fig. A.2). Once the photoresist was patterned, we affixed each test wafer to a silicon wafer with a non-water based wax. The thin-film test wafer and companion substrate test wafer were then loaded into a electron-beam evaporation deposition system (See Fig. A.3) that maintained the samples at room temperature during the deposition of the conductors. The electrode layer was fabricated by depositing a 10 nm Ti adhesion layer followed by a 750 nm thick Au conductor layer.

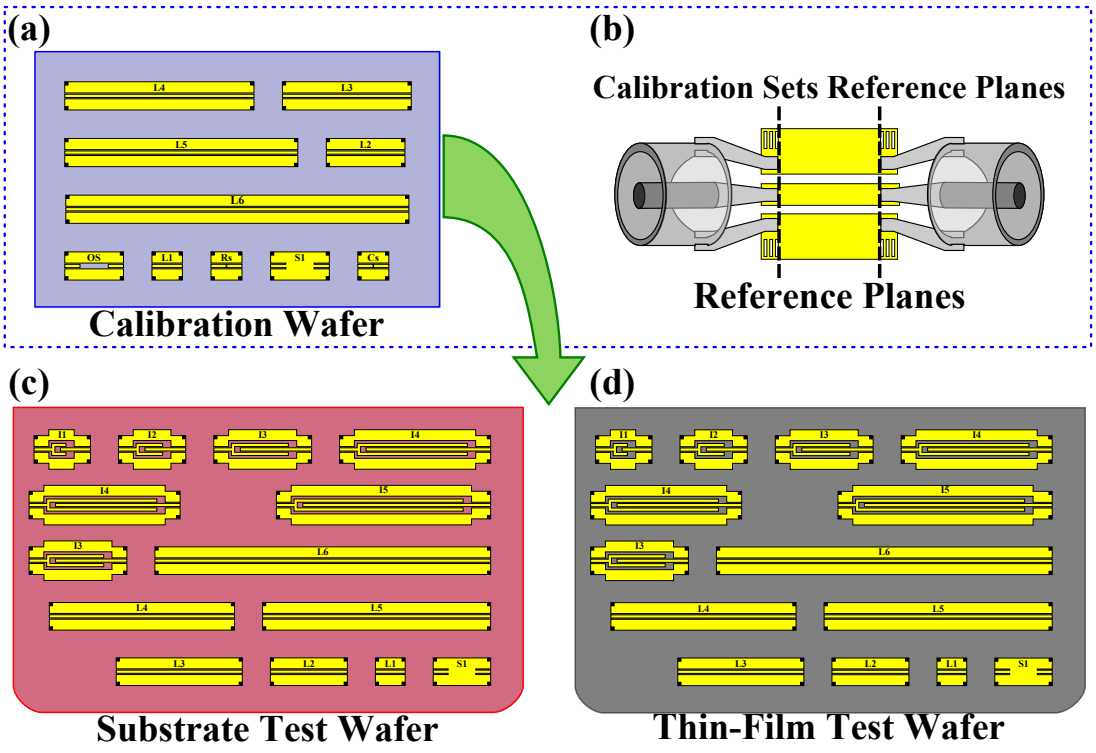

Figure 2.9: Broadband Method for Thin Film Characterization

A schematic of the broadband method used to characterize a thin film. In (a), we show the calibration wafer that was used to set the calibration reference planes to the end of the probes tips (b). These calibrations were applied to a set of measurements on a thin-film test wafer (d) and companion substrate test wafer (c).

In Fig. 2.10, we show an illustration of the substrate test wafer, which was approximately 10 mm × 10 mm in outer dimension. Our test wafer pattern only covers

an area of $10\,\text{mm} \times 5\,\text{mm}$, because in addition to fabricating our own devices we typically also patterned and deposited conductors for experiments conducted at other research facilities. For the experiments discussed in Sec. 2.6 and in Ch. 4, the devices were fabricated on epitaxial thin films grown by MBE special substrates to achieve in-plane biaxial tensile strain. The substrates ($DyScO_3(110)$ and $GdScO_3(110)$) had two beveled corners on one side to indicate the c-axis of the substrate. This was because the substrates have anisotropic in-plane permittivity tensor. It was, therefore, essential that all the devices be aligned in the same way relative to the substrate. Poor alignment resulted in an obvious disagreement between the real part of the in-plane relative permittivity obtained from the CPW and IDC devices. This was particularly challenging because the substrates have irregular thicknesses that varied by much as 0.005 mm. In turn, this meant that the devices had to be aligned and exposed manually rather than by an automated exposure tool, such as a wafer stepper system. The devices on the test wafer included a set of CPWs (L1, L2, L3, L4, L5, L6) and a symmetric 0.210 mm offset short circuit reflect that were also featured on the calibration wafer (See Fig. 2.10). We have also included a set of IDCs that are labeled I1, I2, I3, I4, and I5 in Fig. 2.10 and have active lengths ℓ = (0.100 mm, 0.325 mm, 0.875 mm, 1.835 mm, 2.900 mm), respectively. In addition to fabricating these devices, we fabricated redundant I3 (ℓ = 0.875 mm) and I4 (ℓ = 1.835 mm) IDC devices.

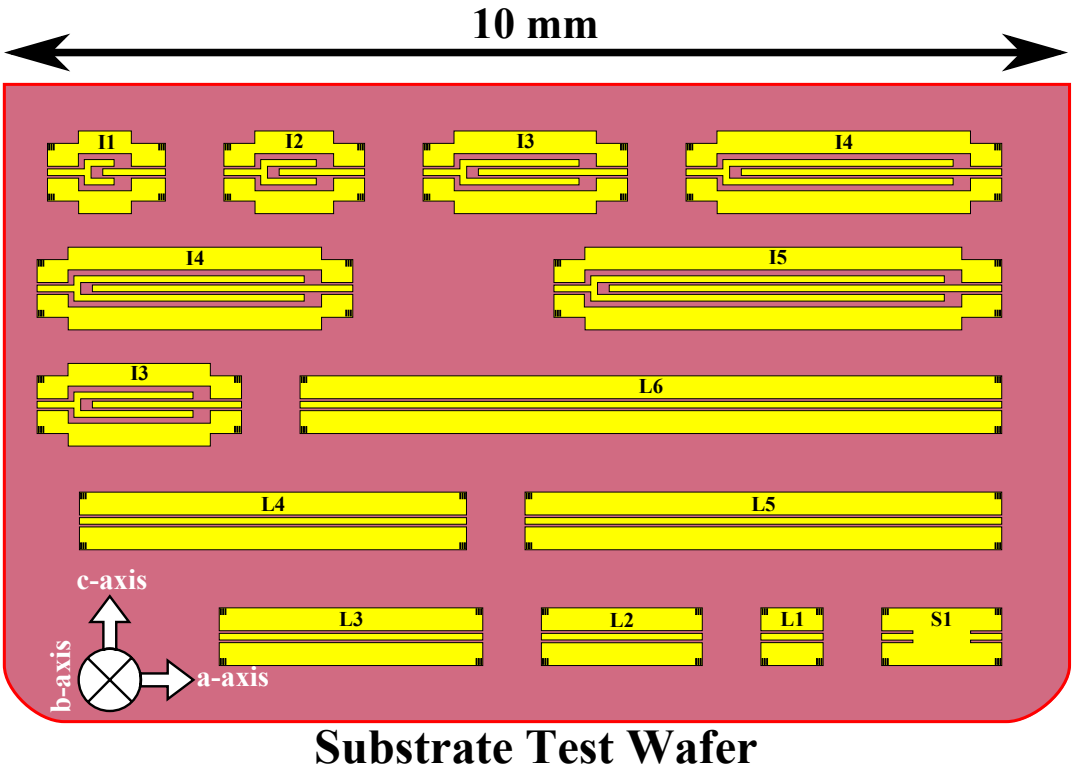

Figure 2.10: Substrate Test Wafer

A schematic of the substrate test wafer. The substrate test wafer was approximately 10 mm × 10 mm. Our devices were fabricated in a 5 mm × 10 mm area. The crystal axis of the substrate is indicated in the bottom left. For $DyScO_3(110)$ and $GdScO_3(110)$, the devices were fabricated on the c-a plane.

The redundant IDCs, I3 ($\ell = 0.875$ mm) and I4 ($\ell = 1.835$ mm), shown in Fig. 2.11 (shaded grey) were used for LF temperature-dependent measurements and electric field dependent measurements. The set of IDCs (I1, I2, I3, I4, and I5) in the light red shaded region in Fig. 2.11 were used for the LF and RF measurements. We did not use the same devices for the frequency-dependent measurements and the temperature-dependent measurements, because the repeated contact of the temperature dependent and electric field dependent measurements caused considerable wear on the electrical contacts and could have affected the RF response of the devices. The L6 CPW in the blue shaded region was used to characterize the γ and Z in RF regime, which was used

to translate the reference planes of the calibration in the RF regime to position shown in Fig. 2.2(a). The CPWs (L1, L2, L3, L4, L5, and L6) and symmetric 0.210 mm offset short circuit reflect (Fig. 2.11 (light blue)) were measured in the HF regime. Although in RF regime it is possible to obtain the distributed circuit parameters of a CPW directly from corrected S-parameters, in the HF regime this approach breaks down at frequencies where the phases of the corrected S-parameter measurements cross zero.

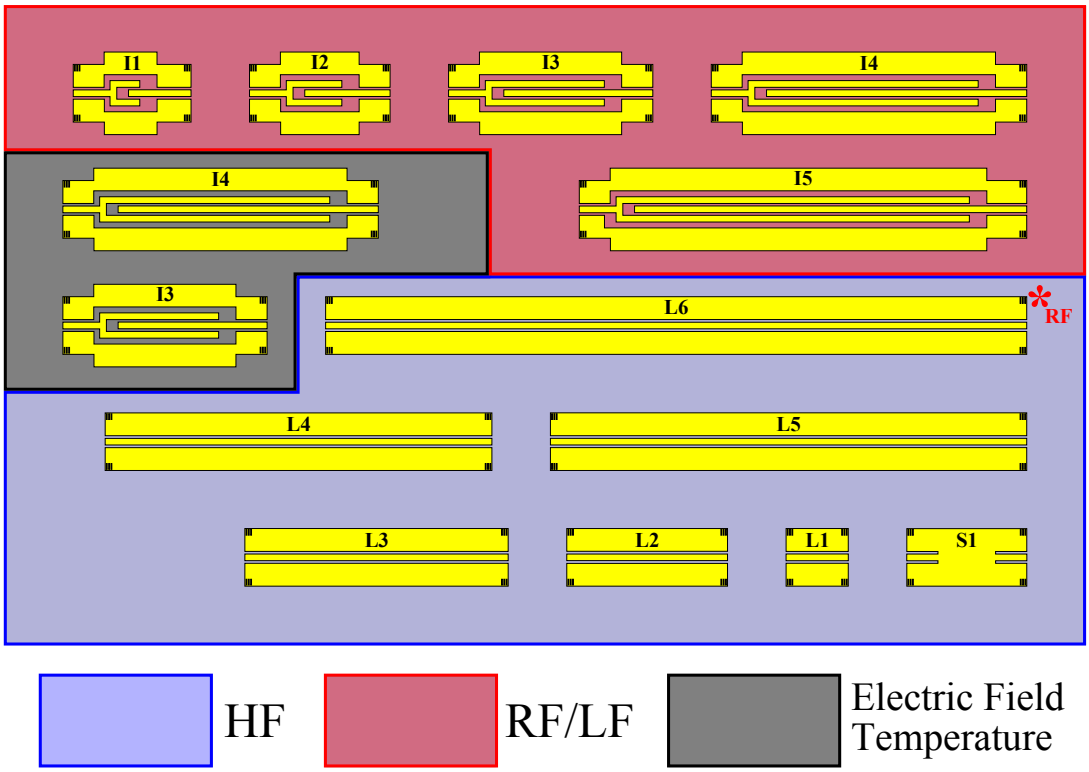

Figure 2.11: Test Wafer Measurement Devices and Procedure

A schematic of the set of devices fabricated on a test wafer and a description of the measurements. Temperature and electric field dependence were characterized by measuring the interdigitated capacitors (I3, I4) in the grey shaded region. The interdigitated capacitors (I1, I2, I3, I4, I5) in the light red region were used to characterize the low frequency (LF) and radio frequency (RF) dependence of the interdigitated capacitors on the test wafer. We characterize the frequency dependence in the HF regime with a set of coplanar waveguides (L2, L3, L4, L5, L6), a thru (L1), and symmetric short circuit reflect (S1).

We extracted the capacitance and conductance per unit length of the IDCs in the LF and RF regimes of the test wafers following the approach discussed in Sec. 2.4.1. In the HF regime, we performed multiline thru-reflect-line calibrations to obtain the γ and Z . This was accomplished by first correcting the HF devices on the test wafer (Fig. 2.11 (light blue)) to 50 Ω with the error boxes obtained from the calibration wafer. This is typically called a first-tier calibration. We then performed a second-tier multiline thru-reflect-line calibration on the corrected HF measurements of the test wafer devices, which enabled us to extract γ with high precision over a broad frequency range. We define a pair of second-tier error boxes X and Y as T_1 and T_2 obtained from corrected S-parameters measurements of a set of CPWs on a test wafer relative to a known reference impedance. We translated X and Y to the probe tips on the test wafer. If both calibrations were perfect and the measurement geometries were identical, then X and Y would simply be impedance transformers, characterizing the mismatch between the 50 Ω reference impedance and the Z of the CPW on the test wafer.

Following this line of logic, we obtained an estimate for Z of the test wafer with the technique discussed in Ref. [32],

$$Z = Z_r \left(\frac{1+\Gamma}{1-\Gamma} \right), \tag{2.17}$$

where Z_r is the reference impedance ($50\,\Omega$) and the Γ is found to be,

$$\Gamma = \frac{\sqrt{(X_{12}+X_{21})^2}}{\sqrt{4-(X_{12}+X_{21})^2}}. \tag{2.18}$$

A similar expression to Eq. 2.18 can be derived from the right hand side error box, Y. It should be noted that both X and Y included a small section of CPW transmission line, *e.g.* the section used for contact between the fiducial marks in Fig. 2.4(a), and that this term can have a small, and in some cases negligible, effect on the extracted

impedance. We have found empirically that for our devices Z extracted using Eq. 2.17 displayed increased variation as a function of frequency between 10^{10} Hz and 10^{11}Hz, which is discussed in detail in Sec. 2.6. It was for this reason that we typically modeled the conductors with 2D finite element simulation software or fit the R and L obtained from γ (extracted from multiline thru-reflect-line) and Z (extracted from Eq. 2.17), as discussed in Sec. 2.4.2. A simplified derivation of Eqs. 2.17 and 2.18 can be found in App. A.5.

2.6 Demonstration on $Sr_7Ti_6O_{19}/DyScO_3(110)$ and $DyScO_3(110)$

In the previous sections, we established in detail the measurement approach and data analysis philosophy used to extract C_{film}, G_{film} and $\tan(\delta_{film})$ (Eqs. 2.4, 2.5, and 2.6) over the continuous frequency range of 100 Hz to 40 GHz. In this section, we demonstrate this technique on a thin-film test wafer and a companion substrate test wafer. The thin-film test wafer was 50 nm of $Sr_7Ti_6O_{19}$ on approximately 1 mm thick $DyScO_3(110)$, and the companion substrate test wafer was $DyScO_3(110)$.

In Fig. 2.12, we show the series capacitance $\left(\frac{\Im(Y_s)}{\omega}\right)$ at 300 K from 1 MHz to 300 MHz (RF) for the IDCs of active lengths ℓ = (0.100 mm, 0.325 mm, 0.875 mm, 1.835 mm, 2.900 mm), as the cyan, dark green, dark yellow, red and blue solid lines, respectively. It should be noted that this is measured data. The measurements in Fig. 2.12 are remarkably flat as a function of frequency, because we performed 3D finite element simulations of each device as a function of frequency before fabricating the devices to ensure that the distributed effects would not play a significant role over our measurement frequency range. At each frequency point in Fig. 2.12, we performed a linear fit as a function of length to extract the distributed capacitance (C) and conductance (G) per unit length (Eq. 2.3). In this same step, we also extracted the uncertainties, ΔC and ΔG. These measurements and analysis steps were repeated for the $Sr_7Ti_6O_{19}/DyScO_3(110)$ thin-film test wafer. After extracting the C_{film}, G_{film},

and their associated errors in the LF and RF regimes, we turned our attention to the HF analysis of the $Sr_7Ti_6O_{19}/DyScO_3(110)$ thin-film test wafer and the companion substrate test wafer, $DyScO_3(110)$.

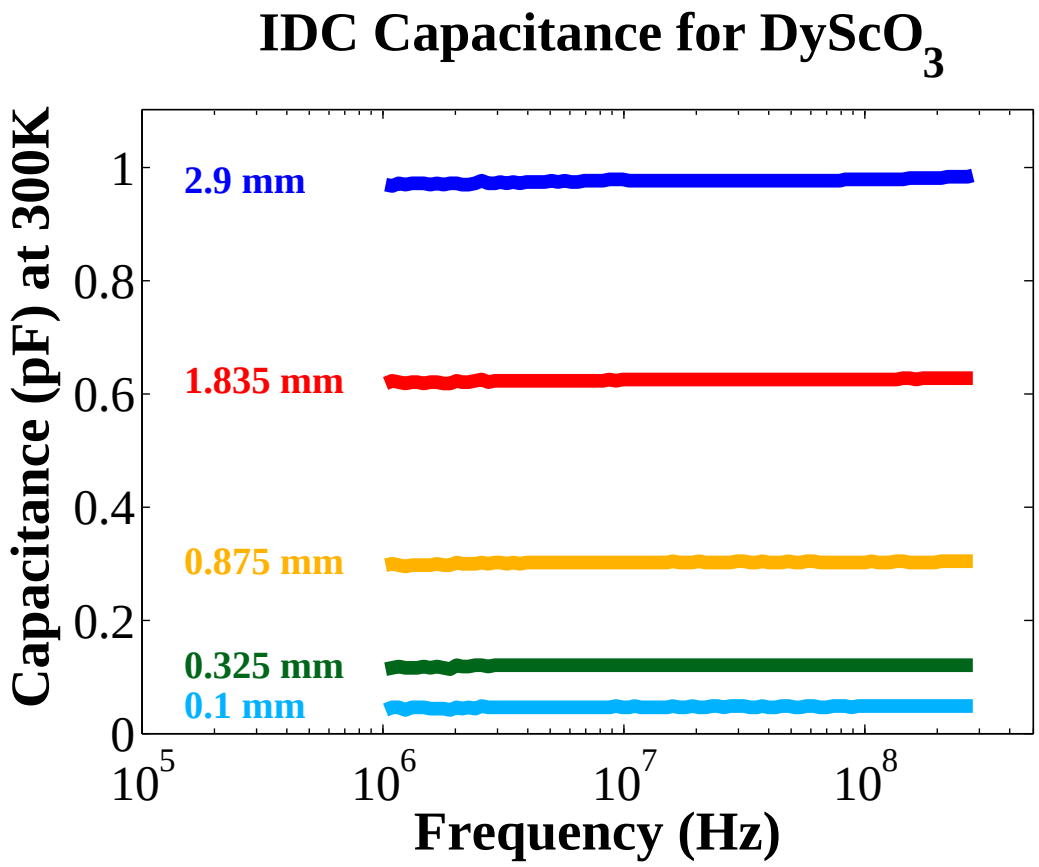

Figure 2.12: Series Capacitance for Interdigitated Capacitors (IDCs) on $DyScO_3(110)$ (110)

The series capacitance at 300 K for a set of interdigitated capacitors (I1, I2, I3, I4, I5) on $DyScO_3(110)$ of active lengths ℓ = (0.100 mm, 0.325 mm, 0.875 mm, 1.835 mm, 2.9 mm) for the radio frequency (RF) measurement regime.

In Fig. 2.13, we show the measured propagation constant (γ) for the CPW structure on the $Sr_7Ti_6O_{19}/DyScO_3(110)$ thin-film test wafer (blue) and the $DyScO_3(110)$ companion substrate test wafer (grey) at 300 K over the entire HF measurement regime (45 MHz to 40 GHz). The imaginary part of the γ is scaled by the inverse of the frequency (f^{-1}) in GHz to reduce the frequency dependence, and it is shown as the dashed lines. The corresponding axis for the imaginary part of the γ is shown on

the right axis in Fig. 2.13. The real part of γ is shown as the solid lines, and their corresponding axis is on the left. We extracted the γ for the companion substrate and thin-film test wafers following the procedure outlined in Sec. 2.4.2 with the algorithm derived in Ref. [30]. After obtaining the γ for the companion substrate and thin-film test wafers, we extracted the characteristic impedance with Eq. 2.17.

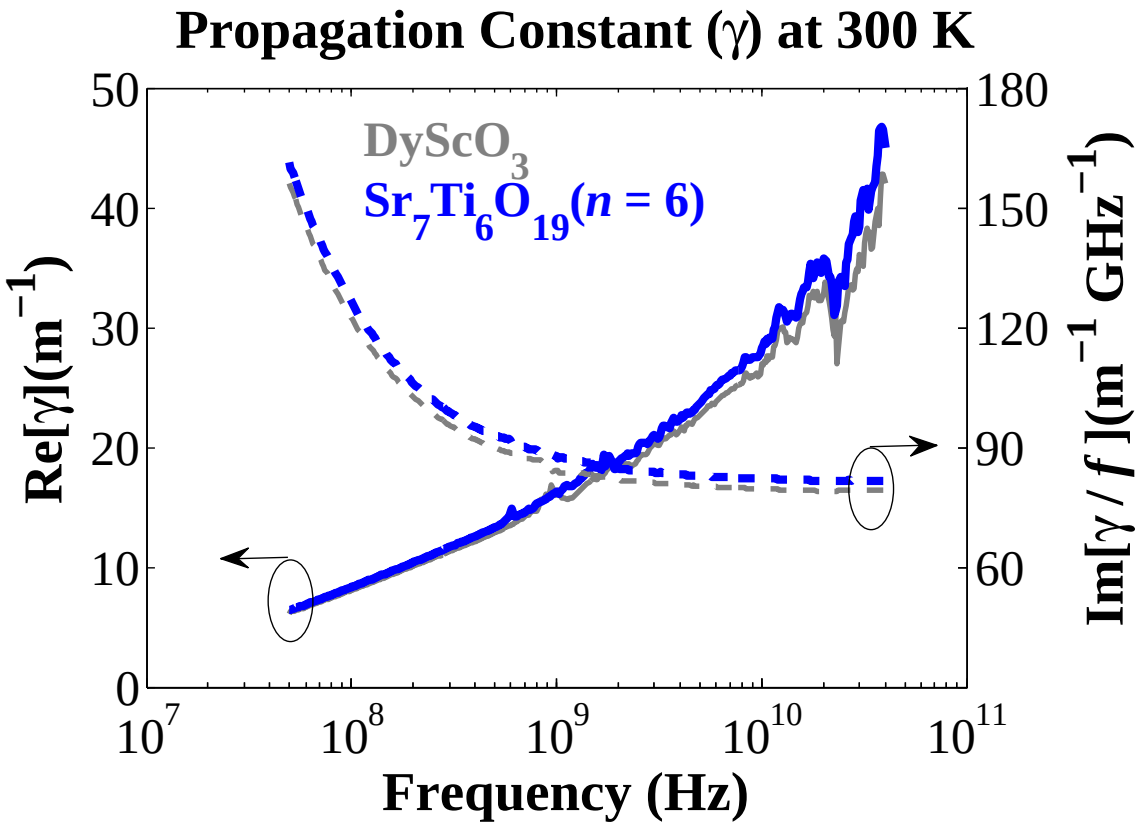

Figure 2.13: Propagation Constant for Coplanar Waveguides on $Sr_7Ti_6O_{19}/DyScO_3(110)$ and $DyScO_3(110)$

The propagation constant (γ) at 300 K for the coplanar waveguides fabricated on a 50 nm thick film of $Sr_7Ti_6O_{19}$ on 1 mm thick $DyScO_3(110)$ thin-film test wafer (blue) and a 1 mm $DyScO_3(110)$ companion substrate test wafer (grey). γ was obtained directly with the multiline thru-reflect-line measurement technique. The active lengths of the coplanar waveguides were ℓ = (0.100 mm, 0.325 mm, 0.875 mm, 1.835 mm, 2.900 mm). The real part of γ for each test wafer is shown as the solid lines, and their corresponding axis is on the left hand side. The imaginary parts of the γ for each test wafer is scaled to the inverse of the frequency in GHz to reduce the frequency dependence. They are shown as the dashed lines, and their corresponding axis is on the right hand side.

Figure 2.14 shows the characteristic impedance (Z) for the CPW structure on the $Sr_7Ti_6O_{19}/DyScO_3(110)$ thin-film test wafer (blue) and the $DyScO_3(110)$ companion substrate test wafer (grey) at 300 K over the entire HF measurement regime (45 MHz to 40 GHz). The imaginary part of the Z was scaled by the frequency (f)

in GHz to reduce the frequency dependence, and it is shown as the dashed lines. The corresponding axis for the imaginary part of the Z is shown on the right axis in Fig. 2.13. The real part of γ is shown as the solid lines, and their corresponding axis is on the left. From Fig. 2.14, it is clear that even though Eq. 2.17 is an effective approach to obtain Z for a large portion of the HF regime, at high frequencies ($f > 10^{10}$) the imaginary part of Z becomes increasingly uncertain for the CPW geometry explored here. We believe that this error could be due to the section of CPW that was embedded in calibration below the g-s-g probes, which is discussed in Ref. [32]. We can get a sense for where this error has the most significant effect by taking the product $\gamma \cdot Z$ and obtaining the resistance ($R = \Re(\gamma \cdot Z)$) and inductance ($L = \Im(\gamma \cdot Z)/\omega$) per unit length.

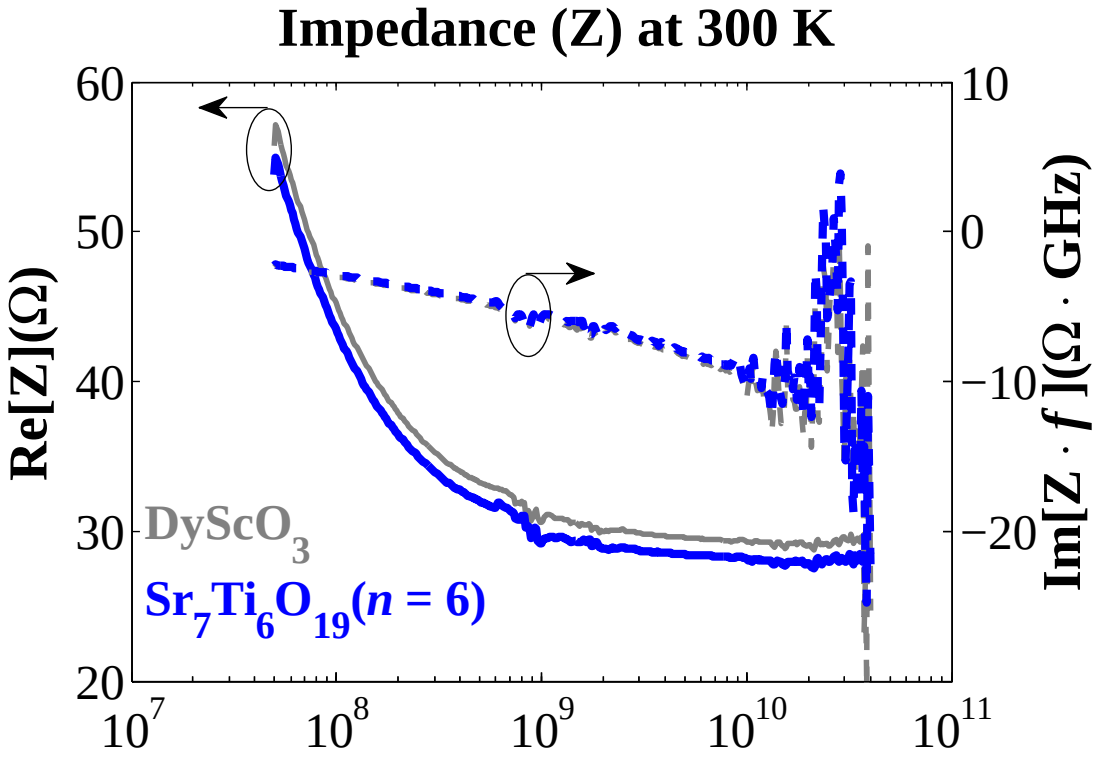

Figure 2.14: Impedance for Coplanar Waveguides on $Sr_7Ti_6O_{19}/DyScO_3(110)$ and $DyScO_3(110)$

The characteristic impedance (Z) at 300 K for the coplanar waveguides fabricated on a 50 nm thick film of $Sr_7Ti_6O_{19}$ on 1 mm thick $DyScO_3(110)$ thin-film test wafer (blue) and a 1 mm $DyScO_3(110)$ companion substrate test wafer (grey). Z was obtained indirectly from the error box method. The active lengths of the coplanar waveguides were ℓ = (0.100 mm, 0.325 mm, 0.875 mm, 1.835 mm, 2.900 mm). The real part of Z for each test wafer is shown as the solid lines, and its corresponding axis is on the left hand side. The imaginary parts of the Z for each test wafer is scaled to the frequency in GHz to reduce the frequency dependence. It is shown as dashed lines, and their corresponding axis is on the right hand side.

In Fig. 2.15, we show R as a function of frequency for the $DyScO_3(110)$ companion substrate test wafer as the solid colored lines at series of different measurement temperatures: 60 K (blue), 120 K (red), 180 K (dark yellow), 240 K (dark green), and 300 K (cyan). R increases with increasing frequency at fixed temperature, and decreases with decreasing temperature at fixed frequency. This dependence is due to

the fact R is proportional to $\frac{1}{(\sigma \cdot \delta)}$ over the HF regime, where δ is the skin depth and σ is the conductivity of the conductors [28, 37]. As frequency increases δ decreases, the area of the conductor that is transmitting the current also decreases, which causes R to increase. Likewise, as temperature decreases, the σ increases, which causes$R$ to decrease. The solid black line at 300 K is the R that was obtained from the 2D finite element simulations (R_{sim}). At 240 K, 180 K, 120 K, and 60 K, the R for each temperature was fit with a shape-preserving interpolants with high smoothness. We have found that the difference between the simulations and the fit was typically on the order of the uncertainty in R_{sim}; however, the 2D finite element simulation is the preferred approach to obtaining the R_{sim} and L_{sim}.

Although somewhat less intuitive, it is instructive to also see the effect of frequency and temperature dependence on L. We show the inductance per unit length as a function of frequency at variable temperature in Fig. 2.16 for the CPW structures on $DyScO_3(110)$: 60 K (blue), 120 K (red), 180 K (dark yellow), 240 K (dark green), and 300 K (cyan). One can see clearly in Fig. 2.16 that the 2D finite element simulations at 300 K (cyan) strongly agree with the extracted inductance per unit length L. At fixed temperature, the high frequency limit of L is a constant, which is inversely proportional to a geometry factor (essentially the gap of the CPW) [37]. Thus all of curves in Fig. 2.16 essentially asymptote to the same high frequency limit. At low frequency, where the current distribution is uniform over the cross section, L again limits to a constant, which is not intuitive in its form and can be found in Ref. [37]. Conductivity controls how rapidly the L transitions between these two limits, but does not effect the limits themselves [37]. Again, we fit the remaining temperatures (60 K (blue), 120 K (red), 180 K (dark yellow), 240 K (dark green)) with shape-preserving interpolants with high smoothness. As was the case with the R, we have found that the difference between the simulations and the fit was typically on the order of the uncertainty in L_{sim}, however, again the 2D finite element simulation is

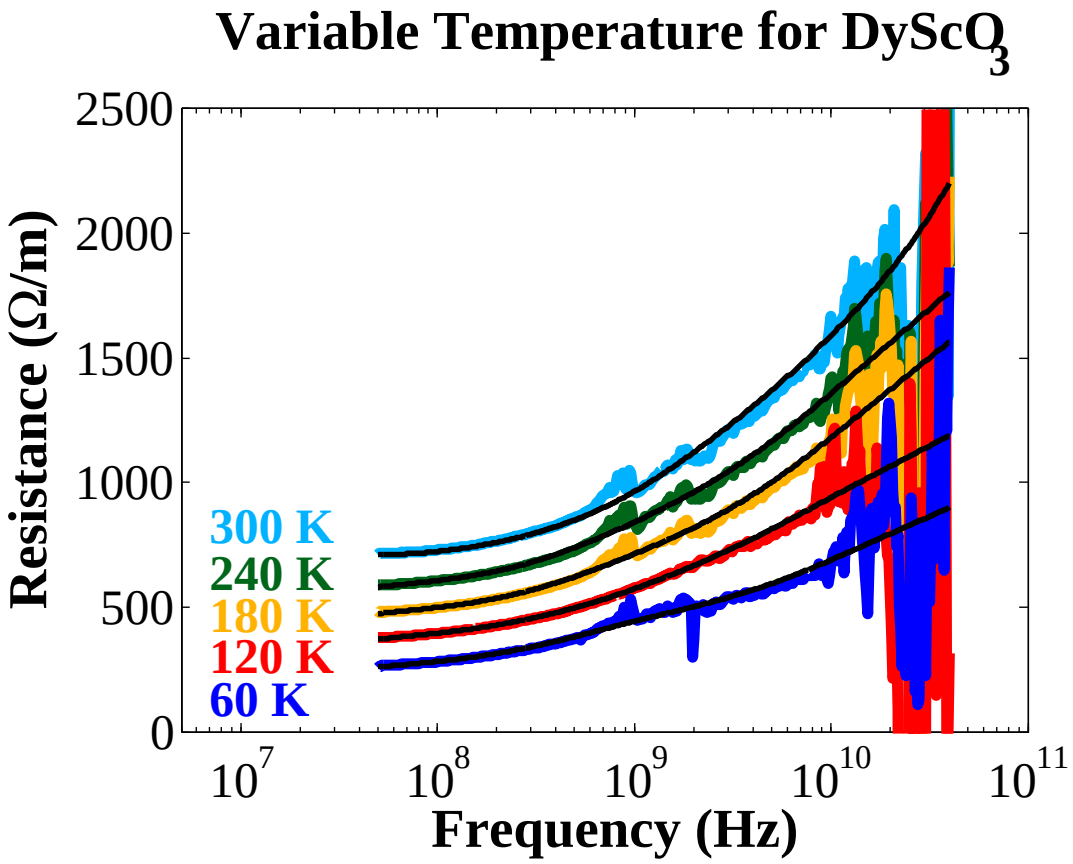

Figure 2.15: Resistance Per Unit Length for a Coplanar Waveguide on $DyScO_3(110)$

The resistance per unit length from 45 MHz to 40 GHz for the coplanar waveguides fabricated on $DyScO_3(110)$ obtained from the characteristic impedance (Z) and the propagation constant (γ) at 60 K (blue), 120 K (red), 180 K (dark yellow), 240 K (dark green), 300 K (cyan). The black solid line at 300 K was obtained from 2D finite element simulations and the remaining black solid lines are fits with shape-preserving interpolants with high smoothness.

the preferred approach. Having obtained expressions for the R_{sim} and L_{sim} at 300 K, we can now extract the C over the entire frequency regime for both ensembles of IDCs and CPWs.

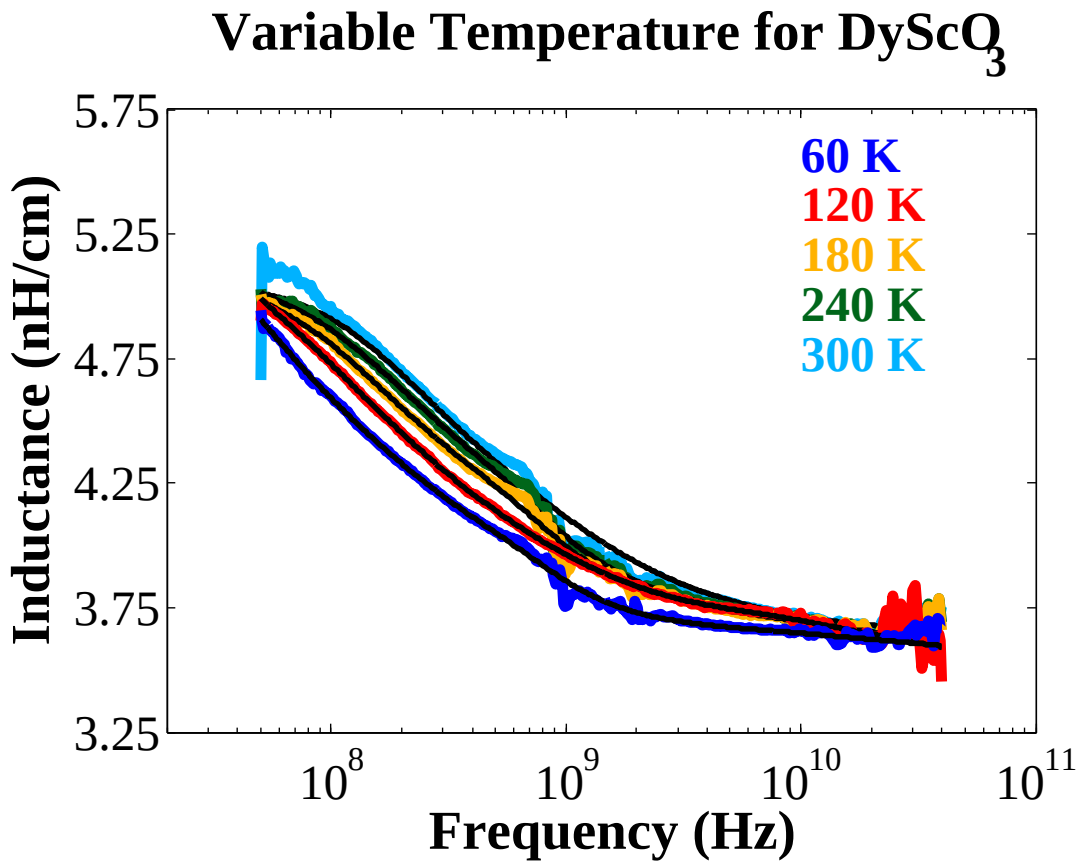

Figure 2.16: Inductance Per Unit Length for a Coplanar Waveguide on $DyScO_3$(110)

The inductance per unit length from 45 MHz to 40 GHz for the coplanar waveguides fabricated on $DyScO_3$(110) obtained from the characteristic impedance (Z) and the propagation constant (γ) at 60 K (blue), 120 K (red), 180 K (dark yellow), 240 K (dark green), 300 K (cyan). The black solid line at 300 K was obtained from 2D finite element simulations and the remaining black solid lines are fits with shape-preserving interpolants with high smoothness.

Following the approach laid out in Secs. 2.4.1 and 2.4.2, we have extracted the C of the IDC and CPW geometry for the $Sr_7Ti_6O_{19}/DyScO_3$(110) thin-film test wafer (blue) and the $DyScO_3$(110) companion substrate test wafer (grey) at 300 K over from 100 Hz to 40 GHz (Fig. 2.17). Recall that the cross-sectional geometries were

different for the IDC compared to the CPW. It was, therefore, unsurprising that the total C for the IDC and CPW geometries are different. The measurements of the IDC devices cover a little over 6 decades of the frequency space, while the measurements of the CPWs cover the remaining 3 decades. One can see that some distributed effects are still evident in the C extracted from the ensemble of IDCs above 100 MHz. Some of these errors can fortunately be subtracted out by taking the difference in the C to obtain the contribution of the film (See Eq. 2.4).

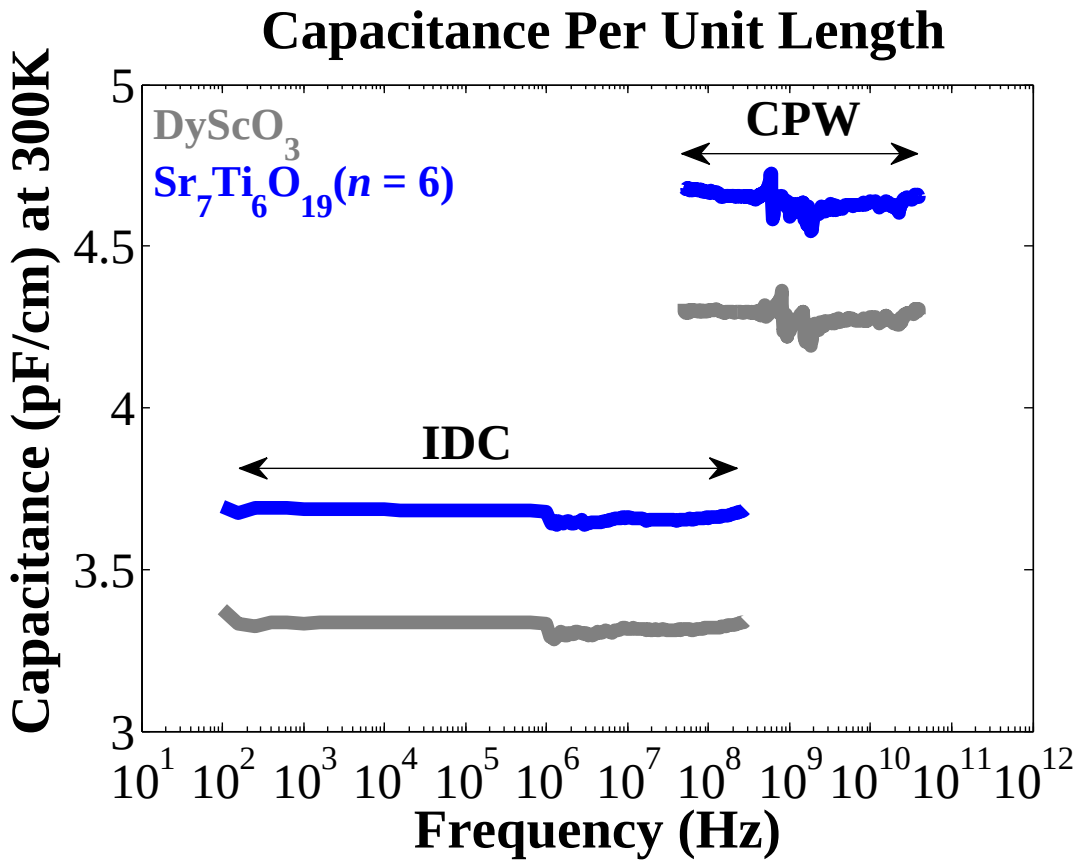

Figure 2.17: Capacitance Per Unit Length for $Sr_7Ti_6O_{19}/DyScO_3(110)$ and $DyScO_3(110)$

The capacitance per unit length at 300 K for a set of coplanar waveguides (CPW) and interdigitated capacitors (IDC) fabricated on a 50 nm thick film of $Sr_7Ti_6O_{19}$ on 1 mm thick $DyScO_3(110)$ and a 1 mm $DyScO_3(110)$ companion substrate test wafer. From 100 Hz to 300 MHz, the capacitance per unit length was obtained from a set of interdigitated capacitors with active lengths ℓ = (0.100 mm, 0.325 mm, 0.875 mm, 1.835 mm, 2.9 mm). From 45 MHz to 40 GHz, the capacitance per unit length was extracted from the propagation constant, where the resistance and inductance per unit length were obtained from 2D finite element simulations of the conductors.

In Fig. 2.18, we show the change in capacitance per unit length at 300 K from the ensemble of CPWs (red) and IDCs (blue) fabricated on the $Sr_7Ti_6O_{19}/DyScO_3(110)$ thin film test wafer and the $DyScO_3(110)$ companion substrate test wafer. This change in capacitance is the contribution of the film, C_{film} (See Eq. 2.4). For geometries employed here, we have designed C_{film} of the CPW to be close to C_{film} of the IDC,

however, this is not a requisite for this technique to work. As we will discuss in the following section, we only need C_{film} and knowledge of the conductor geometry to map to permittivity via 2D finite element simulations.

2.7 Mapping to Complex In-plane Permittivity

Much like the capacitance of a dielectrically loaded parallel-plate capacitor can be written in terms of the geometry and the permittivity of the dielectric, we can relate the capacitance per unit length of the CPW and IDC geometry to the real part of the in-plane permittivity of the dielectric. The function that relates the distributed capacitance to the real part of the in-plane permittivity for a given device is called a mapping function. There are a variety of approaches to obtaining the mapping function for the planar devices discussed in Sec. 2.4; one of the most popular techniques is conformal mapping [21, 38]. Another more computationally rigorous approach is to use 2D finite element simulations of the device geometry [4, 23, 24, 36, 39]. We obtain the mapping functions discussed in this work with 2D finite element simulations.

We constructed the model of our device with the 2D finite element simulation software where the cross-sectional geometry of the model was the measured cross-sectional geometry of our devices (See Figs. 2.2(b) and2.4(b)). The model also included the properties of the conductors (measured directly with dc measurements of the CPWs). For substrates, we simply performed a parametric sweep of the real part of the in-plane relative permittivity of the companion substrate test wafer (K_{sub}) and at each permittivity value obtained the capacitance per unit length of the substrate test wafer (C_{sub}). The result was a simple mapping function that related C_{sub} of a given device to K_{sub} as

$$K_{sub} = f(C_{sub}). \tag{2.19}$$

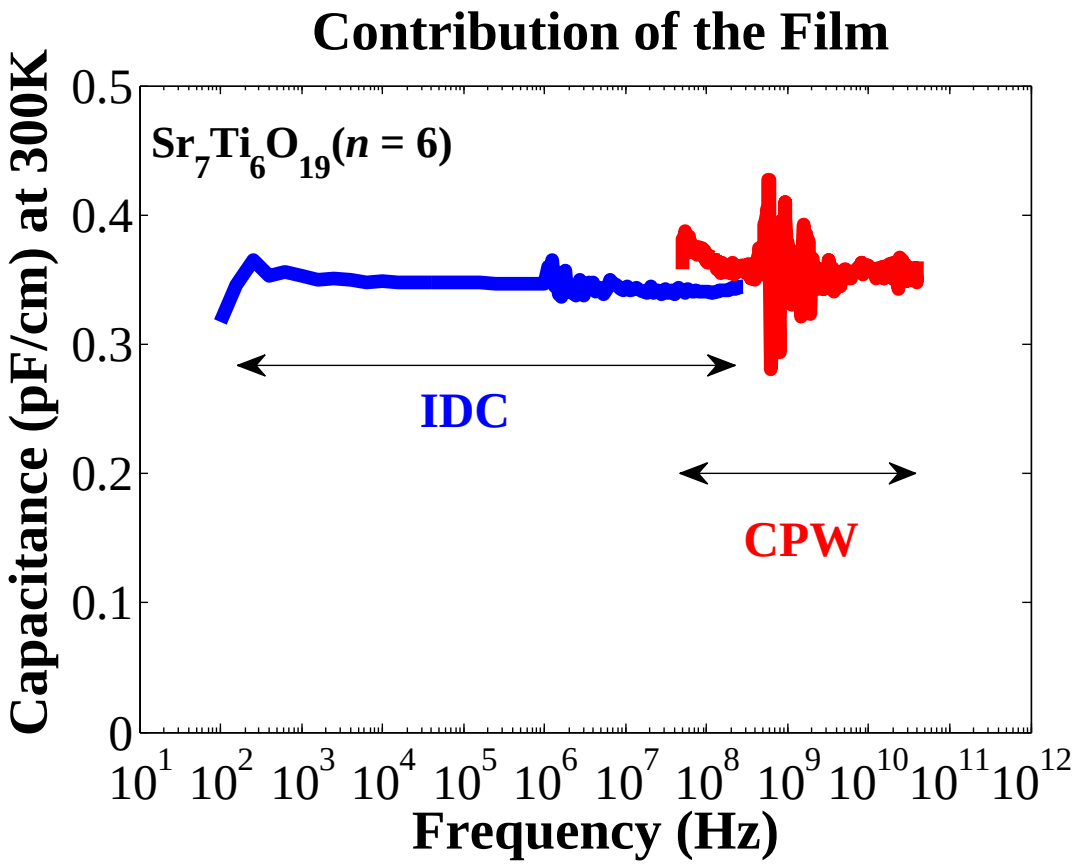

Figure 2.18: Change in Capacitance Per Unit Length for $Sr_7Ti_6O_{19}/DyScO_3(110)$ Relative to Devices on $DyScO_3(110)$

The change in capacitance per unit length at 300 K for a set of coplanar waveguides (CPW) and interdigitated capacitors (IDC) fabricated on a 50 nm thick film of $Sr_7Ti_6O_{19}$ on 1 mm thick $DyScO_3(110)$ with respect to the capacitance per unit length of the same devices measured on a 1 mm $DyScO_3(110)$ companion substrate test wafer. From 100 Hz to 300 MHz, the change in capacitance per unit length obtained from a set of interdigitated capacitors with active lengths ℓ = (0.100 mm, 0.325 mm, 0.875 mm, 1.835 mm, 2.9 mm) is shown in blue. From 45 MHz to 40 GHz, the change in capacitance per unit length extracted from the propagation constant, where the resistance and inductance per unit length were obtained from 2D finite element simulations of the conductors, is shown in red.

Eq. 2.19 must be calculated for the IDC and CPW geometry, independently. If C_{sub} is constant as a function of frequency and large compared to the relative permittivity of free space, then $f(C_{sub})$ in Eq. 2.19 can often be approximated as a first order polynomial. For thin-film test wafers, Eq. 2.19 must be modified to map from the change in capacitance ($C_{film} = C_{tot} - C_{sub}$) to the change in the real part of the in-plane relative permittivity,

$$\begin{aligned} K_{film} - K_{sub} &= f(C_{tot} - C_{sub}) \\ &= f(C_{film}), \end{aligned} \tag{2.20}$$

where K_{film} is the real part of the in-plane relative permittivity of the thin-film test wafer. Procedurally, we first obtained K_{sub} from the measurements of the companion substrate test wafer. We then inserted the mean value of K_{sub} into our model simulation parameters, and then performed a series of 2D finite element simulations continuously varying K_{film}.

In Fig. 2.19, we show the mapping functions obtained from 402 2D finite element simulations. The y-axis of Fig. 2.19 is the change in the real part of the in-plane relative permittivity (ΔK_{11}(in-plane)) or the left hand side of Eq. 2.20. The change in capacitance, or C_{film}, is the x-axis in Fig. 2.19 and it is labeled 'ΔCapacitance'. The x-axis is shown on a logarithmic scale to more clearly show the behavior at small changes in capacitance, which is relevant given the scale of the measurements in Fig. 2.18. We show the IDC (blue dashed line with blue triangles) and CPW (red solid line with red squares) mapping functions for our measurement geometries. Each simulation set represents 201 thin film permittivity values logarithmically spaced between the substrate permittivity ($K_{11} \approx 26$) and the maximum simulated permittivity of $K_{11} = 2500$. In practice, we fit the 2D finite element simu-

lation results to a shape-preserving interpolant. Once we have obtained the mapping functions, we can finally obtain the real part of the in-plane relative permittivity of the $Sr_7Ti_6O_{19}/DyScO_3(110)$ thin-film test wafer.

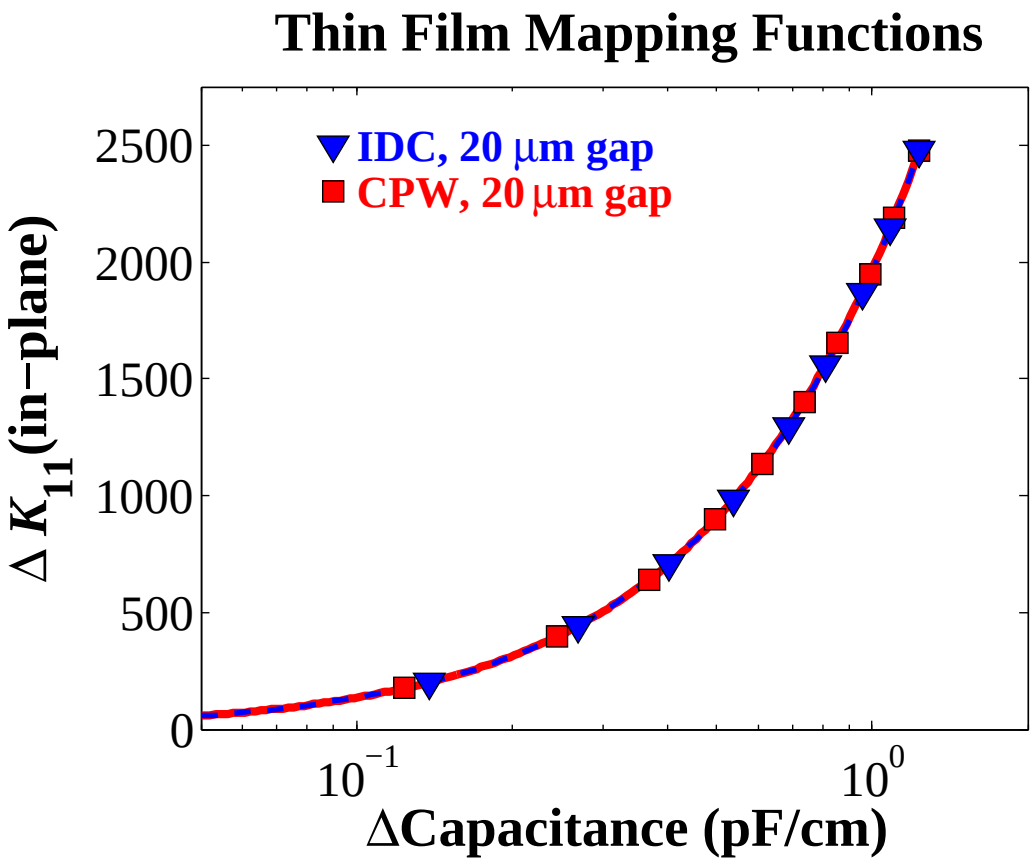

Figure 2.19: Thin Film Mapping Functions for Interdigitated Capacitors (IDC) and Coplanar Waveguides (CPW)

We show the mapping functions obtained from 2D finite element simulations of the device geometry for the interdigitated capacitor (IDC) and coplanar waveguide (CPW). The real part of the in-plane relative permittivity (K_{11}) of the film is obtained by adding the K_{11} of the substrate to the change in K_{11} for the film. The mapping function for the IDC is shown as the blue dashed line and indicated at selected points with red triangles. The corresponding mapping function for the CPW is shown as the red solid line and indicated at selected points with red squares. The curves shown are 201 thin film permittivity values logarithmically spaced between the substrate permittivity ($K_{11} \approx 26$) and the maximum simulated permittivity of $K_{11} = 2500$, for the IDC and CPW geometries, respectively.

The real part of the in-plane relative permittivity K_{11} of the 50 nm thick $Sr_7Ti_6O_{19}(n = 6)$ thin film on 1 mm thick $DyScO_3(110)$ is shown from 100 Hz to 40 GHz in Fig. 2.20. The solid blue line from 100 Hz to 300 MHz in Fig. 2.20 is the K_{11} extracted from the ensemble of IDCs with the approach discussed in Sec. 2.4.1. In this frequency range, many of the systematic errors that were evident in Fig. 2.17 have subtracted out. From 45 MHz to 40 GHz, we show K_{11} obtained from the CPW technique as the red solid line (See Sec. 2.4.2). One can clearly see that there is very good agreement between the IDC and CPW techniques and the different instrument measurement ranges. Although it was essential to confirm that the data is consistent in the overlap frequency range between the IDC and CPW approaches (45 MHz to 300 MHz), we typically cut the HF data off at approximately 2 GHz, because it obscured the frequency dependence. We have found that the intrinsic error around 1 GHz in the measurement instrument was less evident with larger values of C_{film}, and that the uncertainty in the propagation constant was a maximum in this range. For comparison purposes, the measurements presented in throughout this thesis were approximately one to two orders of magnitude smaller than the work presented in Refs. [2, 4, 23–25].

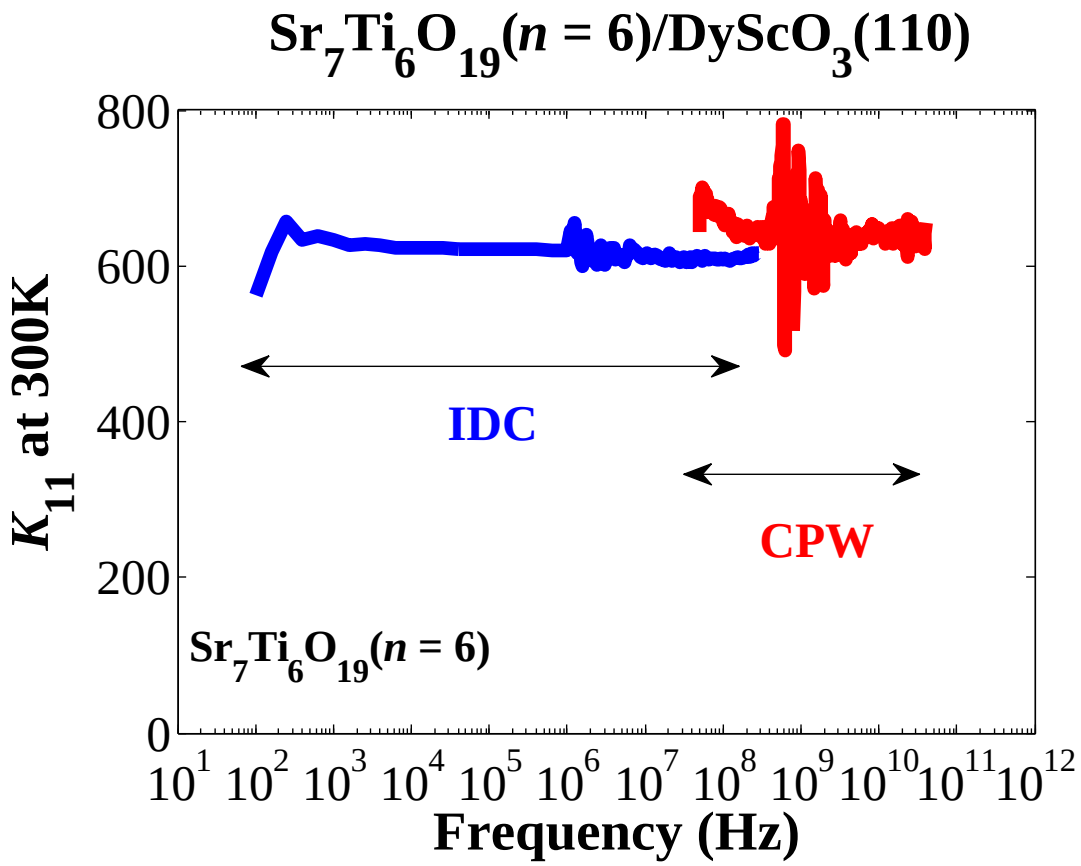

Figure 2.20: Permittivity (K_{11}) of $Sr_7Ti_6O_{19}/DyScO_3(110)$

The real part of the in-plane relative permittivity (K_{11}) of the 50 nm thick $Sr_7Ti_6O_{19}$ thin film on 1 mm thick $DyScO_3(110)$ is shown from 100 Hz to 40 GHz. From 100 Hz to 300 MHz, the real part of the in-plane relative permittivity (blue) is obtained from interdigitated capacitors (IDC). From 45 MHz to 40 GHz, the real part of the in-plane relative permittivity (red) is obtained from coplanar waveguides (CPW).

2.7.1 Propagation of Error for Complex Permittivity

Earlier in Sec. 2.7, we stated that the uncertainty in C_{film} and G_{film} could be obtained from a linear fit as a function of length. We then arrived at Eqs. 2.7 and 2.8, both of which are actually general and can also be used for the CPW devices. Once we have obtained the numeric uncertainty in C_{tot}, C_{sub}, G_{tot}, and G_{sub} from Eq. 2.14, we used Eqs. 2.7 and 2.8 to arrive at the numeric values for ΔC_{film} and ΔG_{film}. We calculated the uncertainty in K_{11} as

$$\Delta K_{11} \approx \sqrt{m^2 \cdot (\Delta C_{film})^2}, \tag{2.21}$$

where m is a linear approximation to the mapping function (Eq. 2.20). The derivation of Eq. 2.21 can be found in App. A.6.

In Fig. 2.21, we show the data shown in Fig. 2.20 with the corresponding uncertainties in both the measurement regimes. From 100 Hz to 300 MHz, it is clear that the uncertainty in K_{11} for the IDC measurements was frequency independent. In contrast, the high frequency uncertainty in the K_{11} extracted from the CPW devices was much larger and had substantially more frequency dependence. This reflects the inherent challenges associated with making measurements in gigahertz frequency range rather than the inadequacy of the measurement geometry and technique. For more accurate characterization at HF, we performed linear frequency measurements over a smaller frequency range.

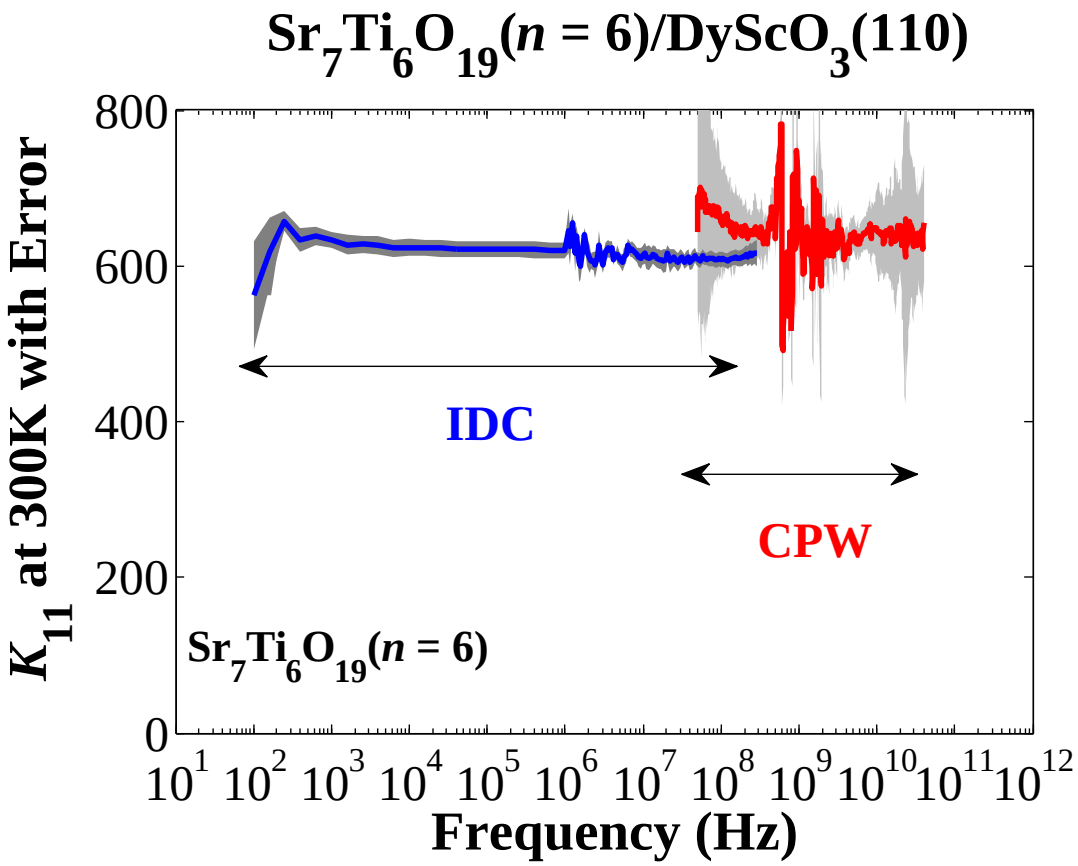

Figure 2.21: Permittivity (K_{11}) of $Sr_7Ti_6O_{19}/DyScO_3(110)$ with Uncertainty

The real part of the in-plane relative permittivity (K_{11}) of the 50 nm thick $Sr_7Ti_6O_{19}$ thin film on 1 mm thick $DyScO_3(110)$ is shown from 100 Hz to 40 GHz. From 100 Hz to 300 MHz, the real part of the in-plane relative permittivity (blue) is obtained from interdigitated capacitors (IDC) with the uncertainty shown in dark grey. From 45 MHz to 40 GHz, the real part of the in-plane relative permittivity (red) is obtained from coplanar waveguides (CPW) with the uncertainty shown in light grey.

In Fig. 2.22, we show the corresponding loss tangent ($\tan(\delta_{11})$) of the $Sr_7Ti_6O_{19}/DyScO_3(110)$ thin-film test wafer. The $\tan(\delta_{11})$ of the $Sr_7Ti_6O_{19}/DyScO_3(110)$ thin-film test wafer is fairly constant over a very broad frequency range. Below 10^3 Hz, the loss tangent becomes uncertain due to the loss of phase sensitivity at such long wavelengths for the IDCs. The decrease in resolution at 10^6 Hz is due to uncertainty in the C_{film}, which is a consequence of the fact that magnitude of the S-parameter measurements of the IDCs were near the sensitivity limits of the RF network analyzer. At low enough frequencies, γ tends to a real-valued number (See Eq. 2.9),

which implies that phase cannot be used to distinguish CPWs of different lengths. This explains the variability below 2 GHz in our measurements and dramatic increase in the uncertainty (light grey). Although we neglect to show it here, we can obtain the imaginary part of the permittivity by,

$$\Im(K_{11}) = \tan(\delta_{11}) \cdot \Re(K_{11}), \tag{2.22}$$

and it has an uncertainty of written as

$$\Delta(\Im(K_{11})) = \sqrt{(\tan(\delta_{11}))^2(\Delta(\Re(K_{11})))^2 + (\Re(K_{11}))^2(\Delta\tan(\delta_{11}))^2}. \tag{2.23}$$

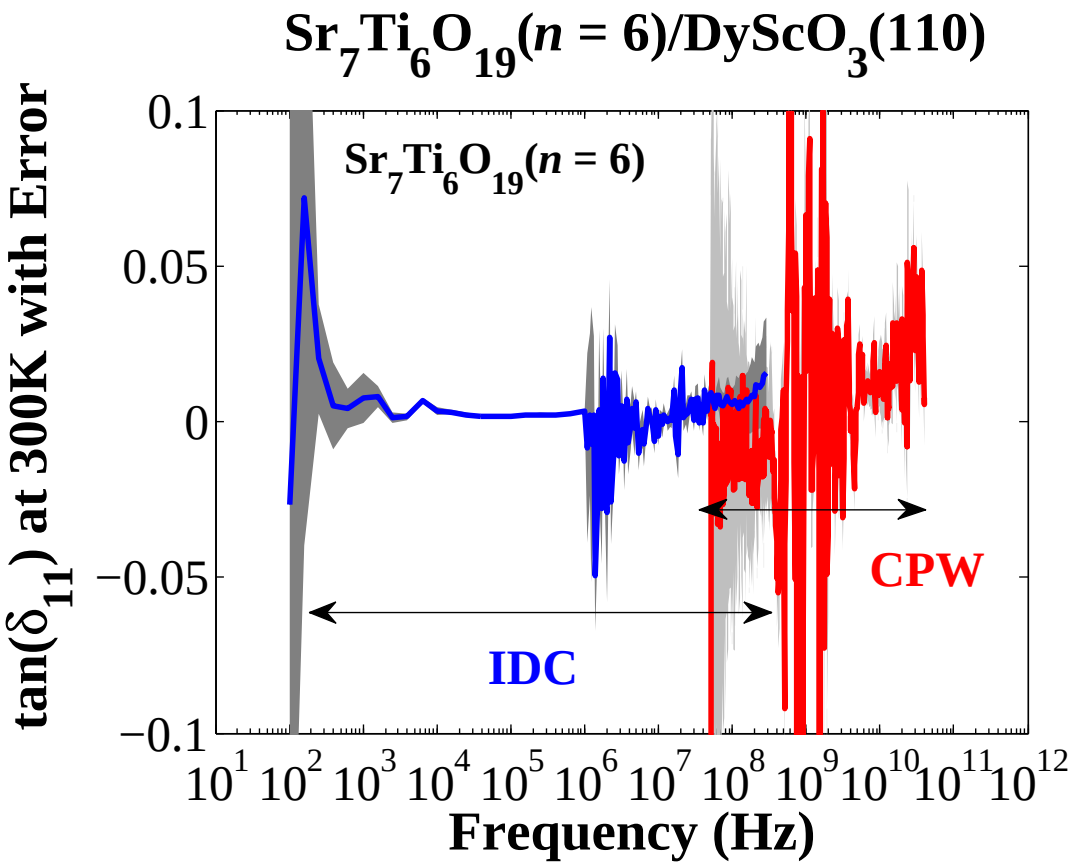

Figure 2.22: Loss Tangent of $Sr_7Ti_6O_{19}/DyScO_3(110)$ with Uncertainty

The loss tangent of the 50 nm thick $Sr_7Ti_6O_{19}$ thin film on 1 mm thick $DyScO_3(110)$ is shown from 100 Hz to 40 GHz. From 100 Hz to 300 MHz, the real part of the in-plane relative permittivity (blue) is obtained from interdigitated capacitors (IDC) with the associated uncertainty in dark grey. From 45 MHz to 40 GHz, the real part of the in-plane relative permittivity (red) is obtained from coplanar waveguides (CPW) with the associated uncertainty in light grey.

2.8 Summary

In summary, we have described a complete measurement approach to make quantitative frequency-dependent measurements of the real part of the in-plane relative permittivity of dielectric thin films from 100 Hz to 40 GHz. We discussed the measurement systems used to acquire measurements of an ensemble of planar devices. We described the modeling techniques and data extraction procedure for the planar interdigitated capacitors and coplanar waveguide devices measured in their specified fre-

quency regimes. We detailed the on-wafer calibration techniques employed in the different frequency regimes and the approach used to extract the distributed capacitance and conductance of the planar devices. We then demonstrated the broadband characterization technique on a $Sr_7Ti_6O_{19}/DyScO_3(110)$ test wafer and a $DyScO_3(110)$ companion substrate test wafer. We found that the real part of the in-plane relative permittivity for $Sr_7Ti_6O_{19}/DyScO_3(110)$ is $K_{11} \approx 560 \pm 20$ at 10 GHz and $K_{11} \approx 590 \pm 20$ at 1 MHz, which indicates that the thin film shows little to no dispersion as a function of frequency. The loss tangent of the $Sr_7Ti_6O_{19}/DyScO_3(110)$ thin film was found to be $\tan(\delta_{11}) \approx 0.01 \pm .01$ at 10 GHz and $\tan(\delta_{11}) \approx 0.003 \pm .001$ at 1 MHz. The 10 GHz loss tangent results is indicative that the loss tangent of the film is at or below the resolution of the measurement for this frequency range and instrument settings.

Chapter 3

Broadband Dielectric Spectroscopy of Ruddlesden-Popper $Sr_{n+1}Ti_nO_{3n+1}(n = 1, 2, 3)$ Thin Films

3.1 Abstract

We explore the frequency-dependent relative permittivity of Ruddlesden-Popper series $Sr_{n+1}Ti_nO_{3n+1}(n = 1, 2, 3)$ thin films as a function of temperature and dc electric field. Interdigitated capacitors and coplanar waveguides were used to extract the frequency response from 500 Hz to 40 GHz. At room temperature, the in-plane relative permittivities (ϵ_{11}) obtained for $Sr_{n+1}Ti_nO_{3n+1}(n = 1, 2, 3)$ were 42 ± 3, 54 ± 3, and 77 ± 2, respectively, and were independent of frequency. At low temperatures, ϵ_{11} increases and electric field tunability develops in $Sr_4Ti_3O_{10}(n = 3)$.

3.2 Introduction

The Ruddlesden-Popper (RP) homologous series $Sr_{n+1}Ti_nO_{3n+1}$ is a unique set of materials whose dielectric properties have yet to be fully explored and have the potential for far reaching applications, much like $SrTiO_3$, the $n = \infty$ member of this series [40]. Series members $n = 1, 2, 3$ were predicted to have fairly high relative permittivities [41]. Although historically RP materials have been the focus of a variety of theoretical [42–44] and experimental [45–48] research, until the recent successful growth of single-phase RP thin films [49–57], detailed dielectric measurements of single-phase materials have been challenging [58]. The synthesis of stable, single-phase RP thin films opens new possibilities for applications in multilayer hetero-structures and suggests

experiments to explore the role of their unique crystal structures in ferroelectricity [43].

The $Sr_{n+1}Ti_nO_{3n+1}$ RP series is of particular interest, because $SrTiO_3$ is already commonly used in a number of applications: a substrate for perovskite films, integrated nonlinear compensation devices [59] and to enhance ferroelectricity [60]. When strained, $SrTiO_3$ can exhibit ferroelectricity even at room temperature and at modest bias fields [1]. This increase in tunability unfortunately comes with a remarkable increase in both the relative permittivity and loss, rendering strained $SrTiO_3$ less useful for high-frequency applications. The $Sr_{n+1}Ti_nO_{3n+1}$ RP series may provide a new class of tunable materials which have decreased loss, yet still retain many of the characteristics that make $SrTiO_3$ so useful.

Typical radio frequency dielectric measurements focus on a single frequency [1] or a small range of frequencies, even though frequency dependence carries important information about disorder and relaxation mechanisms. Resonant techniques, such as evanescent microwave microscopy, yield very accurate measurements of local material properties, but are limited in their ability to extract broadband frequency information [22, 61]. Consequently, lumped-element capacitors are often used, an example of which are interdigitated capacitors (IDCs). Distributed effects, which are often overlooked, can compromise results from such devices at high frequencies, where the guided wavelength is comparable to the length of the device.

Here, we report quantitative measurements of in-plane relative permittivity ϵ_{11} for $Sr_{n+1}Ti_nO_{3n+1}$ thin films (n = 1, 2, 3) by means of an ultra-wideband approach [23]. To obtain the high-frequency behavior of the RP thin-films and their companion substrate (001) $(LaAlO_3)_{0.3} - (SrAl_{0.5}Ta_{0.5}O_3)_{0.7}$ (LSAT), we exploited coplanar waveguides (CPWs) rather than IDCs (which were only used for frequencies below 300 MHz). By deliberately using distributed devices at high frequencies, we have avoided errors arising from distributed effects in IDCs. Our single-phase

(001) $Sr_{n+1}Ti_nO_{3n+1}$ thin-films were grown by molecular-beam epitaxy (MBE) on 0.5 mm thick (001) LSAT substrates with dimensions 10 mm × 10 mm and identical growth conditions to those of Ref. [1]. The 2θ x-ray diffraction results can be found in App. A.7. Four-Circle x-ray diffraction measurements revealed that the c-axis lattice constants of the 160 nm - 170 nm thick $n = 1$, 2, and 3 films were 12.57 ± 0.02 Å, 20.42 ± 0.02 Å, and 28.05 ± 0.02 Å, respectively. The films were commensurate within the experimental error (± 0.0008 Å). The combined CPW and IDC measurements span 500 Hz to 40 GHz, almost eight decades in frequency.

3.3 In-plane Relative Permittivity Measurements

We fabricated CPWs and IDCs onto the RP thin films and a bare (001) LSAT, substrate using standard lithographic techniques. The electrodes were made from Au approximately 330 nm thick with a 20 nm titanium adhesion layer. The CPWs have prescribed lengths, $\ell = \{0.420$ mm, 2.155 mm, 3.220 mm, 5.933 mm$\}$, which improve the measurement accuracy above 300 MHz [30]. Our IDCs also have different active lengths $\ell = \{0$, 0.100 mm, 1.835 mm, 2.900 mm$\}$, so the measured capacitance and conductance could be fit as a function of length.

The CPW measurements were corrected using on-wafer planar standards patterned on a $LaAlO_3(\epsilon_{11} \approx \epsilon_{33} = 24.6 \pm 0.6)$ [62, 63] substrate with identical cross sectional geometries to the test devices. For frequencies below 1 MHz, we measured the complex impedance of the IDCs using an impedance analyzer. Between 1 MHz and 300 MHz, we measured the complex scattering parameters (S-parameters) of the IDCs and from 300 MHz to 1 GHz using a radio frequency vector network analyzer (VNA). At high frequencies, we measured S-parameters of CPWs with a microwave VNA. We extracted the distributed circuit parameters of the bare substrate and thin films for both IDCs and CPWs. After taking the difference between the distributed capacitance of the thin film and substrate, we used 2D finite element simulations of

the cross-sectional geometries of our devices to relate the capacitance difference to the respective in-plane relative permittivity of the thin film.

Figure 3.1 shows ϵ_{11}[1] for $Sr_{n+1}Ti_nO_{3n+1}$ (n = 1, 2, 3) thin films and explicitly demonstrates that it is independent of frequency up to 40 GHz. Additionally, we measured the in-plane relative permittivity of LSAT ($\epsilon_{11} = 23.1 \pm 0.3$) over the same measurement frequency range and found it to be consistent with previous reports [64]. We also found that the present RP materials had relatively low loss tangents, significantly less than 0.04 (the sensitivity of our measurements at the time).

3.4 Temperature Dependence and Comparison with Theory

To further explore the dielectric properties of these materials as a function of temperature, we employed a cryogenic probe station to perform on-wafer measurements at variable temperature. In Fig. 3.2(a), we plot the temperature dependence of ϵ_{11} at 1 MHz for these series members, which we find were consistent with previous reports on the average permittivity in bulk ceramics [58]. The ϵ_{11} for n = 1, 2, 3 increases with decreasing temperature, and this temperature dependence increases with n. The temperature dependence seen in Fig. 3.2(a) for n = 2 and 3 is similar to that of $SrTiO_3$ [65], and is likely due to the temperature dependence of the soft mode [66]. In comparison, n = 1 shows relatively weak temperature dependence, a feature that makes Sr_2TiO_4 attractive as an alternative high-speed, low-loss gate dielectric. Figure 3.2(b) shows that even at 70 K the high-frequency dependence of $Sr_4Ti_3O_{10}(n = 3)$ remains flat up to 40 GHz and shows no evidence of any relaxation processes, which could be connected with defects or high lattice anharmonics.

Table 3.1 shows the ϵ_{11} averaged over the measurement frequency range for temperatures 295 K, 70 K, and 25 K. Measured results were shown with the values

[1]We use the symbol ϵ_{11} in this chapter, as opposed to K_{11}, to represent the real part of the in-plane relative permittivity.

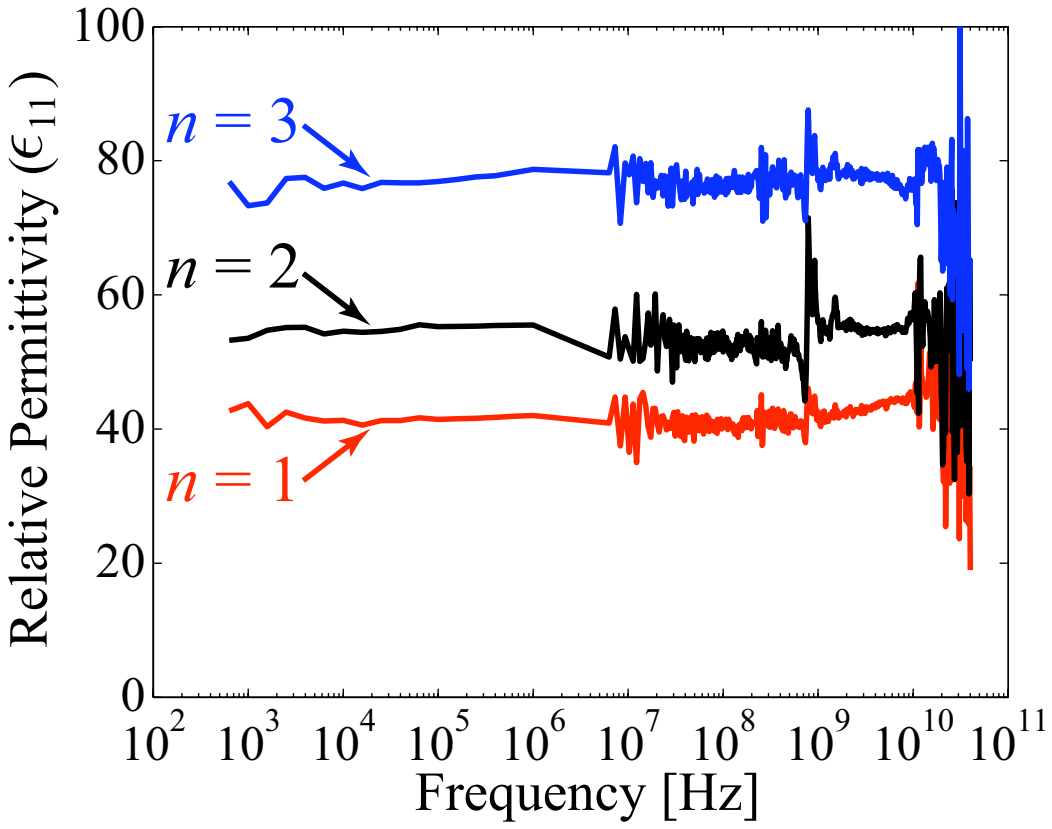

Figure 3.1: Frequency Dependence of In-plane Relative Permittivity (ϵ_{11}) of $Sr_{n+1}Ti_nO_{3n+1}$ ($n = 1, 2, 3$) on (001) $(LaAlO_3)_{0.3} - (SrAl_{0.5}Ta_{0.5}O_3)_{0.7}$

The frequency dependence (500 Hz to 40 GHz) of the in-plane relative permittivity (ϵ_{11}) of $Sr_{n+1}Ti_nO_{3n+1}$ ($n = 1, 2, 3$) thin films on (001) $(LaAlO_3)_{0.3} - (SrAl_{0.5}Ta_{0.5}O_3)_{0.7}$ at room temperature (296 K).

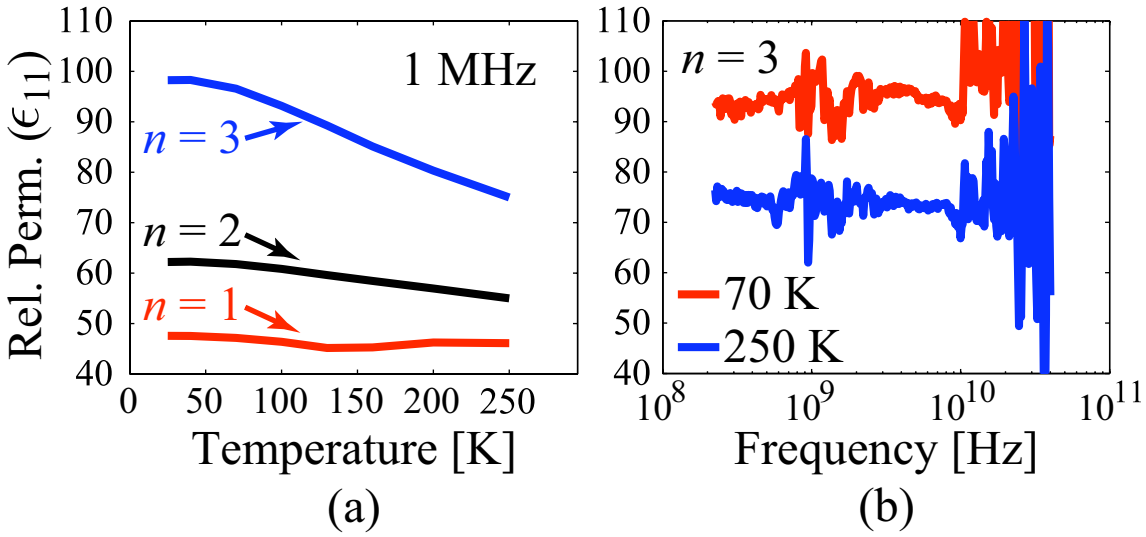

Figure 3.2: Temperature Dependence of the In-plane Relative Permittivity (ϵ_{11}) for $Sr_{n+1}Ti_nO_{3n+1}$ ($n = 1, 2, 3$) on (001) $(LaAlO_3)_{0.3} - (SrAl_{0.5}Ta_{0.5}O_3)_{0.7}$

(a) Temperature dependence of the in-plane relative permittivity (ϵ_{11}) for $Sr_{n+1}Ti_nO_{3n+1}$ ($n = 1, 2, 3$) on (001) $(LaAlO_3)_{0.3} - (SrAl_{0.5}Ta_{0.5}O_3)_{0.7}$. The temperature dependence was extracted from two interdigitated capacitors of lengths $\ell = \{0.1 \text{ mm}, 2.9 \text{ mm}\}$. (b) shows the high frequency dependence of $Sr_4Ti_3O_{10}(n = 3)$ thin-film measured with coplanar waveguides at 70 K and 250 K.

	$n = \mathbf{1}$	$n = \mathbf{2}$	$n = \mathbf{3}$
295 K	42.1 ± 2.5	53.8 ± 2.9	77.2 ± 2.1
70 K	49.0 ± 4.5	61.2 ± 6.8	95.5 ± 4.5
30 K	47.5 ± 0.1	62.1 ± 0.1	98.1 ± 0.2
Theory (T = 0 K)	62	100	150

Table 3.1: ϵ_{11} for $Sr_{n+1}Ti_nO_{3n+1}$ (n = 1, 2, 3) at 295 K, 70 K, and 30 K

calculated using the first principles technique discussed below. The measured values for 295 K were averaged over the frequency range of 500 Hz - 20 GHz. For 70 K, the mean value is taken from 300 MHz to 20 GHz, and the 30 K result is averaged from 1 kHz to 1 MHz. Experiments on bulk ceramics at room temperature measured $\epsilon_{average} = 37.4, 57.9, 76.1$ for n = 1, 2, 3 [45, 47].

First-principles density functional calculations using projector augmented wave potentials were performed within the local density approximation as implemented in VASP [67–70]. The wavefunctions were expanded in plane waves up to a kinetic energy cutoff of 500 eV. Integrals over the Brillouiun zone were approximated by sums on a $6 \times 6 \times 6$ Γ-centered k-point mesh. Phonon frequencies were calculated using the direct method where each symmetry adapted mode was moved by approximately 0.01 . Born effective charge tensors were calculated by finite differences of the polarization using the modern theory of polarization [71] as implemented in VASP. All structures were fully relaxed.

Interestingly, the three RP systems were found to have highly anisotropic permittivity tensors; for (n = 1, 2, 3) , ϵ_{11}= {62, 100, 150} and ϵ_{33}= {18, 25, 34}, a zero temperature result that was previously overlooked. Although the magnitude of ϵ_{11} is highly sensitive to constant biaxial strain for reasons previously discussed[43], the relative change as a function of n is consistent with the presented measurements.

3.5 Low Temperature Tunability in $Sr_4Ti_3O_{10}(n = 3)$

The distinct temperature dependence for $Sr_4Ti_3O_{10}(n = 3)$ in Fig. 2(b), although not by itself a proof of soft mode temperature dependence, is often an indication of tunability. We therefore, performed two independent tests using both IDCs and CPWs to measure the dc electric field dependence for this test wafer. Electric field bias was applied between the center conductor and outer conductor of a 5.933 mm CPW, using a bias tee. Corresponding voltage-biased measurements on two IDCs, ℓ= {0.1 mm, 2.9 mm}, were accomplished using low frequency bias tees, where the bias voltage was applied between the interdigitated fingers of the IDCs.

Figure 3.3 shows the measured relative change in phase $\Delta\phi$ as a function of frequency for a CPW ($\ell = 5.933$ mm) on the $Sr_4Ti_3O_{10}(n = 3)$ thin film. The measured $\Delta\phi$ for this CPW at 30 K and 100 kV/cm corresponds to a change in film in-plane relative permittivity of about 6%, which is consistent with the low-frequency biased measurements. Both IDC and CPW measurements confirm that the $Sr_4Ti_3O_{10}(n = 3)$ thin film can be tuned with modest dc electric fields at low temperatures. For $n =$ 1 and 2, the tunability was less than 3%, which is approximately the uncertainty in the measurement.

3.6 Summary

In summary, we have characterized the ϵ_{11} of the first three members of $Sr_{n+1}Ti_nO_{3n+1}$ RP Series using single-phase epitaxial thin films grown by MBE. The measured ϵ_{11} was consistent with the value obtained from theory. We have systematically explored the dependence of ϵ_{11} on n, temperature, and dc electric field from 500 Hz to 40 GHz by combining data from IDC and CPW devices. The consistency between theory and experiment suggests that these dependencies were intrinsic to the $Sr_{n+1}Ti_nO_{3n+1}$ phases rather than inclusions of $SrTiO_3$.

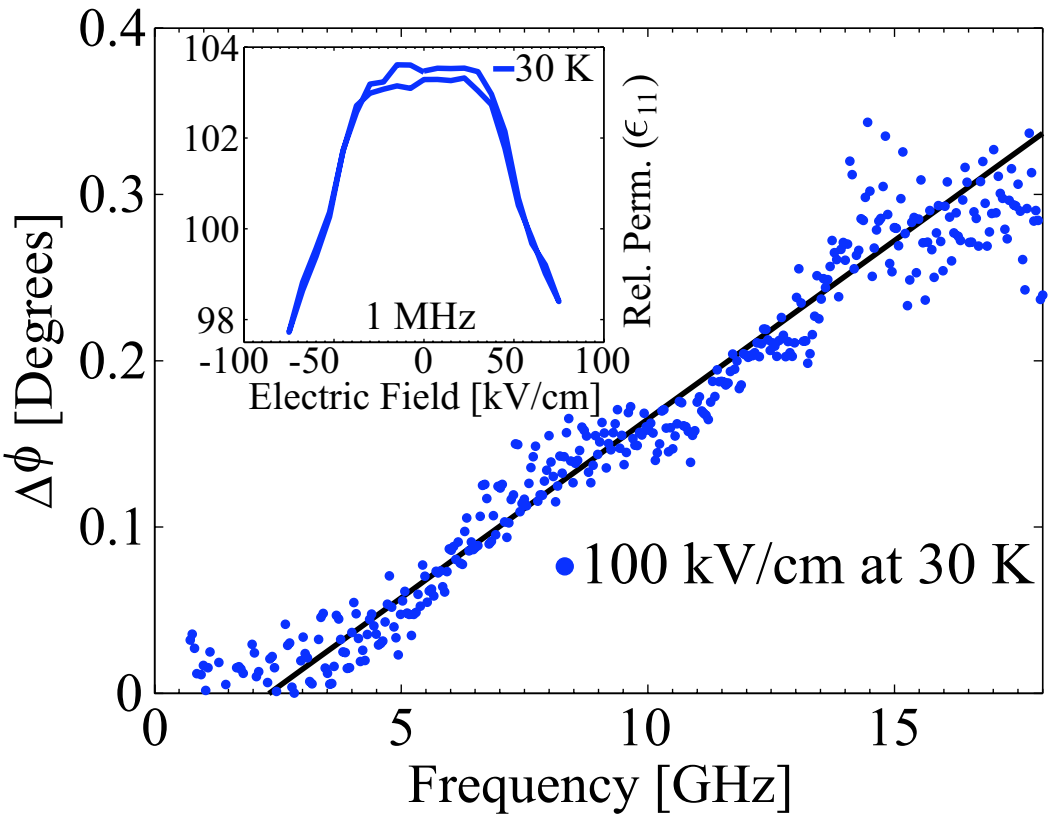

Figure 3.3: Tunability of $Sr_4Ti_3O_{10}(n = 3)$/LSAT(100) under 100 kV/cm at 30 K

The phase change $\Delta\phi$ of a 5.933 mm coplanar transmission line biased at 100 kV/cm relative to the unbiased line, on the $Sr_4Ti_3O_{10}(n = 3)$ thin film. The solid line shows the predicted $\Delta\phi$, a 6% change in relative permittivity, based on the low frequency response in the inset. The inset depicts the tunability of ϵ_{11} for $Sr_4Ti_3O_{10}(n = 3)$ at 1 MHz and 30 K, which was extracted from two interdigitated capacitors of lengths $\ell = \{0.1 \text{ mm}, 2.9 \text{ mm}\}$.

Chapter 4

Strained Ruddlesden-Popper $Sr_{n+1}Ti_nO_{3n+1}$ Thin Films

4.1 Abstract

Understanding the mechanisms for loss is one of central goals to designing new dielectric materials for a wide array of frequency dependent applications. In 2004, J. H. Haeni, *et al.* showed that $SrTiO_3(n = \infty)$ on $DyScO_3(110)$ undergoes a ferroelectric to paraelectric phase transition around room temperature [1]. Unfortunately, these materials also showed significant loss at microwave frequencies ($\tan\delta > .1$). In this study, we discuss the growth and characterization of Ruddlesden-Popper series $Sr_{n+1}Ti_nO_{3n+1}(n = 2, 3, 4, 5, 6)$ epitaxial thin-films grown on the rare-earth scandate substrates, $DyScO_3(110)$ and $GdScO_3(110)$, which correspond to biaxial tensile strain of approximately 1% and 1.7%, respectively. The thin films were 50 nm on $DyScO_3(110)$ and 25 nm thick on $GdScO_3(110)$, which ensured uniform strain throughout the film. We characterized the thin films with seven optimally designed coplanar waveguides from 45 MHz to 40 GHz and with a set of planar interdigitated capacitors of varying active lengths from 100 Hz to 300 MHz. We then extracted the in-plane complex permittivity from 100 Hz to 40 GHz for these thin films. Here, we report the dependence of the critical temperature, tunability, and loss tangent on series number and strain. We also examined the frequency dependent dielectric properties of these thin films as a function of temperature, electric field, series number and strain.

4.2 Introduction

Many tunable ferroelectrics exhibit frequency dependence at gigahertz frequencies [2, 5, 23–25]. This frequency dependence corresponds to an increase in the loss tangent of the materials [72, 73]. For a variety of systems, frequency dependence has been associated with conductivity, polarization domains [6], dipole relaxation [3], disorder [25, 74], and at very high frequencies to phonon modes in the film [66]. This increase in dielectric loss renders many thin-film systems less useful for practical applications in the microwave regime. Despite the high losses in some thin film systems, a variety of experimental techniques have been used to integrate thin films into lumped-element microwave circuits on low-loss substrates to utilize the tunability of the film [13], while minimizing the dielectric loss.

Typically, such devices are narrowband and still operate at frequencies on the edge of where dielectric relaxation becomes significant [13]. Because many of these systems are lossy at high frequencies, device applications have been forced to operate at frequencies significantly less than the onset of the dielectric relaxation. A lower operation frequency implies that the device size is inherently larger than what can be achieved by working at high frequency. By increasing the operation frequency of communication systems data could also be transferred at higher rates, which could have important implications for broadband wireless technology. If one could engineer a tunable dielectric with low loss well into the gigahertz regime, then this material would enable a host of new technology, while simultaneously decreasing the size of the devices and possibly the cost of production. Moreover, if one could understand the mechanisms behind the decreased loss, then we could potentially design new materials with improved characteristics for specific frequency dependent applications.

$Ba_{1-x}Sr_xTiO_3$, an example of a tunable ferroelectric, has been the subject of an extensive amount of experimental and theoretical research exploring the effects various dopants, strain, growth techniques, and layering. In Fig. 4.1, we show the frequency

dependence of 400 nm thick $Ba_{0.3}Sr_{0.7}TiO_3$ thin films on $LaAlO_3$ explored in Ref. [2]. Refs. [2, 75] are some of only a few experiments exploring the high frequency characteristics of $Ba_{1-x}Sr_xTiO_3$, and the conclusions arrived at in these references are very pertinent for many of the practical applications of tunable low-loss ferroelectrics. Among these findings, Ref. [2] showed that even though $Ba_{0.3}Sr_{0.7}TiO_3$ has low loss at frequencies less than 100 MHz; the dispersion rapidly increases in the gigahertz frequency regime. Refs. [2, 75] model this loss with a modified Cole-Cole function and suggest that the dispersion can likely be attributed to coupling into the soft-mode phonon frequency.

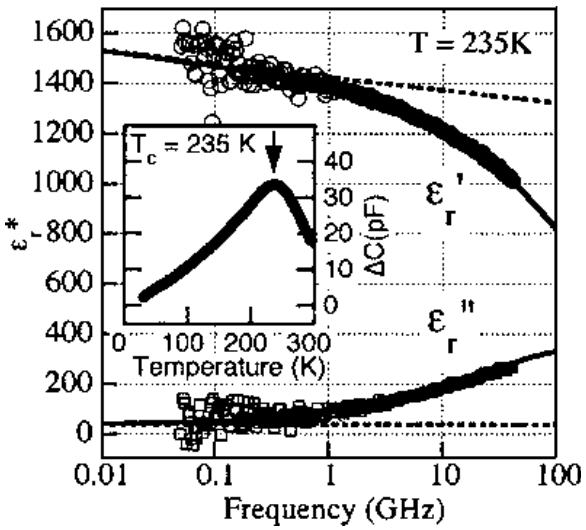

Figure 4.1: Broadband Frequency Dependence of the
Complex Relative Permittivity of $Ba_{0.3}Sr_{0.7}TiO_3$ from Ref. [2]

From Ref. [2], the broadband complex permittivity of $Ba_{0.3}Sr_{0.7}TiO_3$ from 10 MHz to 45 GHz at 235 K. The real part of the relative in-plane permittivity (ϵ_r') are the circles with a Cole-Cole fit as the solid line. The imaginary part of the relative in-plane permittivity (ϵ_r'') are the squares with the corresponding imaginary part obtained from a Cole-Cole fit shown as the solid line. The inset shows the temperature dependence of the change in capacitance (ΔC) as a function of temperature for an interdigitated capacitor.

Aside from doping $SrTiO_3$ with Ba (essentially replacing a percentage of the Sr atoms with Ba atoms), when $SrTiO_3$ is strained on $DyScO_3(110)$ the critical temperature of the paraelectric-ferroelectric phase transition can be increased to room

temperature (Fig. 4.2(a)). This profound increase is impressive, because unstrained $SrTiO_3$ is an incipient ferroelectric [76]. Incipient ferroelectrics show a characteristic peak in the relative permittivity with decreasing temperature, but the relative permittivity saturates at low temperatures indicating that the material never transitions into the ferroelectric state. In Fig. 4.2(b), J. H. Haeni, *et al.* showed that the loss tangent ($\tan\delta$) of $SrTiO_3/DyScO_3(110)$ develops a sharp peak near room temperature and they observed that the film exhibits a significant enhancement in electric field dependence at the transition temperature, almost 80%. Interestingly, $SrTiO_3$ is a member of a family of materials called Ruddlesden-Poppers.

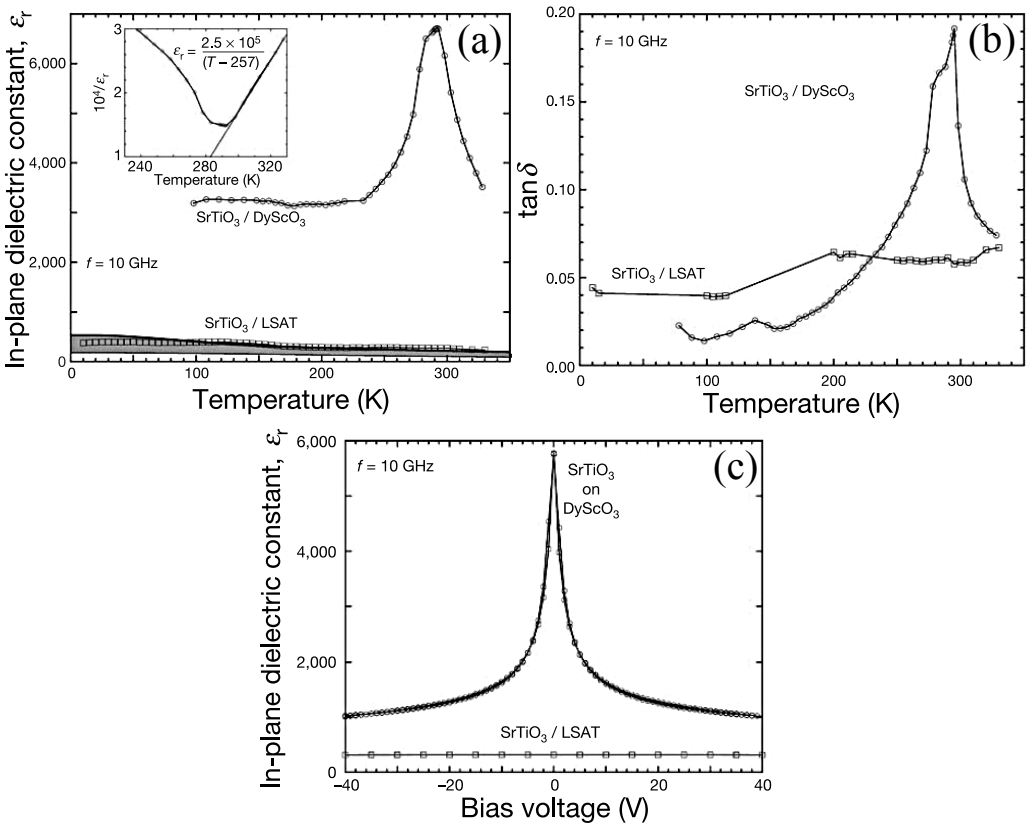

Figure 4.2: Strained $SrTiO_3/DyScO_3(110)(n = \infty)$ Shows Room Temperature Ferroelectricity from Ref. [1]

From Ref. [1], a 50 nm thick film of strained $SrTiO_3/DyScO_3(110)(n = \infty)$ showed room temperature ferroelectricity while an unstrained $SrTiO_3(n = \infty)$ film on $(LaAlO_3)_{0.3} - (SrAl_{0.5}Ta_{0.5}O_3)_{0.7}$ (LSAT(001)) showed no evidence of ferroelectricity. (a) The temperature dependence of the real part of the in-plane relative permittivity of a 50 nm thick film of $SrTiO_3/DyScO_3(110)(n = \infty)$ from 100 K to 330 K at 10 GHz. (b) The loss tangent ($\tan(\delta)$) at 10 GHz as a function of temperature for the $SrTiO_3/DyScO_3(110)(n = \infty)$ film at 10 GHz. (c) The electric field tunability of the $SrTiO_3/DyScO_3(110)(n = \infty)$ film at 10 GHz and at room temperature. In (a), (b), and (c) the results for the $SrTiO_3/LSAT(001)(n = \infty)$ film are also shown for comparison.

4.3 Crystal Structure & Synthesis

A Ruddlesden-Popper (RP) series member is simply a perovskite-like material where the chemical formula can be written as $A_{n+1}B_nO_{3n+1}$ [40]. For $SrTiO_3$, the RP series is $Sr_{n+1}Ti_nO_{3n+1}$, where A is Sr and B is Ti. For a cubic perovskite, like $SrTiO_3$, the

term A-site and B-site originated to refer to the position of the atom in the crystal lattice. In this case, a Ti atom sits inside an O octahedra centered about Sr atoms that can be thought of as positioned on the points of a cube. The $Sr_{n+1}Ti_nO_{3n+1}$ RP series offers an interesting way to explore the role of crystal structure, the emergence of ferroelectricity as a function series number, and as a means to understanding the mechanisms of the losses seen in strained $SrTiO_3/DyScO_3(110)(n = \infty)$.

In Fig. 4.3, we show a 3D schematic of the crystal structure for $Sr_{n+1}Ti_nO_{3n+1}$ (n = 1, 2, 3) or $Sr_2TiO_4(n = 1)$, $Sr_3Ti_2O_7(n = 2)$, and $Sr_4Ti_3O_{10}(n = 3)$. These materials are grown by shutter-growth molecular beam expitaxy (MBE). A single layer of $Sr_2TiO_4(n = 1)$ is synthesized by depositing in succession SrO, TiO_2, and SrO. This pattern is repeated to specified film thickness. A detailed schematic of the crystal growth is shown in App. A.8 in Fig. A.7. A far more intuitive picture of $Sr_{n+1}Ti_nO_{3n+1}$ (n = 1, 2, 3) can be constructed by taking a 2D cross section of the thin films (Fig. 4.4). In Fig. 4.4, we show a 2D cross section of n = 1, 2, and 3 ($Sr_2TiO_4(n = 1)$, $Sr_3Ti_2O_7(n = 2)$, and $Sr_4Ti_3O_{10}(n = 3)$). One can clearly see in Fig. 4.4 that an RP thin film can be thought of as n perovskite layers followed by another n perovskite layers that are offset by half the in-plane lattice constant. In practice, this is achieved by depositing an extra SrO rocksalt layer every n perovskite layers.

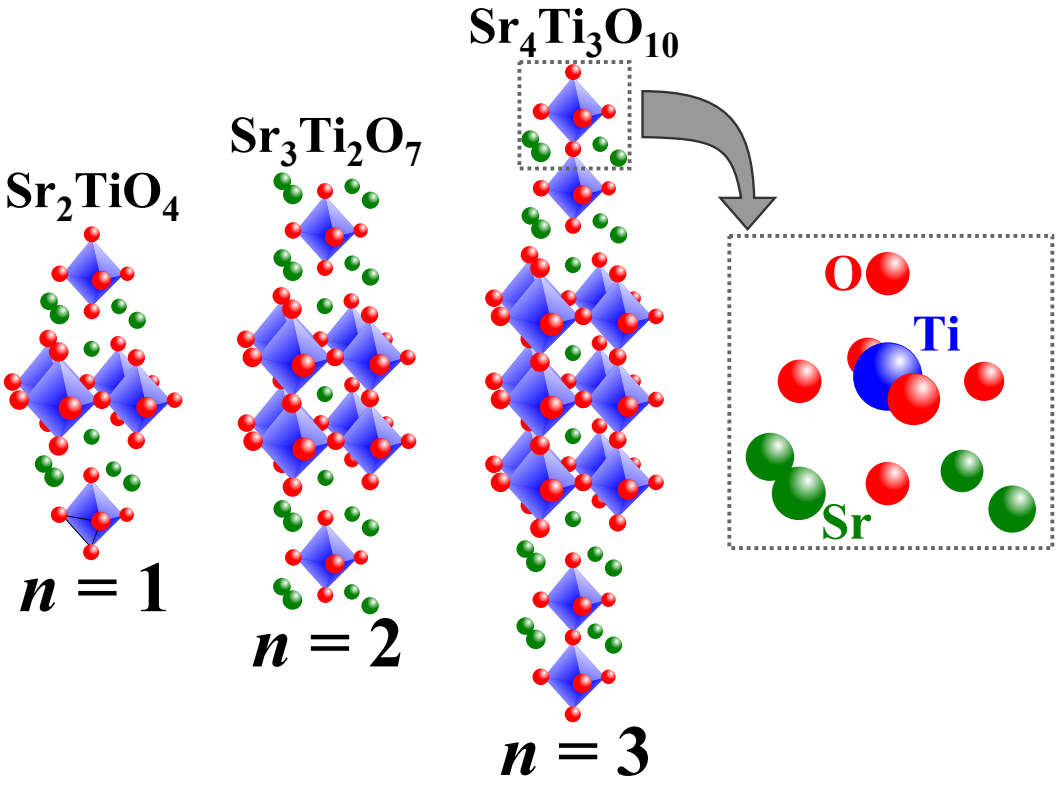

Figure 4.3: Crystal Structure of $Sr_{n+1}Ti_nO_{3n+1}(n = 1, 2, 3)$ Ruddlesden-Popper Series

A 3D schematic of a single lattice of $Sr_{n+1}Ti_nO_{3n+1}(n = 1, 2, 3)$, which are Sr_2TiO_4, $Sr_3Ti_2O_7$, and $Sr_4Ti_3O_{10}$, respectively. The strontium (Sr) atoms are shown as the green spheres, the oxygen (O) atoms are shown as the red spheres, and the titanium (Ti) atoms are shown as the blue spheres. The Ti atom sits in the center of six oxygen atoms arranged at the points of the blue octahedra.

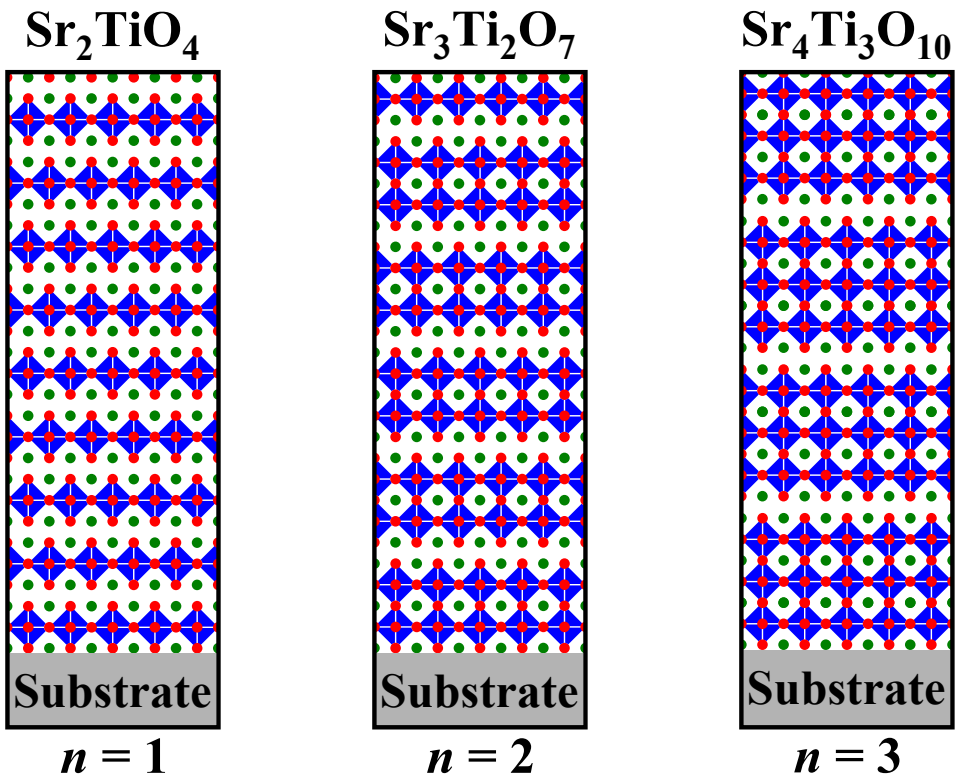

Figure 4.4: 2D Cross section of $Sr_{n+1}Ti_nO_{3n+1}(n = 1, 2, 3)$ Ruddlesden-Popper on a Substrate

A 2D cross section of $Sr_{n+1}Ti_nO_{3n+1}$ or $Sr_2TiO_4(n = 1)$, $Sr_3Ti_2O_7(n = 2)$, and $Sr_4Ti_3O_{10}(n = 3)$ on a substrate (grey). The strontium (Sr) atoms are shown as the green spheres, the oxygen (O) atoms are shown as the red spheres, and the titanium (Ti) atoms are shown as the blue spheres. The Ti atom sits in the center of six oxygen atoms arranged at the points of the blue octahedra, which are shown as blue diamonds in this plane.

In Fig. 4.5, we show X-Ray 2θ diffraction measurements of strained $Sr_{n+1}Ti_nO_{3n+1}(n =$ 2, 3, 4, 5, 6) on $DyScO_3(110)$. The films were 50 nm thick, and were grown by MBE on $DyScO_3(110)$ substrates that were approximately 1 mm thick [1, 4, 15, 49, 51, 53, 54, 77, 78]. We have used color to indicate series number, where $n = 2$, 3, 4, 5, and 6 are represented by cyan, dark green, dark yellow, red, and blue. A schematic of a thin film on a substrate can be found in App. A.8 and is shown in Fig. A.6. The sharp peaks in Fig. 4.5 at approximately 24°, 45°, and 73° are due to the $DyScO_3(110)$

substrate. If we examine $Sr_3Ti_2O_7(n = 2)$ (cyan) in Fig. 4.5, we see that there are 2 peaks between each set of the peaks from the $DyScO_3(110)$ substrate. Further examination of the data presented in Fig. 4.5 reveals that the number of peaks in between the substrate peaks is equal to the series number. By itself X-Ray 2θ diffraction measurements are not sufficient to state definitively that the materials are single phases of RP thin films; however, a variety of crystallographic measurements were performed on each sample to verify that the films were homogeneously strained in the out-of-plane direction and greater than 95% phase pure. We also grew two addition sets of RP series numbers $n = 2$, 3, 4, 5, and 6 to ensure that our measurements were consistent across samples sets. Throughout, this section we refer to these samples sets as $DyScO_3$#1, $DyScO_3$#2, and $DyScO_3$#3. Figure 4.5 are the X-Ray 2θ diffraction measurements for the $DyScO_3$#3 sample set, because it represents the most thoroughly studied sample set in this report. We also grew the same set of samples on $GdScO_3(110)$, which strains the samples by approximately 1.7%. In general, we state the the strain is approximately 1.0% on $DyScO_3(110)$ and 1.7% on $GdScO_3(110)$. This is in fact not true. In reality, the strain is actually decreasing with increasing series number. The in-plane lattice constant for $n = 1$ is 3.88 Å, $n = 2$ is 3.89 Å, $n = 3$ is 3.90 Å, and as n increases, it limits to the in-plane lattice constant of $SrTiO_3$ (3.91 Å). The in-plane lattice constant for $DyScO_3(110)$ is 3.94 and $GdScO_3(110)$ is 3.97. The deviation is approximately 0.5% for $n = 1$ and rapidly limits to the values stated earlier as n increases.

We should also note that the films were meticulously grown by Mr. C.-H. Lee and not by the author of this thesis. A thorough and thoughtful discussion of the growth procedure and parameters can be found in Mr. Lee's dissertation, but are beyond the scope of this thesis. The growth of these materials is a formidable task as each atomic layer must be deposited one at a time, and in succession to the required film thickness [1, 4, 15, 49, 51, 53, 54, 77, 78].

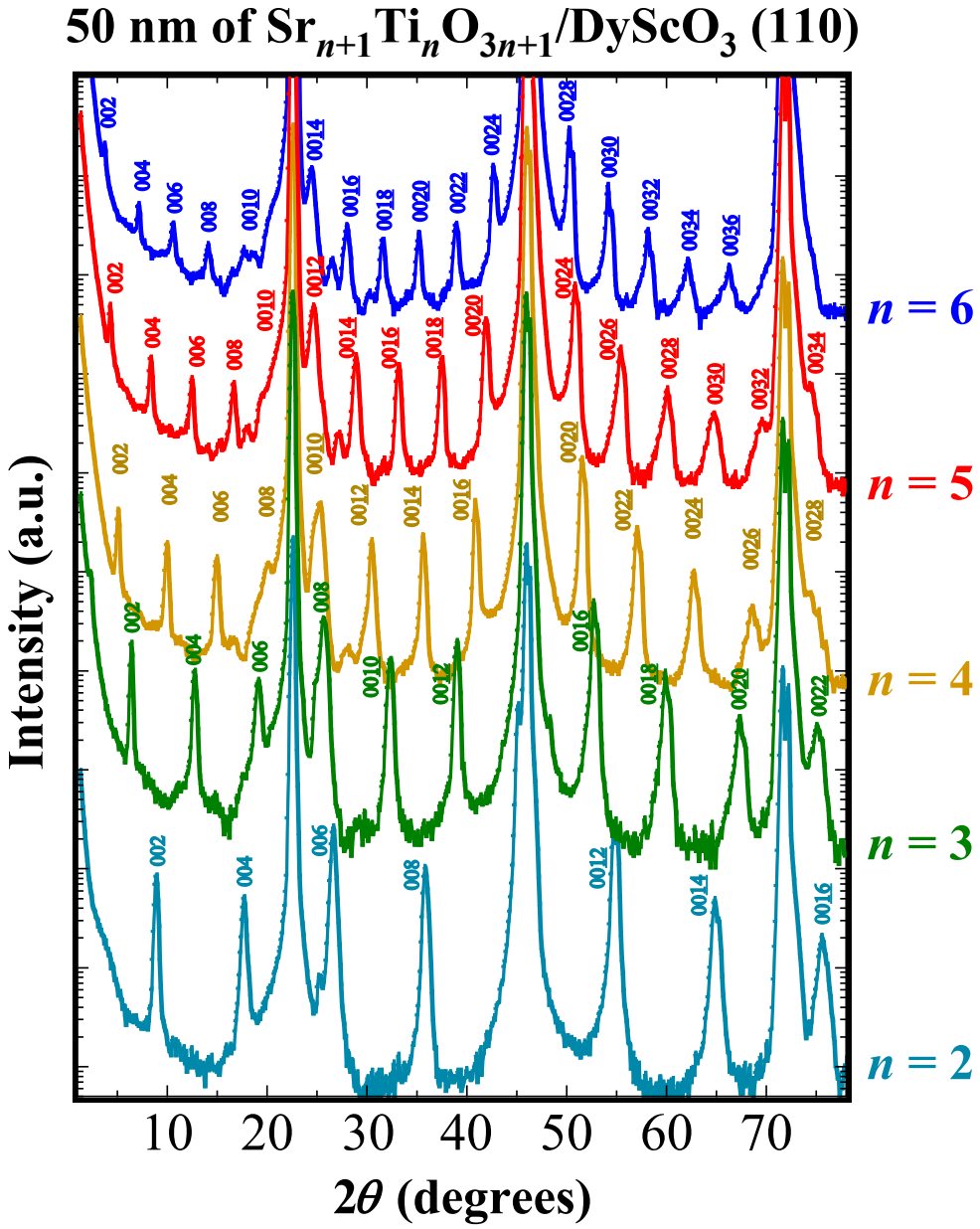

Figure 4.5: X-ray 2θ Diffraction of Strained $Sr_{n+1}Ti_nO_{3n+1}(n = 2, 3, 4, 5, 6)$ on $DyScO_3(110)$

The X-ray 2θ diffraction of strained $Sr_{n+1}Ti_nO_{3n+1}(n = 2, 3, 4, 5, 6)$ on $DyScO_3(110)$. The films are 50 nm thick, and are grown by molecular beam epitaxy on $DyScO_3(110)$ substrates that approximately 1 mm thick. We have used color to indicate series number, where $n = 2$, 3, 4, 5, and 6 are represented by cyan, dark green, dark yellow, red, and blue. Courtesy of C.-H. Lee.

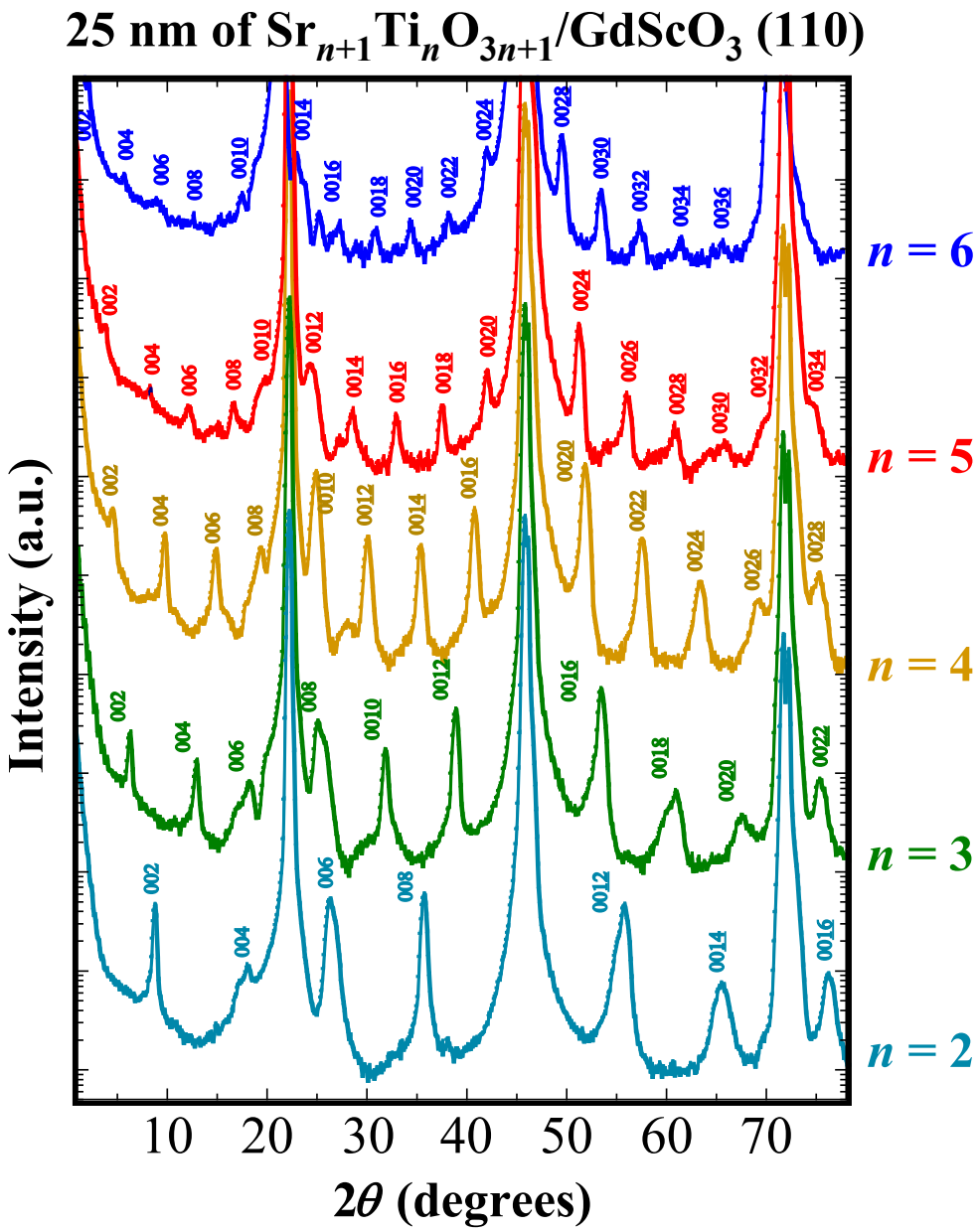

Figure 4.6: X-ray 2θ Diffraction of Strained $Sr_{n+1}Ti_nO_{3n+1}(n = 2, 3, 4, 5, 6)$ on $GdScO_3(110)$

The X-ray 2θ diffraction of strained $Sr_{n+1}Ti_nO_{3n+1}(n = 2, 3, 4, 5, 6)$ on $GdScO_3(110)$. The films are 25 nm thick, and are grown by molecular beam epitaxy on $GdScO_3(110)$ substrates that approximately 1 mm thick. We have used color to indicate series number, where $n = 2$, 3, 4, 5, and 6 are represented by cyan, dark green, dark yellow, red, and blue. Courtesy of C.-H. Lee.

4.4 Low Frequency Temperature Dependence

Perhaps one of the most common approach to both identify and understand a ferroelectric phase transitions in a material system is to explore the dependence of the relative permittivity on temperature. We explored the temperature dependence of real part of the in-plane relative permittivity for the 50 nm thick thin films of $Sr_{n+1}Ti_nO_{3n+1}$(n = 2, 3, 4, 5, 6) on $DyScO_3$(110) and a similar set of thin films on $GdScO_3$(110) by measuring at fixed variable temperature and sweeping frequency. This is relevant, because the most common approach to determine the dependence of the relative permittivity on temperature is to fix frequency and sweep temperature. Although considerably less time consuming, we cannot sweep temperature, because the g-s-g probes (and the manipulator arms) are thermally grounded to the cold finger and they contract with decreasing temperature. Moreover, a considerable amount of care must be taken to ensure that the system is in thermodynamic equilibrium when sweeping temperature and holding the frequency fixed. In contrast, the frequency at a low enough power can be varied without changing the thermodynamic state of the system. Furthermore, for S-parameter measurements in the HF regime the calibrations become invalid when the temperature is changed [34].

The $Sr_{n+1}Ti_nO_{3n+1}$(n = 2, 3, 4, 5, 6) films along with their companion substrates and a $LaAlO_3$ calibration wafer were affixed with silver paste to a custom-fabricated copper chuck with two integrated thermometers and two heaters (Fig. 4.7). We placed the samples in the cryogenic probe station, mechanically bolted the copper chuck to a cold finger, and connected the the thermometers and heaters by a vacuum feed-through to a temperature controller. Microwave g-s-g probes were attached to stainless steel semi-rigid coaxial cables and temperature controlled probe mounts inside the cryogenic probe station (Sec. 2.3). The cyrogenic probe station was pumped down for approximately 24 hours, or until the pressure was 200 μTorr. Once the cryogenic probe station was brought to vacuum, we cooled the samples with an open-flow

of liquid helium without applying dc electric field (*i.e.* zero-field cooled). Once the measurement system was zero-field cooled to the lowest measurement temperature and stabilized, we corrected the LF LCR meter with a series open and a series short on the $LaAlO_3$ calibration test wafer following the approach discussed in Sec. 2.5. We then confirmed the calibration by measuring an IDC on the $LaAlO_3$ calibration wafer to verify the frequency dependent capacitance and loss tangent correction of the calibration. On each test wafer (including the companion substrate test wafer) and at each temperature, we measured two interdigitated capacitors of different active lengths with the LF LCR meter from 100 Hz to 1 MHz. This corresponded to fifteen measurements per measurement temperature. After every 20 K, the LCR meter was recalibrated in the LF regime, as this typically corresponded to 8 hours of virtually uninterrupted measurement. The typical temperature interval was 5 K.

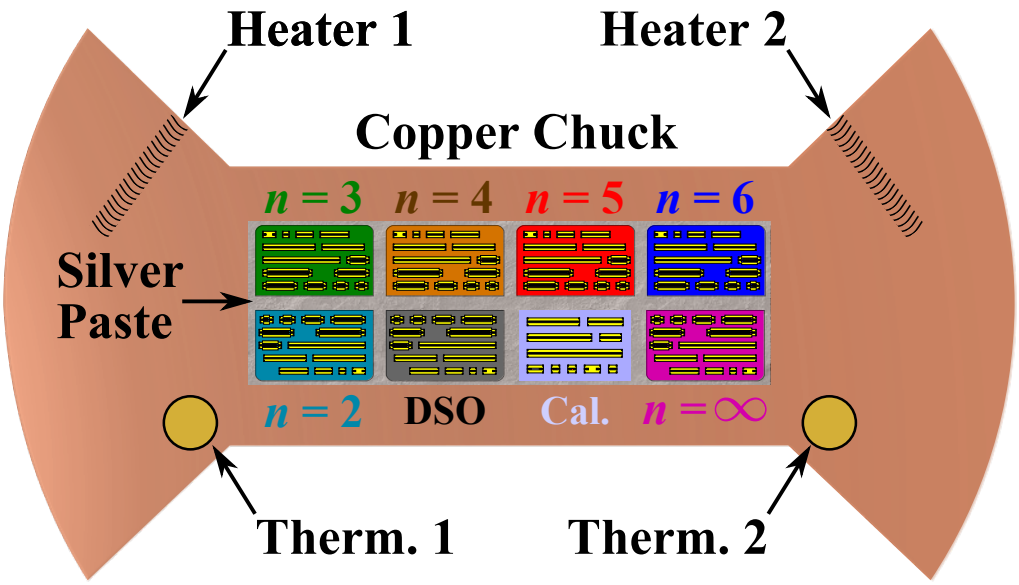

Figure 4.7: A Schematic of the Measurement Layout for $Sr_{n+1}Ti_nO_{3n+1}/DyScO_3(110)(n = 2, 3, 4, 5, 6)$

A schematic of the measurement setup for 50 nm $Sr_{n+1}Ti_nO_{3n+1}/DyScO_3(110)(n = 2, 3, 4, 5, 6)$ thin-film test wafers, $DyScO_3(110)$(DSO) companion substrate test wafer, and the $LaAlO_3$ calibration wafer (Cal.). The heaters, labeled 'Heater 1' and 'Heater 2', are used to uniformly heat the OFHC copper chuck. The test wafers and calibration wafer are affixed to the copper chuck with silver paste. We controlled the temperature with a external feedback loop that measured the temperature with one of the two thermometers ('Therm. 1' and 'Therm. 2') and adjusted the output to the heaters to keep the temperature fixed.

We show the temperature dependence of real part of the in-plane relative permittivity (K_{11}) as a function temperature in Fig. 4.8 for three different sample sets of $Sr_{n+1}Ti_nO_{3n+1}$ thin films on $DyScO_3(110)$. In Fig. 4.8, the solid lines are the series numbers $n = 2$, 3, 4, and 5 for the $DyScO_3$#1 set, the dash-dotted lines are the series numbers $n = 4$, and 5 for the $DyScO_3$#2 set, and dashed lines are the series numbers

$n = 2$, 3, 4, 5, and 6 for the $DyScO_3$#3 set. We have assigned each series number (n) a specific color: $n = 2$ is cyan, $n = 3$ is dark green, $n = 4$ is dark yellow, $n = 5$ is red, and $n = 6$ is blue. The temperature increments varied between samples sets. For the $DyScO_3$#3 sample set, we performed measurements every 5 K from 15 K to 300 K. One important feature of Fig. 4.8 is that the temperature dependence is consistent between sample sets. For $n = 2$(solid cyan line) and $n = 3$(solid dark green line) in the $DyScO_3$#1 set, there is a noticeable kink at 150 K that is most likely due to a poor or degraded calibration. For the $DyScO_3$#3 set, series number $n = 5$ (dashed red line) appears to be inconsistent with the other $n = 5$ samples, however, high frequency measurements show a more consistent temperature dependence. Even though the strain was actually decreasing with increasing series number, it is clear from Fig. 4.8 that as series number increased the temperature where the maximum in K_{11} occurred increased. The temperature at which K_{11} was a maximum may be an indication of a ferroelectric-paraelectric phase transition. For relaxor ferroelectrics, we define this maximum as the Critical Temperature (T_c), and although we use this terminology throughout this section, this temperature should more appropriately called T_{max}. The diffuseness of the peak in K_{11} is also interesting, because it is commonly found in relaxor ferroelectrics [6]. As we alluded to earlier, we do not yet fully understand these materials, but another classic hallmark of relaxor ferroelectrics is temperature dependent dispersion where the T_c increases with increasing frequency.

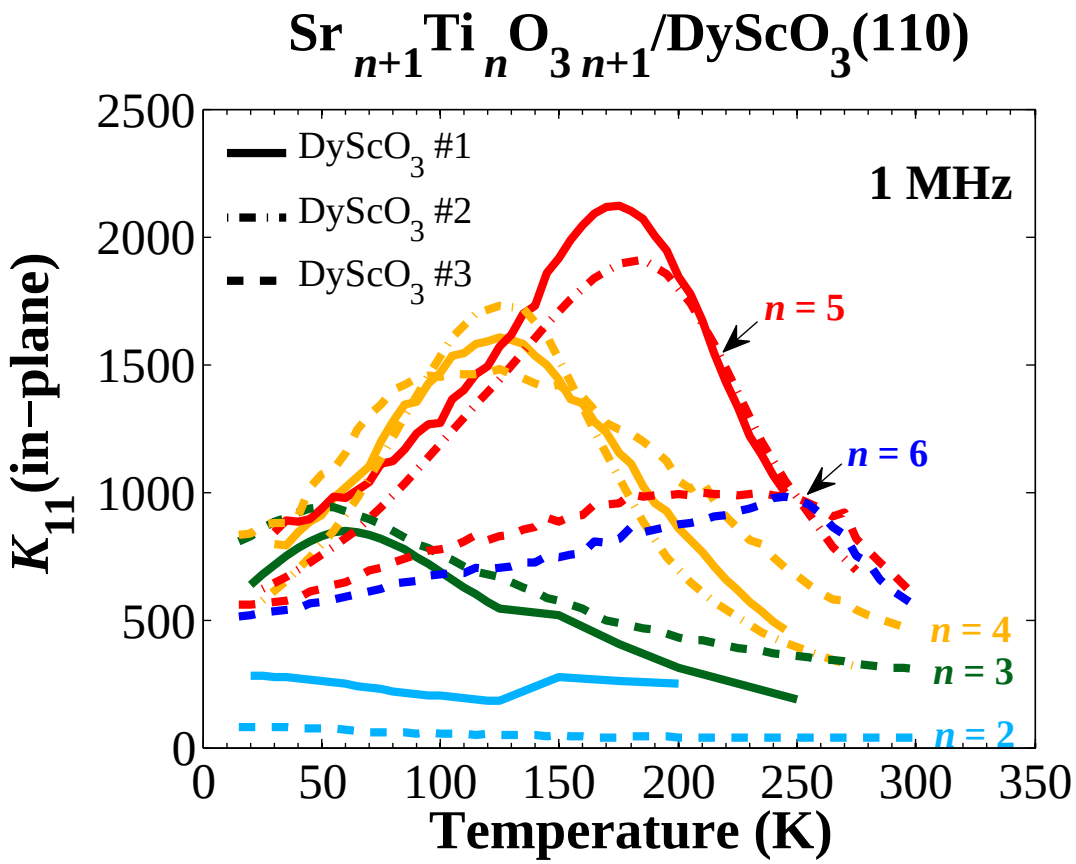

Figure 4.8: Comparison of K_{11}(in-plane) for $DyScO_3$ #1, #2, and #3 of $Sr_{n+1}Ti_nO_{3n+1}$(n = 2, 3, 4, 5, 6) on $DyScO_3$(110)

We show the temperature dependence of the real part of the in-plane relative permittivity, K_{11}(in-plane), for three groups of 50 nm thick thin films of $Sr_{n+1}Ti_nO_{3n+1}$ samples on $DyScO_3$(110) at 1 MHz. Here, we have assigned each series number (n) a specific color: n = 2 is cyan, n = 3 is dark green, n = 4 is dark yellow, n = 5 is red, and n = 6 is blue. The $DyScO_3$ #1 sample set is shown as the solid lines for the series numbers, n = 2, 3, 4, and 5. The $DyScO_3$ #2 sample set is shown as the dash-dot lines for the series numbers, n =4, and 5. The interdigitated capacitors used for the sample sets $DyScO_3$ #1 and $DyScO_3$ #2 had active lengths ℓ = (1.835 mm, 2.900 mm). The $DyScO_3$ #3 sample set is shown as the dashed lines for the series numbers, n = 2, 3, 4, 5, and 6. The interdigitated capacitors used for these films had active lengths ℓ = (0.875 mm, 1.835 mm).

In a relaxor ferroelectric, a physical interpretation of the dispersion around the ferroelectric instability, T_c, is that spontaneous dipoles form in the crystal lattice, and they interact on some characteristic length scale to form dipolar regions. The length scale over which interactions occur are influenced by a number of factors;

however, the result is that polar nanoregions of a distribution of sizes forms in the film. These polar nanoregions behave like small dipoles, where the characteristic time necessary for the polar nanoregions needed to anti-align to the time dependent electric field is dependent on the size of the of the polar nanoregion. In Fig. 4.9, we show the frequency dependence of K_{11} as a function of temperature for the sample sets labeled $DyScO_3$#1 (a) and $DyScO_3$#3 (b), where increasing line thickness indicates increasing frequency. The series numbers (n) measured for the $DyScO_3$#1 sample set are $n = 2$ (cyan), $n = 3$ (dark green), $n = 4$ (dark yellow), and $n = 5$ (red). The interdigitated capacitors used for the $DyScO_3$#1 sample set had active lengths $\ell =$ (1.835 mm, 2.900 mm) (See Fig. 4.9(a)). Likewise, in Fig. 4.9(b), the series numbers (n) measured for the $DyScO_3$#3 sample set are $n = 2$ (cyan), $n = 3$ (dark green), $n = 4$ (dark yellow), $n = 5$ (red), and $n = 6$ (blue). The interdigitated capacitors used for the $DyScO_3$#3 set had active lengths $\ell =$ (0.875 mm, 1.835 mm). One can see in Fig. 4.9 that frequency dependence developed below the maximum in K_{11} at T_c, and significantly decreased at temperatures above T_c.

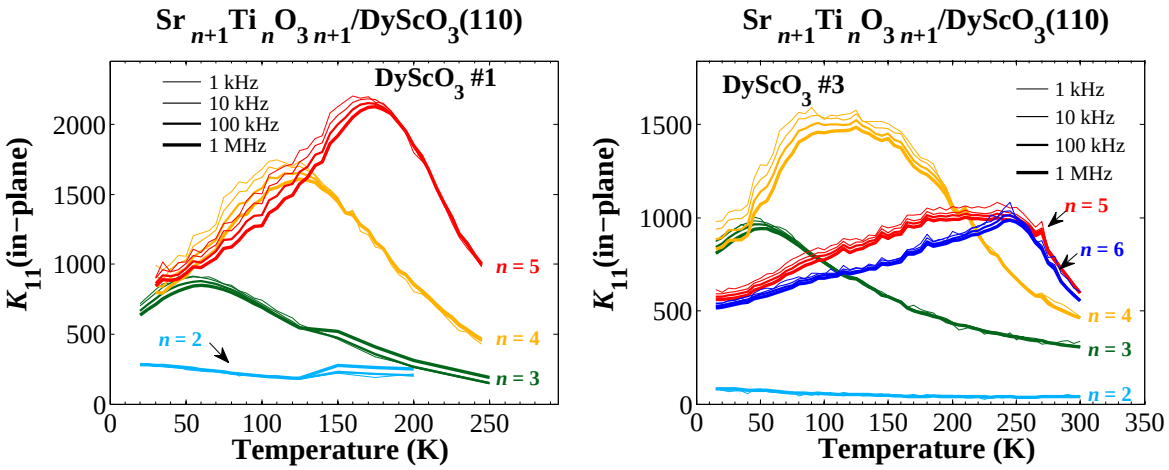

(a) $DyScO_3$ #1 (b) $DyScO_3$ #3

Figure 4.9: Low Frequency Temperature Dependent Dispersion of K_{11}(in-plane) for $Sr_{n+1}Ti_nO_{3n+1}/DyScO_3(110)$ (n = 2, 3, 4, 5) for $DyScO_3$ #1 and $DyScO_3$ #3

(a) We show the temperature dependence of the real part of the in-plane relative permittivity, K_{11}(in-plane), for the $DyScO_3$ #1 sample set of 50 nm thick thin films $Sr_{n+1}Ti_nO_{3n+1}/DyScO_3(110)$ (n = 2, 3, 4, 5) at 1 kHz, 10 kHz, 100 kHz, and 1 MHz, where line thickness indicates frequency. The series numbers (n) measured for this sample set are n = 2 (cyan), n = 3 (dark green), n = 4 (dark yellow), and n = 5 (red). The interdigitated capacitors used for this sample set had active lengths ℓ = (1.835 mm, 2.900 mm). (b) We show the temperature dependence of the real part of the in-plane relative permittivity, K_{11}(in-plane), for the $DyScO_3$ #3 sample set of 50 nm thick thin films $Sr_{n+1}Ti_nO_{3n+1}/DyScO_3(110)$ (n = 2, 3, 4, 5, 6) at 1 kHz, 10 kHz, 100 kHz, and 1 MHz, where line thickness indicates frequency. The interdigitated capacitors used for this sample set had active lengths ℓ = (0.875 mm, 1.835 mm).

Strain is another important variable that we used to control the behavior of K_{11} for these materials. The soft-mode phonon frequency has been shown to decrease with increased biaxial tensile strain for $SrTiO_3/DyScO_3(110)$ [77]. By decreasing the soft-mode phonon frequency, we increase the transition temperature at which the polar nanoregion form. In Fig. 4.10, we show K_{11} as a function of temperature for $Sr_{n+1}Ti_nO_{3n+1}/DyScO_3(110)$($n$ = 2, 3, 4, 5) (solid lines) and $Sr_{n+1}Ti_nO_{3n+1}/GdScO_3(110)$($n$ = 2, 3, 4, 5) (dashed lines) labeled $DyScO_3$#1 and $GdScO_3$#1. The $Sr_{n+1}Ti_nO_{3n+1}/GdScO_3(110)$ (n = 2, 3, 4, 5) thin films are 25 nm thick under approximately 1.7% biaxial tensile

strain and the $Sr_{n+1}Ti_nO_{3n+1}/DyScO_3(110)$ (n = 2, 3, 4, 5) thin films are 50 nm thick under approximately 1% biaxial tensile strain. It is striking that while the T_c of any given series number has been dramatically increased, the T_c still increased monotonically with increasing series number. As with the samples on $DyScO_3(110)$, we again examined K_{11} for the sample set on $GdScO_3(110)$ as function of temperature for fixed frequencies to explore how T_c evolved with increasing frequency and the effect of strain.

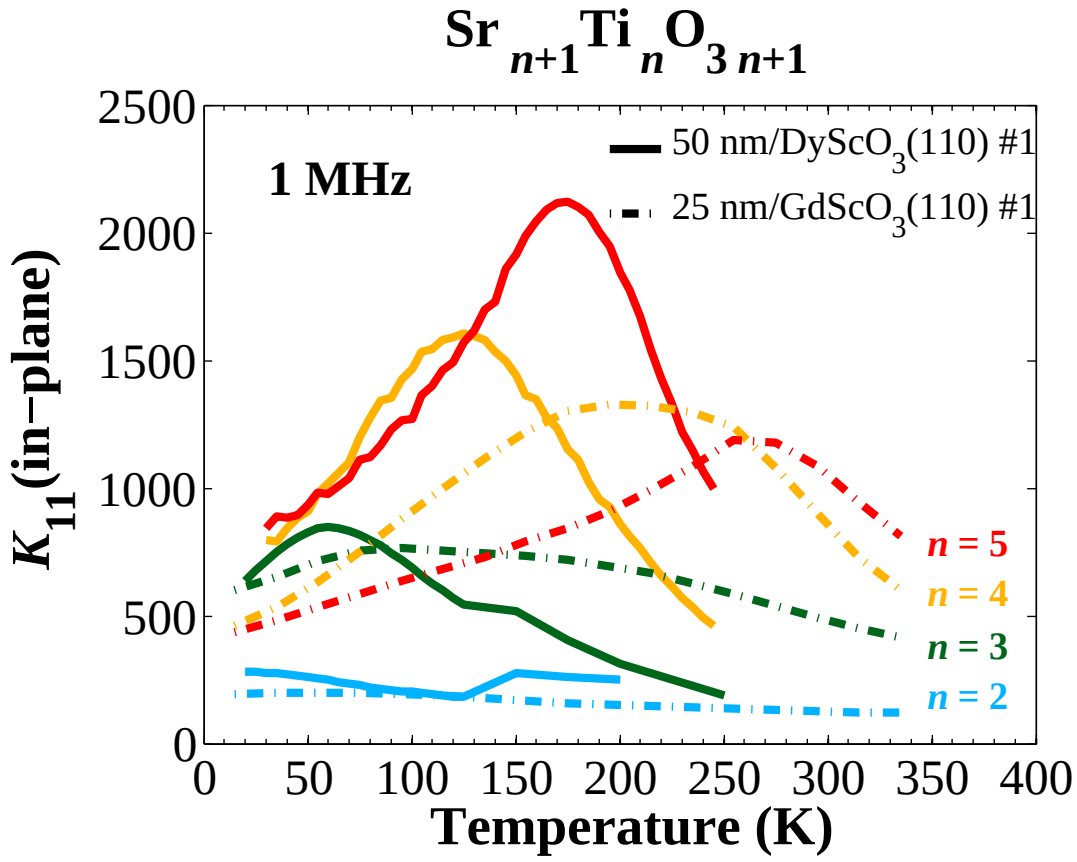

Figure 4.10: Comparison of K_{11}(in-plane) for $DyScO_3$ #1 of $Sr_{n+1}Ti_nO_{3n+1}(n = 2, 3, 4, 5)/DyScO_3(110)$ to $GdScO_3$ #1 of $Sr_{n+1}Ti_nO_{3n+1}(n = 2, 3, 4, 5)/GdScO_3(110)$

We show the effect of biaxial tensile strain on the temperature dependence of the real part of the in-plane relative permittivity, K_{11}(in-plane), at 1 MHz. For 50 nm thick thin films of $Sr_{n+1}Ti_nO_{3n+1}(n = 2, 3, 4, 5)$ samples on $DyScO_3(110)$ ($DyScO_3$ #1) the biaxial tensile strain is approximately 1%. For the 25 nm thick thin films of $Sr_{n+1}Ti_nO_{3n+1}(n = 2, 3, 4, 5)$ samples on $GdScO_3(110)$ ($GdScO_3$ #1) the biaxial tensile strain is approximately 1.7%. We have used color to indicate series number, where $n = 2$, 3, 4, and 5 are represented by cyan, dark green, dark yellow, and red. The $DyScO_3$ #1 sample set is shown as the solid lines for the series numbers, $n = 2$, 3, 4, and 5. The interdigitated capacitors used for the sample set $DyScO_3$ #1 had active lengths $\ell = (1.835$ mm, 2.900 mm). The $GdScO_3$ #1 sample set is shown as the dash-dot lines for the series numbers, $n = 2$, 3, 4, and 5. The interdigitated capacitors used for these films had active lengths $\ell = (0.875$ mm, 1.835 mm).

In Fig. 4.11, we show the temperature dependence of K_{11} for 25 nm thick films of $Sr_{n+1}Ti_nO_{3n+1}/GdScO_3(110)(n = 2, 3, 4, 5, 6)$ at 1 kHz, 10 k Hz, 100 kHz, and

1 MHz, where the line thickness indicates the frequency. Note that $n = 6$ (blue) was not shown in Fig. 4.10, because we were not able to reach the maximum in K_{11} given the upper temperature limit of the probe station (T $\approx$ 350 K). There are several features of interest in Fig. 4.10. First, in comparison to Fig. 4.8, K_{11} appears to be in general broader as function of temperature for the series members explored on $GdScO_3(110)$. Second, the maximum value of K_{11} for the samples on $GdScO_3(110)$ appeared to be unchanged or less than the values obtained for the same series members on $DyScO_3(110)$. From the LST relation we know that the low frequency limit for the permittivity can be written as a constant times the soft-mode phonon frequency, hence this last observation is unexpected. One would expect that as the soft-mode phonon decreased in frequency the static permittivity limit of K_{11} should have increased. Along this premise, one would have naively expected that as series number increased, K_{11} at T_c would have also increased, and that it would have limited to the behavior of $SrTiO_3/DyScO_3(110)(n = \infty)$ (See Fig. 4.2[1]).

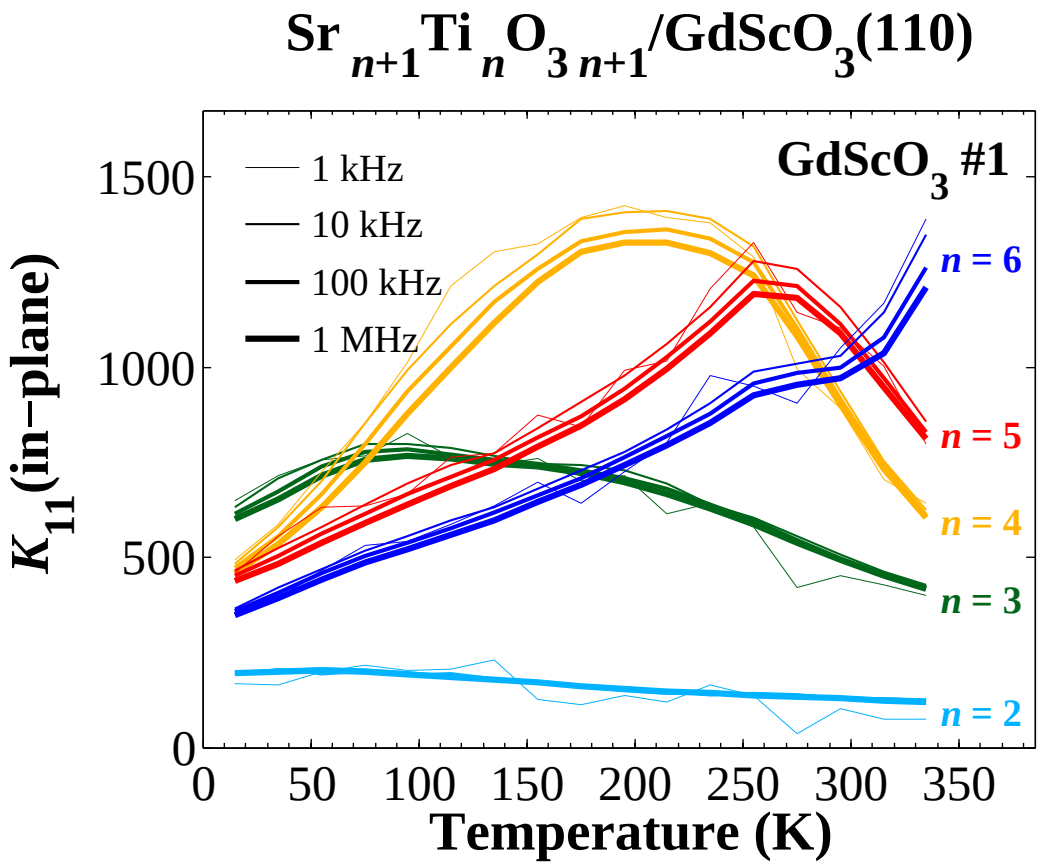

Figure 4.11: Low Frequency Temperature Dependent Dispersion of K_{11}(in-plane) for $Sr_{n+1}Ti_nO_{3n+1}/GdScO_3(110)$ (n = 2, 3, 4, 5, 6) for $GdScO_3$ #1

We show the temperature dependence of the real part of the in-plane relative permittivity, K_{11}(in-plane), for the $GdScO_3$ #1 sample set of 25 nm thick thin films $Sr_{n+1}Ti_nO_{3n+1}/GdScO_3(110)$ (n = 2, 3, 4, 5, 6) at 1 kHz, 10 kHz, 100 kHz, and 1 MHz, where line thickness indicates frequency. We have used color to indicated series number, where n = 2, 3, 4, 5, and 6 are represented by cyan, dark green, dark yellow, red, and blue. The interdigitated capacitors used for this sample set had active lengths ℓ = (0.875 mm, 1.835 mm).

In Fig. 4.12, we show the dependence of T_c as a function of series number (n) at 1 MHz for $Sr_{n+1}Ti_nO_{3n+1}$ for the sample sets $DyScO_3$ #1 (squares), $DyScO_3$ #2 (triangles), $DyScO_3$ #3 (circles), and $GdScO_3$ #1 (stars). We have used color to indicated series number, where n = 2, 3, 4, 5, 6, and ∞ are represented by cyan, dark green, dark yellow, red, blue, and magenta, respectively. It is clear from

Fig. 4.12 that as n increased T_c also increased, and trended toward the T_c of $SrTiO_3/DyScO_3(110)(n = \infty)$. This behavior seems to suggest that T_c as a function of n asymptotically increased as a positive monotonic function towards the T_c of $SrTiO_3/DyScO_3(110)(n = \infty)$. We also note the strong agreement between the T_c of a given series member for different $DyScO_3(110)$ sample sets, which impressive from an experimental perspective. We also found from Fig. 4.12 that strain appeared to shift the T_c almost uniformly up in temperature by approximately 60 K, except that the T_c of $n = 6$ on $GdScO_3(110)$ was found to be greater than 335 K, which implied a shift in T_c greater than 80 K.

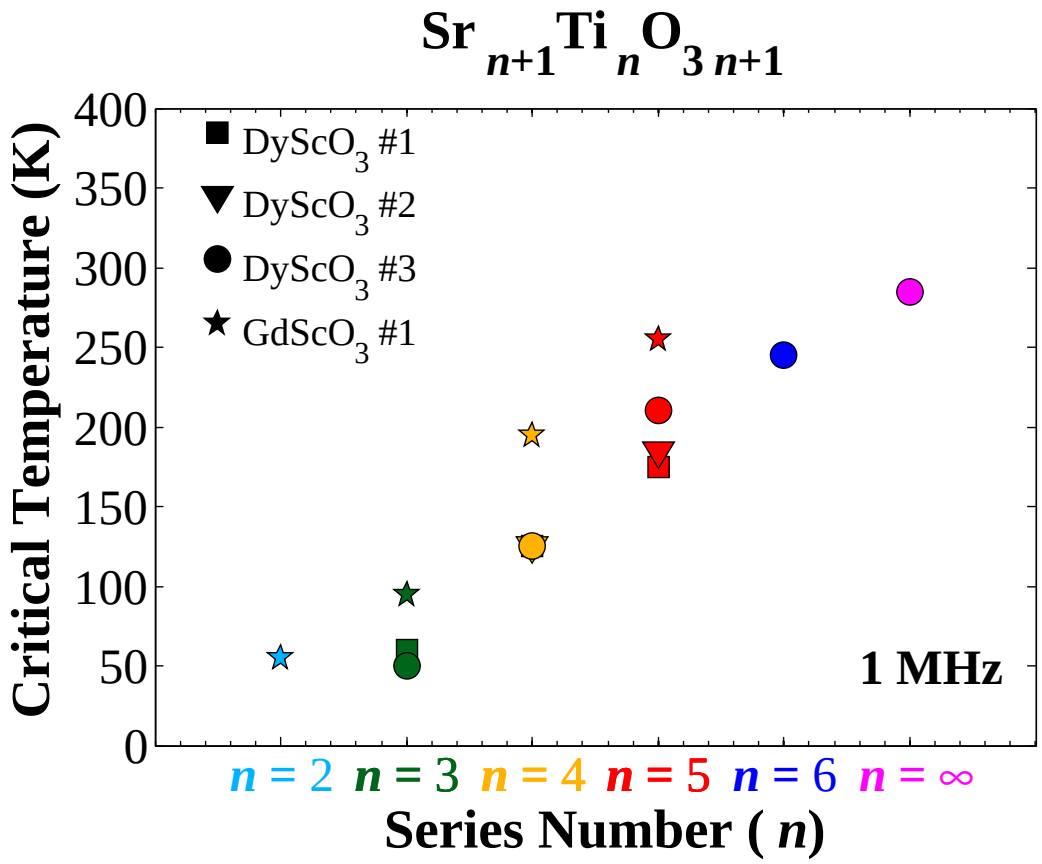

Figure 4.12: Critical Temperature as a Function of Series Number for $Sr_{n+1}Ti_nO_{3n+1}(n = 2, 3, 4, 5, 6, \infty)$ for samples on $DyScO_3(110)$ and $GdScO_3(110)$

We show the effect of strain and series number on the Critical Temperature (T_c) obtained from low frequency fixed temperature dependent measurements of interdigitated capacitors at 1 MHz. The sample sets shown are $DyScO_3$ #1 (squares), $DyScO_3$ #2 (triangles), $DyScO_3$ #3 (circles), and $GdScO_3$ #1 (stars). The measured series numbers (n) include $n = 2$ (cyan), $n = 3$ (dark green), $n = 4$ (dark yellow), $n = 5$ (red), $n = 6$ (blue), and $n = \infty$ (magenta).

4.5 Low Frequency Electric Field Dependence

Another indicator of a relaxor ferroelectric is hysteresis in the electric field dependence of K_{11} above T_c [6]. We explored the electric field dependence of K_{11} at 1 MHz by measuring two IDCs at fixed temperature and frequency as a function of applied electric field. External low frequency bias tees were attached to the rigid

coaxial cables outside the cyrogenic probe station shown in Fig. 2.1. The dc voltage for these measurements were applied between the center conductors of Port 1 and Port 2 (See Fig. 2.1). After the system was pumped down to approximately 200 μTorr, the samples were zero-field cooled to the measurement temperature. Once the temperature was stabilized, the LCR meter was corrected with the series open and series short fabricated on the $LaAlO_3$ calibration wafer, following the approach outlined in Sec. 2.5. We then confirmed the calibration by measuring an IDC on the $LaAlO_3$ calibration wafer to verify the frequency dependent capacitance and loss tangent correction of the calibration.

At each measurement temperature, we measured two IDCs with different active lengths. For the 50 nm $Sr_{n+1}Ti_nO_{3n+1}/DyScO_3(110)(n = 2, 3, 4, 5)$ films labeled $DyScO_3$ #3 in the Sec. 4.4, the IDCs had active lengths ℓ = (0.875 mm, 1.835 mm). In order to ensure that we did not destroy the samples in the process of the measurement, we first manually stepped through the applied voltage on each test wafer to verify that the samples did not show significant leakage, which can damage the films. After we had established the maximum applied voltage, we measured both IDCs on each test wafer, including the companion test wafer substrate.

For the $DyScO_3$ #3 sample set, we performed a four quadrant electric sweep (0 to V_{max}, V_{max} to $-V_{max}$, $-V_{max}$ to V_{max}, V_{max} to 0) with 7.5 kV/cm steps to a maximum applied electric field of 75 kV/cm (or 150 V over a 20 μm gap). We show the electric field dependence of K_{11} at 1 MHz of $Sr_{n+1}Ti_nO_{3n+1}/DyScO_3(110)$ ($n = 2, 3, 4, 5$) for $DyScO_3$ #3 in Figs. 4.13, 4.14, 4.15, and 4.16 for $n = 3, 4, 5,$ and 6, respectively. We have used color to indicate the series number, where $n = 3, 4, 5,$ and 6 are represented by dark green, dark yellow, red, and blue, respectively. For each sample, we performed the electric field dependent experiments at T = 60 K, 120 K, 180 K, and 240 K to explore how hysteresis and tunability developed as a function of temperature. The T_c of $n = 3, 4, 5,$ and 6 are at approximately T $\approx$ 60 K, 120 K, 180 K, and 240 K,

respectively. In Figs. 4.13, 4.14, 4.15, and 4.16, it is interesting that both tunability and hysteresis in K_{11} persist well above T_c for the 50 nm thick $Sr_{n+1}Ti_nO_{3n+1}/DyScO_3(110)$ (n = 2, 3, 4, 5) thin films. This is especially evident in n = 6 (Fig. 4.16), where a significant amount of hysteresis is apparent at 300 K despite the fact that these measurements are approximately 60 K above the T_c. It is possible that the hysteresis above T_c is due to the material being driven back into the ferroelectric state by the application of the dc electric field. We can encapsulate some of the electric field dependence by simply calculating the maximum change in K_{11} and dividing by the maximum in K_{11}, which we define as the %Tunability.

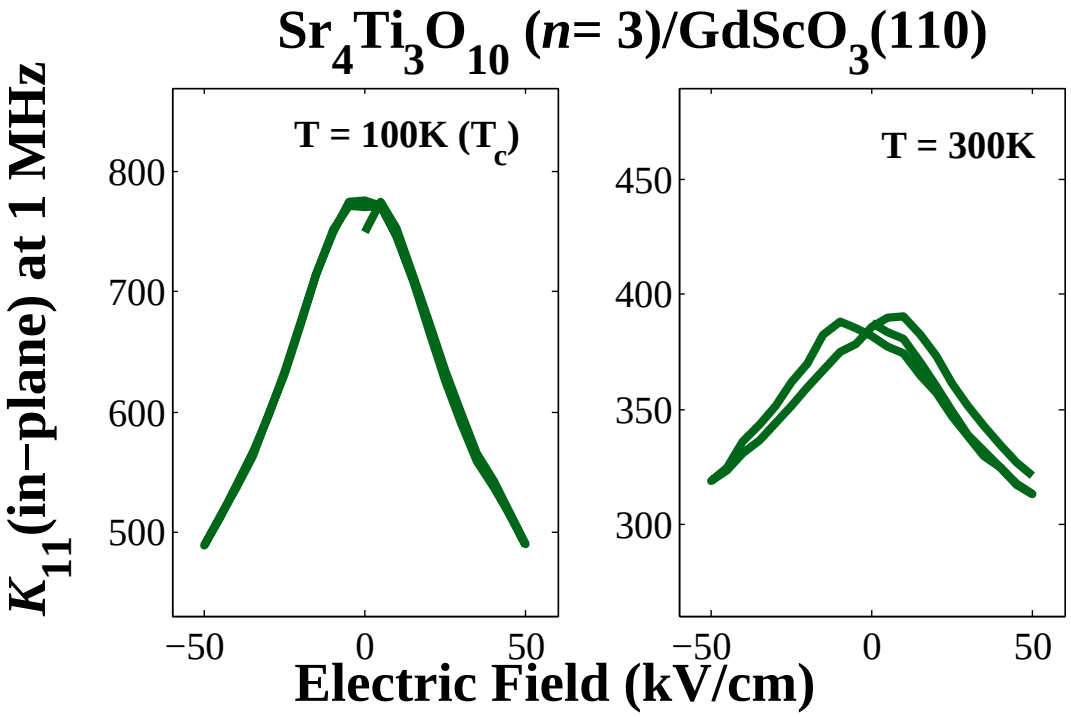

Figure 4.13: Electric Field Dependence at 1 MHz of
$Sr_4Ti_3O_{10}/DyScO_3(110)$ $(n = 3)$
at 60 K, 120 K, 180 K (T_c), and 300 K.

The electric field dependence of the real part of the in-plane relative permittivity (K_{11}(in-plane)) at 1 MHz of $Sr_4Ti_3O_{10}/DyScO_3(110)$ $(n = 3)$ at 30 K (top left), 60 K (Critical Temperature (T_c)) (top right), 120 K (bottom left), and 300 K (bottom right). The maximum electric field was 75 kV/cm and was stepped by 7.5 kV/cm. The interdigitated capacitors used for this measurement had active lengths $\ell =$ (0.875 mm, 1.835 mm).

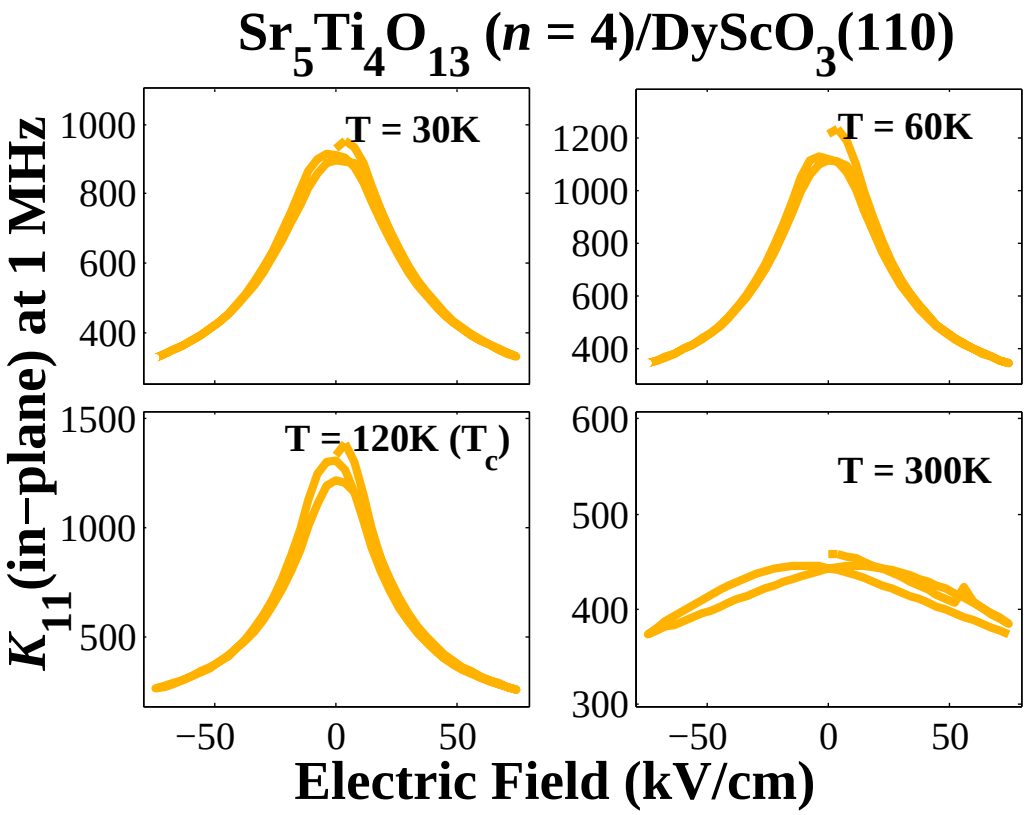

Figure 4.14: Electric Field Dependence at 1 MHz of
$Sr_5Ti_4O_{13}/DyScO_3(110)$ $(n = 4)$
at 30 K, 60 K, 120 K (T_c), and 180 K.

The electric field dependence of the real part of the in-plane relative permittivity (K_{11}(in-plane)) at 1 MHz of $Sr_5Ti_4O_{13}/DyScO_3(110)$ $(n = 4)$ at 30 K (top left), 60 K (top right), 120 K (Critical Temperature (T_c)) (bottom left), and 180 K (bottom right). The maximum electric field was 75 kV/cm and was stepped by 7.5 kV/cm. The interdigitated capacitors used for this measurement had active lengths $\ell =$ (0.875 mm, 1.835 mm).

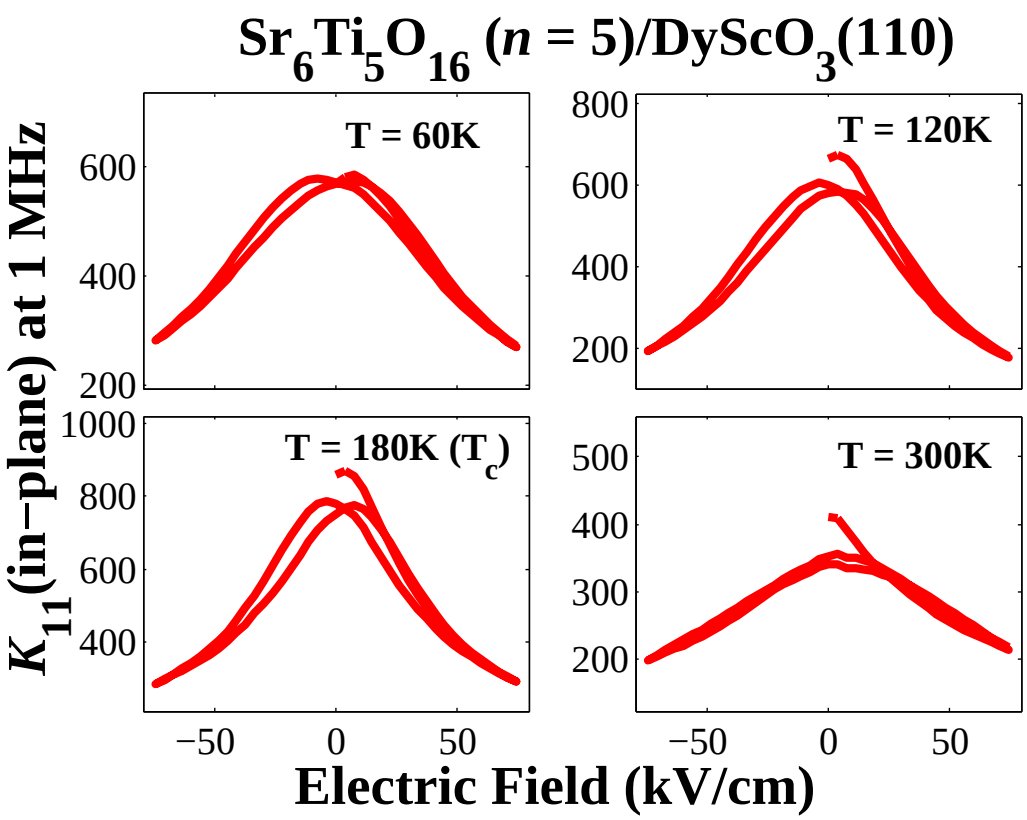

Figure 4.15: Electric Field Dependence at 1 MHz of
$Sr_6Ti_5O_{16}/DyScO_3(110)$ $(n = 5)$
at 60 K, 120 K, 180 K (T_c), and 300 K.

The electric field dependence of the real part of the in-plane relative permittivity (K_{11}(in-plane)) at 1 MHz of $Sr_6Ti_5O_{16}/DyScO_3(110)$ $(n = 5)$ at 60 K (top left), 120 K (top right), 180 K (Critical Temperature (T_c)) (bottom left), and 300 K (bottom right). The maximum electric field was 75 kV/cm and was stepped by 7.5 kV/cm. The interdigitated capacitors used for this measurement had active lengths $\ell =$ (0.875 mm, 1.835 mm).

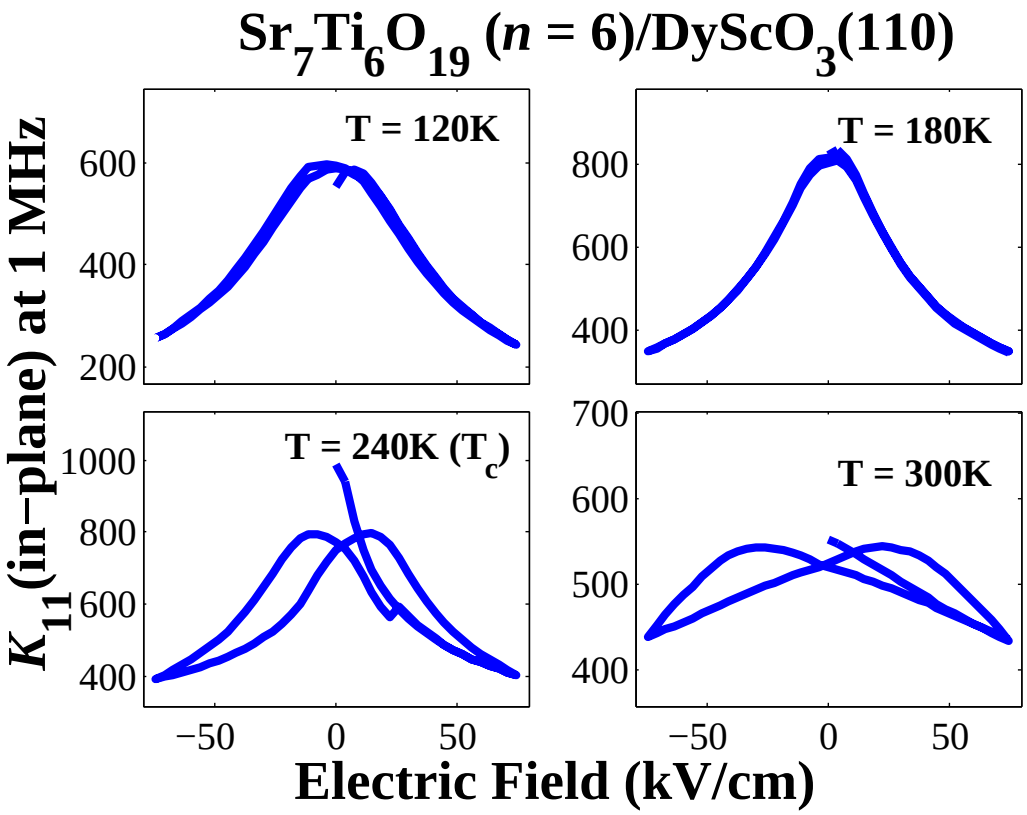

Figure 4.16: Electric Field Dependence at 1 MHz of
$Sr_7Ti_6O_{19}/DyScO_3(110)$ $(n = 6)$
at 120 K, 180 K, 240 K (T_c), and 300 K.

The electric field dependence of the real part of the in-plane relative permittivity (K_{11}(in-plane)) at 1 MHz of $Sr_7Ti_6O_{19}/DyScO_3(110)$ $(n = 6)$ at 120 K (top left), 180 K (top right), 240 K (Critical Temperature (T_c)) (bottom left), and 300 K (bottom right). The maximum electric field was 75 kV/cm and was stepped by 7.5 kV/cm. The interdigitated capacitors used for this measurement had active lengths $\ell =$ (0.875 mm, 1.835 mm).

We calculated the %Tunability from the maximum value of K_{11} obtained after the film had been poled to V_{max}, which excludes the initial portion of the electric field sweep from 0 to V_{max}. Formally, the tunability of the thin films can be written as

$$\%\text{Tuning} = 100 \times \left(1 - \frac{K_{11}(V_{max})}{max(K_{11})}\right). \tag{4.1}$$

For a less conservative estimate of the %Tuning, K_{11} can be taken from the unpoled state. In practice, we cannot recover this state by changing the electric field once the material has been poled, therefore, we use $max(K_{11})$ after this initial sweep. We show the %Tuning of K_{11} as a function of temperature for the 50 nm $Sr_{n+1}Ti_nO_{3n+1}/DyScO_3(110)$ (n = 2, 3, 4, 5, 6) in Fig. 4.17. We have used color to indicated series number, where n = 2, 3, 4, 5, and 6 are represented by cyan, dark green, dark yellow, red, and blue, respectively. As shown in Fig. 4.17, we found that tunability persists above the T_c, and unsurprisingly, the temperature dependence of the %Tuning appears to track the temperature dependence of K_{11}. We also show the temperature dependence of the $DyScO_3$ #2 sample set for n = 4 (dark yellow) and n = 5 (red) as dashed lines with triangles (Fig. 4.18). For these measurements, we were able to apply a field of 100 kV/cm. This shows that with higher field were are to achieve even greater tuning. During the measurement of the $DyScO_3$ #2 sample set, we also learned that too much applied field can induce dielectric breakdown and the subsequent and irreparable destruction of the measurement devices.

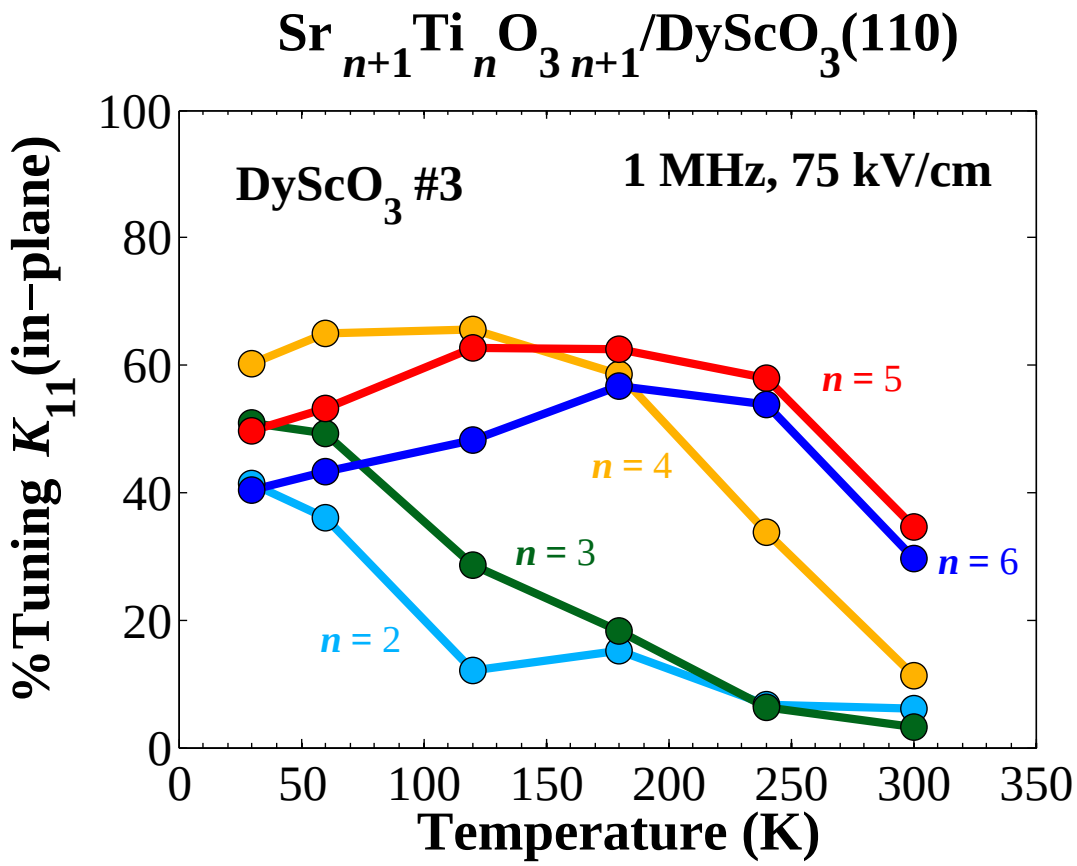

Figure 4.17: %Tuning of K_{11}(in-plane) as a Function of Temperature for $Sr_{n+1}Ti_nO_{3n+1}/DyScO_3(110)(n = 2, 3, 4, 5, 6)$ for the sample set $DyScO_3$ #3

The %Tuning of the real part of the in-plane relative permittivity (%Tuning K_{11}(in-plane)) as a function of temperature for 50 nm thick film of $Sr_{n+1}Ti_nO_{3n+1}/DyScO_3(110)(n = 2, 3, 4, 5, 6,)$ for sample set $DyScO_3$ #3 at 1 MHz at a maximum applied field of 75 kV/cm. We have used color to indicated series number, where $n = 2$, 3, 4, 5, and 6 are represented by cyan, dark green, dark yellow, red, and blue, respectively.

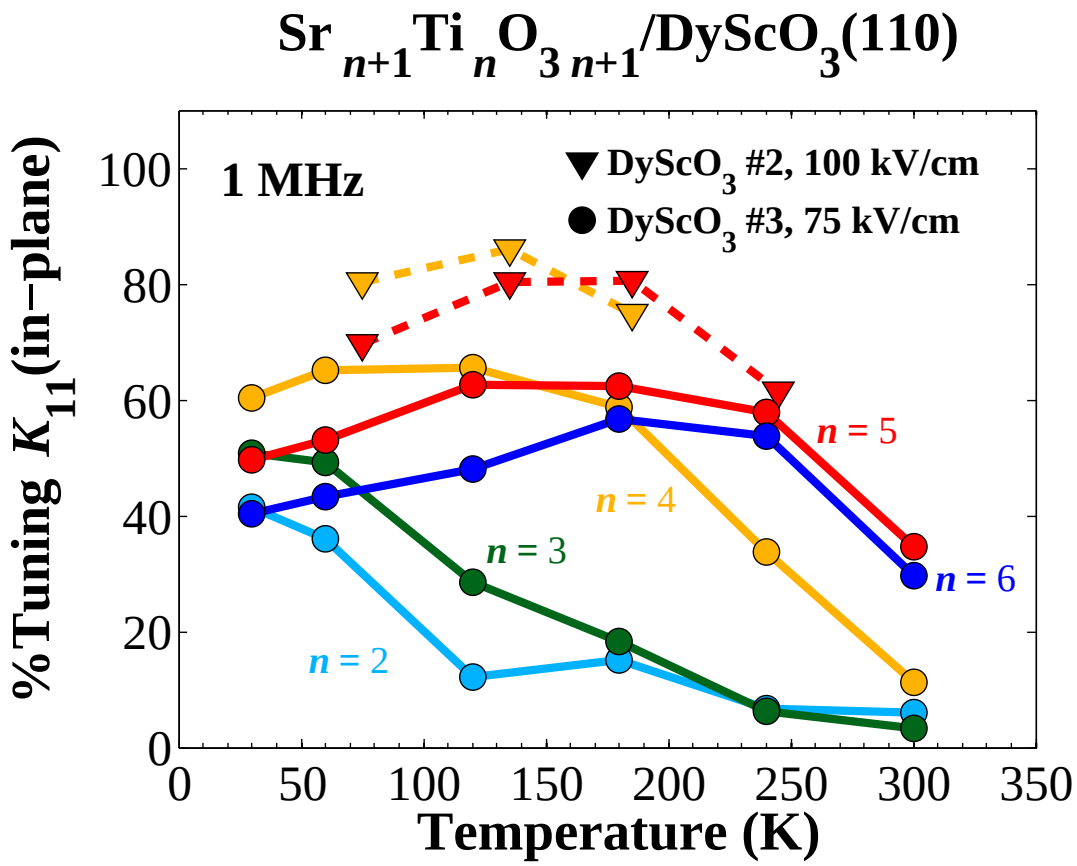

Figure 4.18: %Tuning of K_{11}(in-plane) as a Function of Temperature for $Sr_{n+1}Ti_nO_{3n+1}/DyScO_3(110)(n = 2, 3, 4, 5, 6,)$ for sample sets $DyScO_3$ #2 and$DyScO_3$ #3

The %Tuning of the real part of the in-plane relative permittivity (%Tuning K_{11}(in-plane)) as a function of temperature for 50 nm thick films of $Sr_{n+1}Ti_nO_{3n+1}/DyScO_3(110)(n = 2, 3, 4, 5, 6,)$ at 1 MHz at a maximum applied field of 75 kV/cm and another set of measurements on 50 nm thick films of $Sr_{n+1}Ti_nO_{3n+1}/DyScO_3(110)(n = 4, \text{and } 5)$ at 1 MHz at a maximum applied field of 100 kV/cm. The samples sets shown are $DyScO_3$ #2 (dashed lines with triangles) and $DyScO_3$ #3 (solid lines with circles). We have used color to indicated series number, where $n = 2, 3, 4, 5, \text{and } 6$ are represented by cyan, dark green, dark yellow, red, and blue, respectively.

We then performed the similar series of electric field dependence measurements at several temperatures for the 25 nm $Sr_{n+1}Ti_nO_{3n+1}/GdScO_3(110)(n = 2, 3, 4, 5, 6)$ films labeled $GdScO_3$ #1 in the Sec. 4.4. For these measurements, the IDCs had active lengths $\ell = (0.875 \text{ mm}, 1.835 \text{ mm})$ and the maximum applied electric field was

50 kV/cm stepped by 5 kV/cm. The results are shown in Figs. 4.19, 4.20, 4.21, and 4.22. In these measurements, we performed the electric field dependent measurements at each respective T_c for each film and at 300 K. From Figs. 4.19, 4.20, 4.21, and 4.22, we again see that hysteresis persists well above T_c of each film.

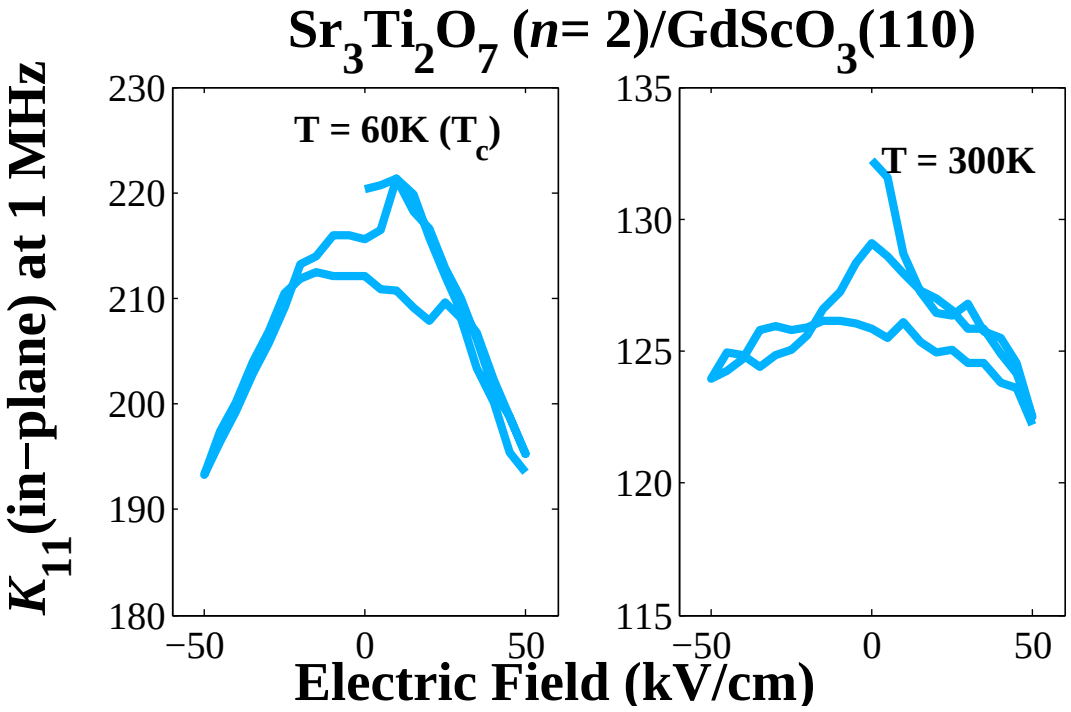

Figure 4.19: Electric Field Dependence at 1 MHz of $Sr_3Ti_2O_7/GdScO_3(110)$ ($n = 2$) at 60 K (T_c), and 300 K.

The electric field dependence of the real part of the in-plane relative permittivity (K_{11}(in-plane)) at 1 MHz of $Sr_3Ti_2O_7/GdScO_3(110)$ ($n = 2$) at 60 K (Critical Temperature (T_c)) (left), and 300 K (right). The maximum electric field was 50 kV/cm and the electric field was stepped by 5 kV/cm. The interdigitated capacitors used for this measurement had active lengths ℓ = (0.875 mm, 1.835 mm).

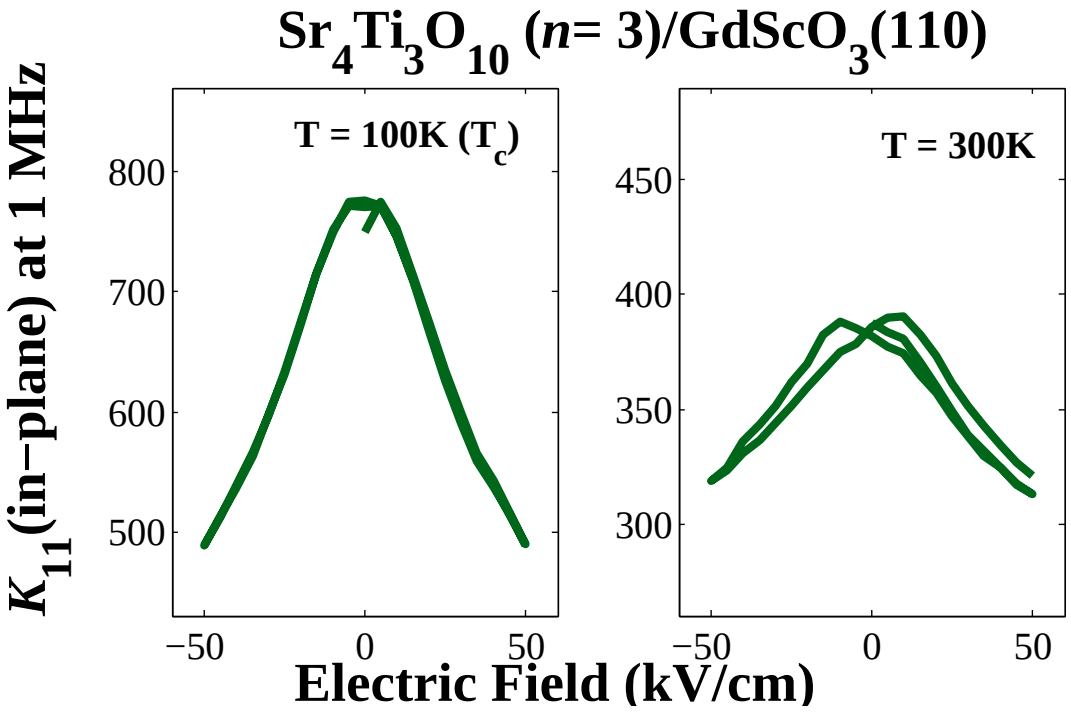

Figure 4.20: Electric Field Dependence at 1 MHz of $Sr_4Ti_3O_{10}/GdScO_3(110)$ $(n = 3)$ at 100 K (T_c), and 300 K.

The electric field dependence of the real part of the in-plane relative permittivity (K_{11}(in-plane)) at 1 MHz of $Sr_4Ti_3O_{10}/GdScO_3(110)$ $(n = 3)$ at 100 K (Critical Temperature (T_c)) (left), and 300 K (right). The maximum electric field was 50 kV/cm and the electric field was stepped by 5 kV/cm. The interdigitated capacitors used for this measurement had active lengths ℓ = (0.875 mm, 1.835 mm).

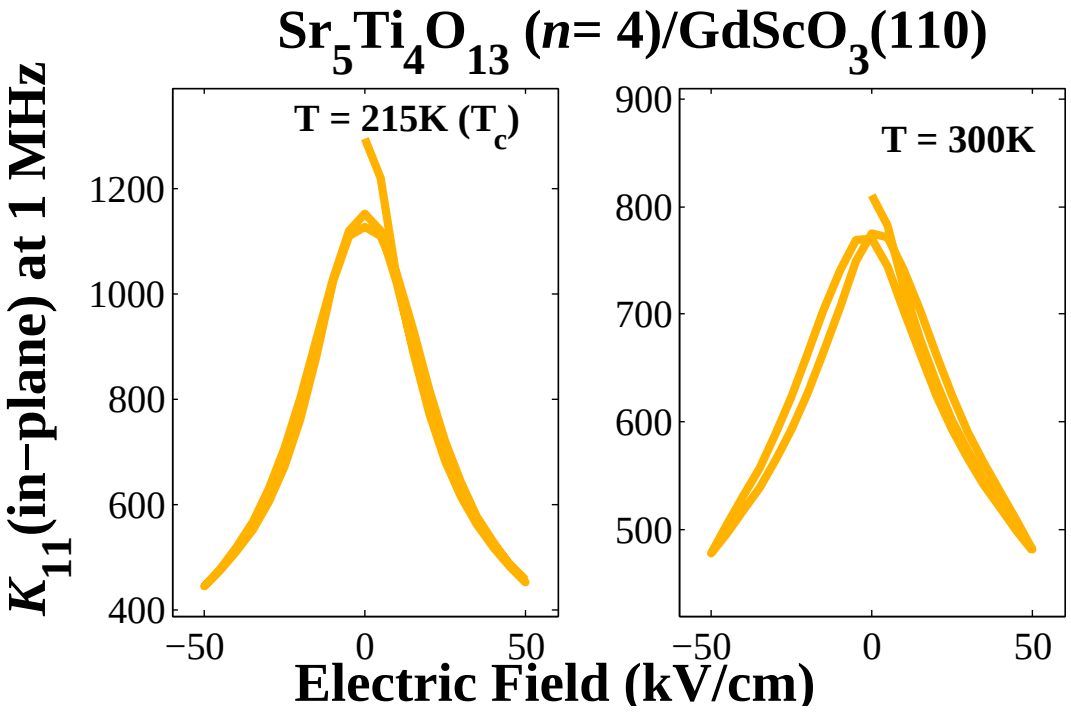

Figure 4.21: Electric Field Dependence at 1 MHz of $Sr_5Ti_4O_{13}/GdScO_3(110)$ ($n = 4$) at 215 K (T_c), and 300 K.

The electric field dependence of the real part of the in-plane relative permittivity (K_{11}(in-plane)) at 1 MHz of $Sr_5Ti_4O_{13}/GdScO_3(110)$ ($n = 4$) at 215 K (Critical Temperature (T_c)) (left), and 300 K (right). The maximum electric field was 50 kV/cm and the electric field was stepped by 5 kV/cm. The interdigitated capacitors used for this measurement had active lengths ℓ = (0.875 mm, 1.835 mm).

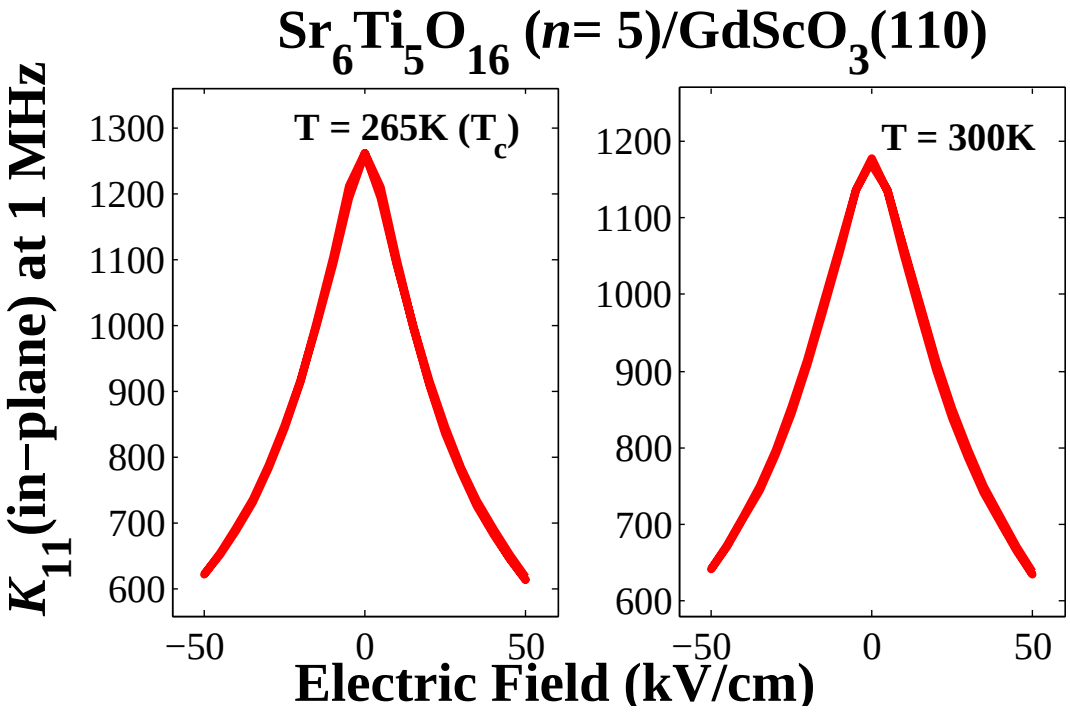

Figure 4.22: Electric Field Dependence of K_{11}(in-plane) at 1 MHz of $Sr_6Ti_5O_{16}/GdScO_3(110)$ $(n = 5)$ at 265 K (T_c), and 300 K.

The electric field dependence of the real part of the in-plane relative permittivity (K_{11}(in-plane)) at 1 MHz of $Sr_6Ti_5O_{16}/GdScO_3(110)$ $(n = 5)$ at 265 K (Critical Temperature (T_c)) (left), and 300 K (right). The maximum electric field was 50 kV/cm and the electric field was stepped by 5 kV/cm. The interdigitated capacitors used for this measurement had active lengths ℓ = (0.875 mm, 1.835 mm).

As we showed earlier, a central aspect of this study has been to explore the role of series number and the limiting behavior as the material approaches pure $SrTiO_3/DyScO_3(110)(n = \infty)$. Although for practical applications the tunability at 300 K is more relevant (See Fig. 4.23(b)), from perspective of trying to understand the underlying physics it is more instructive to examine the tuning as a function of series number at T_c (Fig. 4.23(a)). In Fig. 4.23, we show the %Tuning of K_{11} at 1 MHz calculated with Eq. 4.1 as a function of series number (n) for the samples on the two substrates, $DyScO_3(110)$ and $GdScO_3(110)$. We measured the samples sets $DyScO_3$ #2 (triangles) at 100 kV/cm, $DyScO_3$ #3 (circles)

at 75 kV/cm, and $GdScO_3$ #1 (stars) at 50 kV/cm. The series numbers (n) measured are $n = 2$ (cyan), $n = 3$ (dark green), $n = 4$ (dark yellow), $n = 5$ (red), and $n = 6$ (blue). For the samples sets on $DyScO_3$(110), the approximate Critical Temperatures for $n = 3$, 4, 5, and 6 are T = 60 K, 120 K, 180 K, and 240 K, respectively. For the sample set on $GdScO_3$(110), the approximate Critical Temperatures for $n = 2$, 3, 4, and 5 are T = 60 K, 100 K, 215 K, and 265 K, respectively. Figure 4.23(b) shows that there is no clear relationship between increased strain and %Tuning of K_{11} at 1 MHz for a given n at T_c; however, the %Tuning at T_c appears to increase and possibly stabilize with increasing n. The relationship with %Tuning and n at 1 MHz clearly increases with increasing n at 300 K. We can attribute this behavior to the distance away from T_c for a given n.

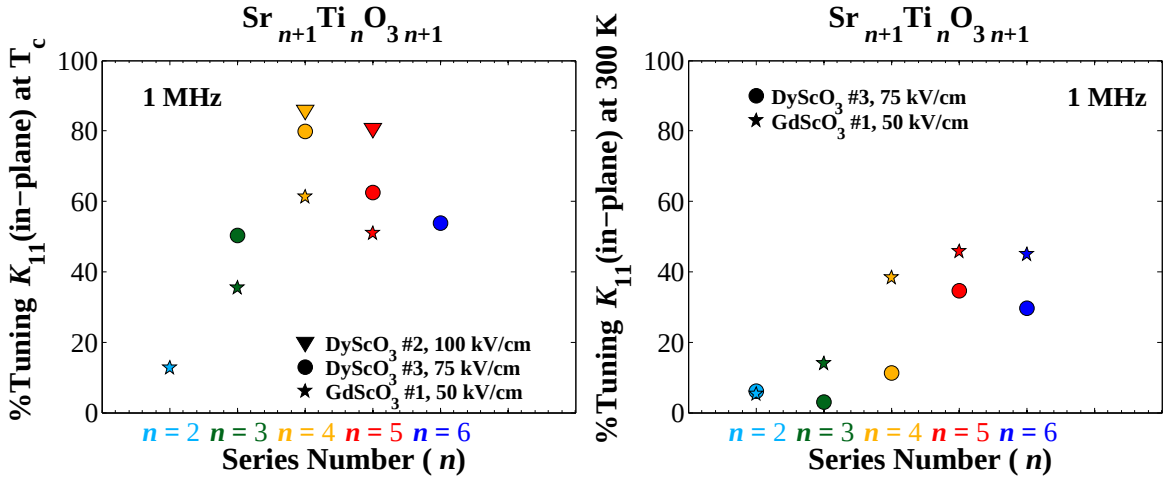

(a) %Tuning at T_c (b) %Tuning at 300 K

Figure 4.23: %Tuning of K_{11}(in-plane) as a Function of Series Number at T_c and 300 K for
$Sr_{n+1}Ti_nO_{3n+1}$(n = 2, 3, 4, 5, 6) for samples on
$DyScO_3$(110) and $GdScO_3$(110)

(a) The %Tuning of the real part of the in-plane relative permittivity (K_{11}(in-plane)) $Sr_{n+1}Ti_nO_{3n+1}$(n = 2, 3, 4, 5, 6) at the respective Critical Temperatures of the different series numbers (n) for the different samples sets at 1 MHz. The samples sets measured are $DyScO_3$ #2 (triangles) at 100 kV/cm, $DyScO_3$ #3 (circles) at 75 kV/cm, and $GdScO_3$ #1 (stars) at 50 kV/cm. The series numbers (n) measured are n = 2 (cyan), n = 3 (dark green), n = 4 (dark yellow), n = 5 (red), and n = 6 (blue). For the samples sets on $DyScO_3$(110), the approximate Critical Temperatures for n = 3, 4, 5, and 6 are T = 60 K, 120 K, 180 K, and 240 K, respectively. For the sample set on $GdScO_3$(110), the approximate Critical Temperatures for n = 2, 3, 4, and 5 are T = 60 K, 100 K, 215 K, and 265 K, respectively. (b) At 300 K and 1 MHz, the %Tuning of the real part of the in-plane relative permittivity (K_{11}(in-plane)) $Sr_{n+1}Ti_nO_{3n+1}$(n = 2, 3, 4, 5, 6) of the different series numbers on samples sets $DyScO_3$ #3 (circles) at 75 kV/cm, and $GdScO_3$ #1 (stars) at 50 kV/cm. The series numbers (n) measured are n = 2 (cyan), n = 3 (dark green), n = 4 (dark yellow), n = 5 (red), and n = 6 (blue).

4.6 Broadband Frequency Dependence

Frequency dependence in the very high megahertz and gigahertz regimes is often neglected for in-plane relative permittivity characterization of thin-film materials, because it is very challenging and time-consuming [2]. Lumped-element devices, like

IDCs, can be used at high frequencies, but in the gigahertz regime measurement artifacts from the microwave probes and instruments can affect the complex S-parameters to yield artificial frequency dependence. Even after careful microwave on-wafer calibrations, IDCs will show distributed type behavior when the guided wavelength is comparable to the length of the device. At such high frequencies, parasitic capacitances can also influence the results without careful 2D finite element simulations and extensive engineering.

As we discussed in Ch. 2, we have developed a very accurate measurement technique that overcomes many of the challenges associated with thin film dielectric characterization from 100 Hz to 40 GHz, and in principle to 110 GHz. We used a combination of instruments to cover such a broad frequency range (Fig. 2.1). We performed measurements with an LF LCR meter, which covered the range from 100 Hz to 1 MHz. From 1 MHz to 300 MHz, we measured complex S-parameters with an RF vector network analyzer. We also measured complex S-parameters with an HF vector network analyzer from 45 MHz to 40 GHz. The vector network analyzers were first corrected with coaxial calibration standards and then the calibrations were verified with a pair of zero-delay length symmetric short circuit reflect standards (or flush shorts). For more details about the measurement configuration setup, we refer the reader to Ch. 2 and App. A.1.

After the measurement instruments were corrected to the end of the flexible phase-maintaining coaxial cable (See Fig. 2.1), we performed a series of on-wafer measurements to remove the effects of the g-s-g probes and the cables. The LF LCR meter was corrected on-wafer with a planar series open and planar series short fabricated on a $LaAlO_3$ calibration wafer. The RF vector network analyzer was corrected to the g-s-g probe tips with the series-resistor calibration technique [34, 35]. We corrected the HF measurements following the multiline thru-reflect-line calibration technique and series-resistor calibration technique [30, 31, 34]. For both LF and RF regimes,

we measured a set of IDCs with active lengths ℓ = (0.100 mm, 0.325 mm, 0.875 mm, 1.835 mm, 2.900 mm) on each test wafer. In the HF regime, we measured a set of CPWs with active lengths ℓ = (0.420 mm, 1.270 mm, 2.155 mm, 3.22 mm, 3.993 mm, 5.933 mm), a planar 0.210 mm offset symmetric short circuit reflect on each test wafer. This series of measurements, including the on-wafer calibrations, were performed at each measurement temperature presented in this section.

4.6.1 Samples on $DyScO_3(110)$

Even though the T_c evolves as a function of n, it is useful to explore the properties of the $Sr_{n+1}Ti_nO_{3n+1}/DyScO_3(110)$($n$ = 2, 3, 4, 5, 6) at 300 K. In Fig. 4.24, we show K_{11} for n = 2, 3, 4, 5, and 6 as the solid cyan, dark green, dark yellow, red and blue lines, respectively. Aside from noting the clear progression with increasing n, it is interesting that these materials seem to exhibit little to no frequency dependence at 300 K despite showing marked tunability at 1 MHz as shown in Fig. 4.23. This is particularly surprising considering that for n = 6 (blue) these measurements are approximately 60 K above T_c. Measurements of many other tunable ferroelectrics, like $Ba_{1-x}Sr_xTiO_3$, with a comparable tunability T_c and K_{11} show dispersion in the gigahertz regime and a power-law like frequency dependence at low frequencies [2].

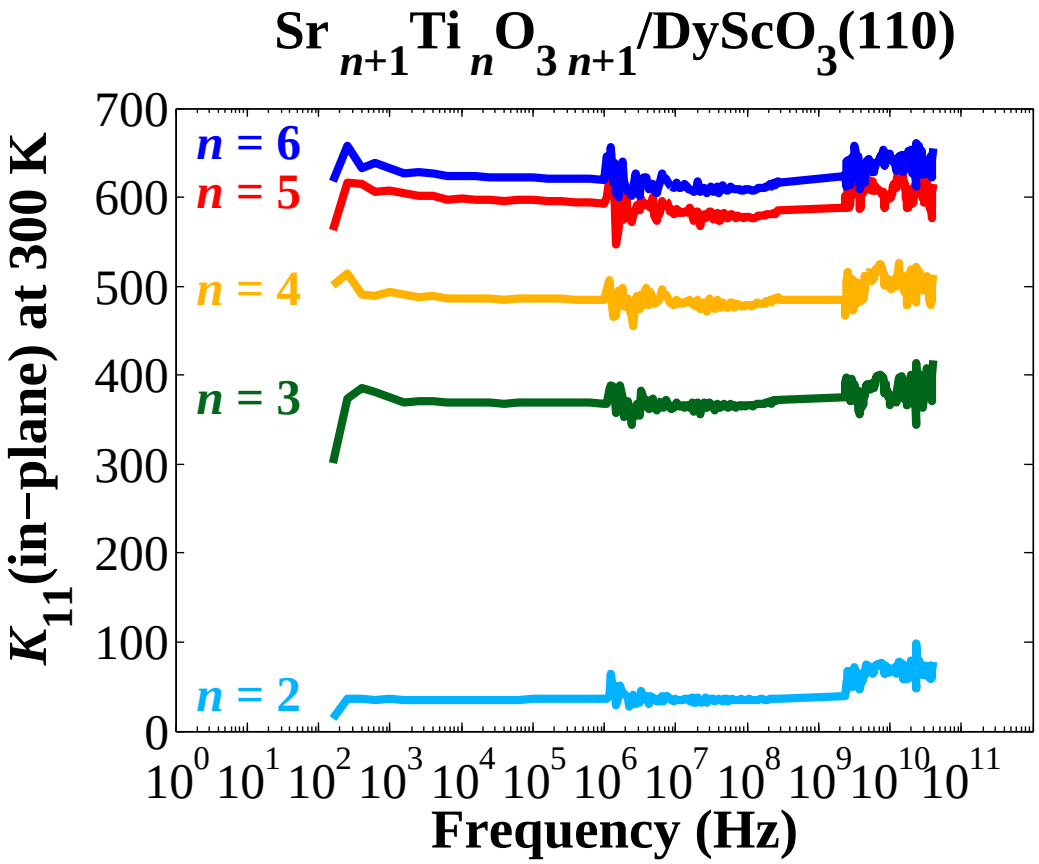

Figure 4.24: Frequency Dependence of K_{11}(in-plane) $Sr_{n+1}Ti_nO_{3n+1}/DyScO_3(110)(n = 2, 3, 4, 5, 6)$ at 300 K

At 300 K, the frequency dependence of the real part of the in-plane relative permittivity (K_{11}(in-plane)) from 100 Hz to 40 GHz for 50 nm thick films of $Sr_{n+1}Ti_nO_{3n+1}/DyScO_3(110)(n = 2, 3, 4, 5, 6)$ from sample set $DyScO_3$ #3. The series number (n) measured are $n = 2$ (cyan), $n = 3$ (dark green), $n = 4$ (dark yellow), $n = 5$ (red), and $n = 6$ (blue).

In the low frequency temperature dependent measurements in Sec. 4.4, we showed that the temperature dependence of K_{11} was frequency dependent in a series of figures (Figs. 4.9, and 4.11). We stated that this behavior is often seen in relaxor ferroelectrics and it is understood within the context of polar nanoregions that form in the materials. We now take the same approach to the K_{11} measurement from 100 Hz to 40 GHz. Instead of a fine temperature spacing at just a few frequencies, we performed our broadband characterization technique at a select set of temperatures

(60 K, 120 K, 180 K, 240 K, and 300 K) over the full range of frequencies (100 Hz to 40 GHz). We show the complex K_{11} from 100 Hz to 40 GHz for $n = 3$, 4, 5, and 6 at a variety of temperatures in Figs. 4.25, 4.26, 4.27, and 4.28. In Fig. 4.25(a), we show the real part of K_{11} as a function of frequency at variable temperature for $n = 3$. For this material, it is evident that frequency dependence develops above 1 GHz in the sample in the vicinity of 60 K (T_c), but there is no obvious dispersion below 300 MHz for temperature above T_c. The frequency dependence, or increase in dispersion, is even more obvious in 4.25(b), where we show the imaginary part of K_{11} as a function of frequency at variable temperature. In this figure, we see that the loss appears to be a maximum at the 60 K. The trend in the real part of K_{11} is consistent with the low frequency temperature dependent measurements shown in Fig. 4.9(b). The imaginary part and real part are essentially a maximum at T_c for the measurement temperatures and all the series numbers explored in these experiments and the frequency dependence is qualitatively similar to that found in Refs. [2, 5, 75].

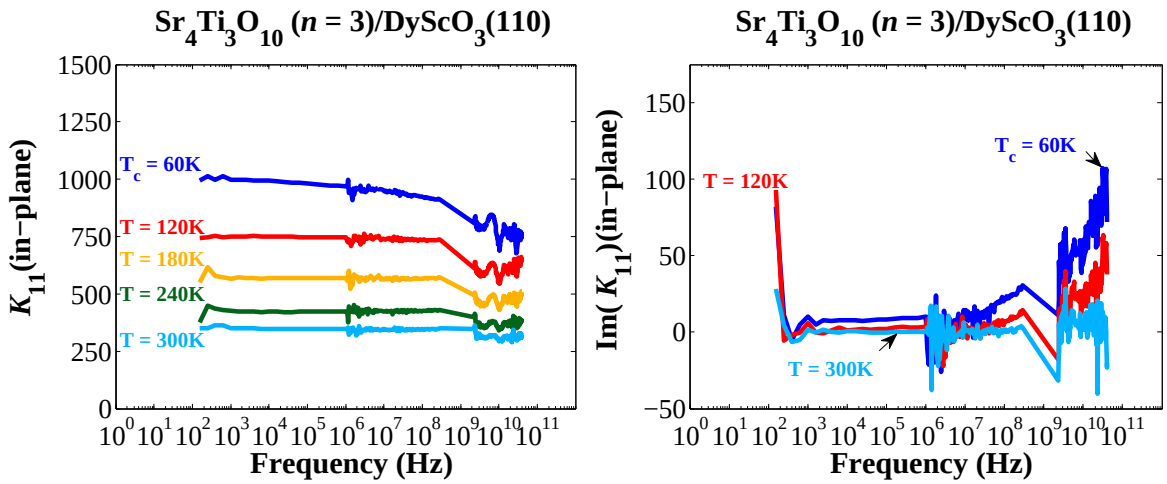

(a) K_{11}(in-plane) (b) Im(K_{11})(in-plane)

Figure 4.25: Frequency Dependence of Complex K_{11}(in-plane) $Sr_4Ti_3O_{10}/DyScO_3(110)(n = 3)$ at Variable Temperature

(a) The frequency dependence of the real part of the in-plane relative permittivity (K_{11}(in-plane)) from 100 Hz to 40 GHz at variable temperature for 50 nm thick film of $Sr_4Ti_3O_{10}/DyScO_3(110)(n = 3)$ from sample set $DyScO_3$ #3. The temperatures (T) measured are 300 K (cyan), 240 K (dark green), 180 K (dark yellow), 120 K (red), and 60 K (Critical Temperature (T_c)) (blue). (b) The frequency dependence of the imaginary part of the in-plane relative permittivity (Im(K_{11})(in-plane)) from 100 Hz to 40 GHz at variable temperature for 50 nm thick film of $Sr_4Ti_3O_{10}/DyScO_3(110)(n = 3)$ from sample set $DyScO_3$ #3. The temperatures (T) measured are 300 K (cyan), 120 K (red), and 60 K (Critical Temperature (T_c)) (blue).

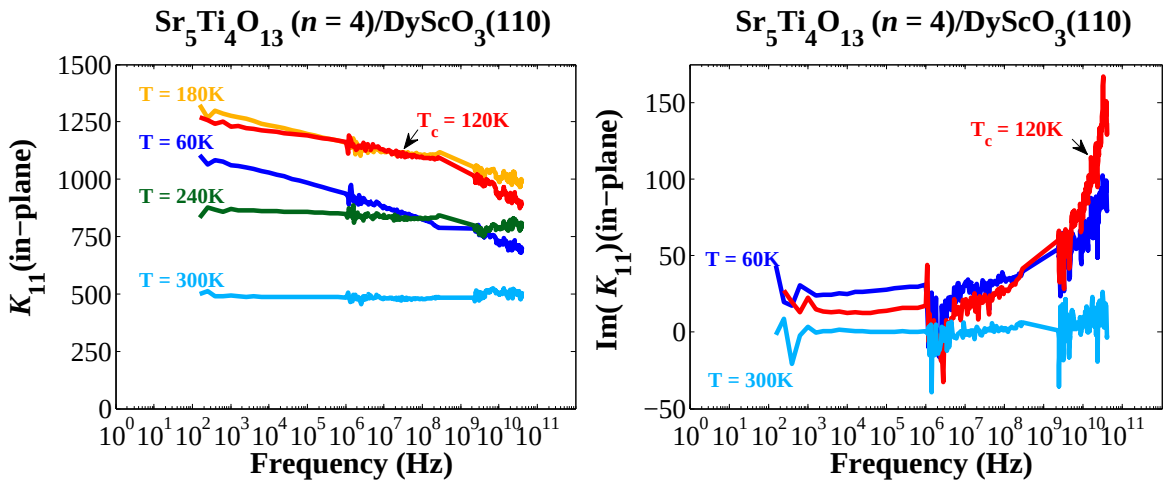

(a) K_{11}(in-plane) (b) Im(K_{11})(in-plane)

Figure 4.26: Frequency Dependence of Complex K_{11}(in-plane) $Sr_5Ti_4O_{13}/DyScO_3(110)(n = 4)$ at Variable Temperature

(a) The frequency dependence of the real part of the in-plane relative permittivity (K_{11}(in-plane)) from 100 Hz to 40 GHz at variable temperature for 50 nm thick film of $Sr_5Ti_4O_{13}/DyScO_3(110)(n = 4)$ from sample set $DyScO_3$ #3. The temperatures (T) measured are 300 K (cyan), 240 K (dark green), 180 K (dark yellow), 120 K (Critical Temperature (T_c)) (red), and 60 K (blue). (b) The frequency dependence of the imaginary part of the in-plane relative permittivity (Im(K_{11})(in-plane)) from 100 Hz to 40 GHz at variable temperature for 50 nm thick film of $Sr_5Ti_4O_{13}/DyScO_3(110)(n = 4)$ from sample set $DyScO_3$ #3. The temperatures (T) measured are 300 K (cyan), 120 K (Critical Temperature (T_c)) (red), and 60 K (blue).

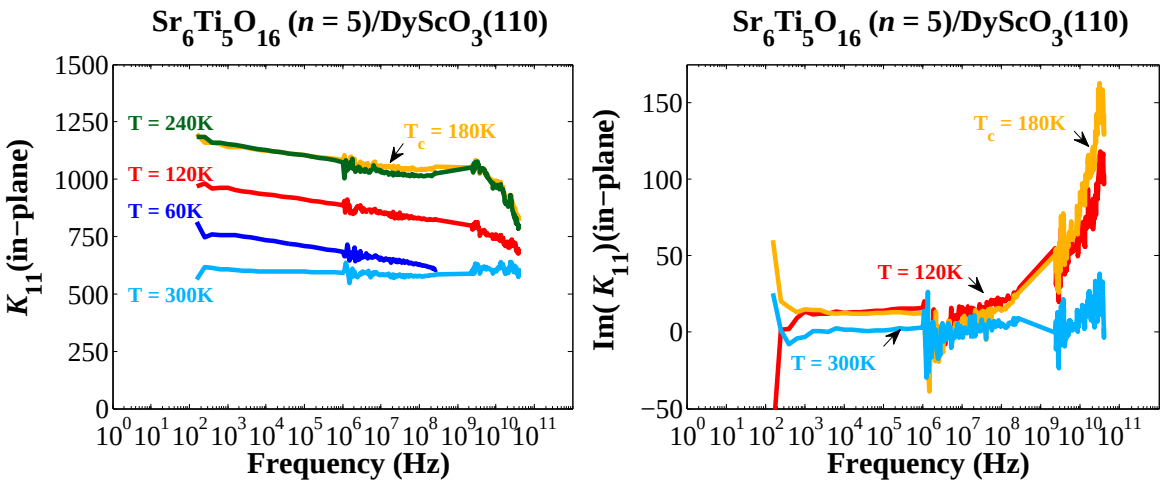

(a) K_{11}(in-plane) (b) Im(K_{11})(in-plane)

Figure 4.27: Frequency Dependence of Complex K_{11}(in-plane) $Sr_6Ti_5O_{16}/DyScO_3(110)(n = 5)$ at Variable Temperature

(a) The frequency dependence of the real part of the in-plane relative permittivity (K_{11}(in-plane)) from 100 Hz to 40 GHz at variable temperature for 50 nm thick film of $Sr_6Ti_5O_{16}/DyScO_3(110)(n = 5)$ from sample set $DyScO_3$ #3. The temperatures (T) measured are 300 K (cyan), 240 K (dark green), 180 K (Critical Temperature (T_c)) (dark yellow), 120 K (red), and 60 K (blue). (b) The frequency dependence of the imaginary part of the in-plane relative permittivity (Im(K_{11})(in-plane)) from 100 Hz to 40 GHz at variable temperature for 50 nm thick film of $Sr_6Ti_5O_{16}/DyScO_3(110)(n = 5)$ from sample set $DyScO_3$ #3. The temperatures (T) measured are 300 K (cyan), 240 K (dark green), 180 K (Critical Temperature (T_c)) (dark yellow), and 120 K (red).

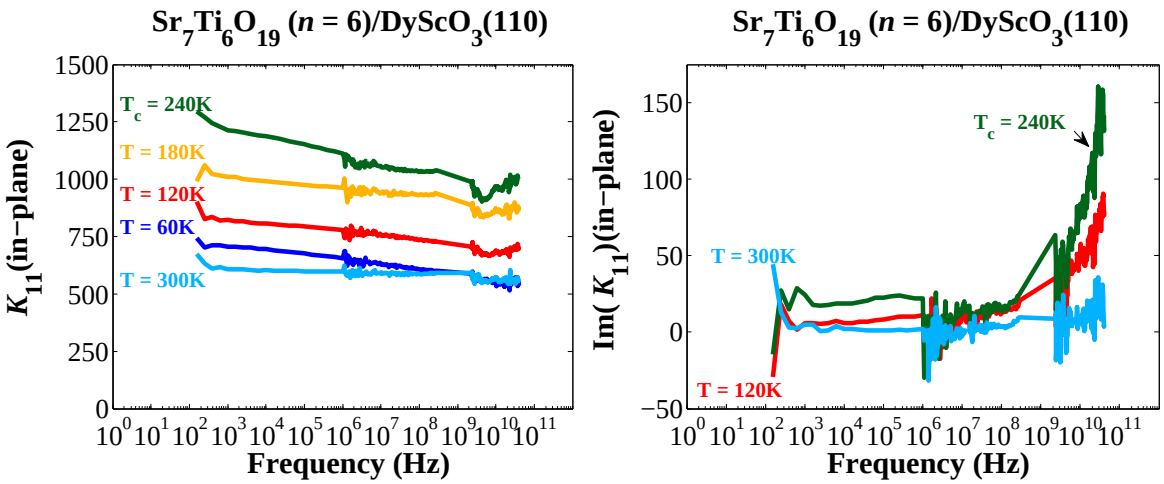

(a) K_{11}(in-plane) (b) Im(K_{11})(in-plane)

Figure 4.28: Frequency Dependence of Complex K_{11}(in-plane) $Sr_7Ti_6O_{19}/DyScO_3(110)(n = 6)$ at Variable Temperature

(a) The frequency dependence of the real part of the in-plane relative permittivity (K_{11}(in-plane)) from 100 Hz to 40 GHz at variable temperature for 50 nm thick film of $Sr_7Ti_6O_{19}/DyScO_3(110)(n = 6)$ from sample set $DyScO_3$ #3. The temperatures (T) measured are 300 K (cyan), 240 K (Critical Temperature (T_c)) (dark green), 180 K (dark yellow), 120 K (red), and 60 K (blue). (b) The frequency dependence of the real part of the in-plane relative permittivity (Im(K_{11})(in-plane)) from 100 Hz to 40 GHz at variable temperature for 50 nm thick film of $Sr_7Ti_6O_{19}/DyScO_3(110)(n = 6)$ from sample set $DyScO_3$ #3. The temperatures (T) measured are 300 K (cyan), 240 K (Critical Temperature (T_c)) (dark green), and 120 K (red).

In such a large data set, it is likely that some of the details have been missed; however, there are some conspicuous features that persist through Figs. 4.25, 4.26, 4.27, and 4.28. Above T_c, all of series numbers measured show little to no dispersion in the real part of K_{11}. As we approach T_c, frequency dependence rapidly develops and imaginary part of K_{11} increases. At and below T_c, the frequency dependence below 300 MHz of the real part of K_{11} decreases like a power-law, and correspondingly the imaginary part is constant. In the gigahertz regime, at and below T_c a very weak Debye-like relaxation takes over and gives rise to a sharper increase in the imaginary part of K_{11}. As a function of decreasing temperature, the slope of K_{11} below T_c as a function of logarithmic frequency either decreases by a small amount or remains

constant for frequencies below 300 MHz. This important observation will be addressed in more detail in Ch. 5.

We can reduce the broadband frequency dependent complex K_{11} measurements taken at different temperatures into slices at fixed frequency versus temperature to see how frequency affects the temperature dependence of the complex K_{11}. In Fig. 4.29 (a), we show the real part of K_{11} at 1 MHz (dashed lines) and 10 GHz (solid lines) for $n = 3$ (dark green, top left), $n = 4$ (dark yellow, top right), $n = 5$ (red, bottom left), and $n = 6$ (blue, bottom right). In Fig. 4.29 (b), we show the imaginary part of $\mathrm{Im}(K_{11})$ at 1 MHz (dashed lines), 10 GHz (solid lines), and 30 GHz (dotted lines) for $n = 3$ (dark green, top left), $n = 4$ (dark yellow, top right), $n = 5$ (red, bottom left), and $n = 6$ (blue, bottom right). The T_c that can be estimated from the broadband measurements were in strong agreement to those obtained from the low frequency measurements shown in Fig. 4.9. Moreover, the somewhat ambiguous T_c obtained from the low frequency measurement of $n = 5$ in Fig. 4.9(b) (red lines) is strongly supported by both imaginary part and real part of K_{11} broadband measurements (Figs. 4.29). In Fig. 4.30, we show the respective loss tangent obtained from the broadband measurement taken at 1 MHz (dashed lines), 10 GHz (solid lines), and 30 GHz (dotted lines) for $n = 3$ (dark green, top left), $n = 4$ (dark yellow, top right), $n = 5$ (red, bottom left), and $n = 6$ (blue, bottom right).

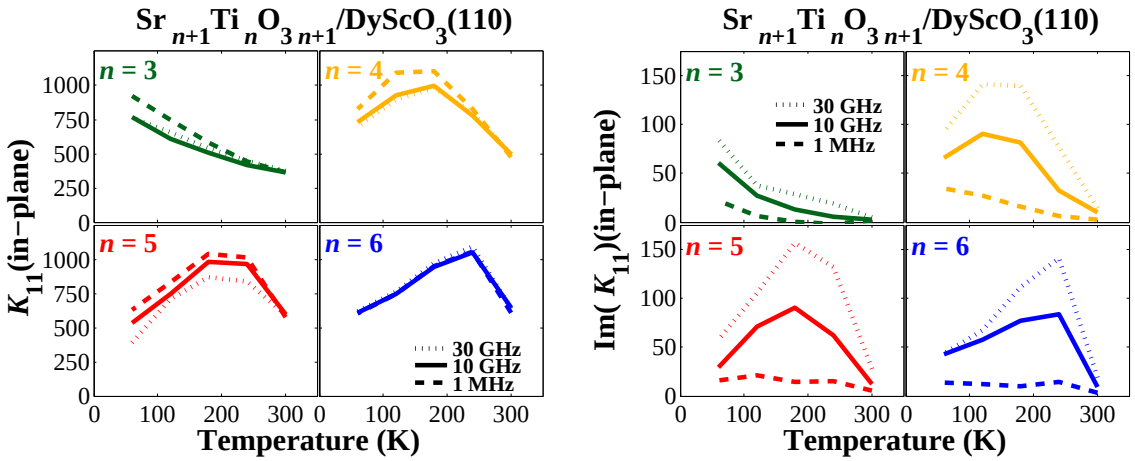

(a) K_{11}(in-plane)

(b) Im(K_{11})(in-plane)

Figure 4.29: Temperature Dependence of Complex K_{11}(in-plane) $Sr_{n+1}Ti_nO_{3n+1}/DyScO_3(110)(n = 3, 4, 5, 6)$ at 1 MHz and 10 GHz

(a) The temperature dependence of the real part of the in-plane relative permittivity (K_{11}(in-plane)) of 50 thick films of $Sr_{n+1}Ti_nO_{3n+1}/DyScO_3(110)(n = 3, 4, 5, 6)$ at 1 MHz (dashed lines), 10 GHz (solid lines), and 30 GHz (dotted lines). The series number (n) measured are $n = 3$ (dark green), $n = 4$ (dark yellow), $n = 5$ (red), and $n = 6$ (blue). (b) The temperature dependence of the imaginary part of the in-plane relative permittivity (Im(K_{11}(in-plane))) of 50 thick films of $Sr_{n+1}Ti_nO_{3n+1}/DyScO_3(110)(n = 3, 4, 5, 6)$ at 1 MHz (dashed lines), 10 GHz (solid lines), and 30 GHz (dotted lines). The series number (n) measured are $n = 3$ (dark green), $n = 4$ (dark yellow), $n = 5$ (red), and $n = 6$ (blue).

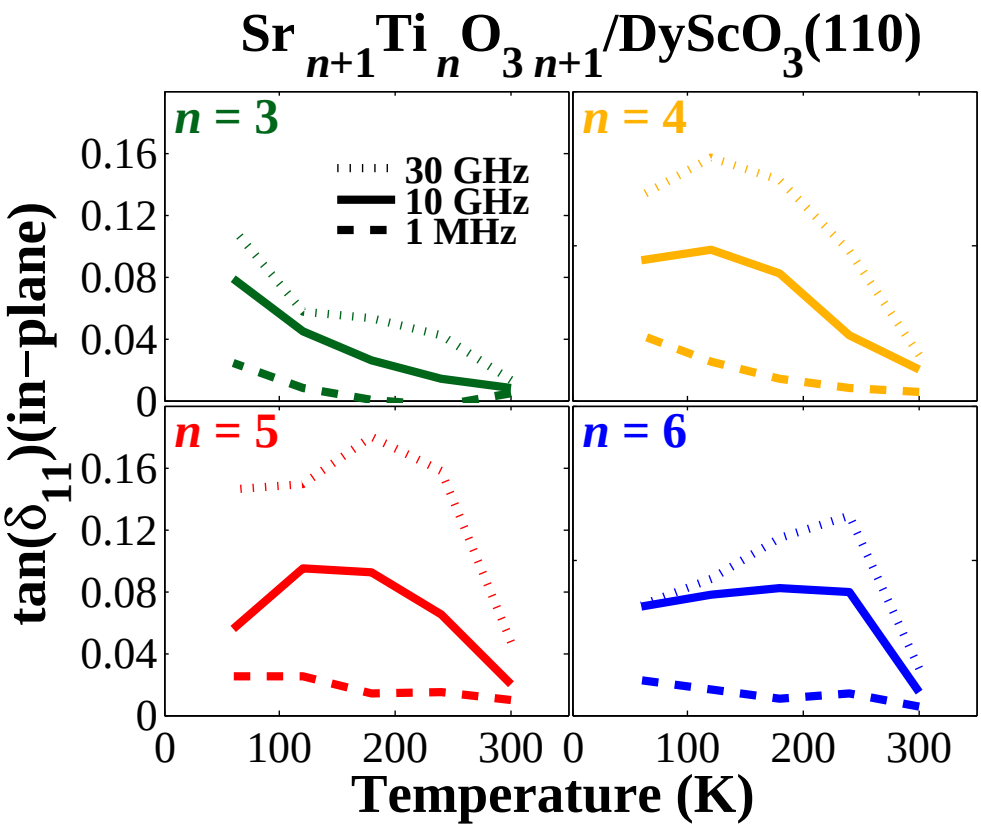

Figure 4.30: Temperature Dependence of tan(δ_{11})(in-plane) $Sr_{n+1}Ti_nO_{3n+1}/DyScO_3(110)$($n$ = 3, 4, 5, 6) at 1 MHz, 10 GHz, and 30 GHz

The temperature dependence of the in-plane loss tangent (tan(δ_{11})(in-plane)) of 50 thick films of $Sr_{n+1}Ti_nO_{3n+1}/DyScO_3(110)$($n$ = 3, 4, 5, 6) at 1 MHz (dashed lines), 10 GHz (solid lines), and 30 GHz (dotted lines). The series number (n) measured are $n = 3$ (dark green), $n = 4$ (dark yellow), $n = 5$ (red), and $n = 6$ (blue).

4.6.2 Samples on $GdScO_3(110)$

We also performed a series of broadband dielectric spectroscopy measurements on 25 nm thick films of $Sr_{n+1}Ti_nO_{3n+1}/GdScO_3(110)$($n$ = 2, 3, 4, 5, 6) at the 300 K. The frequency dependence of K_{11} from 100 Hz to 40 GHz from sample set $GdScO_3$ #1 is shown in Fig. 4.31. The series number (n) measured are $n = 2$ (cyan), $n = 3$ (dark green), $n = 4$ (dark yellow), $n = 5$ (red), and $n = 6$ (blue). Again, these measurements are all performed at different temperature distances away from T_c, but

they illustrate that even in such high strain these materials do not show significant amounts of dispersion. For $n = 2$ (cyan) and $n = 3$ (dark green), we are sufficiently far enough above T_c that materials are likely well into the paraelectric state. Both $n = 4$ (dark yellow) and $n = 5$ (red) are just above their respective transition temperatures and show some slight frequency dependence, but still remain relatively flat into the gigahertz regime. The discontinuity between the CPW and IDC data in $n = 4$ (dark yellow) could be due to poor alignment devices relative to the c-axis of the thin film. Series member $n = 6$ (blue) is still well below T_c; hence, the crystal lattice has begun to harden, which results in a decreased in the K_{11}.

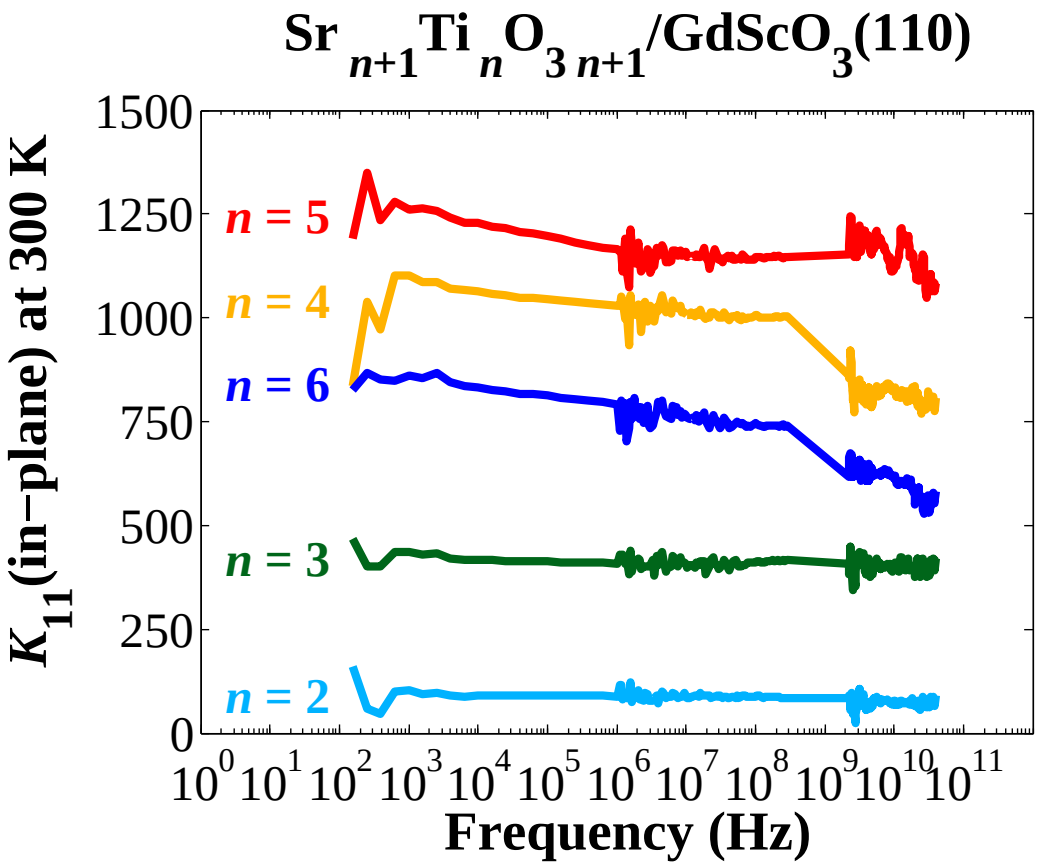

Figure 4.31: Frequency Dependence of K_{11}(in-plane) $Sr_{n+1}Ti_nO_{3n+1}/GdScO_3(110)(n = 2, 3, 4, 5, 6)$ at 300 K

At 300 K, the frequency dependence of the real part of the in-plane relative permittivity (K_{11}(in-plane)) from 100 Hz to 40 GHz for 25 nm thick films of $Sr_{n+1}Ti_nO_{3n+1}/GdScO_3(110)(n = 2, 3, 4, 5, 6)$ from sample set $GdScO_3$ #1. The series number (n) measured are $n = 2$ (cyan), $n = 3$ (dark green), $n = 4$ (dark yellow), $n = 5$ (red), and $n = 6$ (blue).

As we explored earlier with the $DyScO_3$ samples, it is instructive to look at how the frequency dependence evolves in the thin films as function of series number and temperature. This also provides a comparison for understanding how strain has affected the high frequency loss tangents of the materials. We performed a series of broadband permittivity measurements at T_c of the complex K_{11} on the 25 nm thick film of $Sr_{n+1}Ti_nO_{3n+1}/GdScO_3(110)(n = 4, 5)$ from sample set $GdScO_3$ #1. In Fig. 4.32, we show the broadband frequency response of the complex K_{11} from

100 Hz to 40 GHz at 300 K (cyan), and 220 K (T_c) (dark yellow) for 25 nm thick film of $Sr_5Ti_4O_{13}/GdScO_3(110)(n = 4)$ from sample set $GdScO_3$ #1. In Fig. 4.33, we show the broadband frequency response of the complex K_{11} from 100 Hz to 40 GHz at 300 K (cyan), and 265 K (T_c) (dark yellow) for 25 nm thick film of $Sr_6Ti_5O_{16}/GdScO_3(110)(n = 5)$ from sample set $GdScO_3$ #1. In comparison with their counterparts on $DyScO_3$ in Figs. 4.26, and 4.27, the samples show comparable loss at T_c, but significantly more loss at 300 K. If we compare two different series numbers with comparable transition temperatures, like $Sr_6Ti_5O_{16}/GdScO_3(110)(n = 5)$ to $Sr_7Ti_6O_{19}/DyScO_3(110)(n = 6)$, the sample on $DyScO_3(110)$ has a smaller imaginary part of K_{11} above T_c than the sample on $GdScO_3(110)$. For comparable series number, the dispersion of K_{11} at T_c for samples on $GdScO_3(110)$ appears to be greater than the same series number at T_c on $DyScO_3(110)$. In summary, for practical applications this family of RP thin films appear to have lower loss and weaker dispersion on $DyScO_3(110)$.

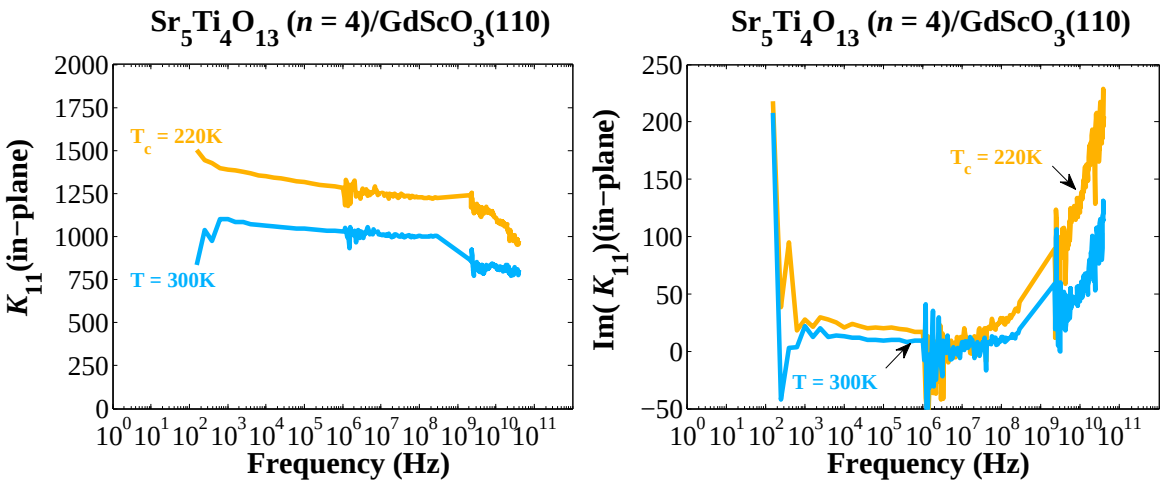

(a) K_{11}(in-plane) (b) Im(K_{11})(in-plane)

Figure 4.32: Frequency Dependence of Complex K_{11}(in-plane) $Sr_5Ti_4O_{13}/GdScO_3(110)(n = 4)$ at Variable Temperature

(a) The frequency dependence of the real part of the in-plane relative permittivity (K_{11}(in-plane)) from 100 Hz to 40 GHz at variable temperature for 25 nm thick film of $Sr_5Ti_4O_{13}/GdScO_3(110)(n = 4)$ from sample set $GdScO_3$ #1. The temperatures (T) measured are 300 K (cyan), and 220 K (Critical Temperature (T_c)) (dark yellow). (b) The frequency dependence of the imaginary part of the in-plane relative permittivity (Im(K_{11})(in-plane)) from 100 Hz to 40 GHz at variable temperature for 25 nm thick film of $Sr_5Ti_4O_{13}/GdScO_3(110)(n = 4)$ from sample set $GdScO_3$ #1. The temperatures (T) measured are 300 K (cyan), and 220 K (Critical Temperature (T_c)) (dark yellow).

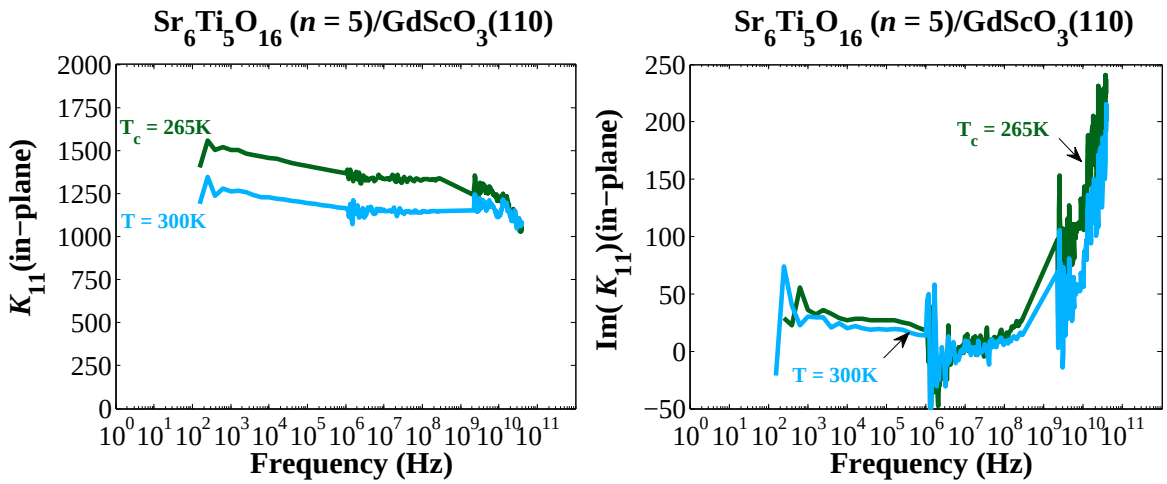

(a) K_{11}(in-plane) (b) Im(K_{11})(in-plane)

Figure 4.33: Frequency Dependence of Complex K_{11}(in-plane) $Sr_6Ti_5O_{16}/GdScO_3(110)(n = 5)$ at Variable Temperature

(a) The frequency dependence of the real part of the in-plane relative permittivity (K_{11}(in-plane)) from 100 Hz to 40 GHz at variable temperature for 25 nm thick film of $Sr_6Ti_5O_{16}/GdScO_3(110)(n = 5)$ from sample set $GdScO_3$ #1. The temperatures (T) measured are 300 K (cyan), and 265 K (Critical Temperature (T_c)) (dark green). (b) The frequency dependence of the imaginary part of the in-plane relative permittivity (Im(K_{11})(in-plane)) from 100 Hz to 40 GHz at variable temperature for 25 nm thick film of $Sr_6Ti_5O_{16}/GdScO_3(110)(n = 5)$ from sample set $GdScO_3$ #1. The temperatures (T) measured are 300 K (cyan), and 265 K (Critical Temperature (T_c)) (dark green).

4.6.3 Dependence on Series Number

We have shown empirically in the previous sections that complex K_{11} is dependent on temperature, electric field, frequency, strain and series number. Reducing the dimensionality of the data by taking a slice at a given n, temperature, frequency, or electric field is dangerous, because we can misconstrue the dependence on a given variable. At the conclusions of each section, we have attempted to encapsulate some of the important information in a single figure or a set of figures to illustrate a crucial point. The dependence on series number is not be overlooked. When we consider the crystal structure of this RP series as we increase n the materials limit to $SrTiO_3$. One

would intuitively expect that if n had any effect on the electrodynamics of the system that the behavior would approach the characteristics of $SrTiO_3$ as n was increased. Clearly, we have shown that this behavior is convoluted by the different transition temperatures of the different series numbers. It is ,therefore, necessary to compare the behavior at T_c as function of n as opposed to an arbitrary temperature that is not scaled relative to T_c.

Earlier we cautioned that dependence on n should always be thought of in context as relative to the T_c. Fortunately, for the films on $DyScO_3(110)$ we have three sets of films all measured at 300 K. we used these measurements to understand the variability between the different samples sets. In Sec. 4.4, we compared the different sample sets on the same substrate at low frequencies. Local defects could also affect the high frequency response, hence it is necessary to see if the high frequency measurements of K_{11} for different series numbers are also consistent between sample sets. In Fig. 4.34, we show a comparison between K_{11} versus series number for $Sr_{n+1}Ti_nO_{3n+1}/DyScO_3(110)(n = 2 - 6)$ for the three different groups $DyScO_3$ #1 (squares), $DyScO_3$ #2 (triangles), and $DyScO_3$ #3 (circles). The vertical grey lines are the estimates of the uncertainty in K_{11}. We show two different frequencies 1 MHz (Fig. 4.34(a)) and 10 GHz (Fig. 4.34(b)). It is clear from Fig. 4.34 that the K_{11} values were consistent between samples sets and at different frequencies. At T_c, we can explore the limiting behavior of K_{11} as n is increased at selected fixed frequencies.

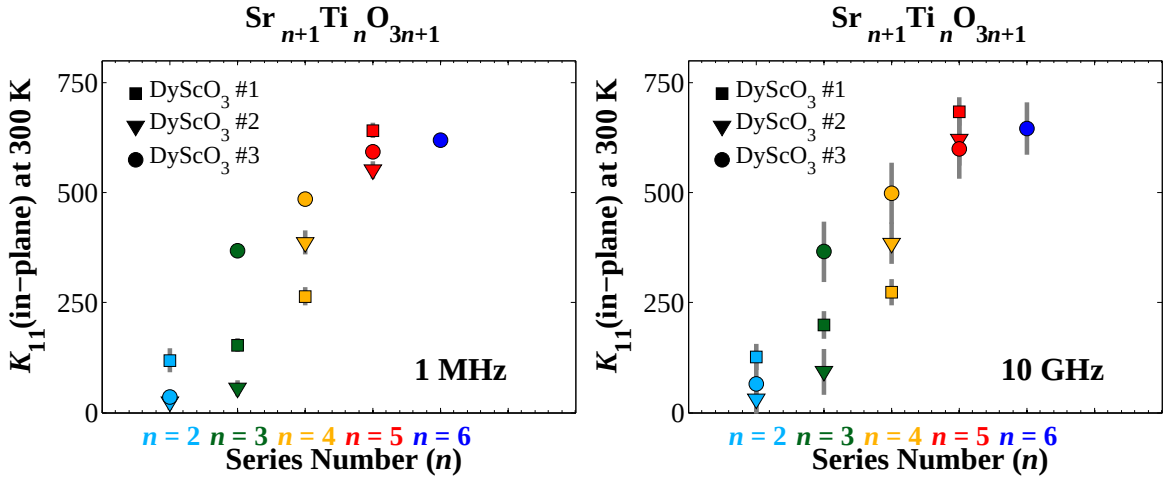

(a) K_{11}(in-plane) at 300 K and 1 MHz (b) K_{11}(in-plane) at 300 K and 10 GHz

Figure 4.34: A Comparison at 300 K of $DyScO_3$ #1, $DyScO_3$ #2, and $DyScO_3$ #3, of Frequency Dependence of K_{11}(in-plane) $Sr_{n+1}Ti_nO_{3n+1}/DyScO_3(110)(n = 3, 4, 5, 6)$ at 1 MHz and 10 GHz

We show a comparison of the real part of the in-plane relative permittivity (K_{11}(in-plane)) at 300 K for three sets of $Sr_{n+1}Ti_nO_{3n+1}/DyScO_3(110)$ (n = 2, 3, 4, 5, 6) samples at 1 MHz and 10 GHz. The sample sets shown are $DyScO_3$ #1 (squares), $DyScO_3$ #2 (triangles), and $DyScO_3$ #3 (circles). The measured series numbers (n) include $n = 2$ (cyan), $n = 3$ (dark green), $n = 4$ (dark yellow), $n = 5$ (red), and $n = 6$ (blue). The grey lines are error bars.

We show the dependence of $K_{11}(T_c)$ at 1 MHz in Fig. 4.35(a) and at 10 GHz in Fig. 4.35(b) versus series number ($n = 3, 4, 5, 6$) for the sample sets $DyScO_3$ #3 (circles), and $GdScO_3$ #1 (stars). The grey vertical lines are the estimated uncertainty in K_{11}, which are roughly the size of the points in Fig. 4.35(a). Figure 4.35 seems to show that K_{11} at T_c is weakly dependent on n, which is consistent with the low frequency measurements results. This is surprising for the reasons that will be discussed in context of the Lyddane-Sachs-Teller (LST) relation [79]. One possible explanation is that it may be necessary to cool the samples under applied dc electric field in order to provide the necessary energy to align all of the polar nanoregions and clarify the dependence of K_{11} on n at T_c [6]. For our measurement setup, it was not possible to apply a dc electric field as we simultaneously changed the temperature of samples.

This technique is referred to as field cooling. Our samples were zero-field cooled, which means that the polar nanoregions were randomly oriented as the sample was brought through T_c. Field cooling has been shown to sharpen the temperature dependence of K_{11} for strained $SrTiO_3/DyScO_3(110)$ [77].

Another possible explanation is that K_{11} is non-linearly dependent n at T_c. In this case, for a specific n greater than $n = 6$, K_{11} at T_c dramatically increases as n approaches $n = \infty$. At this point, it is unclear which of these explanations is in fact the correct answer. Referring back to Fig. 4.12, if the trend continued between $n = 6$ and $n = \infty$, then one might naively suppose that for $n > 6$ the T_c would behave like an increasing asymptotic function towards the T_c of $n = \infty$. Given that there is only 60 K that separate $n = 6$ and $n = \infty$, this would imply that the soft mode frequencies would be close together for $\infty > n > 6$. The soft mode frequency can be directly related to K_{11} by the LST relation [79]. We can use the LST relation to write K_{11} as function that is linearly proportional to the square of the soft mode frequency. If all of the other terms are approximately equal, then this would seem to suggest that the maximum value of K_{11} would also behave like an increasing asymptotic function towards the K_{11} of $n = \infty$. Further studies, like terahertz spectroscopy [47] or field cooled capacitance measurements [77], would be needed to clarify this issue.

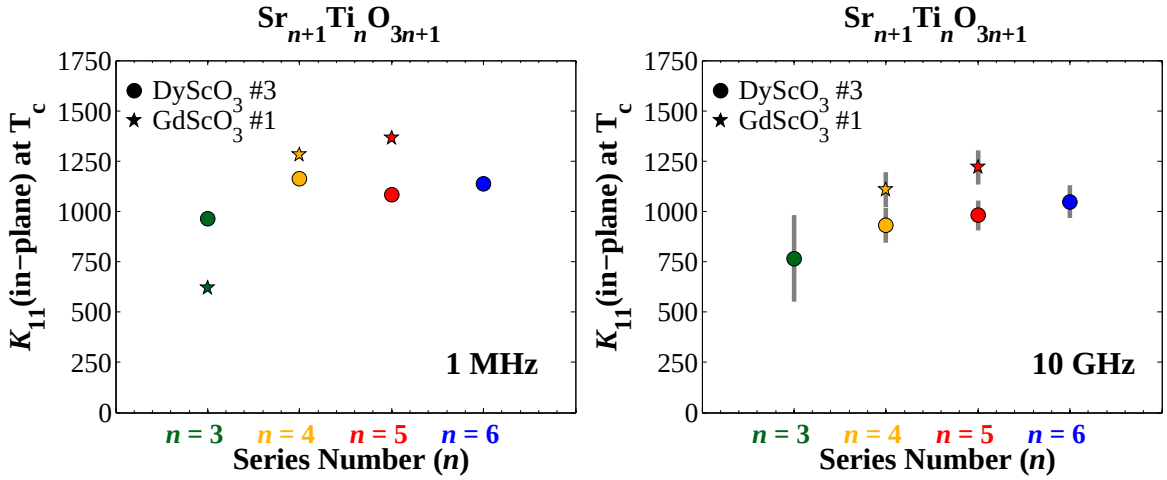

(a) K_{11}(in-plane) at T_c and 1 MHz

(b) K_{11}(in-plane) at T_c and 10 GHz

Figure 4.35: A Comparison at T_c of $DyScO_3$ #3, $GdScO_3$ #1, of Frequency Dependence of K_{11}(in-plane) $Sr_{n+1}Ti_nO_{3n+1}/DyScO_3(110)(n = 3, 4, 5, 6)$ at 1 MHz and 10 GHz

We show a comparison of the real part of the in-plane relative permittivity (K_{11}(in-plane)) at T_c for a sample set of $Sr_{n+1}Ti_nO_{3n+1}/DyScO_3(110)$ ($n = 3, 4, 5, 6$) and a sample set $Sr_{n+1}Ti_nO_{3n+1}/GdScO_3(110)$ ($n = 3, 4, 5$) at 1 MHz and 10 GHz. The sample sets shown are $DyScO_3$ #3 (circles), and $GdScO_3$ #1 (stars). The measured series numbers (n) include $n = 3$ (dark green), $n = 4$ (dark yellow), $n = 5$ (red), and $n = 6$ (blue). The grey lines are error bars.

4.7 High Frequency Electric Field Dependence & Figure of Merit

Another very interesting attribute that stands out in the previous sections is that these materials show very low loss over almost the entire frequency range of the measurements. As we discussed in Ch. 1, there are many important applications for electric-field-tunable dielectrics. If a material does in fact show low loss and high electric field tunability at high frequencies, then it could clarify our understanding of the origins of loss in other dielectrics as well.

We characterized the high frequency electric field tunability by again performing the high frequency characterization technique on the CPW structures as described in Sec. 2.5. We first corrected the HF vector network analyzer with the coaxial calibra-

tion standards, and verified the accuracy of the calibration with a set of zero-delay length symmetric short circuit reflect standards. In this measurement configuration, high frequency (4 GHz to 18 GHz) high voltage bias tees were affixed externally to the stainless steel semi-rigid coaxial cables that were routed into the cryogenic probe station through compression seals. The bias tees were connected to a voltage source that allowed us to apply a bias voltage between the center conductor and the ground planes of the CPWs. At zero applied field, we performed a series of measurements on the $LaAlO_3$ calibration wafer to correct the on-wafer S-parameter measurements to the end of the g-s-g probe tips and remove most of the frequency dependent effects of the bias tees. We then measured the CPW devices on the $LaAlO_3$ calibration wafer at the maximum applied voltage (V_{max} = 100 kV/cm) to confirm that under an applied field the propagation constant of the calibration wafer was identical to the measurement at zero-field. This demonstrated that the S-parameter correction was not electric field dependent for a known substrate.

Accurate broadband high frequency tunability measurements are very time consuming, hence we were only able to perform the measurements at zero applied field and V_{max}, which was limited by our bias tees. For each CPW on each test wafer, we measured the S-parameters of a CPW at zero field. In the same contact, we then applied the maximum field, V_{max}, and made an additional measurement of the S-parameters of a CPW. After measuring each CPW on a given test wafer, we measured the planar 0.210 mm offset symmetric short circuit reflect standard (labeled S1 in Fig. 2.10) at zero applied field. We cannot apply a field and measure S1, because the planar reflect standard connects the center conductor to the ground plane. This does not affect the propagation constant extracted from the multiline thru-reflect-line technique, but it does contribute to an error in the error boxes.

Before we show the tunability of the thin film and the measured loss tangent, it is useful to show that we obtained consistent results between the measurement frequency

domains. In Fig. 4.36, we show K_{11} at 300 K of the $Sr_{n+1}Ti_nO_{3n+1}/DyScO_3(110)$ for the series numbers $n = 2$, 3, 4, 5, and 6, which are represented by the cyan, dark green, dark yellow, and red solid lines, respectively. Comparing Fig. 4.36 to Fig. 4.24, we see that K_{11} is consistent between the two measurements conducted months apart over different frequency ranges. The slight discrepancy is in $n = 6$. For this sample, we had to repeat the set of measurements, and had ,therefore, already poled the sample, which caused a slight decrease in K_{11} relative to the measurements shown in Fig. 4.24. After we extracted K_{11} at zero field and at 100 kV/cm, we calculated the tunability from

$$\%\text{Tuning} = 100 \times \left(1 - \frac{K_{11}(\text{V}_{max})}{K_{11}(0)}\right). \tag{4.2}$$

This is differs from Eq. 4.1, and it is possible that this may have increased our calculation of the %Tuning (for $n \neq 6$). We have omitted $n = 2$ from Fig. 4.37, because it is close to zero. We can qualitatively check the results from Fig. 4.37 by comparing them to the measurements in Fig. 4.17. One should note that these measurements are at different bias voltages, which was a limitation of the bias tees. We note that $n = 5$ does not show as much tunability when compared to the 1 MHz measurement. Aside from this inconsistency, the tunability of K_{11} for the other series numbers was qualitatively similar to their low frequency counterparts.

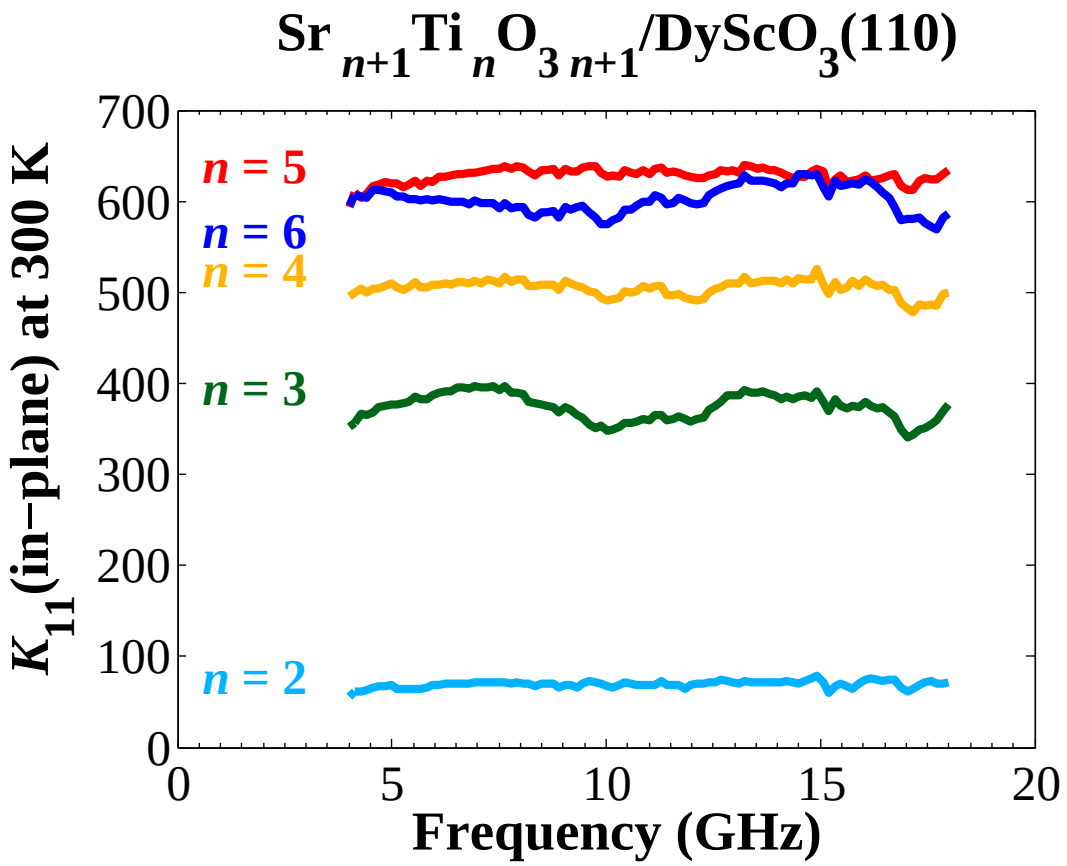

Figure 4.36: 4GHz to 18 GHz, Frequency Dependence of K_{11}(in-plane) $Sr_{n+1}Ti_nO_{3n+1}/DyScO_3(110)(n = 2, 3, 4, 5, 6)$ at 300 K

At 300 K, we show the frequency dependence of the real part of the in-plane relative permittivity (K_{11}(in-plane)) from 4 Hz to 18 GHz for 50 nm thick films of $Sr_{n+1}Ti_nO_{3n+1}/DyScO_3(110)(n = 2, 3, 4, 5, 6)$ from sample set $DyScO_3$ #3. The series number (n) measured are $n = 2$ (cyan), $n = 3$ (dark green), $n = 4$ (dark yellow), $n = 5$ (red), and $n = 6$ (blue).

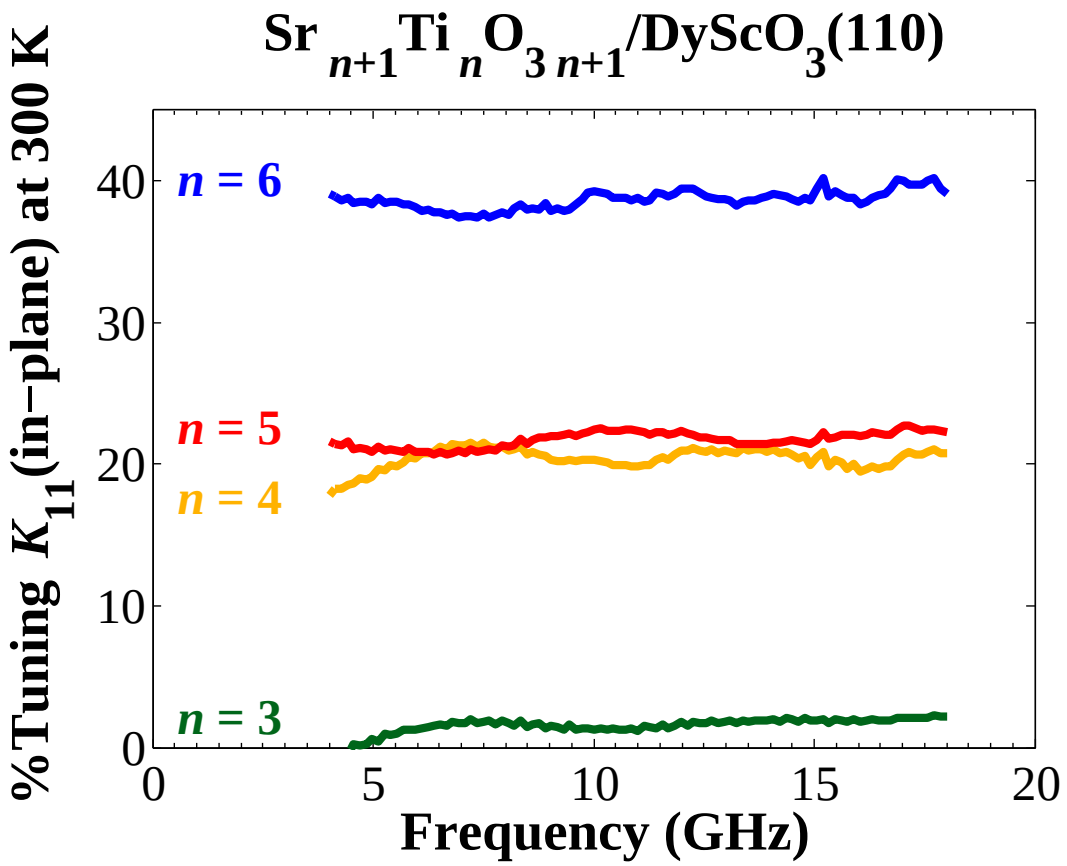

Figure 4.37: 4GHz to 18 GHz, Frequency Dependence of %Tuning K_{11}(in-plane) $Sr_{n+1}Ti_nO_{3n+1}/DyScO_3(110)(n = 2, 3, 4, 5, 6)$ at 300 K

At 300 K, we show the frequency dependence of the percent tuning of the real part of the in-plane relative permittivity (%Tuning K_{11}(in-plane)) from 4 GHz to 18 GHz for 50 nm thick films of $Sr_{n+1}Ti_nO_{3n+1}/DyScO_3(110)(n = 3, 4, 5, 6)$ from sample set $DyScO_3$ #3. The series number (n) measured are $n = 3$ (dark green), $n = 4$ (dark yellow), $n = 5$ (red), and $n = 6$ (blue).

We also used these measurements to obtain the high frequency in-plane loss tangent ($\tan(\delta_{11})$) as a function of frequency, which is shown in Fig. 4.38. In Fig. 4.38, the series numbers shown are $n = 3$ (dark green), $n = 4$ (dark yellow), $n = 5$ (red), and $n = 6$ (blue). The grey thick line in the background is the approximate uncertainty in $\tan(\delta_{11})$ for the $n = 6$ (blue) as described in Sec. 2. The measured loss tangents are very small and around the sensitivity limits of the measurement over a significant portion of the frequency range from 5 GHz to 15 GHz (Fig. 4.38(a)). The down-turn

below 5 GHz, as well as the sharp up-turn just above 15 GHz, was most likely due to the bias tees. This was because bias tees was limited to operate in the 4 GHz to 18 GHz frequency band. The small undulations around 10 GHz could be due to frequency dependent errors in the calibration. The gradual increase as a function of frequency may in fact be due to intrinsic effects, like coupling to the soft-mode phonon [2], or possibly a decrease in the measurement resolution due to a decreased signal-to-noise ratio of the S-parameters at high frequency. In the band around 6 GHz to 7 GHz (Fig. 4.38(b)), the uncertainty in the percent tuning as well as the uncertainty in the loss tangents are a minimum. We estimated the figure of merit in these regions, but given the measurement uncertainty it is difficult to accurately place an upper bound on the figure of merit.

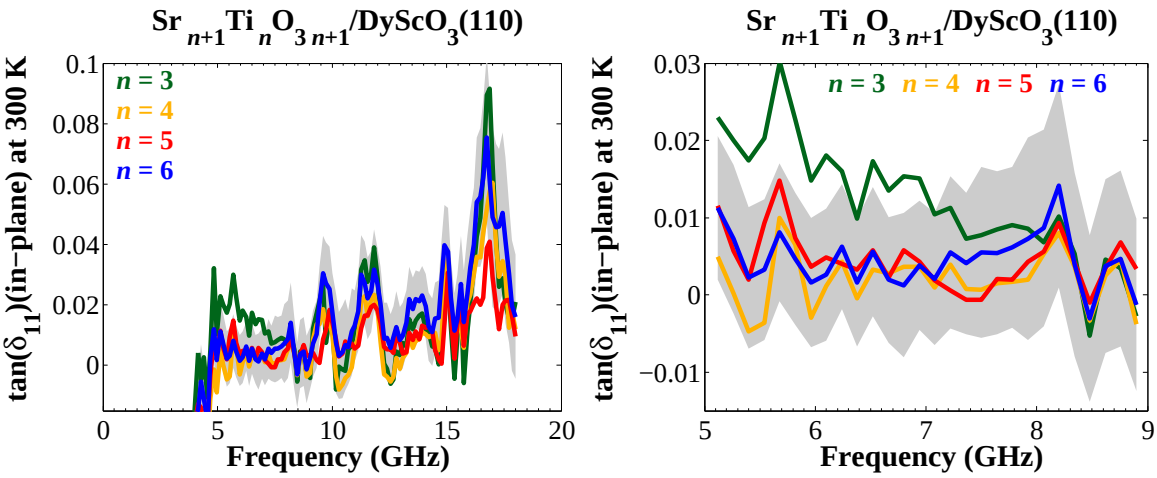

(a) 4 GHz to 18 GHz

(b) 5 GHz to 9 GHz

Figure 4.38: 4GHz to 18 GHz, Frequency Dependence of $\tan(\delta_{11})$(in-plane) $Sr_{n+1}Ti_nO_{3n+1}/DyScO_3(110)(n = 3, 4, 5, 6)$ at 300 K

(a) At 300 K, we show the frequency dependence of the in-plane loss tangent ($\tan(\delta_{11})$(in-plane)) from 4 GHz to 18 GHz for 50 nm thick films of $Sr_{n+1}Ti_nO_{3n+1}/DyScO_3(110)(n = 3, 4, 5, 6)$ from sample set $DyScO_3$ #3. The series number (n) measured are $n = 3$ (dark green), $n = 4$ (dark yellow), $n = 5$ (red), and $n = 6$ (blue). The grey line is the uncertainty in the in-plane loss tangent. (b) We show of the in-plane loss tangent a close up from 5 GHz to 9 GHz.

	$n=3$	$n=4$	$n=5$	$n=6$
min FOM	1	50	40	60
median FOM	1	60	50	140
max FOM	2	190	90	300
lower bound FOM	1	40	30	60

Table 4.1: 6 GHz to 7 GHz, Figure of Merit $Sr_{n+1}Ti_nO_{3n+1}/DyScO_3(110)(n = 3, 4, 5, 6)$ at 300 K

There are several ways to calculate a figure of merit for electric field tunable dielectrics. We prefer one that encapsulates information about the loss at zero field and the maximum tunability of the film. For this reason, we have used the following figure of merit,

$$\begin{aligned} \textbf{Figure of Merit (FOM)} &= \left(1 - \frac{K_{11}(\mathrm{V}_{max})}{K_{11}(0)}\right) \frac{1}{\tan(\delta_{11}(0))} \\ &= \frac{\%\text{Tuning}}{100} \cdot \mathrm{Q}_{11}(0), \end{aligned} \tag{4.3}$$

where the in-plane quality factor at zero applied field is $\mathrm{Q}_{11}(0) = (\tan(\delta_{11}(0)))^{-1}$, and the percent tuning was given in Eq. 4.2[1]. We calculated the figure of merit as a function of series number for the frequencies between 6 GHz and 7 GHz, and then took the median as to not weight any outliers unfairly. In Fig. 4.39, we show the figure of merit for $n = 3$ (dark green), $n = 4$ (dark yellow), $n = 5$ (red), and $n = 6$ (blue). The grey lines are not error bars for reasons that are discussed in App. A.12, but are rather the minimum and maximum figure of merit calculated in this range. The values for the figure of merit are presented in Table 4.1, where aside from $n = 3$ we have rounded the figures of merit to the nearest decade.

[1]The definition of figure of merit depends on the applied electric field bias.

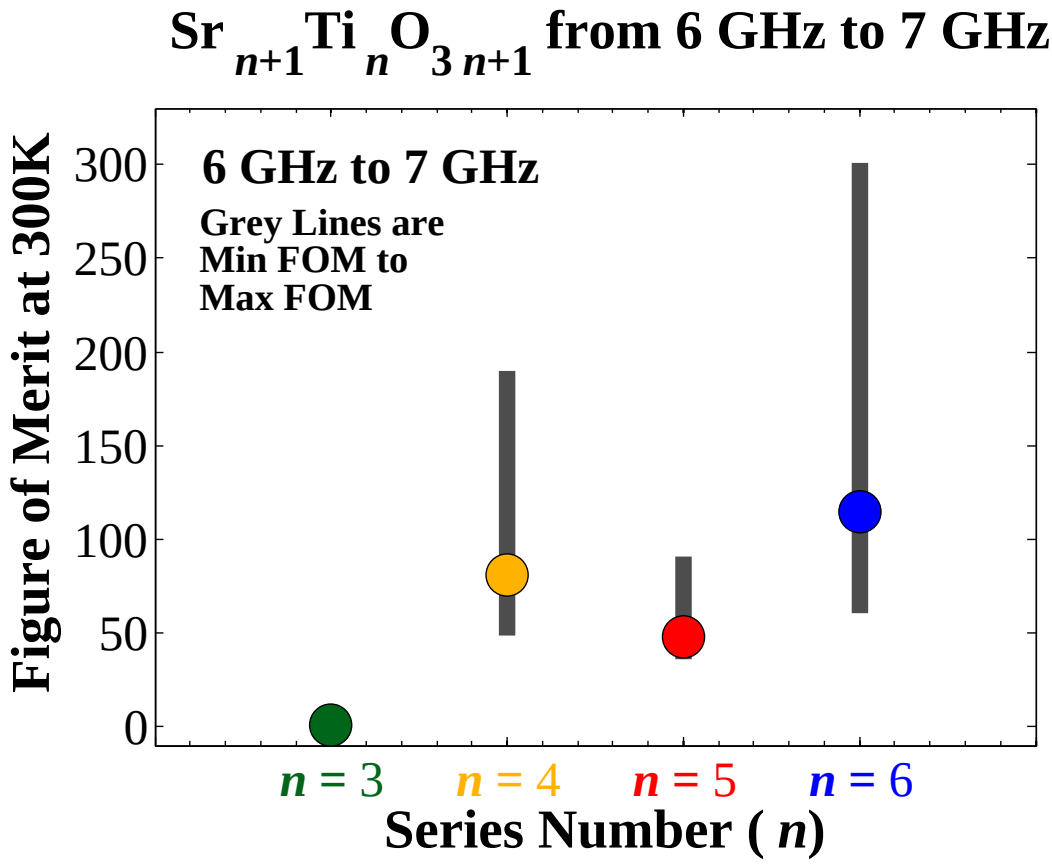

Figure 4.39: 6 GHz to 7 GHz, Figure of Merit $Sr_{n+1}Ti_nO_{3n+1}/DyScO_3(110)(n = 3, 4, 5, 6)$ at 300 K

At 300 K, we show the figure of merit (FOM) taken as a median from 6 GHz to 7 GHz for 50 nm thick films of $Sr_{n+1}Ti_nO_{3n+1}/DyScO_3(110)(n = 3, 4, 5, 6)$ from sample set $DyScO_3$ #1. The series number (n) measured are $n = 3$ (dark green), $n = 4$ (dark yellow), $n = 5$ (red), and $n = 6$ (blue). The solid grey lines are the minimum and maximum value of the figure of merit in this frequency range. The median values for the figure of merit are 1, 60, 50, 140 for $n = 3$, 4, 5, and 6, respectively. The minimum values for the figure of merit are 1, 50, 30, 60 for $n = 3$, 4, 5, and 6, respectively. The maximum values for the figure of merit are 2, 190, 90, 300 for $n = 3$, 4, 5, and 6, respectively.

The median figures of merit in Fig. 4.39 correspond to loss tangents that range from $\tan(\delta_{11}) = 0.003$ (FOM($n = 3$) = 40) to $\tan(\delta_{11}) = 0.004$ (FOM($n = 5$) = 50). For $n = 6$, the loss tangent in the range from 6 GHz to 7 GHz was $\tan(\delta_{11}) = 0.003 \pm 0.003$, which would put an absolute lower bound of FOM = 60 on the figure of merit. As we discussed in Sec. 2.4.3, the uncertainty in the loss tangent is an overestimate

of the actual error. While we believe that we have improved the resolution of the loss tangent with the approach discussed in Sec. 2.5, future experiments comparing known loss tangents obtained from other techniques, such as split cylinder resonators [19], would be necessary to quantify the accuracy and limitations of this technique. Regardless of their actual value, the figures of merit for these materials are remarkably high, and are perhaps among the highest ever reported in the regime between 6 GHz and 7 GHz.

4.8 Summary

It is clear that through strain we have dramatically changed the the dielectric response of the $Sr_{n+1}Ti_nO_{3n+1}$ Ruddlesden-Popper series. The unstrained $Sr_{n+1}Ti_nO_{3n+1}$ Ruddlesden-Popper series on LSAT(001) showed frequency dependence and temperature dependence that was consistent with an incipient ferroelectric [4]. The temperature dependence of these materials, on both $DyScO_3$(110) (tensile strain, 1%) and $GdScO_3$(110) (tensile strain, 1.7%), systematically increases with increasing series number. The same series numbers grown on $GdScO_3$(110) were found to have transition temperatures by approximately 60 K higher than those on $DyScO_3$(110). By straining these films, we have increased the real part of the relative permittivity for most of the films by nearly an order of magnitude at the transition temperature. All of sets of strained $Sr_{n+1}Ti_nO_{3n+1}$ Ruddlesden-Popper series measured in these experiments showed significantly greater electric field tunability when compared to their unstrained counterparts in Ref. [4]. Despite the presence of a high permittivity, high electric field tunability, and transition temperatures that in some cases were close to room temperature, the materials exhibited little to no dispersion above the transition temperature. Below the transition temperatures, the materials showed power-law like dispersion, which has been seen in several relaxor ferroelectrics [5]. These materials share many characteristics with relaxor ferroelectrics, yet their losses have remained

near the threshold of the measurement well into the gigahertz frequency regime. This is in direct contrast with strained $SrTiO_3/DyScO_3(110)$, which had significant losses even well above the transition temperature at 300 K [1]. We found that several of these materials have figures of merit at least greater than 30 between 6 GHz to 7 GHz, which is remarkably high. For 50 nm thick $Sr_7Ti_6O_{19}$ ($n = 6$), the loss tangent in the range from 6 GHz to 7 GHz was 0.003 ± 0.003 and it had a figure of merit of 140 with an absolute lower bound of 60, which is quite possibly one of the highest figure of merit ever reported in this frequency range.

Chapter 5

Conclusions

In summary, we have developed an accurate on-wafer technique to characterize the quantitative in-plane complex relative permittivity of thin films and substrates from 100 Hz to 40 GHz, which is nearly nine decades in frequency. We have applied this approach to the $Sr_{n+1}Ti_nO_{3n+1}$ Ruddlesden-Popper series for thin films grown by molecular beam epitaxy [15, 53] as a function of series number (n). The films studied were approximately 160 nm to 170 nm thick on (001) $(LaAlO_3)_{0.3}-(SrAl_{0.5}Ta_{0.5}O_3)_{0.7}$ (LSAT), 50 nm thick on $DyScO_3$(110), and 25 nm thick on $GdScO_3$(110), which respectively correspond to a nominally relaxed film, a tensile strain of 1%, and tensile strain of 1.7%. We characterized the behavior of all of the films as a function of temperature, electric field, and frequency.

Despite the successful characterization of the $Sr_{n+1}Ti_nO_{3n+1}$ Ruddlesden-Popper series thin films that have also pushed the measurement procedure to the current limits of our technique, a considerable amount of work remains. Perhaps the most conspicuous remaining challenge is the development of theory to explain why these materials exhibit the properties that we presented in Ch. 4. In the last section of this dissertation, we present a logical line of reasoning to explain some of the phenomena that we reported in the previous sections. We also introduce a plausible model that may be used to understand the frequency dependence at variable temperature. Finally, we conclude by discussing a set of experiments that could be used to verify some elements of the model. We note that we use the symbols ϵ and K for the relative permittivity almost interchangeably in the following section.

5.1 A Possible Explanation of Dielectric Behavior of the $Sr_{n+1}Ti_nO_{3n+1}$ Ruddlesden-Popper Series

Throughout the previous chapter we hinted that these materials show characteristics that could be consistent with a relaxor ferroelectric. As we discussed in Ch. 1, frequency dependence carries with it important information that can be used to understand the fundamental electrodynamics of a thin-film material system. In Refs. [2, 75], it was shown that a modified Cole-Cole equation could be used to fit the high frequency complex permittivity of $Ba_{1-x}Sr_xTiO_3$. In Ref. [25, 74], it was shown that the frequency dependence could be used to understand the electrodynamics of the distribution of relaxation times as a function of temperature for bismuth zinc niobate pyrochlore dielectric thin films. The following argument combines these two ideas: a distribution of domains and a relaxation that could be interpreted as due to the soft-mode phonon.

What is the soft-mode phonon behavior? In Ref. [79], Lyddane *et al.* wrote an expression for the static permittivity for a cubic lattice as the product of the phonon modes,

$$\frac{\epsilon_s}{\epsilon_\infty} = \prod_j^N \frac{(\omega_{LOj})^2}{(\omega_{TOj})^2}. \tag{5.1}$$

Despite the approximations and crystal structure assumed in the derivation, Eq. 5.1 has been found to be a very good approximate description for many material systems. For not so obvious reasons, the lowest order transverse optical phonon has the strongest temperature dependence [79]. The lowest order transverse optical phonon is commonly referred to as the soft-mode phonon (ω_{TO1}), because it decreases in frequency as the crystal lattice 'softens' [6]. In a proper ferroelectric, as the temperature approaches the T_c, a different crystal structure becomes energetically more favorable, hence the atoms in the crystal distort to form a different structure; this corresponds

to a phase transition [6]. In an improper ferroelectric, or relaxor ferroelectric, the behavior is much more complicated. Although the crystal lattice still softens around T_c, the crystal does not go through a structural phase transition [6]. Typically, in a relaxor ferroelectrics T_c is interpreted as the temperature where the correlation length between polar nanoregions diverge [6]. As we discussed to a limited extent in Ch. 4, when the temperature decreases to T_c polar entities in the crystal lattice interact locally to form polar nanoregions [6]. This causes an increase in the permittivity as temperature decreases to T_c. For both a proper and relaxor ferroelectric, the soft-mode phonon moves up in frequency as the crystal lattice hardens when the temperature continues to decrease below T_c, which in turn causes the permittivity to decrease. From Eq. 5.1, we can understand that some of the temperature dependence of ϵ_s could be due to the temperature dependence of ω_{TO1}.

If we approximate the other terms as a constant, then we can rewrite ϵ_s as inversely proportional to ω_{TO1}^2,

$$\epsilon_s \approx \frac{c \cdot \epsilon_\infty}{\omega_{TO1}^2}, \tag{5.2}$$

where the temperature independent phonons are lumped into the constant c. Qualitatively, we can approximate the behavior of ω_{TO1} around T_c like a quadratic function with a minimum at T_c. In the absence of any polar domains or more complicated phenomena, the real part of the complex permittivity of any material that is treated in this way will have a peak in the permittivity at T_c due to the temperature-dependent behavior of the soft-mode phonon. Moreover, if there were an asymmetry in the quadratic-like temperature dependence of the soft-mode phonon, then that would also give rise to an asymmetry in the temperature dependence of real part of the permittivity. This could easily explain the peak and asymmetry in the permittivity as a function of temperature as seen in Sec. 4.4, but it does not capture the frequency dispersion as a function of temperature.

For soft-mode driven dispersion, the permittivity will remain constant (See Fig. 1.2) until the measurement frequency approaches the soft-mode phonon frequency. This would result in a Debye-like relaxation process that occurs at the relaxation time of the soft-mode phonon, $\tau_{TO1}(= \omega_{TO1}^{-1})$. The down turn at high frequency in the real part of the relative in-plane permittivity (and the corresponding up turn in the imaginary part) in Sec. 4.6 could be directly related to this behavior. If all the polar entities in the thin film have the same dipole moments and do not interact, then the frequency dependence can be described by the Cole-Cole equation,

$$\tilde{\epsilon}_{ph}(\omega) = \epsilon_\infty + \frac{\Delta\epsilon_1}{1 - (i\omega\tau_1)^{\beta_1}}. \tag{5.3}$$

We have modified the Cole-Cole equation from Ch. 1 to include a polar increment $\Delta\epsilon_1$ and a relaxation time τ_1 that could be related to soft-mode phonon. We have also included β_1, which describes a Gaussian distribution of relaxation times around τ_1. As in Ch. 1, ϵ_∞ is the high frequency limit of the permittivity function. For most thin films this relaxation process only occurs in the terahertz, which begs a number of questions: What is responsible for the relaxation mechanisms below T_c and why does it vanish above T_c?

Thus far we have presented some plausible explanations for the high frequency behavior of complex permittivity and the peak in the real part of the permittivity at T_c, but there are several other observations that can be made from the results presented in Ch. 4. Unfortunately, there are a variety of models for frequency-dependent dispersion of relaxor ferroelectrics. Perhaps, the most intuitive way to set up the problem is to point out some key observations.

Behavior of K_{11}	
Behavior of K_{11} Below T_c	
(1)	$\mathrm{Re}(K_{11})$ decreases with increasing frequency like a power law at low frequency.
(2)	$\mathrm{Im}(K_{11})$ is constant as a function of frequency at low frequency.
(3)	$\mathrm{Re}(K_{11})$ gradually increases temperature increases.
(4)	The dispersion in $\mathrm{Re}(K_{11})$ increases as temperature increases to approach T_c.
(5)	Tunability of $\mathrm{Re}(K_{11})$ with applied dc electric field increases as temperature approaches T_c.
Behavior of K_{11} Around T_c	
(6)	$\mathrm{Re}(K_{11})$ shows the strongest dispersion.
(7)	Hysteresis in $\mathrm{Re}(K_{11})$ with applied dc electric field is present.
Behavior of K_{11} Above T_c	
(8)	$\mathrm{Re}(K_{11})$ shows negligible (if any) dispersion as function of frequency.
(9)	$\mathrm{Re}(K_{11})$ sharply decreases as temperature increases.
(10)	Hysteresis in $\mathrm{Re}(K_{11})$ with applied dc electric field is present, but tunability is decreased.
(11)	$\mathrm{Re}(K_{11})$ shows negligible dispersion as function of frequency with applied dc field.

Below T_c, most of these behaviors are consistent with a relaxor ferroelectric [6]. In these systems, we stated that the peak in the permittivity was interpreted as a consequence of polar nanoregions. These polar nanoregions could be responsible for (1) through (6). In Ref. [6], it was observed that for many relaxor ferroelectrics the polar nanoregions act cooperatively to increase the permittivity to a value larger than the static permittivity that can be obtained from the LST relation (Eq. 5.2).

Although in principle the different relaxation mechanisms could be related, this would suggest two contributions to the permittivity function

$$\tilde{\epsilon}(\omega) = \tilde{\epsilon}_{ph}(\omega) + \tilde{\epsilon}_{PNR}(\omega). \tag{5.4}$$

The first term in Eq. 5.4, $\tilde{\epsilon}_{ph}(\omega)$, was discussed earlier. We now address the second term in Eq. 5.4, $\tilde{\epsilon}_{PNR}(\omega)$. The polar nanoregions in a relaxor ferroelectric randomly form in the crystal lattice with a distribution of sizes [5, 6]. This has also been seen in disordered dielectrics like bismuth zinc niobate pyrochlore [25, 74]. From Ref. [5], we know that if all of the polar nanoregions have equally strong dipole moments, then $\tilde{\epsilon}_{PNR}(\omega)$ can be thought of as an infinite number of Debye relaxors with a uniform distribution of relaxations between a lower bound relaxation time τ_b and an upper bound relaxation time τ_a ,

$$\tilde{\epsilon}_{PNR}(\omega) = \frac{\Delta\epsilon_2}{\ln(\frac{\tau_b}{\tau_a})} \int_{\tau_b}^{\tau_a} \frac{1}{1 - i\omega\tau} d(\ln \tau). \tag{5.5}$$

As in Ref. [5], we can evaluate Eq. 5.5 to find,

$$\tilde{\epsilon}_{PNR}(\omega) = \frac{\Delta\epsilon_2}{\ln(\frac{\tau_b}{\tau_a})} \left[\frac{1}{2} \cdot \ln\left(\frac{\tau_b^{-2} + \omega^2}{\tau_a^{-2} + \omega^2} \right) - i \cdot \left(\arctan\left(\frac{\tau_b^{-1}}{\omega} \right) - \arctan\left(\frac{\tau_a^{-1}}{\omega} \right) \right) \right]. \tag{5.6}$$

Both τ_b and τ_a could be related to an intrinsic lower and upper bound size of the polar nanoregions, respectively.

While it is certainly not obvious from the form of Eq. 5.6, the result is a frequency dependence that is similar to that seen in Sec. 4.6. As in Refs. [25, 74], typically the value of τ_b is so small that the $\arctan\left(\frac{\tau_b^{-1}}{\omega}\right) \Rightarrow 0$ and τ_a is so large that $\arctan\left(\frac{\tau_b^{-1}}{\omega}\right) \Rightarrow \frac{\pi}{2}$. The real part of the permittivity as a function of logarithmic frequency of Eq. 5.6 essentially reduces to a linearly decreasing function between

the lower bound relaxation time τ_b and the upper bound relaxation time τ_a. Above τ_a (low frequency), all of the polar nanoregions contribute to the permittivity and $\tilde{\epsilon}_{PNR}(\omega)$ limits to a static real permittivity. Below τ_b (high frequency), none of the polar nanoregions contribute to the permittivity and $\tilde{\epsilon}_{PNR}(\omega)$ limits to zero. Here, we have neglected the ϵ_∞ term as it is already included in the $\tilde{\epsilon}_{ph}(\omega)$ part of the permittivity function. In summary, we have two components to the permittivity function: the first accounts for the sharp high-frequency dispersion that is more evident near T_c (Eq. 5.4), and the second accounts for the power-law dispersion in the permittivity below T_c (Eq. 5.6).

This second term could also contribute to the temperature dependence of the complex permittivity below T_c. As the correlation length between polar nanoregion diverges as the temperature is decreased to T_c, one might naively expect that when the polar nanoregions first nucleate they occur with the smallest distribution of sizes (or τ_b is at its closest to τ_a). This would lead to the sharpest frequency dependence at T_c and significant hysteresis, as each polar nanoregion could be individually poled by the dc applied electric field. Observation (5) is also consistent with a relaxor ferroelectric, which exhibit thin hysteresis loops (or permittivity versus dc applied electric field) [6]. This tunability in permittivity also decreases with decreasing temperature as the crystal hardens [6].

Polarization measurements with applied ac current under a dc electric field could be used to measure the remnant polarization as a function of temperature [77]. These measurements would determine if remnant polarization remains above T_c, which is another signature of a relaxor ferroelectric. We could confirm this behavior with temperature-dependent optical second harmonic generation measurements on the films [80]. A detailed review explaining temperature-dependent optical second harmonic generation measurements can be found in Ref. [**?**]. Moreover, we could directly measure the temperature dependence of the soft-mode phonon frequency with trans-

mission terahertz spectroscopy to understand the high frequency behavior and the phase transition [47]. In fact, all of these measurements are currently underway, but there are still many challenges to performing these measurement that are in large part due to the thickness of the film. For many types of measurements the thickness of the film plays a dominant role in determining the order of magnitude of the perturbation on a given measurement parameter relative to the substrate. Although we did not dwell on it, even the very robust dielectric measurements were very challenging; we often measured changes in capacitance on the order of ten femtofarads. Efforts to resolve the properties of the films by several of our collaborators are ongoing.

Following the previous arguments, it is clear that these polar nanoregions are a crucial part of our model of this thin-film system. While it would be very useful to directly perform scanning probe dielectric measurements to confirm the size of the regions on a local scale, these measurements have their own set of challenges. In Ch. 3, we reported the out-of-plane permittivity components for the unstrained films as calculated by density functional theory [4, 41]. Along these same lines, it is believed that the materials presented in Ch. 4 do not show significant enhancement of the out-of-plane permittivity with increased strain. Intuitively, as the crystal is stretched by biaxial tensile strain the dipole moment in the out-of-plane direction actually decreases because the lattice decreases in that dimension. Although additional calculations would need to be done to estimate the out-of-plane permittivity for the strained films, we believe that the largest component of the permittivity tensor is in-plane. We remind the reader that the capacitive gap of the CPW and IDC devices is 400 times the thickness of the 50 nm thick films, and extensive finite element simulations support the claim that were are predominantly sensitive to the in-plane component of the permittivity tensor for these devices.

All of these factors imply that any scanning probe technique (See for example Ref. [81]) would need to be able to distinguish the in-plane component from the out-of-

plane component in order to resolve the polar nanoregions. Furthermore, in order to determine the distribution of domains accurately the measurements would need to be perform as a function of temperature and over a scanning area that is large relative to polar nanoregions, yet still retain a high enough resolution to measure individual polar nanoregions. These conditions will present a formidable task to direct measurement of polar nanoregions in the $Sr_{n+1}Ti_nO_{3n+1}$ Ruddlesden-Popper series thin films and these measurements will also be difficult given the thickness of the films. Another complication is that at this point these materials cannot be grown on a conducting substrate to improve the field confinement of the scanning probe techniques, like scanning evanescent microwave microscopy [61, 82]. Regardless, recent developments in evanescent scanning probe microscopy may meet the challenges presented by this material system and may provide a direct means to confirm the model for the polar nanoregions [83]. Up to this point, if we were only describing the behavior at T_c and below T_c, we could make a compelling case that these materials are relaxor ferroelectrics. The savvy reader will immediately recognize that we have completely avoided discussing the behavior above T_c.

Despite all of the rigorous measurements and extensive data analysis, we have yet to formulate a definitive explanation about why these materials lack dispersion above T_c. The hysteresis in the real part of the permittivity as a function of dc applied field is consistent with a relaxor ferroelectric, but the lack of dispersion almost immediately above T_c and under an applied field and at high frequencies is not consistent with reports on $Ba_{1-x}Sr_xTiO_3$[2, 75]. One hypothesis is that the long range order of the polar nanoregions is abruptly disrupted at T_c, perhaps by an interaction or lack thereof with the interstitial SrO rocksalt layers. These interstitial rocksalt layers may also have a 'gettering effect', where they absorb or give out oxygen atoms to sites inside the crystal. Reducing the lattice defects in the perovskite layers could lead to a sharpening of the soft-mode phonon, which can be modeled in Eq. 5.4 by increasing

β toward one. A dramatic decrease in the correlation length, however, would also rapidly decrease the permittivity (because the interaction between polar nanoregions would vanish). This would also correspond to decreased tunability and the absence of hysteresis in the permittivity with dc applied field, which clearly conflicts with (10). Even though a rapidly decreasing correlation length seems convincing, it is not clear that it is entirely consistent with our observations. Another possible explanation is that above T_c all the polar nanoregions essentially collapse to the smallest possible size (consistent with no dispersion) and these nanoregions behave like completely independent dipoles (prevents long range order), which can be individually poled by an electric field (provides hysteresis above T_c).

5.2 Summary

From our work on the $Sr_{n+1}Ti_nO_{3n+1}$ Ruddlesden-Popper series, it is also clear that layering can be used to grow materials that could potentially be used to push applications higher in frequency and thereby decrease size, power consumption, and cost of some electric-field-tunable dielectric components. Although the entirety of this dissertation has focused on $Sr_{n+1}Ti_nO_{3n+1}$ Ruddlesden-Popper series thin films, we have applied this approach to a variety of other material systems. Measurements of the broadband dielectric spectroscopy of bismuth zinc niobate pyrochlore thin films showed the effects of uniform distribution of relaxation times for a material that was not a ferroelectric [25]. We also applied this technique to microfluidic measurements of nanoliter volumes of fluids, including a demonstration on a known reference fluid [36], bovine serum albumin and insulin, and varying concentrations of inorganic nanoparticles. In addition to these thin-film systems, we used this technique for the accurate broadband measurements of other thin-film systems, which enabled us to accurately model self-heating effects, nonlinear ferroelectric response, and other source of non-linearity as shown in Refs. [23, 24, 59, 84–87]. The in-plane dielectric

characterization technique is based on a compact on-wafer calibration procedure [34] that provided a means to perform calibrations over a wide range of frequencies (30 kHz to 40 GHz), and has been shown to be stable down to very low temperatures (20 K) while occupying a very small area on the calibration wafer. The in-plane dielectric characterization technique developed in this dissertation is ideal for studying new films that cannot be grown on a bottom electrode and for direct measurement of the broadband dielectric response of materials like magneto-electrics, nanostructured thin films and materials, and in the future could be applied to magnetic thin films.

Appendix A

Supplemental Information, Figures and Derivations

A.1 Instrument Settings

- The LF LCR meter (100 Hz - 1 MHz) is set to measure a capacitance and loss tangent (MEAS SETUP > FUNC > Cp,D). The averages are set to 4 (MEAS SETUP > AVG > 4), the integration times is set to long (MEAS SETUP > INT > LONG), and the frequency is set to 1 MHz (MEAS SETUP>FREQ>1 MHz). The correction type is set for a series short and series open: (MEAS SETUP > CORRECTION > SHORT > ON) and (MEAS SETUP > CORRECTION > OPEN > ON).

- The RF vector network analyzer (30 kHz - 6 GHz) is set to measure corrected S-parameters. The IF bandwidth is 30 Hz, power is -10 dBm, number of points is 201, frequency type is LOG.

- The HF vector network analyzer (45 MHz - 40 GHz) is set to measure corrected S-parameters. The IF bandwidth is set 15 Hz, power is -10 dBm, number of points is 401, frequency type is LOG, sweep type is stepped, and dwell time is 2 μs.

A.2 S-parameters, Y-parameters, T-parameters

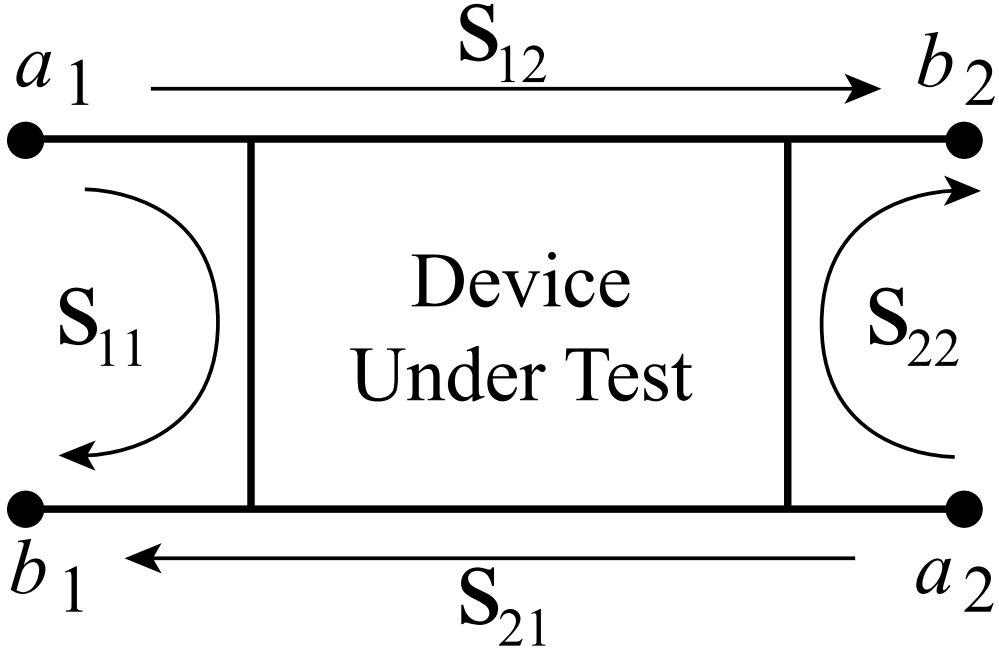

Figure A.1: What are S-Parameters?

Scattering parameters (S-parameters) are complex power ratios of a signal. For transmission from Port 2 to Port 1 (S_{21}), the S-parameter is the ratio of the power received (b_2) to the power sourced (a_1). For transmission from Port 1 to Port 2 (S_{12}), the S-parameter is the ratio of the power received (b_1) to the power sourced (a_2). For reflection from Port 1 to Port 1 (S_{11}), the S-parameter is the ratio of the power received (b_1) to the power sourced (a_1). For reflection from Port 2 to Port 2 (S_{22}), the S-parameter is the ratio of the power received (b_2) to the power sourced (a_2).

Definition of S-parameters from power ratios.

$$S = \begin{pmatrix} \frac{b_1}{a_1} & \frac{b_2}{a_1} \\ \frac{b_1}{a_2} & \frac{b_2}{a_2} \end{pmatrix} \tag{A.1}$$

Conversion S-parameters to Y-parameters.

$$
\begin{aligned}
Y &= \left(\frac{1}{Z_r}\right)\frac{1}{((1+S_{11})(1+S_{22})-S_{12}S_{21})}\cdot \\
&\begin{pmatrix} (1-S_{11})(1+S_{22})+S_{12}S_{21} & -2S_{12} \\ -2S_{12} & (1+S_{11})(1-S_{22})+S_{12}S_{21} \end{pmatrix}
\end{aligned}
$$

Conversion S-parameters to T-Parameters.

$$
T = \frac{1}{S_{21}}\begin{pmatrix} -\det(S) & S_{11} \\ -S_{22} & 1 \end{pmatrix} \tag{A.2}
$$

A.3 Error Propagation for Coplanar Waveguides

In Sec. 2.4.3, we commented that the error in the fit made was negligible, in what follows it will become evident that this is true for our measurements. For our mathematical convenience, we will redefine the propagation constant as

$$
\begin{aligned}
\gamma &= \sqrt{(R+i\omega L)}\sqrt{(G+i\omega C)} \\
&= \sqrt{A}\sqrt{B},
\end{aligned}
$$

where $A = R + i\omega L$ and $B = G + i\omega C$. We can obtain the uncertainty in B,

$$
(\Delta B_r)^2 = 4\cdot\left(\Re\left(\frac{\gamma}{A}\right)\right)^2(\Delta\gamma_r)^2 + \left(\Re\left(\frac{\gamma}{A}\right)\right)^4(\Delta A_r)^2 \tag{A.3}
$$

$$
(\Delta B_i)^2 = 4\cdot\left(\Im\left(\frac{\gamma}{A}\right)\right)^2(\Delta\gamma_i)^2 + \left(\Im\left(\frac{\gamma}{A}\right)\right)^4(\Delta A_i)^2 \tag{A.4}
$$

$$
\Delta B = \Delta B_r + i\cdot\Delta B_i. \tag{A.5}
$$

We have decomposed the uncertainty in B into the uncertainty in the real part (Eq. A.3) and the uncertainty in the imaginary part (Eq. A.4). Renaming the variables, although slightly confusing, significantly decreases the complexity of the math.

In practice, we would like to simplify Eqs. A.3 and A.4 to contain only information we know. We can do this by calculating the order of magnitude for the different components and neglecting the smallest terms. We can easily calculate the coefficient $(\frac{\gamma}{A})^2$,

$$\left(\frac{\gamma}{A}\right)^2 = \frac{(R+i\omega L)(G+i\omega C)}{(R+i\omega L)^2} = \frac{(G+i\omega C)}{(R+i\omega L)} = Z^{-2}. \tag{A.6}$$

Empirically, we can calculate Z^{-2} to find that it is always less than 1, and its order of magnitude is always less than 10^{-3}. This is not surprising. At low frequencies, $Z^{-2} \Rightarrow \frac{G}{R}$ and G for these material is small and close to zero and R is finite. In this regime, Z^{-2} has an order of magnitude no less than 10^{-3}. At high frequencies, $Z^{-2} \Rightarrow \frac{C}{L}$, which has an order of magnitude no less than of 10^{-3}. This is true for both the real and imaginary parts. In Eqs. A.3 and A.4 , the terms proportional to $(\Delta A)^2$ are multiplied by Z^{-4}, which is of an order of magnitude 10^{-6}. We can not immediately eliminate the terms proportional to $(\Delta A)^2$, because we do not know the order of magnitude $(\Delta A)^2$.

We can estimate the order of magnitude of $(\Delta A)^2$ in the following way by evaluating the partial derivatives for the real and the imaginary parts,

$$(\Delta A)^2 = (\Delta R)^2 + i \cdot (\omega^2.(\Delta L)^2). \tag{A.7}$$

Again, empirically, we know that the order of magnitude for the uncertainty in the resistance, ΔR, is approximately 10, and the order of magnitude for the uncertainty in the inductance, ΔL, is at most 10^{-10}. Our highest measurement frequency is approximately 10^{11}, evaluating Eq. A.7 at the frequency limits reveals that it is

always of the order of magnitude around 10^2. Therefore, the terms proportional to $(\Delta A)^2$ are of the order of magnitude 10^{-8}. Now, we only need to obtain an order of magnitude for $(\Delta\gamma)^2$ and we can determine if any of the other terms are negligible.

We can calculate $(\Delta\gamma)^2$ using the results from StatistiCAL, the calibration software used to extract the propagation constant, and Eq. 2.13. We find that the order of magnitude of $(\Delta\gamma)^2$ is approximately 1 for both the real and imaginary parts, hence, we find that Eqs. A.3 and A.4 reduce to,

$$(\Delta B_r)^2 \approx 4 \cdot \left(\Re\left(\frac{\gamma}{A}\right)\right)^2 (\Delta\gamma_r)^2 \tag{A.8}$$

$$(\Delta B_i)^2 \approx 4 \cdot \left(\Im\left(\frac{\gamma}{A}\right)\right)^2 (\Delta\gamma_i)^2. \tag{A.9}$$

A.4 Lift-Off-Resist Lithography and Deposition Process

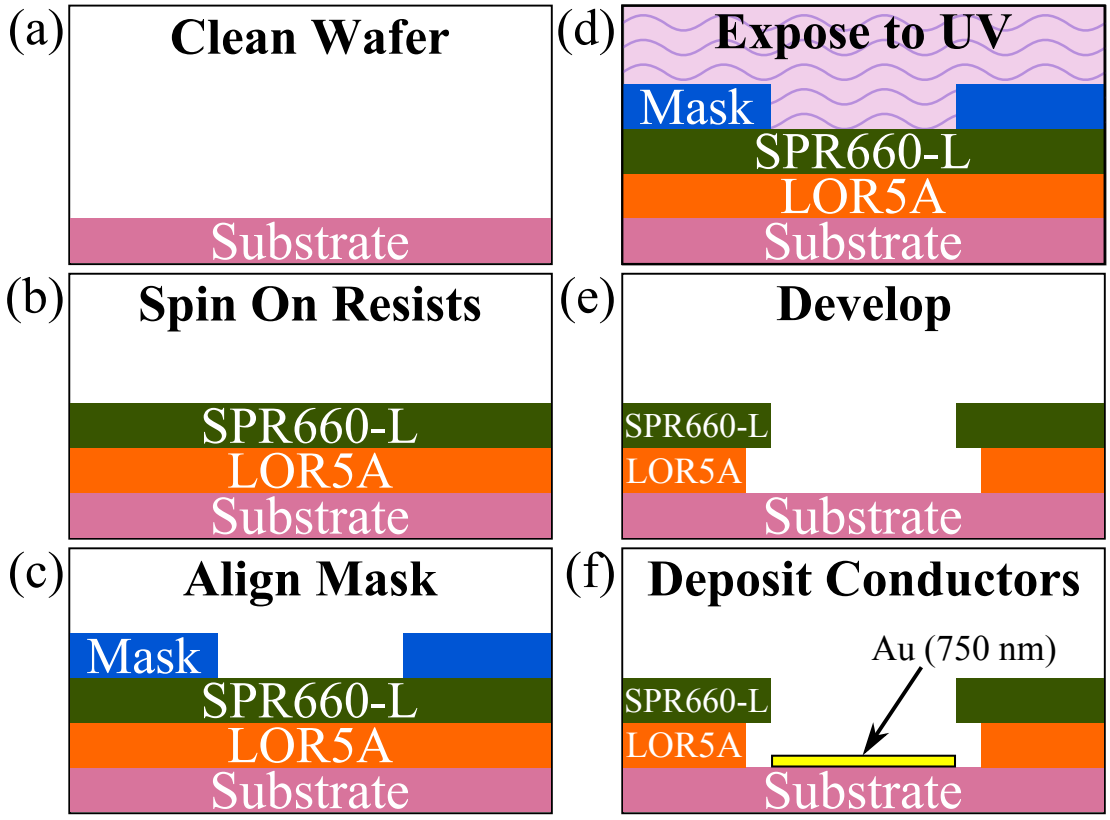

Figure A.2: Lift-Off-Resist Lithography

We show a graphical representation of the lift-off-resist lithography process. (a) We show a substrate (light red) that has been cleaned with acetone, and isopropanol. (b) The wafer is dehydration baked at 150°C for 2 minutes, and allowed to cool. We spin on LOR5A lift-off-resist onto the wafers, such that the resist is three times the thickness of the metallic deposition layer. The wafer is baked at 150°C for 5 minutes and allowed to cool. SPR660-L imaging resist is spun onto the substrate. The wafer is baked at 90°C for 1 minute and allowed to cool. (c) The substrate is aligned to a mask. In this illustration, we have shown a contact aligner mask; however, we also commonly use projection masks that do not come in contact with the photoresist. (d) The photoresist and mask are exposed to ultraviolet radiation. The wafer is post exposure baked at 110°C for 1 minute and allowed to cool. (e) We develop the photoresist in a base (MF-701) for 1 minute, and then rinse in deionized water for 30 seconds. We blow dry nitrogen onto the wafer to get rid of the water and then bake the substrate for 10 seconds to be certain that no water is left on the substrate. (f) The substrate is loaded into an automated electron-beam vapor deposition chamber that deposits specific conductors to a desired thickness.

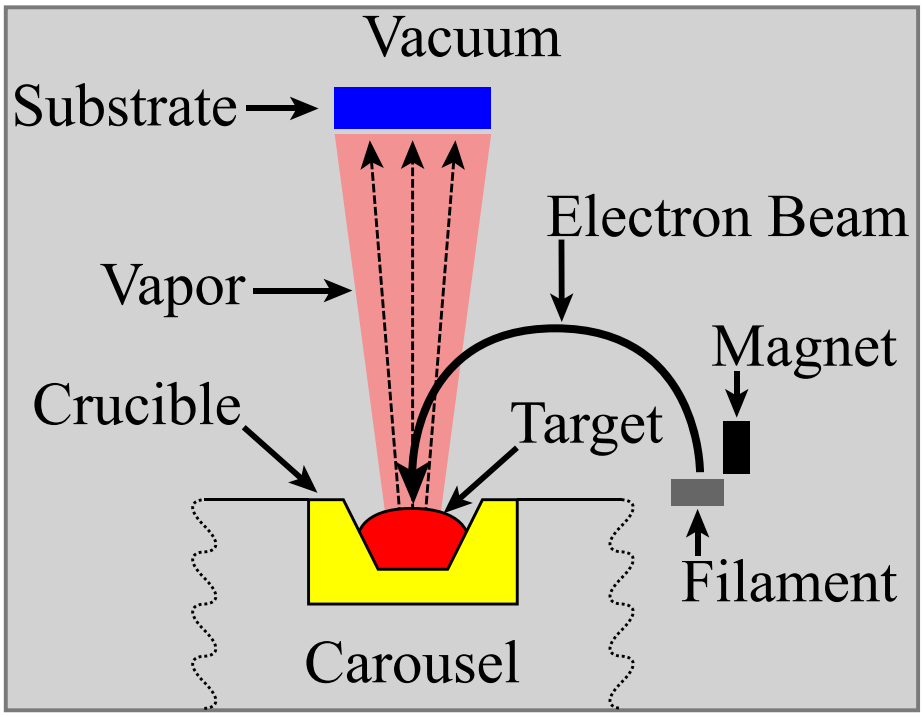

Figure A.3: Electron-Beam Vapor Deposition System

We show a simple schematic of a electron-beam vapor deposition system. The substrate (blue) was mounted to a rotating water-cooled chuck. A beam of electrons coming off a filament hits a crucible where a target metal sits. The metal is heated until it produces a vapor at a known deposition rate, which is measured with sensors inside the chamber.

A.5 Characteristic Impedance from an Error Box

The T-matrix model for the error box given in Ref. [32] has the form,

$$X = \frac{1}{\sqrt{1-\Gamma^2}}\left[\begin{pmatrix} 1 & \Gamma \\ \Gamma & 1 \end{pmatrix} + (1+\Gamma)\left(\frac{Y \cdot Z_r}{2}\right)\begin{pmatrix} -1 & -1 \\ 1 & 1 \end{pmatrix}\right], \tag{A.10}$$

where Z_r is the reference impedance, Y is the pad admittance (or the admittance under the g-s-g probe), and

$$\Gamma = \frac{Z - Z_r}{Z + Z_r}. \tag{A.11}$$

In Eq. A.11, the characteristic impedance of the CPW is denoted by Z. If we take the average of the off-diagonal components of X, we find,

$$\begin{aligned} \beta &= \frac{1}{2}(X_{12} + X_{21}) \\ &= \frac{\Gamma}{\sqrt{1 - \Gamma^2}}. \end{aligned} \tag{A.12}$$

Note that in Eq. A.12 the terms proportional to Y completely cancel. We can solve Eq. A.11 for Z,

$$Z = Z_r \left(\frac{1 + \Gamma}{1 - \Gamma} \right). \tag{A.13}$$

Then we can solve Eq. A.12 for Γ ,

$$\Gamma = \frac{\sqrt{\beta}}{\sqrt{1 - \beta}} \tag{A.14}$$

Inserting Eq. A.14 into Eq. A.13, we arrive at

$$Z = \frac{(X_{12} + X_{21})}{\sqrt{4 - (X_{12} + X_{21})^2}}. \tag{A.15}$$

A.6 Uncertainty in Permittivity

Over a small enough range, Eq. 2.20 can effectively be approximated as a line,

$$K_{film} = m \cdot C_{film} + K_{sub}, \tag{A.16}$$

where K_{film} is the real part of the in-plane relative permittivity of the thin film, K_{sub} is the real part of the in-plane relative permittivity of the substrate, and m is the slope of the linear approximation to the mapping function for the thin film. The uncertainty in K_{film} is then given by,

$$(\Delta K_{film})^2 = m^2 \cdot (\Delta C_{film})^2 + (C_{film})^2 (\Delta m)^2, \tag{A.17}$$

	m^2	$(\Delta m)^2$	$(C_{film})^2$	$(\Delta C_{film})^2$
Order of Magnitude	10^{13}	10^{11}	10^{-11}	10^{-12}

Table A.1: Order of Magnitude for K_{11} Uncertainty Analysis

where Δm is the uncertainty in the slope. As in App. A.3, we can again look at the order of magnitude for the different components in Eq. A.17.

Inserting the values from the Table A.1 in Eq. A.17, we find that $(C_{film})^2(\Delta m)^2$ is an order of magnitude smaller than $m^2 \cdot (\Delta C_{film})^2$ and would result in a correction less than 5%. We choose to neglect this term to obtain,

$$(\Delta K_{film})^2 \approx m^2 \cdot (\Delta C_{film})^2. \tag{A.18}$$

In practice, we have found that adding this term is typically a 1% correction to the error.

A.7 X-ray 2θ Diffraction of Unstrained $Sr_{n+1}Ti_nO_{3n+1}(n = 1, 2, 3)$ on LSAT(100)

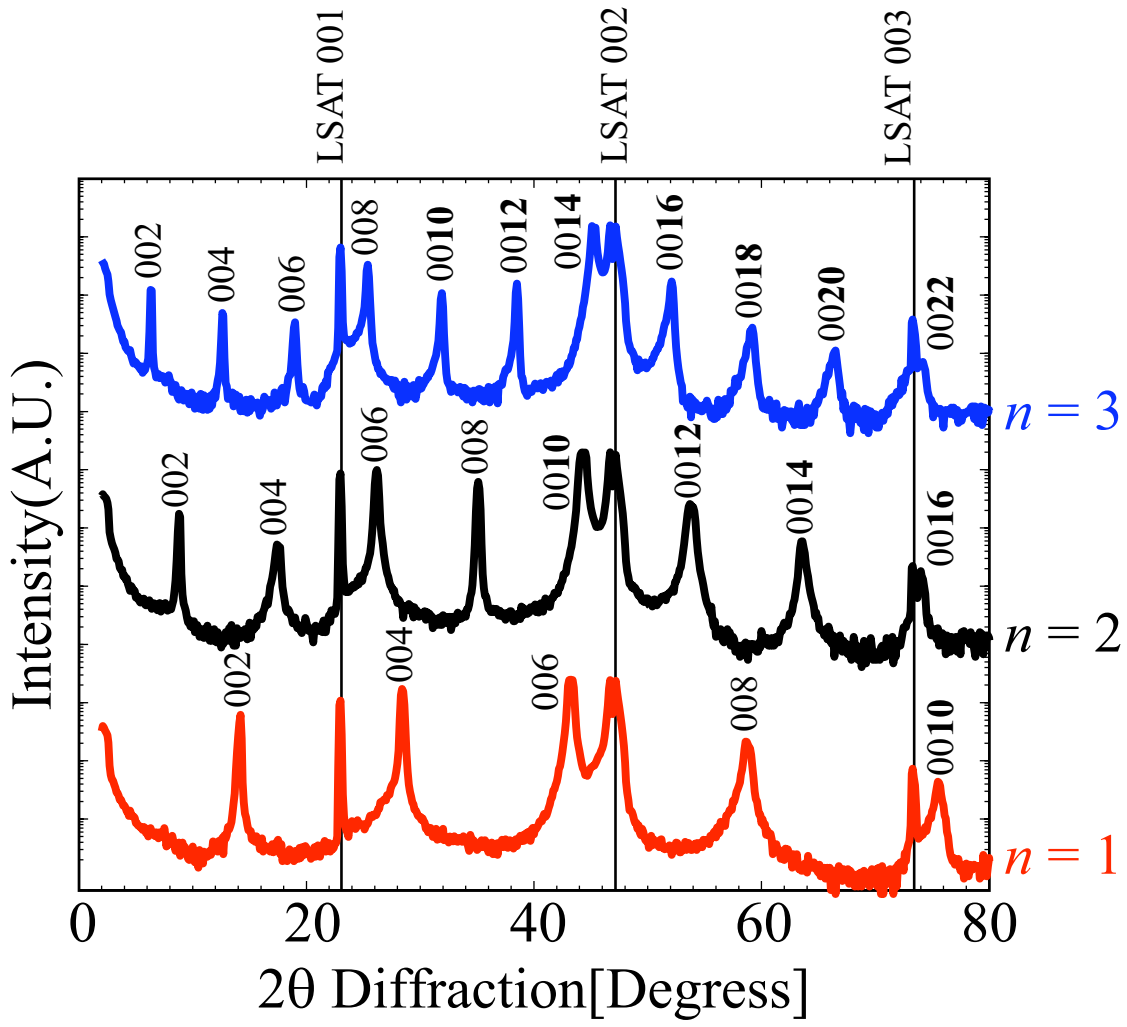

Figure A.4: X-ray 2θ Diffraction of Unstrained $Sr_{n+1}Ti_nO_{3n+1}(n = 1, 2, 3)$ on (001)LSAT

We show the X-ray 2θ diffraction of nominally unstrained $Sr_{n+1}Ti_nO_{3n+1}(n = 1, 2, 3)$ on (001)LSAT. The red, black, and blue solid lines are for the $n = 1$, 2, and 3, respectively. The substrate peaks are indicated at approximately $2\theta \approx 23°(001)$, $46°(002)$, and $69(003)$.

A.8 Supplemental Figure for Crystal Synthesis

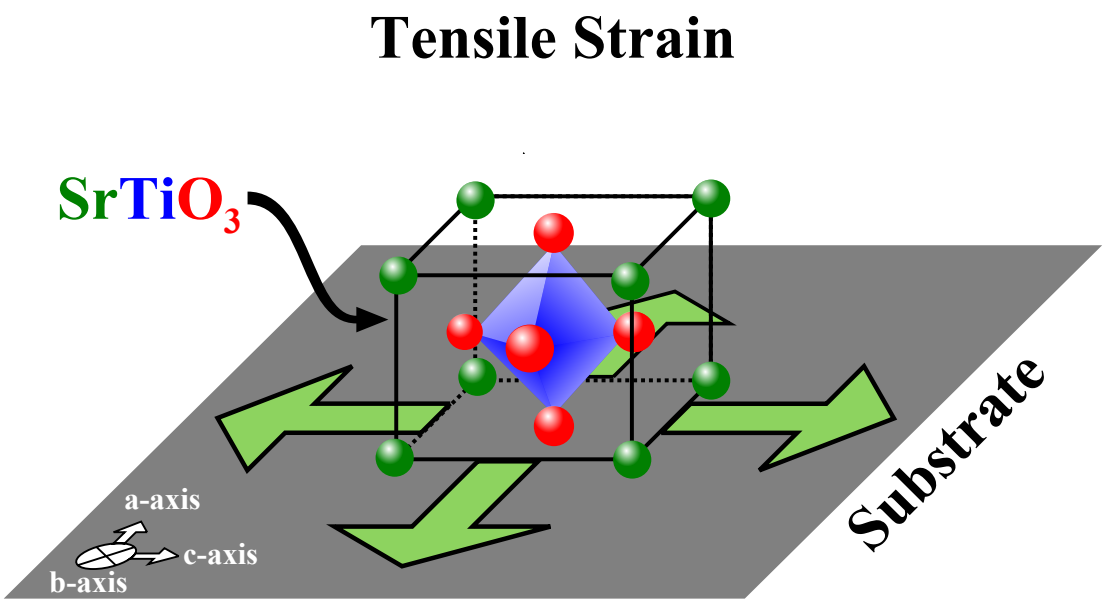

Figure A.5: Explanation of Biaxial In-plane Tensile Strain

Tensile strain was achieved by growing the thin films on a substrate (grey) with an in-plane lattice constant of the substrate that was larger than the in-plane lattice constant of the thin film. The strontium (Sr) atoms are shown as the green spheres, and the oxygen (O) atoms are shown as the red spheres. The Ti atom sits in the center of six oxygen atoms arranged at the points of the blue octahedron. Here, we show a $SrTiO_3(n = \infty)$ crystal on a substrate. The green arrows indicate the direction of the strain, which is in-plane. This type of strain is commonly called biaxial in-plane tensile strain.

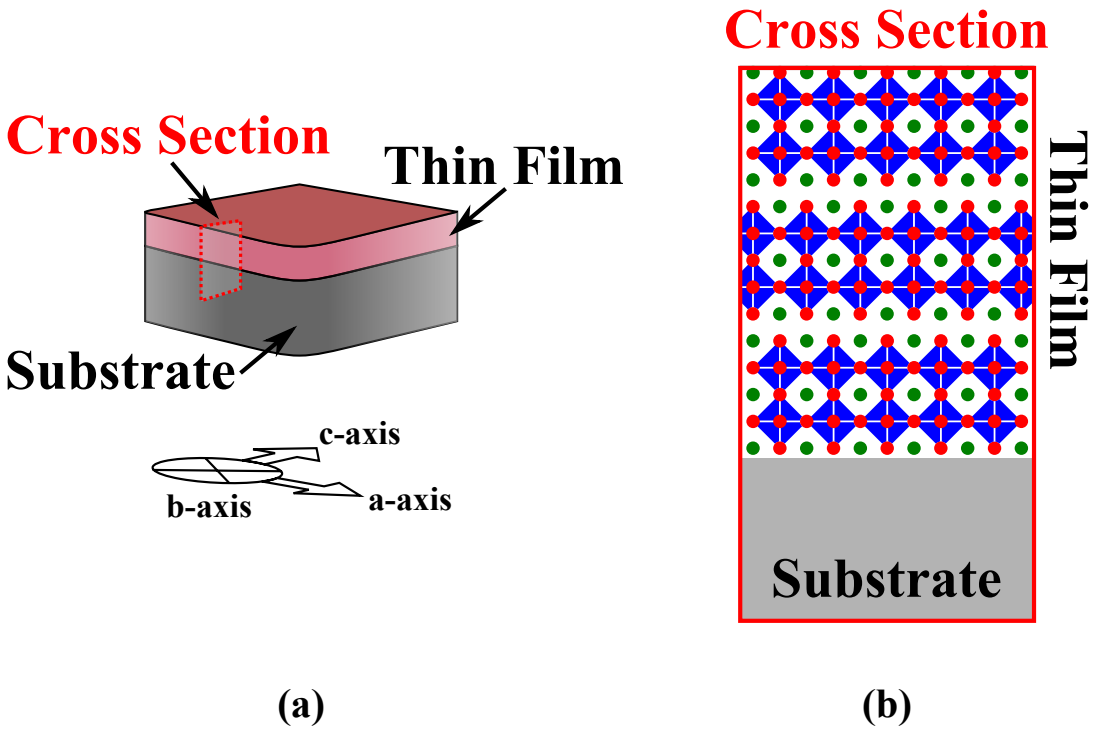

Figure A.6: Diagram of a Thin-Film on a Substrate

(a) We show a thin film (light red) on a substrate (grey). The b-axis is pointed down, and the film is oriented in the c-a plane. The region over which the cross section (b) is shown as the red dashed line. (b) We show the cross section of a thin film ($Sr_3Ti_2O_7(n = 2)$) on a substrate (grey).

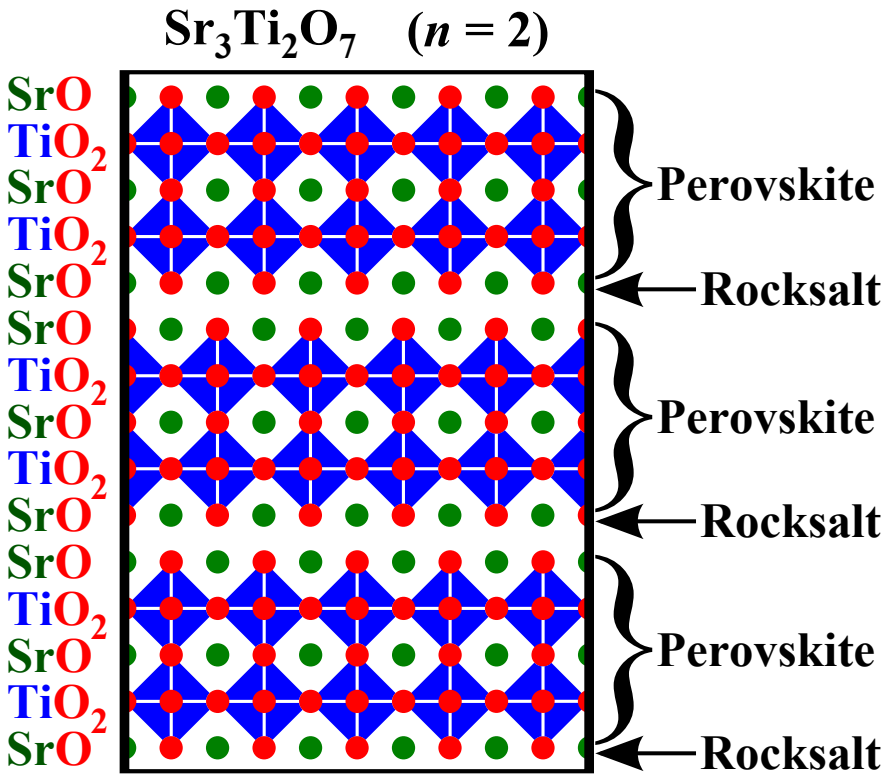

Figure A.7: Using Layering to Create a $Sr_{n+1}Ti_nO_{3n+1}(n = 2)$ Phases

A close-up of $Sr_3Ti_2O_7(n = 2)$ Ruddlesden-Popper phase. The strontium (Sr) atoms are shown as the green spheres, and the oxygen (O) atoms are shown as the red spheres. The Ti atom sits in the center of six oxygen atoms arranged at the points of the blue octahedra. On the right, we show an interpretation of the crystal structure, which can be thought of $n = 2$ perovskite layers terminated by a SrO rocksalt layer. The series number (n) indicates the number of perovskite layers, which is spaced by a rocksalt layer every n. The rocksalt causes the lattice to offset horizontally by half the in-plane lattice constant, and the structure repeats the perovskite-rocksalt pattern throughout the film. On the left, we show the growth technique used to create the Ruddlesden-Popper phases.

A.9 Supplemental Figures for Low Frequency Temperature Dependence

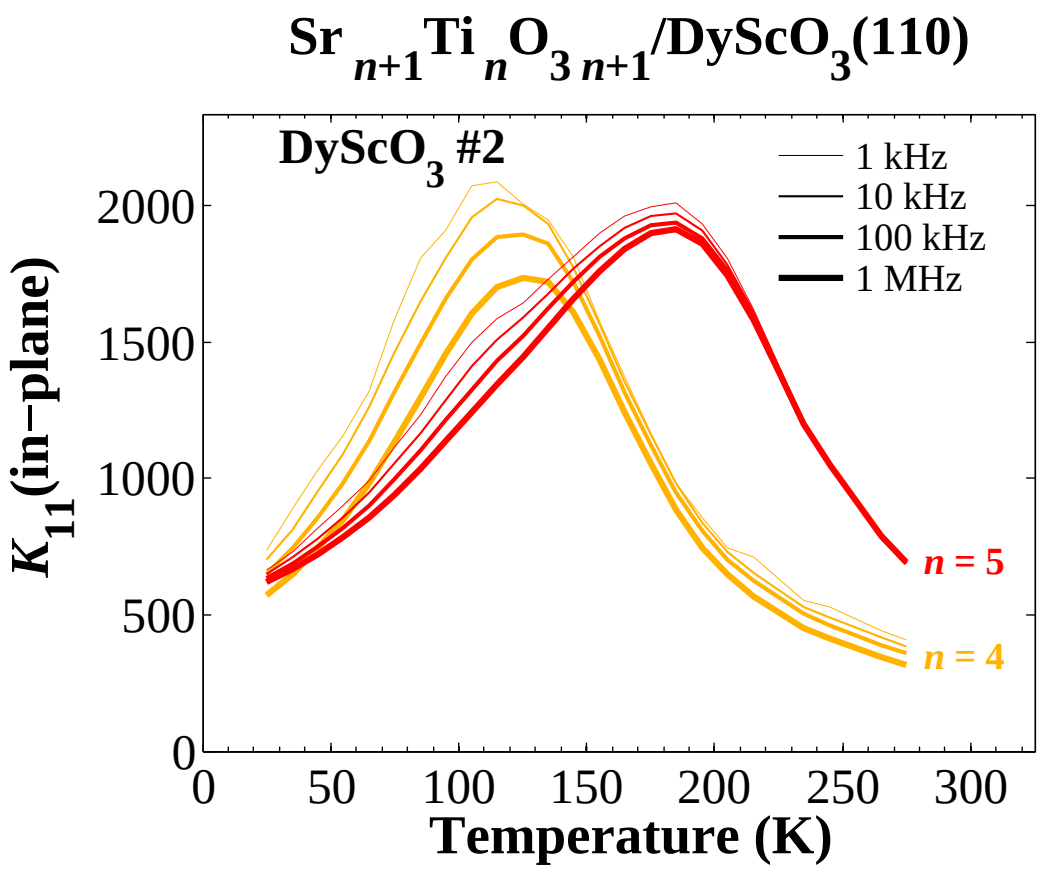

Figure A.8: Low Frequency Temperature Dependent Dispersion of $Sr_{n+1}Ti_nO_{3n+1}/DyScO_3(110)$ ($n = 4, 5$) for $DyScO_3$ #2

We show the temperature dependence of the real part of the in-plane relative permittivity, K_{11}(in-plane), for the $DyScO_3$ #2 sample set of 50 nm thick thin films $Sr_{n+1}Ti_nO_{3n+1}/DyScO_3(110)$ ($n = 4, 5$) at 1 kHz, 10 kHz, 100 kHz, and 1 MHz, where line thickness indicates frequency. The series number (n) measured for this set was $n = 4$ (dark yellow), and $n = 5$ (red). The interdigitated capacitors used for this sample set had active lengths $\ell = (1.835$ mm, 2.900 mm).

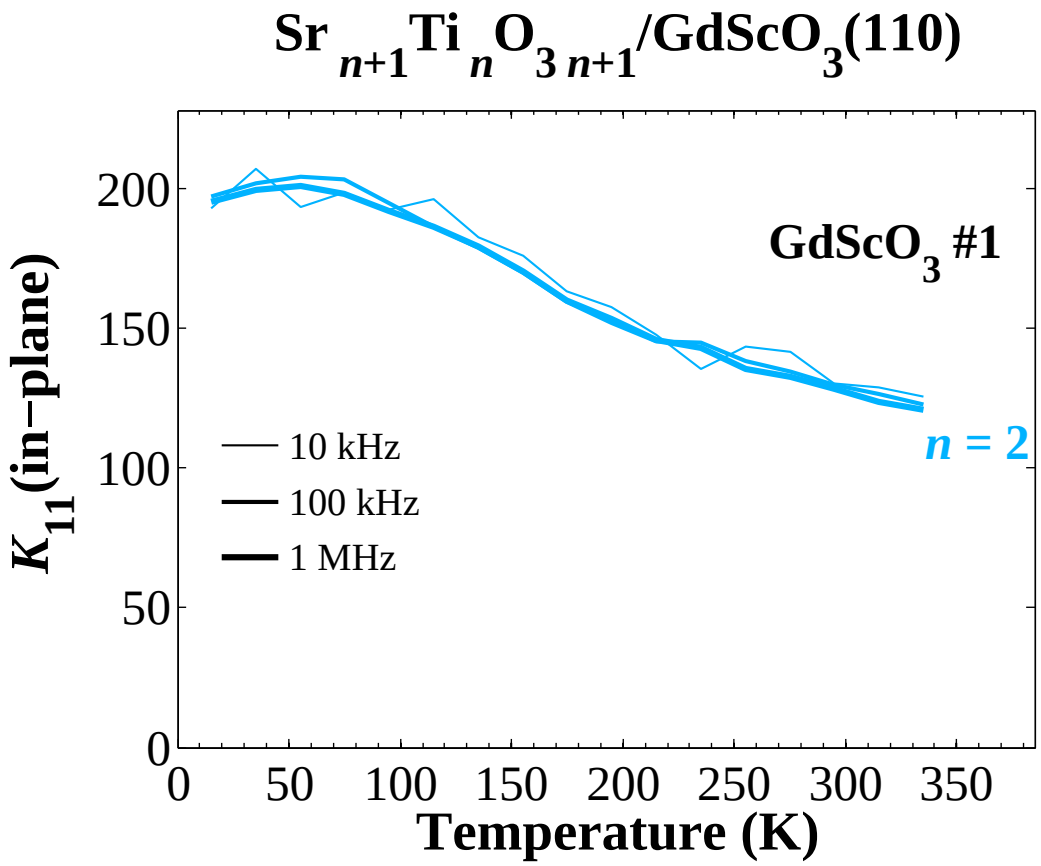

Figure A.9: Low Frequency Temperature Dependent Dispersion of $Sr_3Ti_2O_7/GdScO_3(110)$ for $GdScO_3$ #1

We show the temperature dependence of the real part of the in-plane relative permittivity, K_{11}(in-plane), for 25 nm thick thin film $Sr_3Ti_2O_7/GdScO_3(110)$ from $GdScO_3$ #1 at 10 kHz, 100 kHz, and 1 MHz, where line thickness indicates frequency. The interdigitated capacitors used for this sample set had active lengths ℓ = (0.875 mm, 1.835 mm).

A.10 Supplemental Figures for Low Frequency Electric Field Dependence

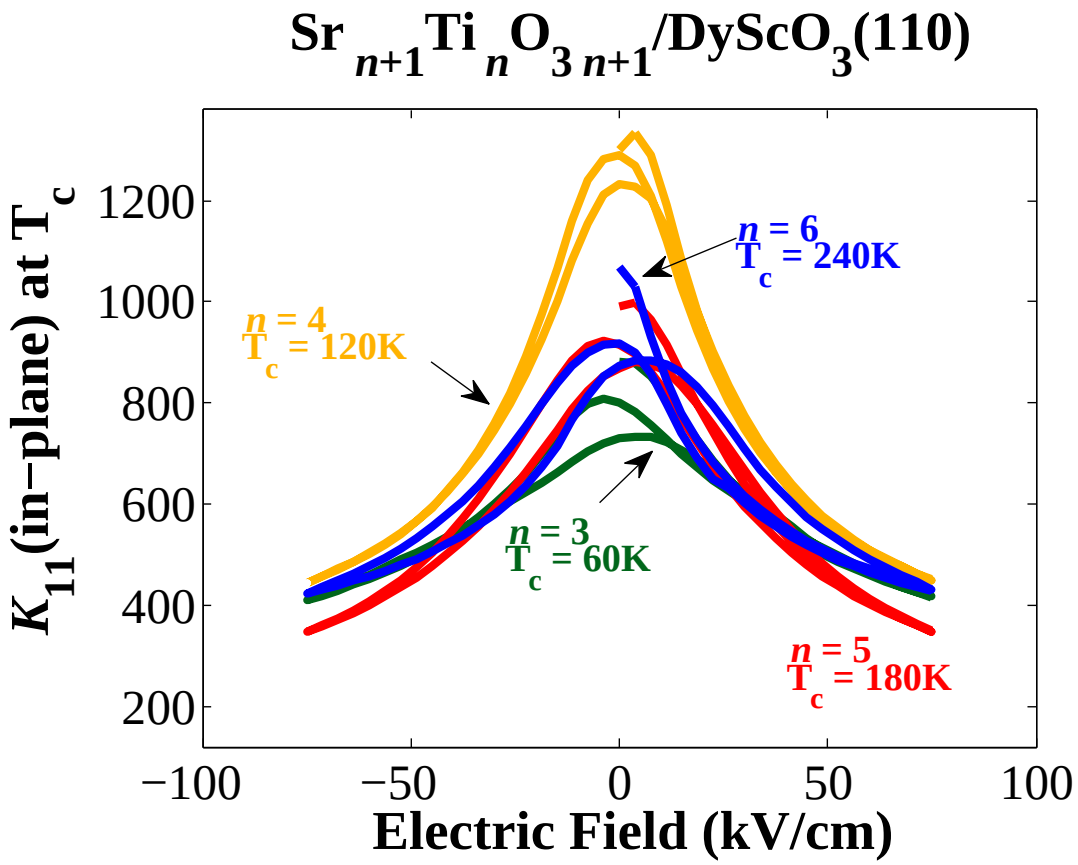

Figure A.10: Electric Field Dependence of K_{11}(in-plane) at 1 MHz and T_c for $Sr_{n+1}Ti_nO_{3n+1}/DyScO_3(110)(n = 2, 3, 4, 5, 6)$

The electric field dependence of the real part of the in-plane relative permittivity (K_{11}(in-plane)) at 1 MHz at the Critical Temperatures (T_c) of 50 nm thick films of $Sr_{n+1}Ti_nO_{3n+1}/DyScO_3(110)(n = 3, 4, 5, 6)$ for sample set $DyScO_3$ #3. The maximum electric field was 75 kV/cm and was stepped by 7.5 kV/cm. The interdigitated capacitors used for this measurement had active lengths $\ell = (0.875$ mm, 1.835 mm). We measured the series numbers (n) $n = 3$ (dark green), $n = 4$ (dark yellow), $n = 5$ (red), and $n = 6$ (blue). The approximate Critical Temperatures of $n = 3, 4, 5,$ and 6 are T = 60 K, 120 K, 180 K, and 240 K, respectively.

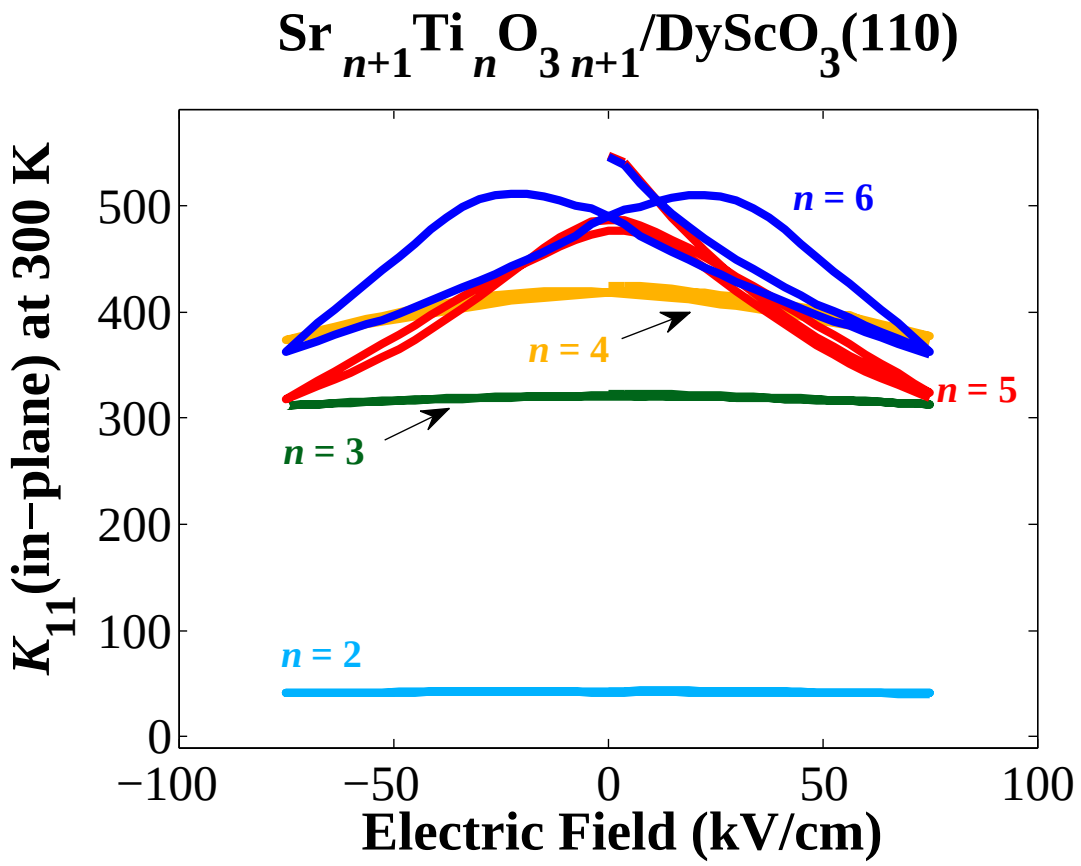

Figure A.11: Electric Field Dependence of K_{11}(in-plane) at 1 MHz and 300 K for $Sr_{n+1}Ti_nO_{3n+1}/DyScO_3(110)(n = 2, 3, 4, 5, 6)$

The electric field dependence of the real part of the in-plane relative permittivity (K_{11}(in-plane)) at 1 MHz at the 300 K of 50 nm thick films of $Sr_{n+1}Ti_nO_{3n+1}/DyScO_3(110)(n = 3, 4, 5, 6)$ for sample set $DyScO_3$ #3. The maximum electric field was 75 kV/cm and was stepped by 7.5 kV/cm. The interdigitated capacitors used for this measurement had active lengths $\ell = (0.875$ mm, 1.835 mm). We measured the series numbers (n) $n = 2$ (cyan), $n = 3$ (dark green), $n = 4$ (dark yellow), $n = 5$ (red), and $n = 6$ (blue).

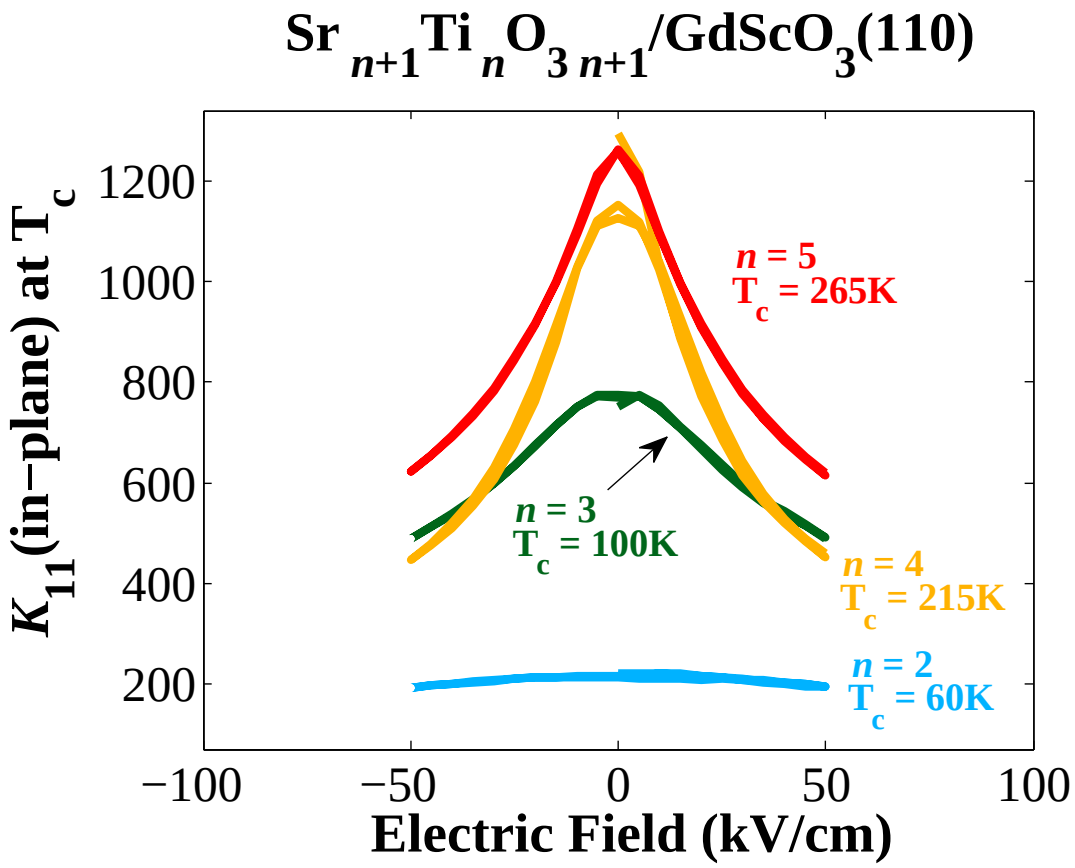

Figure A.12: Electric Field Dependence of K_{11}(in-plane) at 1 MHz and T_c for $Sr_{n+1}Ti_nO_{3n+1}/GdScO_3(110)(n = 2, 3, 4, 5, 6)$

The electric field dependence of the real part of the in-plane relative permittivity (K_{11}(in-plane)) at 1 MHz at the Critical Temperatures (T_c) of 25 nm thick films of $Sr_{n+1}Ti_nO_{3n+1}/GdScO_3(110)(n = 2, 3, 4, 5)$ for sample set $GdScO_3$ #1. The maximum electric field was 50 kV/cm and was stepped by 10 kV/cm. The interdigitated capacitors used for this measurement had active lengths ℓ = (0.875 mm, 1.835 mm). The series numbers (n) measured are $n = 2$ (cyan), $n = 3$ (dark green), $n = 4$ (dark yellow), and $n = 5$ (red). The approximate Critical Temperatures for $n = 2, 3, 4,$ and 5 are T = 60 K, 100 K, 215 K, and 265 K , respectively.

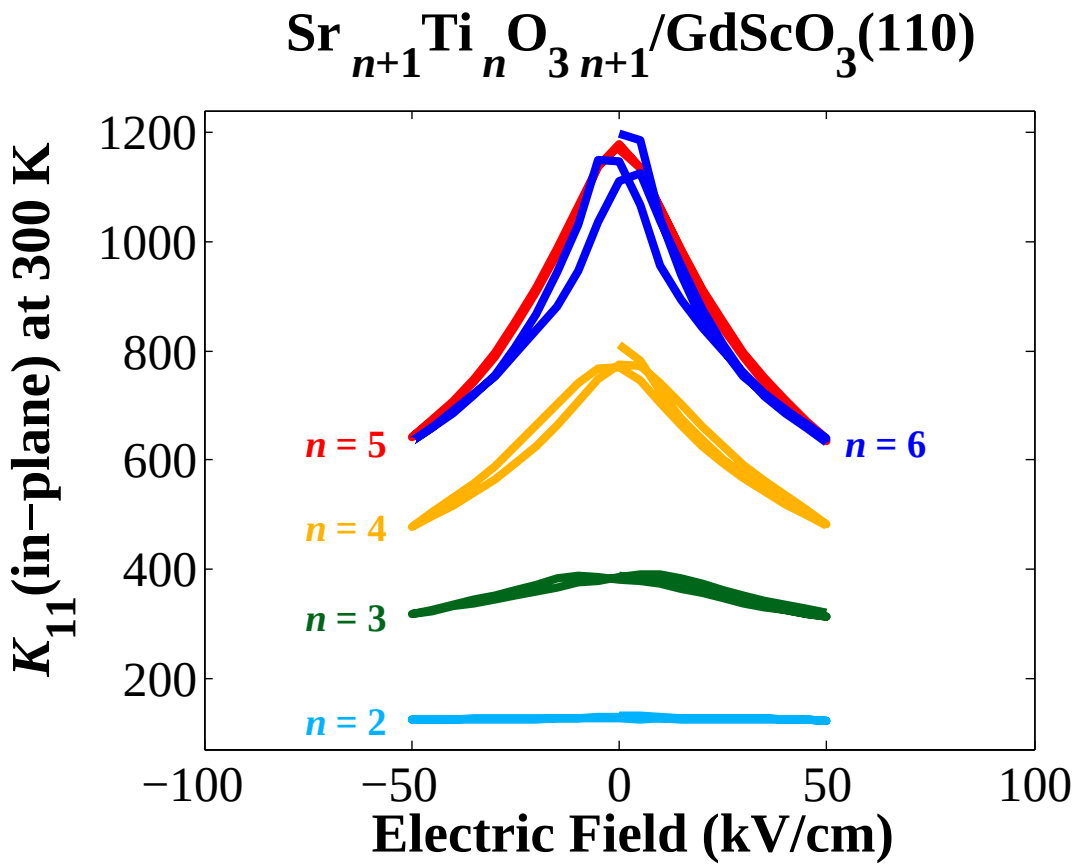

Figure A.13: Electric Field Dependence of K_{11}(in-plane) at 1 MHz and 300 K for $Sr_{n+1}Ti_nO_{3n+1}/GdScO_3(110)(n = 2, 3, 4, 5, 6)$

The electric field dependence of the real part of the in-plane relative permittivity (K_{11}(in-plane)) at 1 MHz at the 300 K of 25 nm thick films of $Sr_{n+1}Ti_nO_{3n+1}/GdScO_3(110)(n = 2, 3, 4, 5, 6)$ for sample set $GdScO_3$ #1. The maximum electric field was 75 kV/cm and was stepped by 7.5 kV/cm. The interdigitated capacitors used for this measurement had active lengths ℓ = (0.875 mm, 1.835 mm). We measured the series numbers (n) $n = 2$ (cyan), $n = 3$ (dark green), $n = 4$ (dark yellow), $n = 5$ (red), and $n = 6$ (blue).

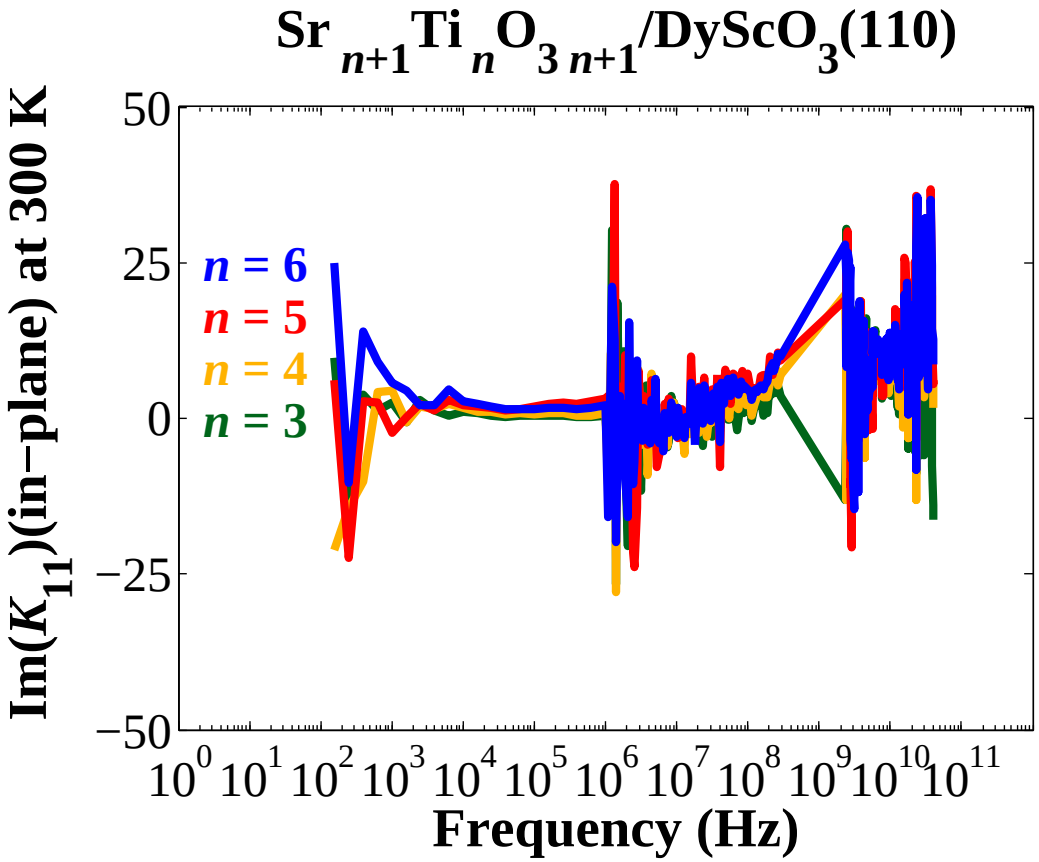

Figure A.14: Frequency Dependence of Im(K_{11})(in-plane) $Sr_{n+1}Ti_nO_{3n+1}/DyScO_3(110)$($n$ = 3, 4, 5, 6) at 300 K

The broadband frequency dependence of the imaginary part of the in-plane relative permittivity (Im(K_{11})(in-plane)) of 50 nm thick films of $Sr_{n+1}Ti_nO_{3n+1}/DyScO_3(110)$($n$ = 3, 4, 5, 6) from 100 Hz to 40 GHz at 300 K. We measured the series numbers (n) $n = 3$ (dark green), $n = 4$ (dark yellow), $n = 5$ (red), and $n = 6$ (blue).

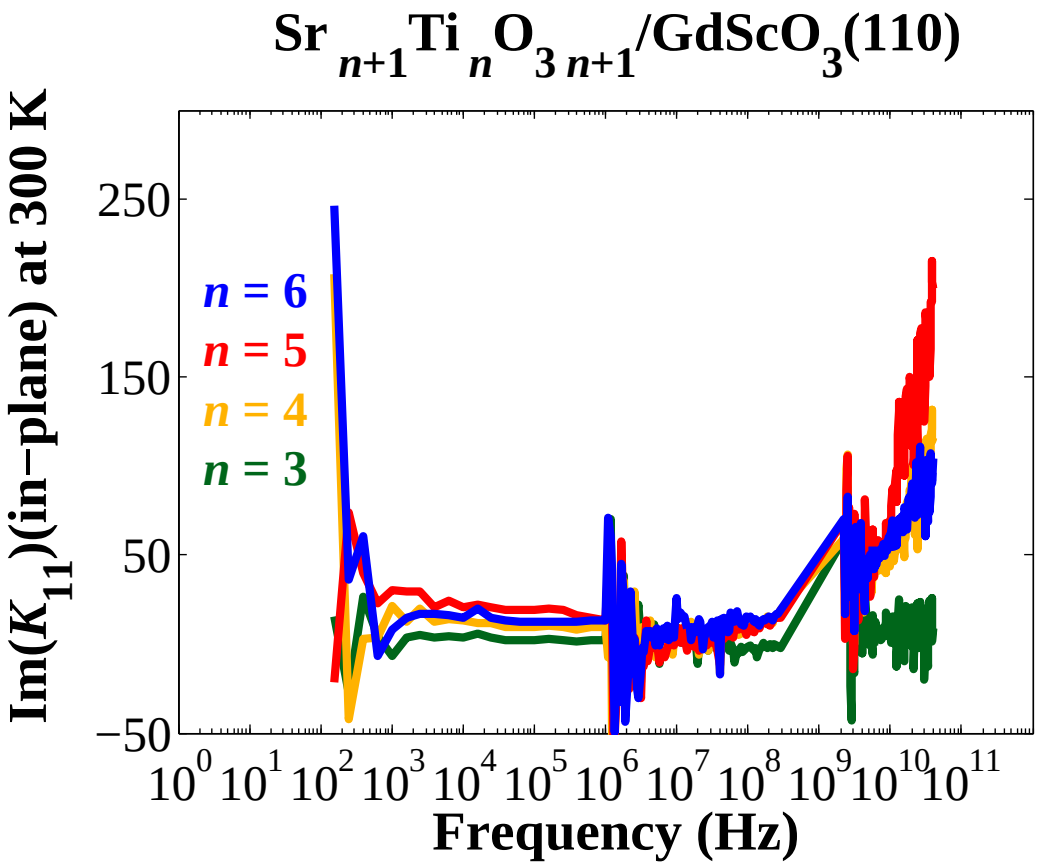

Figure A.15: Frequency Dependence of Im(K_{11})(in-plane) $Sr_{n+1}Ti_nO_{3n+1}/GdScO_3(110)$($n$ = 3, 4, 5, 6) at 300 K

The broadband frequency dependence of the imaginary part of the in-plane relative permittivity (Im(K_{11})(in-plane)) of 25 nm thick films of $Sr_{n+1}Ti_nO_{3n+1}/GdScO_3(110)$ (n = 3, 4, 5, 6) from 100 Hz to 40 GHz at 300 K. We measured the series numbers (n) n = 3 (dark green), n = 4 (dark yellow), n = 5 (red), and n = 6 (blue).

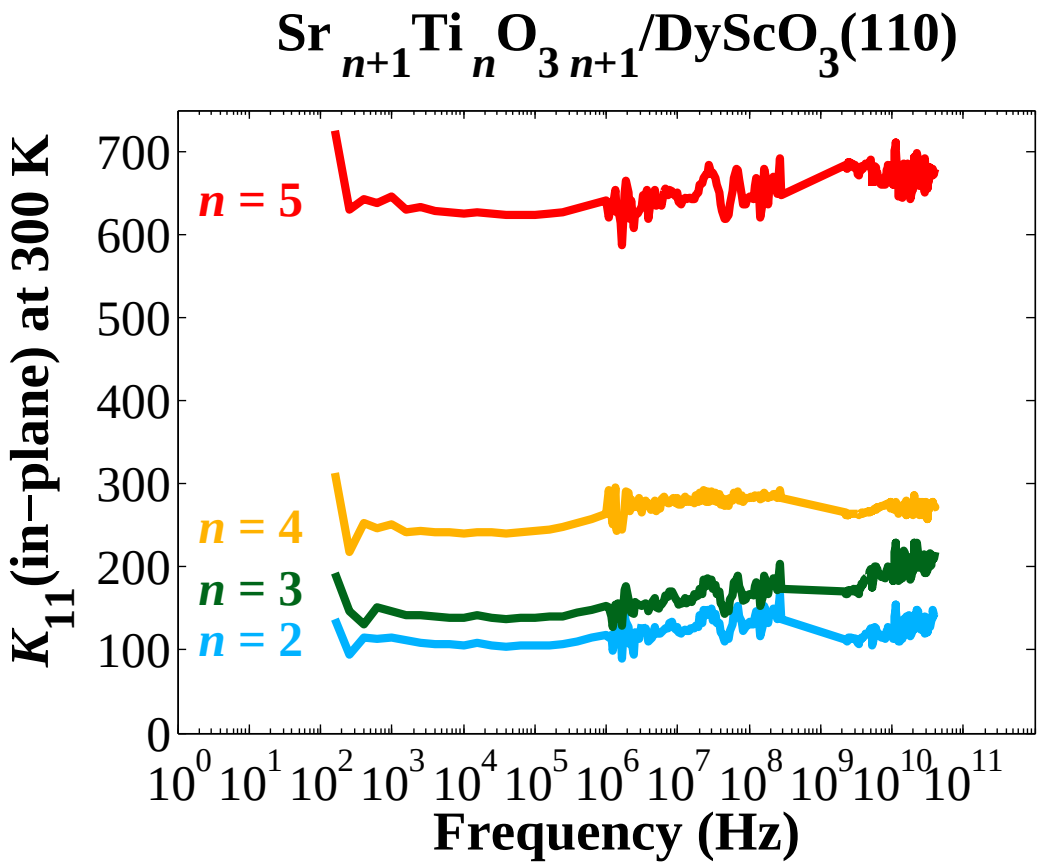

Figure A.16: Frequency Dependence of K_{11}(in-plane) $Sr_{n+1}Ti_nO_{3n+1}/DyScO_3(110)(n = 2, 3, 4, 5, 6)$ at 300 K

The broadband frequency dependence of the imaginary part of the in-plane relative permittivity (Im(K_{11})(in-plane)) of 50 nm thick films of $Sr_{n+1}Ti_nO_{3n+1}/DyScO_3(110)(n = 2, 3, 4, 5, 6)$ from 100 Hz to 40 GHz at 300 K. We measured the series numbers (n) $n = 2$ (cyan), $n = 3$ (dark green), $n = 4$ (dark yellow), $n = 5$ (red), and $n = 6$ (blue).

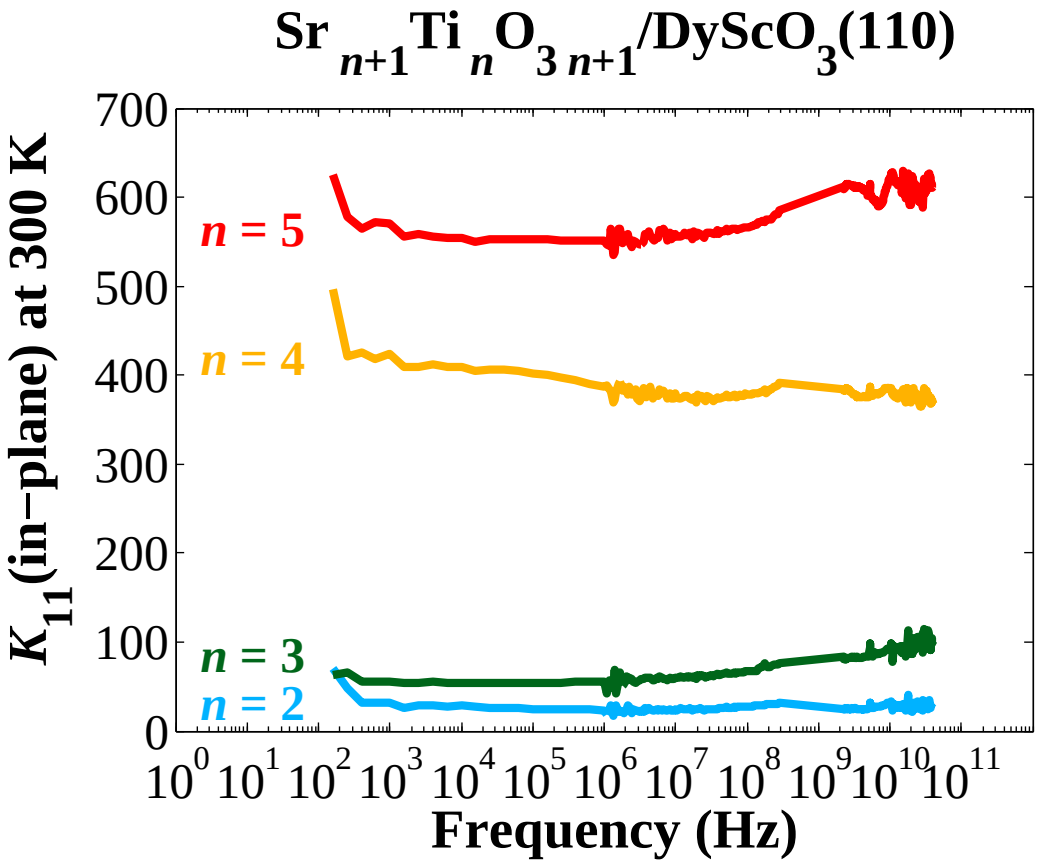

Figure A.17: Frequency Dependence of K_{11}(in-plane) $Sr_{n+1}Ti_nO_{3n+1}/DyScO_3(110)(n = 2, 3, 4, 5, 6)$ at 300 K

The broadband frequency dependence of the imaginary part of the in-plane relative permittivity (Im(K_{11})(in-plane)) of 50 nm thick films of $Sr_{n+1}Ti_nO_{3n+1}/DyScO_3(110)(n = 2, 3, 4, 5, 6)$ from 100 Hz to 40 GHz at 300 K. We measured the series numbers (n) $n = 2$ (cyan), $n = 3$ (dark green), $n = 4$ (dark yellow), $n = 5$ (red), and $n = 6$ (blue).

A.12 Uncertainty in Figure of Merit

Why not just calculate the uncertainty in the figure of merit by propagating the error?

The uncertainty in the figure of merit is proportional to $Q_{11}(0)$, and is given by,

$$\mathbf{\Delta FOM} = |Q_{11}| \sqrt{(\frac{\Delta T}{100})^2 + (\frac{T}{100} \cdot Q_{11})^2 (\Delta \tan(\delta_{11}))^2}. \quad \text{(A.19)}$$

If $Q_{11}(0)$ is large, then the uncertainty in the figure of merit will also be very large. We can show this by an order of magnitude calculation.

	Q_{11}	ΔT	T	$\Delta \tan(\delta_{11})$
Order of Magnitude	10^3	10^0	10^2	10^{-3}

$$\mathbf{\Delta FOM} \approx 10^3\sqrt{10^{-4} + (10^0 \cdot 10^3)^2(10^{-3})^2} = 10^3 \tag{A.20}$$

Recall, that the figure of merit it is bounded by $Q_{11}(0)$ and here we have shown that the uncertainty in the figure of merit is the same order of magnitude as the figure of merit. This implies that the uncertainty will always be large relative to the figure of merit. It is for this reason that we do not calculate the uncertainty in the figure of merit.

Bibliography

[1] J.H. Haeni, P. Irvin, W. Chang, R. Uecker, P. Reiche, Y.L. Li, S. Choudhury, W. Tian, M.E. Hawley, B. Craigo, A.K. Tagantsev, X.Q. Pan, S.K. Streiffer, L.Q. Chen, S.W. Kirchoefer, J. Levy, and D.G. Schlom. Room-Temperature Ferroelectricity in Strained $SrTiO_3$. *Nature*, 430(7001):758–761, Aug. 2004. ISSN 0028-0836. doi: {10.1038/nature02773}.

[2] James C. Booth, Ichiro Takeuchi, and Kao-Shuo Chang. Microwave-Frequency Loss and Dispersion in Ferroelectric $ba_{0.3}Sr_{0.7}TiO_3$ Thin Films. *Applied Physics Letters*, 87(8):082908, 2005. doi: 10.1063/1.2033139.

[3] K.S. Cole and R.H. Cole. Dispersion and Absorption in Dielectrics i. Alternating Current Characteristics. *Journal of Chemical Physics*, 9(4):341–351, Apr. 1941. ISSN 0021-9606.

[4] N.D. Orloff, W. Tian, C.J. Fennie, C.H. Lee, D. Gu, J. Mateu, X.X. Xi, K.M. Rabe, D.G. Schlom, I. Takeuchi, and J.C. Booth. Broadband Dielectric Spectroscopy of Ruddlesden-Popper $Sr_{n+1}Ti_nO_{3n+1}$ (n=1,2,3) Thin Films. *Applied Physics Letters*, 94(4):042908, 2009. doi: 10.1063/1.3046792.

[5] S Kamba, V Bovtun, J Petzelt, I Rychetsky, R Mizaras, A Brilingas, J Banys, J Grigas, and M Kosec. Dielectric dispersion of the relaxer PLZT ceramics in the frequency range 20 Hz-100 THz. *Journal of Physics-Condensed Matter*, 12 (4):497–519, Jan 2000. ISSN 0953-8984.

[6] GA Samara. The relaxational properties of compositionally disordered ABO_3 perovskites. *Journal of Physics-Condensed Matter*, 15(9):367–411, Mar 2003. ISSN 0953-8984.

[7] U. Arz, J. Leinhos, and M. D. Janezic. Broadband Dielectric Material Characterization: A Comparison of On-Wafer and Split-Cylinder Resonator Measurements. In *Proc. 38th European Microwave Conf. EuMC 2008*, pages 913–916, 2008. doi: 10.1109/EUMC.2008.4751602.

[8] Bui Ai, P. Destruel, M. Farzaneh, and Hoang The Giam. Pressure and temperature dependence of the dielectric properties of polyethylene used in submarine telecommunication cables. *Journal of Applied Physics*, 52(1):525–526, 1981. doi: 10.1063/1.328450.

[9] P. Guerin, Hoang the Giam, Bui Ai, P. Destruel, L. Deschamps, and J. Perret. Pressure and temperature dependence of the dielectric breakdown of polyethylene used in submarine power cables. *Journal of Applied Physics*, 57(10):4805–4807, 1985. doi: 10.1063/1.335346.

[10] U. Karthaus and M. Fischer. Fully integrated passive uhf rfid transponder ic with 16.7-μw minimum rf input power. 38(10):1602–1608, 2003. doi: 10.1109/JSSC.2003.817249.

[11] Jingkuang Chen, Xiaoyang Cheng, Chien-Chang Chen, Pai-Chi Li, Jian-Hung Liu, and Yu-Ting Cheng. A capacitive micromachined ultrasonic transducer array for minimally invasive medical diagnosis. *Journal of Microelectromechanical Systems*, 17(3):599–610, 2008. doi: 10.1109/JMEMS.2009.922076.

[12] P. Padmini, T. R. Taylor, M. J. Lefevre, A. S. Nagra, R. A. York, and J. S. Speck. Realization of high tunability barium strontium titanate thin films by rf magnetron sputtering. *Applied Physics Letters*, 75(20):3186–3188, 1999. doi: 10.1063/1.125272.

[13] B. Acikel, T. R. Taylor, P. J. Hansen, J. S. Speck, and R. A. York. A new high performance phase shifter using baxsr1-x tio3 thin films. 12(7):237–239, 2002. doi: 10.1109/LMWC.2002.801129.

[14] D. Dijkkamp, T. Venkatesan, X. D. Wu, S. A. Shaheen, N. Jisrawi, Y. H. Min-Lee, W. L. McLean, and M. Croft. Preparation of Y-Ba-Cu oxide superconductor thin films using pulsed laser evaporation from high Tc bulk material. *Applied Physics Letters*, 51(8):619–621, 1987. doi: 10.1063/1.98366.

[15] A. Y. Cho. Morphology of Epitaxial Growth of GaAs by a Molecular Beam Method: The Observation of Surface Structures. *Journal of Applied Physics*, 41 (7):2780–2786, 1970. doi: 10.1063/1.1659315.

[16] John A. Thornton. Influence of apparatus geometry and deposition conditions on the structure and topography of thick sputtered coatings. *Journal of Vacuum Science and Technology*, 11(4):666–670, 1974. doi: 10.1116/1.1312732.

[17] C.A. Schmuttenmaer. Exploring dynamics in the far-infrared with terahertz spectroscopy. *Chemical Reviews*, 104(4):1759–1779, Apr. 2004. ISSN 0009-2665.

[18] D.K. Ghodgaonkar, W. Varadan, and V.K. Varadan. A Free-Space Method for Measurement of Dielectric-Constants and Loss Tangents at Microwave-Frequencies. *IEEE Transactions on Instrumentation and Measurement*, 38(3): 789–793, Jun. 1989. ISSN 0018-9456.

[19] M.D. Janezic and J. Baker-Jarvis. Full-Wave Analysis of a Split-Cylinder Resonator for Nondestructive Permittivity Measurements. *IEEE Transactions on Microwave Theory and Techniques*, 47(10):2014–2020, 1999. doi: 10.1109/22.795077.

[20] J. Krupka. Frequency domain complex permittivity measurements at microwave frequencies. *Measurement Science & Technology*, 17(6):55–70, JUN 2006. ISSN 0957-0233. doi: {10.1088/0957-0233/17/6/R01}.

[21] S. Gevorgian, L.J.P. Linner, and E.L. Kollberg. CAD Models for Shielded Multilayered CPW. *IEEE Transactions on Microwave Theory and Techniques*, 43 (4):772–779, 1995. doi: 10.1109/22.375223.

[22] M.D. Janezic, D.F. Williams, V. Blaschke, A. Karamcheti, and C.S. Chang. Permittivity Characterization of Low-k Thin Films from Transmission-Line Measurements. *IEEE Transactions on Microwave Theory and Techniques*, 51(1, Part 1):132–136, Jan. 2003. ISSN 0018-9480. doi: {10.1109/TMTT.2002.806925}.

[23] N. Orloff, J. Mateu, M. Murakami, I. Takeuchi, and J. C. Booth. Broadband Characterization of Multilayer Dielectric Thin-Films. In *Proc. IEEE/MTT-S Int. Microwave Symp*, pages 1177–1180, 2007. doi: 10.1109/MWSYM.2007.380340.

[24] N.D. Orloff, J.C. Booth, M. Murakami, and I. Takeuchi. Broadband Permittivity Measurements of Thin-Film Ferroelectrics to 40 GHz. In *Proc. 17th IEEE Int. Symp. the Applications of Ferroelectrics ISAF 2008*, volume 2, pages 1–2, 2008. doi: 10.1109/ISAF.2008.4693752.

[25] J.C. Booth, N.D. Orloff, J. Cagnon, J. Lu, and S. Stemmer. Temperature-dependent Relaxation in Bismuth Zinc Niobate Thin Films. *Applied Physics Letters*, 97(2):022902, 2010. doi: 10.1063/1.3455897. URL `http://link.aip.org/link/?APL/97/022902/1`.

[26] Roger B. Marks. Formulations of the Basic Vector Network Analyzer Error Model including Switch-Terms. In *Proc. th ARFTG Conf. Digest-Fall*, volume 32, pages 115–126, 1997. doi: 10.1109/ARFTG.1997.327265.

[27] C.P. Wen. Coplanar Waveguide: A Surface Strip Transmission Line Suitable for Nonreciprocal Gyromagnetic Device Applications. *IEEE Transactions on Microwave Theory and Techniques*, 17(12):1087–1090, Dec. 1969.

[28] J.C. Rautio. An Investigation of Microstrip Conductor Loss. *IEEE Microwave Magazine*, 1(4):60–67, 2000. doi: 10.1109/6668.893247.

[29] R.B. Marks and D.F. Williams. A General Wave-guide Ciruit Theory. *Journal of Research of the National Institute of Standards and Technology*, 97(5):533–562, Sep. - Oct. 1992. ISSN 1044-677X.

[30] R.B. Marks. A Multiline Method of Network Analyzer Calibration. *IEEE Transactions on Microwave Theory and Techniques*, 39(7):1205–1215, Jul. 1991. doi: 10.1109/22.85388.

[31] D.F. Williams, J.C.M. Wang, and U. Arz. An Optimal Vector-Network-Analyzer Calibration Algorithm. *IEEE Transactions on Microwave Theory and Techniques*, 51(12):2391–2401, Dec. 2003. doi: 10.1109/TMTT.2003.819211.

[32] D.F. Williams, U. Arz, and H. Grabinski. Characteristic-Impedance Measurement Error on Lossy Substrates. *IEEE Microwave and Wireless Components Letters*, 11(7):299–301, 2001. doi: 10.1109/7260.933777.

[33] W.H. Yang, D.S. Hou, C.Z. Li, Fan N., and H.Y. Zhang. $LaAlO_3$ Single Crystal Substrate for Epitaxial Superconducting Thin Films. *Solid State Communications*, 75(5):421–424, Aug. 1990. ISSN 0038-1098.

[34] N.D Orloff, M. Mateu, A. Lewandowski, E. Rocas, J. King, D. Gu, X. Lu, C. Collado, I. Takeuchi, and J.C. Booth. A Compact Variable-Temperature Broadband Series-Resistor Calibration. *IEEE Transactions on Microwave Theory and Techniques*, Under Review:1–7, 2010.

[35] Dylan F. Williams and David K. Walker. Series-Resistor Calibration. In *Proc. th ARFTG Conf. Digest-Fall*, volume 32, pages 131–137, 1997. doi: 10.1109/ARFTG.1997.327267.

[36] J.C. Booth, N.D. Orloff, J. Mateu, M. Janezic, M. Rinehart, and J.A. Beall. Quantitative Permittivity Measurements of Nanoliter Liquid Volumes in Microfluidic Channels to 40 GHz. *IEEE Transactions on Instrumentation and Measurement*, (99):1–10, 2010. doi: 10.1109/TIM.2010.2047141. Early access.

[37] A.R. Djordjevic and T.K. Sarkar. Closed-form Formulas for Frequency-Dependent Resistance and Inductance Per Unit Length of Microstrip and Strip Transmission Lines. *IEEE Transactions on Microwave Theory and Techniques*, 42(2):241–248, 1994. doi: 10.1109/22.275254.

[38] S.S. Gevorgian, T. Martinsson, P.L.J. Linner, and E.L. Kollberg. CAD Models for Multilayered Substrate Interdigital Capacitors. *IEEE Transactions on Microwave Theory and Techniques*, 44(6):896–904, 1996. doi: 10.1109/22.506449.

[39] E. Carlsson and S. Gevorgian. Conformal Mapping of the Field and Charge Distributions in Multilayered Substrate CPWs. *IEEE Transactions on Microwave Theory and Techniques*, 47(8):1544–1552, 1999. doi: 10.1109/22.780407.

[40] S.N. Ruddlesden and P. Popper. The Compound $Sr_3Ti_2O_7$ and its Structure. *Acta Crystallographica*, 11(1):54–55, 1958. ISSN 0108-7673.

[41] C.J. Fennie and K.M. Rabe. Structural and Dielectric Properties of Sr_2TiO_4 From First Principles. *Phys. Rev. B*, 68(18):184111, Nov. 2003. ISSN 1098-0121. doi: {10.1103/PhysRevB.68.184111}.

[42] C. Noguera. Theoretical Investigation of the Ruddlesden-Popper Compounds $Sr_{n+1}Ti_nO_{3n+1}$ (n=1-3). *Philosophical Magazine Letters*, 80(3):173–180, Mar. 2000. ISSN 0950-0839.

[43] C.J. Fennie and K.M. Rabe. First-Principles Investigation of Ferroelectricity in Epitaxially Strained Pb_2TiO_4. *Phys. Rev. B*, 71(10):100102–, Mar. 2005. URL `http://link.aps.org/doi/10.1103/PhysRevB.71.100102`.

[44] D. Music and J.M. Schneider. Elastic Properties of Amorphous Boron Suboxide Based Solids Studied Using *ab initio* Molecular Dynamics. *Journal of Physics-Condensed Matter*, 20(19):195203, May 2008. ISSN 0953-8984. doi: {10.1088/0953-8984/20/19/195203}.

[45] P.L. Wise, I.M. Reaney, W.E. Lee, T.J. Price, D.M. Iddles, and D.S. Cannell. Structure-Microwave Property Relations of Ca and Sr Titanates. *Journal of the European Ceramic Society*, 21(15):2629–2632, 2001. ISSN 0955-2219. Meeting of the Microwave Materials and their Applications 2000, Bled, Slovenia, Aug. 30-Sep. 02, 2000.

[46] P.L. Wise, I.M. Reaney, W.E. Lee, D.M. Iddles, D.S. Cannell, and T.J. Price. Tunability of $\tau(f)$ in Perovskites and Related Compounds. *Journal of Materials Research*, 17(8):2033–2040, Aug. 2002. ISSN 0884-2914.

[47] S. Kamba, P. Samoukhina, F. Kadlec, J. Pokorny, J. Petzelt, I.M. Reaney, and P.L. Wise. Composition Dependence of the Lattice Vibrations in $Sr_{n+1}Ti_nO_{3n+1}$ Ruddlesden-Popper Homologous Series. *Journal of the European Ceramic Society*, 23(14):2639–2645, 2003. ISSN 0955-2219. doi: {10.1016/S0955-2219(03)00150-X}. International Conference on Microwave Materials and Their Applications (MMA 2002), York, England, Sep. 01-03, 2002.

[48] J.H. Sohn, Y. Inaguma, M. Itoh, and T. Nakamura. Cooperative Interaction of Oxygen Octahedra for Dielectric Properties in the Perovskite-Related Layered Compounds $Sr_{n+1}Ti_nO_{3n+1}$, $Ca_{n+1}Ti_nO_{3n+1}$ and Sr_{n+1} $(Ti_{0.5}Sn_{0.5})_nO_{43n+1}$ (n=1, 2, 3 and ∞). *Materials Science and Engineering B-Solid State Materials for Advanced Technology*, 41(1):50–54, Oct. 1996. ISSN 0921-5107. 2nd International Symposium on Oxide Electronics, Yokohama, Japan, Dec. 14-15, 1995.

[49] S. Madhavan, D.G. Schlom, A. Dabkowski, H.A. Dabkowska, and Y. Liu. Growth of Epitaxial a-Axis and c-Axis Oriented Sr_2RuO_4 Films. *Applied Physics Letters*, 68(4):559–561, Jan. 1996. ISSN 0003-6951.

[50] Y. Konishi, T. Kimura, M. Izumi, M. Kawasaki, and Y. Tokura. Fabrication and Physical Properties of c-Axis Oriented Thin Films of Layered Perovskite $La_{2-2x}Sr_{1+2x}Mn_2O_7$. *Applied Physics Letters*, 73(20):3004–3006, Nov. 1998. ISSN 0003-6951.

[51] Y. Jia, M.A. Zurbuchen, S. Wozniak, A.H. Carim, D.G. Schlom, L.N. Zou, S. Briczinski, and Y. Liu. Epitaxial Growth of Metastable Ba_2RuO_4 Films with the K_2NiF_4 Structure. *Applied Physics Letters*, 74(25):3830–3832, Jun. 1999. ISSN 0003-6951.

[52] Y. Iwazaki, T. Suzuki, S. Sekiguchi, and M. Fujimoto. Artificial $SrTiO_3$/SrO Superlattices by Pulsed Laser Deposition. *Japanese Journal of Applied Physics Part 2-Letters*, 38(12A):L1443–L1446, Dec. 1999. ISSN 0021-4922.

[53] J.H. Haeni, C.D. Theis, D.G. Schlom, W. Tian, X.Q. Pan, H. Chang, I. Takeuchi, and X.D. Xiang. Epitaxial Growth of the First Five Members of the $Sr_{n+1}Ti_nO_{3n+1}$ Ruddlesden-Popper Homologous Series. *Applied Physics Letters*, 78(21):3292–3294, May 2001. ISSN 0003-6951.

[54] W. Tian, J. H. Haeni, D. G. Schlom, E. Hutchinson, B. L. Sheu, M. M. Rosario, P. Schiffer, Y. Liu, M. A. Zurbuchen, and X. Q. Pan. Epitaxial Growth and Magnetic Properties of the First Five Members of the Layered $Sr_{n+1}Ru_nO_{3n+1}$ Oxide Series. *Applied Physics Letters*, 90(2):022507, Jan. 2007. ISSN 0003-6951. doi: {10.1063/1.2430941}.

[55] M. Burriel, G. Garcia, M. D. Rossell, A. Figueras, G. Van Tendeloo, and J. Santiso. Enhanced High-Temperature Electronic Transport Properties in Nanostructured Epitaxial Thin Films of the $La_{n+1}Ni_nO_{3n+1}$ Ruddlesden-Popper Series (n=1, 2, 3, ∞). *Chemistry of Materials*, 19(16):4056–4062, Aug. 2007. ISSN 0897-4756. doi: {10.1021/cm070804e}.

[56] K. Shibuya, S. Mi, C. Jia, P. Meuffels, and R. Dittmann. Sr_2TiO_4 Layered Perovskite Thin Films Grown by Pulsed Laser Deposition. *Applied Physics Letters*, 92(24):241918, Jun. 2008. ISSN 0003-6951. doi: {10.1063/1.2945640}.

[57] A. Okude, M.and Ohtomo, T. Kita, and M. Kawasaki. Epitaxial Synthesis of $Sr_{n+1}Ti_nO_{3n+1}$ (n=2-5) Ruddlesden-Popper Homologous Series by Pulsed-Laser Deposition. *Applied Physics Express*, 1(8):081201, Aug. 2008. ISSN 1882-0778. doi: {10.1143/APEX.1.081201}.

[58] D. Noujni, S. Kamba, A. Pashkin, V. Bovtun, J. Petzelt, A.K. Axelsson, N.M. Alford, P.L. Wise, and I.M. Reaney. Temperature Dependence of Microwave and THz Dielectric Response in $Sr_{n+1}Ti_nO_{3n+1}$ (n=1-4). *Integrated Ferroelectrics*, 62:199–203, 2004. ISSN 1058-4587. doi: {10.1080/10584580490457820}. 10th European Meeting on Ferroelectricity, Cambridge, England, Aug. 03-08, 2003.

[59] J. Mateu, J.C. Booth, and S.A. Schima. Fequency Tuning and Spurious Signal Generation at Microwave Frequencies in Ferroelectric $SrTiO_3$ Thin-Film Transmission Lines. *IEEE Transactions on Microwave Theory and Techniques*, 55 (2, Part 2):391–396, Feb. 2007. ISSN 0018-9480. doi: {10.1109/TMTT.2006.889346}.

[60] S.W. Liu, Y. Lin, J. Weaver, W. Donner, X. Chen, C.L. Chen, J.C. Jiang, E. Meletis, and A. Bhalla. High-Dielectric-Tunability of Ferroelectric (Pb, Sr)TiO_3 Thin Films on (001) $LaAlO_3$. *Applied Physics Letters*, 85(15):3202–3204, Oct. 2004. ISSN 0003-6951. doi: {10.1063/1.1801176}.

[61] C. Gao, B. Hu, I. Takeuchi, K.S. Chang, X.D. Xiang, and G. Wang. Quantitative Scanning Evanescent Microwave Microscopy and its Applications in Characterization of Functional Materials Libraries. *Measurement Science & Technology*, 16 (1):248–260, Jan. 2005. ISSN 0957-0233. doi: {10.1088/0957-0233/16/1/033}.

[62] T.E. Harrington, J. Wosik, and S.A. Long. Open Resonator Mode Patterns for Characterization of Anisotropic Dielectric Substrates for HTS Thin Films. *IEEE Transactions on Applied Superconductivity*, 7(2, Part 2):1861–1864, Jun. 1997. ISSN 1051-8223. 1996 Applied Superconductivity Conference, Pittsburgh, PA, Aug. 25-30, 1996.

[63] R. Schwab, R. Sporl, P. Severloh, R. Heidinger, and J. Halbritter. Temperature and Orientation Dependent Dielectric Measurements of $LaAlO_3$ Substrates. In H. Rogalla and D.H.A. Blank, editors, *Applied Superconductivity 1997, Vols 1 and 2 - Vol 1: Small Scale and Electronic Applications; Vol 2: Large Scale and Power Applications*, number 158 in Institute of Physics Conference Series, pages 61–64, Techno House, Redcliffe Way, Bristol, England BS1 6NX, 1997. ASM Lithog BV, The Netherlands; GEC ALSTROM Intermagnet; Philips Med Syst Magnet Resonance; European Commiss, TMR Programme; Esprit Network Superconducting Electr; Dutch Technol Fdn; Dutch Fdn Fundamental Res Matter; Univ Twente, IOP Publishing LTD. ISBN 0-7503-0487-1. 3rd European Conference on Applied Superconductivity (EUCAS 1997), Veldhoven, Netherlands, Jun. 30 - Jul. 03, 1997.

[64] S.C. Tidrow, A. Tauber, W.D. Wilber, R.T. Lareau, C.D. Brandle, G.W. Berkstresser, A.J. VenGraitis, D.M. Potrepka, J.I. Budnick, and J.Z. Wu. New Substrates for HTSC Microwave Devices. *IEEE Transactions on Applied Superconductivity*, 7(2, Part 2):1766–1768, Jun. 1997. ISSN 1051-8223. 1996 Applied Superconductivity Conference, Pittsburgh, PA, Aug. 25-30, 1996.

[65] J. Hemberger, P. Lunkenheimer, R. Viana, R. Bohmer, and A. Loidl. Electric-Field-Dependent Dielectric-Constant and Nonlinear Susceptibility in $SrTiO_3$. *Phys. Rev. B*, 52(18):13159–13162, Nov. 1995. ISSN 0163-1829.

[66] A.A. Sirenko, I.A. Akimov, J.R. Fox, A.M. Clark, H.C. Li, W.D. Si, and X.X. Xi. Observation of the First-Order Raman Scattering in $SrTiO_3$ Thin Films. *Physical Review Letters*, 82(22):4500–4503, May 1999. ISSN 0031-9007.

[67] G. Kresse and J. Hafner. Abinito Molecular-Dynamics for Liquid Metals. *Phys. Rev. B*, 47(1):558–561, Jan. 1993. ISSN 0163-1829.

[68] G. Kresse and J. Furthmuller. Efficient Iterative Schemes for *ab initio* Total-Energy Calculations Using a Plane-Wave Basis Set. *Phys. Rev. B*, 54(16):11169–11186, Oct. 1996. ISSN 0163-1829.

[69] G. Kresse and D. Joubert. From Ultrasoft Pseudopotentials to the Projector Augmented-Wave Method. *Phys. Rev. B*, 59(3):1758–1775, Jan. 1999. ISSN 0163-1829.

[70] P.E. Blochl. Projector Augmented-Wave Method. *Phys. Rev. B*, 50(21):17953–17979, Dec. 1994. ISSN 0163-1829.

[71] R.D. Kingsmith and D. Vanderbilt. Theory of Polarization of Crystalling Solids. *Phys. Rev. B*, 47(3):1651–1654, Jan. 1993. ISSN 0163-1829.

[72] H.A. Kramers. On the theory of X-ray absorption and of the continuous X- ray spectrum. *Philosophical Magazine*, 46(275, Sp. Iss. 6TH SERIES):836–871, NOV 1923. ISSN 1478-6443.

[73] R. D. L. Kronig. On the theory of dispersion of x-rays. *Journal of the Optical Society of America and Review of Scientific Instruments*, 12(6):547–557, JUN 1926. ISSN 0093-4119.

[74] H. Wang, S. Kamba, M. Zhang, X. Yao, S. Denisov, F. Kadlec, and J. Petzelt. Microwave and infrared dielectric response of monoclinic bismuth zinc niobate based pyrochlore ceramics with ion substitution in A site. *Journal of Applied Physics*, 100(3):034109, 2006. doi: 10.1063/1.2219161.

[75] G. Houzet, L. Burgnies, G. Velu, J.-C. Carru, and D. Lippens. Dispersion and loss of ferroelectric Ba0.5Sr0.5TiO3 thin films up to 110 GHz. *Applied Physics Letters*, 93(5):053507, 2008. doi: 10.1063/1.2969469.

[76] V.V. Lemanov, A.V. Sotnikov, E.P. Smirnova, M. Weihnacht, and R. Kunze. Perovskite $CaTiO_3$ as an incipient ferroelectric. *Solid State Communications*, 110(11):611–614, 999. ISSN 0038-1098.

[77] M. D. Biegalski, E. Vlahos, G. Sheng, Y. L. Li, M. Bernhagen, P. Reiche, R. Uecker, S. K. Streiffer, L. Q. Chen, V. Gopalan, D. G. Schlom, and S. Trolier-McKinstry. Influence of anisotropic strain on the dielectric and ferroelectric properties of $SrTiO_3$ thin films on $DyScO_3$ substrates. *Physical Review B.*, 79 (22):224117, Jun 2009. doi: 10.1103/PhysRevB.79.224117.

[78] D. Nuzhnyy, J. Petzelt, S. Kamba, P. Kuzel, C. Kadlec, V. Bovtun, M. Kempa, J. Schubert, C. M. Brooks, and D. G. Schlom. Soft mode behavior in SrTiO3/DyScO3 thin films: Evidence of ferroelectric and antiferrodistortive phase transitions. *Applied Physics Letters*, 95(23):232902, 2009. doi: 10.1063/1.3271179.

[79] R. H. Lyddane, R. G. Sachs, and E. Teller. On the Polar Vibrations of Alkali Halides. *Phys. Rev.*, 59(8):673–676, Apr 1941. doi: 10.1103/PhysRev.59.673.

[80] H. W. Jang, A. Kumar, S. Denev, M. D. Biegalski, P. Maksymovych, C. W. Bark, C. T. Nelson, C. M. Folkman, S. H. Baek, N. Balke, C. M. Brooks, D. A. Tenne, D. G. Schlom, L. Q. Chen, X. Q. Pan, S. V. Kalinin, V. Gopalan, and C. B. Eom. Ferroelectricity in Strain-Free SrTiO3 Thin Films. *Phys. Rev. Lett.*, 104 (19), MAY 14 2010. ISSN 0031-9007. doi: {10.1103/PhysRevLett.104.197601}.

[81] Atif Imtiaz and Steven M. Anlage. A novel microwave frequency scanning capacitance microscope. *Ultramicroscopy, Volume*, 94,:Issues3–4,Pages209–216, April 2003.

[82] Y. Qi, H. Zheng, R. Ramesh, and S. M. Anlage. Local Dielectric Measurements of $BaTiO_3$-$CoFe_2O_4$ Nano-composites Through Microwave Microscopy. *J. Mat. Res.*, 22,:1193–1199, 2007.

[83] J. Lee, C. J. Long, H. Yang, X.-D. Xiang, and I. Takeuchi. Atomic resolution imaging at 2.5 GHz using near-field microwave microscopy. July 2010.

[84] J. Mateu, N. Orloff, M. Rinehart, and J. C. Booth. Broadband Permittivity of Liquids Extracted from Transmission Line Measurements of Microfluidic Channels. In *Proc. IEEE/MTT-S Int. Microwave Symp*, pages 523–526, 2007. doi: 10.1109/MWSYM.2007.380523.

[85] J.C. Booth, N.D. Orloff, and J.M. Mateu. Nonlinear Effects in Thin-Film Ferroelectric Transmission Lines at Microwave Frequencies. In *Proc. 17th IEEE Int. Symp. the Applications of Ferroelectrics ISAF 2008*, volume 2, pages 1–2, 2008. doi: 10.1109/ISAF.2008.4693758.

[86] J.C. Booth, N.D. Orloff, and J. Mateu. Measurement of the Microwave Nonlinear Response of Combined Ferroelectric-Superconductor Transmission Lines. *IEEE Transactions on Applied Superconductivity*, 19(3):940–943, 2009. doi: 10.1109/TASC.2009.2018087.

[87] J. Mateu, C. Collado, N. Orloff, J. C. Booth, E. Rocas, A. Padilla, and J. M. O'Callaghan. Third-Order Intermodulation Distortion and Harmonic Generation in Mismatched Weakly Nonlinear Transmission Lines. *IEEE Transactions on Microwave Theory and Techniques*, 57(1):10–18, 2009. doi: 10.1109/TMTT.2008.2009083.

Nathan D. Orloff

Electromagentics Division
National Institute of
Standards and Technology
325 Broadway Ave.
Boulder, CO 80305

2718 Moorhead Ave. #101
Boulder, CO 80305
(c) 303.999.6512
nathan.orloff@gmail.com

Education

2010 **Ph.D., Physics** University of Maryland,

Thesis Title: *Broadband In-plane Relative Permittivity Characterization of Ruddlesden-Popper* $Sr_{(n+1)}\,Ti_{(n)}\,O_{(3n+1)}$ *Thin Films*

Advisor: Prof. Ichiro Takeuchi, and James C. Booth

2007 **M.S., Physics** University of Maryland,

2004 **B.S., Physics** University of Maryland,

Thesis Title: *Experimental Verification of Transmission Characteristics, Negative Index of Refraction,*
and Negative Goos-Hanchen Effect in Negative Index of refraction Media

Advisor: Prof. Steven M. Anlage

Awards

2010 *Dr. Michael J. Pelczar Award for Excellence in Graduate Study*,
The Graduate School of the University of Maryland, University of Maryland ($1000)

2010 *Honorable Mention, Block Award for Best Poster Presentation, Experiment*, Aspen Center For Physics ($250)

2010 *Graduate Student Travel Support*, Fundamental Physics of Ferroelectrics and Related Materials,
Aspen Center For Physics ($500)
*Awarded to graduate students accepted to present research

2009 *Graduate Student Travel Support*, Physics & Chemistry of Microfluidics, Gordon Research Conference ($450)
*Awarded to graduate students accepted to present research

2005 *Dean's Award for Excellence: Graduate Teaching Assistant Award*,
College of Computer, Mathematical, and Physical Science, University of Maryland ($700)

2005 *Award for Excellence in Teaching*, Department of Physics, University of Maryland

2004 *Monroe H. Martin Prize for Undergraduate Research,* Institute for Physical Sciences and Technology,
University of Maryland ($500)

2004 *High Honors,* Department of Physics, University of Maryland ($250)

Funding

2008 NIST, Director's Reserve Funding, J. C. Booth, C. Holloway, N. D. Orloff, *Superconducting Metamaterials*, $450K/3 years

---

Book Chapters

1. J. C. Booth, N. D. Orloff, J. Mateu, and I. Takeuchi, *Ferroelectric Films at Microwave Frequencies*, edited by T.J. Jackson, P.M. Suherman and P. Bao, ISBN: 978-81-308-0379-1

Peer-Reviewed Publications

In Review

10. E. Rocas, C. Collado, A. Padilla, J. Mateu, N. D. Orloff, J. O'Callaghan, J. C. Booth, *On the third-order intermodulation distortion of Bulk Acoustic Wave resonators*, IEEE Trans. Microwave Theory Tech., (2010).

9. E. Rocas, C. Collado, N. D. Orloff, A. Padilla, J. Mateu, J. O'Callaghan, J. C. Booth, *On the third-order intermodulation distortion due to self heating in transmission lines*, IEEE Trans. Microwave Theory Tech., (2010).

Published

8. C. Collado, E. Rocas, A. Padilla, J. Mateu, N. D. Orloff, J. O'Callaghan, J. C. Booth, *Characterization of the First Order Nonlinear Stiffened Elasticity of the Piezoelectric Layer in Bulk Acoustic Wave Resonators*, IEEE Trans. Microwave Theory Tech., Accepted (2010).

7. N. D. Orloff, J. Mateu, A. Lewandowski, E. Rocas, J. King, X. Lu, C. Collado, I. Takeuchi, J. C. Booth, *A Compact Variable-Temperature Broadband Series-Resistor Calibration*, IEEE Trans. Microwave Theory Tech., Accepted (2010).

6. J. C. Booth, N. D. Orloff, Joel Cagnon, Jiwei Lu, S. Stemmer, *Temperature dependent relaxation in Bismuth Zinc Niobate Thin Films*, Appl. Phys. Lett., Accepted (2010).

5. J. C. Booth, N. Orloff, J. Mateu, M. Janezic, M. Rinehart, J. A. Beall, *Quantitative Permittivity Measurements of Nanoliter Liquid Volumes in Microfluidic Channels to 40 GHz*, IEEE Instr. Measurement, Accepted (2010).

4. N. D. Orloff, W. Tian, C. J. Fennie, D. Gu, K. M. Rabe, D. G. Schlom, I. Takeuchi, and J. C. Booth, *Broadband Dielectric Spectroscopy of Ruddlesden-Popper* $Sr_{n+1}Ti_nO_{3n+1}$ *(n = 1, 2, 3) Thin Films*, Appl. Phys. Lett. **94**, 042908 (2009).

3. J. Mateu, C. Collado, N. Orloff, J. C. Booth, E. Rocas, A. Padilla, J. M. O'Callaghan, *Third order Intermodulation Distortion and Harmonic Generation in Mismatched Weakly Nonlinear Transmission Lines*, IEEE Trans. Microwave Theory Tech., **57**, 1 (2009).

2. J. C. Booth, N. Orloff, J. Mateu, *Nonlinear Compensation in Combined HTS/Ferroelectric Devices at Microwave Frequencies*, IEEE Trans. Appl. Supercon., **19**, 3 (2009).

1. M. Ricci, N. Orloff, and S. M. Anlage, *Superconducting Metamaterials*, Appl. Phys. Lett., **87**, 034102 (2005).

Published Conference Proceedings

7. E. Rocas, C. Collado, N. D. Orloff, and J. C. Booth, *Third-order intermodulation distortion due to self-heating in gold coplanar waveguides*, 2010 International Microwave Symposium, IEEE-MTT, Piscataway, NJ, 2010 (Accepted)

6. E. Rocas, C. Collado, N. D. Orloff, and J. C. Booth, *Third-order intermodulation distortion due to self-heating in gold coplanar waveguides*, 2010 International Microwave Symposium, IEEE-MTT, Piscataway, NJ, 2010 (Accepted)

5. N. D. Orloff, J. C. Booth, M. Murakami, and I. Takeuchi, *Broadband Permittivity Measurements of Thin-Film Ferroelectrics to 40 GHz*, 2008 International Symposium on Applications of Ferroelectrics, IEEE-ISAF, Piscataway, NJ, 2008.

4. J. C. Booth, N. Orloff, J. Mateu, *Nonlinear Effects in Thin-Film Ferroelectric Transmission Lines at Microwave Frequencies*, IEEE-ISAF, Piscataway, NJ, 2008.

3. N. Orloff, J. Mateu, M. Murakami, J. C. Booth, and I. Takeuchi, *Broadband characterization of multilayer dielectric thin-films*, 2007 International Microwave Symposium, IEEE-MTT, Piscataway, NJ, 2007, pp. 1177-1180.

2. J. Mateu, N. Orloff, M. Rinehart, J. C. Booth, and J. A. Beall, *Broadband permittivity of liquids extracted from transmission line measurements of microfluidic channels*, 2007 International Microwave Symposium, IEEE-MTT, Piscataway, NJ, 2007, pp. 523-526.

1. S. M. Anlage, M. Ricci, and N. Orloff, *Superconducting Metamaterials*, 2006 IEEE Antennas and Propagation Society International Symposium, IEEE, Piscataway, NJ, 2006, p. 546.

Invited Talks

2. N. D. Orloff, C.-H. Lee, C. J. Fennie, L. Fitting Kourkoutis, H.Q. Wang, Y. Kim, N.J. Podraza, R.F. Berger, E. Vlahos, M. Bernhagen, R. Uecker, V. Gopalan, X.X. Xi, J.B. Neaton, J.D. Brock, D.A. Muller, I. Takeuchi, J.C. Booth, D. G. Schlom, *Strain-induced Ferroelectricity in Ruddlesden-Popper Homologous Series* $Sr_{n+1}\,Ti_n\,O_{3n+1}$, International Symposium on Integrated Functionalities, San Juan, Puerto Rico (2010).

1. N. D. Orloff, *Dielectric Characterization of Proteins and Binary Fluids for Metrology, Diagnostic & Biological*, NIST, Gaithersburg, MD (2009).

Selected Contributed Talks

2. N. D. Orloff, C.-H. Lee, C. J. Fennie, X. X. Xi, I. Takeuchi, J. C. Booth, and D. G. Schlom, *Strain-Induced Ferroelectricity in $Sr_{n+1}Ti_nO_{3n+1}$ Phases on $GdScO_3$*, Advances in the Fundamental Physics of Ferroelectrics and Related Materials, Aspen Center for Physics (2010).

1. N. D. Orloff, J. R. Dennis, X. Lu, J. King, I. Takeuchi, and J. C. Booth, *Broadband Microwave Sensing of Bovine Serum Albumin and Insulin Solutions at Nanoliter Volumes*, Physics & Chemistry of Microfluidics, Gordon Research Conference (2009).

Author of over 14 contributed talks, co-author of over 8 contributed talks, and the co-author of over 6 invited talks.

Graduate Teaching Assistant Experience

PHYS122, Spring 2005
Taught discussion and laboratory sections for "Physics for Biologist", *Awarded Departmental Honors for a Teaching Assistant

PHYS122, Fall 2004
Taught discussion and laboratory sections for "Physics for Biologist", *Awarded CMPS Outstanding Graduate Teaching Assistant

Undergraduate Student Mentoring

Josh P. King (joshua.p.king@colorado.edu), Undergraduate Student at University of Colorado, Boulder.

Research Skills

Laboratory Agilent/Hewlett-Packard Vector Network Analyzers (E8361C, 8510, 8722D), Anritsu Vector Network Analyzer (Lightning 37000D), Agilent Precision LCR Meter (E4980A), Metal Inert Gas (MIG) Welding, ASLM Stepper,Suss Contact Aligner, Cyrogenics, Microwave Engineering, Lithography and E-beam

Computer AutoCad, Xic Graphical Editor, High Frequency Simulation Software (HFSS), Maxwell Q3D, Sonnet, MatLab, Mathematica, LabView, Origin, LaTeX, Adobe Illustrator, Inkscape, KeyNote, Microsoft Office, etc.

Extensive cleanroom experience and programming experience in MatLab.

Professional Affiliations

American Physical Society (APS)
Institute of Electrical and Electronics Engineers (IEEE)
Materials Research Society (MRS)
Biophysical Society (BPS)

References

James C. Booth, Ph. D.
National Institute of
Standards and Technology
Mail Stop 818.01
325 Broadway
Boulder, CO 80305
ph: 303.497.7900
booth@boulder.nist.gov

Prof. Ichiro Takeuchi
University of Maryland,
College Park
Department of Materials Science
and Engineering
Room 1242
Jeong H. Kim Engineering Building
College Park, MD 20742
ph: 301.405.6809
takeuchi@umd.edu

Michael Kelley, Ph. D.,
Division Chief
National Institute of
Standards and Technology
Mail Stop 817.03
325 Broadway
Boulder, CO 80305
ph: 303.497.4736
michael.kelley@nist.gov

Prof. J. Robert Dorfman
University of Maryland,
College Park
Department of Physics
1108 IPST
College Park, MD 20742
ph: 301.405.4804
jrd@glue.umd.edu

Ron Ginely, Group Leader
National Institute of
Standards and Technology
Mail Stop 818.01
325 Broadway
Boulder, CO 80305
ph: 303.497.3634
rginley@nist.gov

Prof. Steven M. Anlage
University of Maryland,
College Park
Department of Physics
1363 Physics Building
ph: 301.405.7321
anlage@umd.edu

Pavel Kabos, Ph. D.
National Institute of
Standards and Technology
Mail Stop 818.01
325 Broadway
Boulder, CO 80305
ph: 303.497.3997
kabos@boulder.nist.gov

Prof. Carlos Collado
Universitat
Politècnica de Catalunya
collado@tsc.upc.edu

Prof. Darrell G. Schlom
Cornell University
Department of Materials
Science and Engineering
230 Bard
ph: 607.255.6504
ds636@cornell.edu

Prof. Jordi Mateu
Universitat
Politècnica de Catalunya
jmateu@tsc.upc.edu